

University of Nevada, Reno

**Activating Methane and Other Small Molecules: Computational study of Zeolites and Actinides**

A dissertation completed in partial fulfillment of the  
requirements for the degree of **Doctor of Philosophy** in  
Chemistry

by

Olajumoke .D. Adeyiga

Dr. Samuel .O. Odoh/Dissertation Advisor

December 2022

Copyright © 2022 by Olajumoke Adeyiga  
All Rights Reserved

UNIVERSITY OF NEVADA, RENO  
THE GRADUATE SCHOOL

We recommend that the dissertation  
prepared under our supervision by

**OLAJUMOKE DUNSIN ADEYIGA**

entitled

**Activating Methane and Other Small Molecules: Computational study of Zeolites and Actinides**

be accepted in partial fulfillment of the requirements for the degree of

**DOCTOR OF PHILOSOPHY**

Samuel Odoh, Ph.D., Advisor

David Leitner, Ph.D.,  
*Committee Member*

Sergey Varganov, Ph.D.,  
*Committee Member*

Victor Vasquez, Ph.D.,  
*Committee Member*

David Alvarez-Ponce, Ph.D.,  
*Graduate School Representative*

Markus Kemmelmeier, Ph.D., Dean  
*Graduate School*

December, 2022

## ABSTRACT

Exploring the catalytic properties and reactivity of actinide complexes towards activation of small molecules is important as human activities have led to the increased distribution of these species in nature. Toward this end, it is important to have a computational protocol for studying these species, in this thesis we provide details on the performance of multiconfigurational pair-density functional theory (MC-PDFT) in actinide chemistry. MC-PDFT and Kohn-Sham Density Functional Theory (KS-DFT) perform well for these species with indications that the former can be used for species with even greater static electron correlation effect. In addition, we study the activity of organometallic trans-uranium complexes towards the electrocatalytic reduction of water. We conclude that, with a guided choice of ligand, neptunium complexes can provide similar reactivity when compared to organometallic uranium complexes.

Conversion of methane to methanol has been a major focus of research interest over the years. This is largely due to the abundance of natural gas, of which methane is the major constituent. Copper-exchanged zeolites have been shown to be able to kinetically trap activated methane as strongly-bound methoxy groups, preventing over-oxidation to CO<sub>2</sub>, CO and HCOOH. In this stepwise process, there are three cycles; an initial activation step to form the copper oxo active site, methane C-H activation and lastly simultaneous desorption of methanol and re-activation of the active site.. We provide detailed description of the pathway for the formation of over oxidation products. It is observed that to ensure high selectivity to methanol and prevent further hydrogen atom abstraction by extra-framework species, the methyl group must be stabilized from the copper-oxo active sites. There is a temperature gradient between the steps in the methane-to-methanol conversion cycle which is an impediment to industrial adoption of this approach for methane-to-methanol conversion. To mitigate this, we have investigated the impact of heterometallic extra-framework motifs on the temperature gradients of each step. Using periodic DFT, we provide detailed descriptions of the mechanistic pathways for each of the three steps. We were subsequently able to design motif(s) with great methane C-H activities as well as the abilities to be formed and regenerated at nearly the same temperatures. We found [Cu-O-Ag] and [Cu-O-Pd] to be potential candidates for isothermal or near-isothermal operations of the methane-to-methanol conversion cycle.

Finally, we provide insights to the changes in optical spectra of activated copper-exchanged zeolites, gaining an understanding of the evolution of these systems on a molecular level will provide opportunities to achieve improved reactivity.

**DEDICATION**

Dedicated to my daughter, Irekanmi  
I hope this inspires you to reach for greater heights.

## ACKNOWLEDGEMENTS

I extend my unreserved thanks to Dr. Samuel Odoh, you are an impressive supervisor. From you I learned a ton about Chemistry, critical and analytical thinking, but even more than that I learned to be patient, encouraging, and dutiful. I can only hope to be as impactful to my students when the time comes. I also acknowledge the rest of my committee members, Dr. David Leitner, Dr. Sergey Varganov, Dr. Victor Vasquez and Dr. David Alvarez-Ponce, their helpful insights and generosity with their time is greatly appreciated.

I am especially grateful to the National Science Foundation and University of Nevada, Reno for the financial support I was granted. I want to thank my group members Dr. Naveen Dandu (postdoc), Dr. Dipak Panthi, Olabisi Suleiman, and Kevin Curtis for their assistance and teamwork on multiple projects.

To my parents, Samson and Oyenike Adeyiga I will like to use this opportunity to thank you for instilling discipline and the value of education in me. Without you, this would not be achievable. To my lovely husband, Olawole, you are without doubt my biggest support system, thank you for being ever present and loving. To my elder brother, Olajide and the rest of my siblings Japheth and Pelumi, thank you for your support and encouragement. Finally, I will like to thank my relatives (Julius and Dr. Valda Adeyiga) and friends; Temitayo, Oluwatosin, Taiwo, and Mitra from whom I received tremendous support.

## TABLE OF CONTENTS

LIST OF TABLES .....	ix
LIST OF FIGURES .....	x
CHAPTER 1. INTRODUCTION .....	1
1.1 Zeolites and their applications.....	1
1.2 Actinides and their uses.....	2
1.3 Quantum-Mechanical Methods .....	3
1.3.1 Hartree-Fock Theory .....	3
1.3.2 Coupled Cluster .....	4
1.3.3 Complete Active Space Self-Consistent Field (CASSCF) Theory .....	5
1.3.4 Multiconfiguration Pair Density Functional Theory (MC-PDFT).....	5
1.3.5 Kohn-Sham Density Functional Theory (KS-DFT) .....	6
1.3.5.1 Local Density Approximation (LDA).....	7
1.3.5.2 Generalized Gradient Approximation (GGA) .....	7
1.3.5.3 Meta-Generalized Gradient Approximation (meta-GGA).....	7
1.3.5.4 Hybrid Functionals.....	8
1.3.6 Periodic Density Functional Theory (Periodic DFT) .....	8
1.3.7 Time Dependent Density Functional Theory (TD- DFT) .....	9
1.4 Relativistic Effects .....	9
1.5 Solvation Effects .....	10
1.6 Dispersion Effects .....	10
1.7 Basis Sets.....	11
1.8 Organization of Thesis .....	13
CHAPTER 2. GROUND-STATE ACTINIDE CHEMISTRY WITH SCALAR-RELATIVISTIC MULTICONFIGURATION PAIR-DENSITY FUNCTIONAL THEORY.....	20
2.1 INTRODUCTION.....	21
2.2 COMPUTATIONAL DETAILS.....	23
2.2.1 Basis Set and Relativistic Effects: .....	23
2.2.2 Systems Studied:.....	24
2.2.3 Geometries:.....	24
2.2.4 Vibrational Frequencies:.....	25
2.2.5 Symmetry: .....	25
2.2.6 Multireference Calculations .....	26



2.2.6.1. Complete active space self-consistent field calculations:.....	26
2.2.6.2 Complete active space second order perturbation theory calculations:.....	26
2.2.6.3 Complete active space pair-density functional theory calculations: .....	26
2.2.7 Kohn-Sham DFT Calculations: .....	26
2.2.8 Coupled Cluster Calculations: .....	26
2.2.9 Software:.....	27
2.3. RESULTS AND DISCUSSIONS .....	27
2.3.1 Structural Properties of the Actinyl Groups. ....	27
2.3.2 Potential Energy Curves. ....	29
2.3.2.1. $\text{NpO}_2^{3+}$ : .....	29
2.3.2.2. Actinyl-Ligand Bonds: .....	31
2.3.2.3 Actinyl-Ligand Bond Dissociation Energies: .....	32
2.3.2.4 Vibrational Frequencies:.....	33
2.3.3 Reaction Energies. ....	34
2.3.3.1 Water-induced redox processes: .....	34
2.3.3.2 Redox potentials: .....	35
2.4. CONCLUSIONS .....	36
CHAPTER 3. ACTIVATING WATER AND HYDROGEN BY LIGAND-MODIFIED URANIUM AND NEPTUNIUM COMPLEXES: A DFT STUDY .....	42
3.1 INTRODUCTION.....	43
3.2 COMPUTATIONAL DETAILS .....	45
3.3 RESULTS AND DISCUSSION .....	46
3.3.1 Hydrogen Evolution from Water: .....	46
3.3.1.1. Confirmation of trends for the HER: .....	48
3.3.2 Hydrogen Capture and Hydride Transfer by Bis-Uranium Nitrides: .....	49
3.3.2.1. Structural and electronic properties: .....	49
3.3.2.2. Reaction energies for $\text{H}_2$ capture and hydride transfer: .....	50
3.3.2.3. $\text{H}_2$ capture and hydride transfer by Np analogues .....	52
3.4 CONCLUSIONS .....	54
CHAPTER 4. METHANE OVER-OXIDATION BY EXTRA-FRAMEWORK COPPER-OXO ACTIVE SITES OF COPPER-EXCHANGED ZEOLITES: CRUCIAL ROLE OF TRAPS FOR THE SEPARATED METHYL GROUP .....	59
4.1 INTRODUCTION.....	60

4.2 COMPUTATIONAL METHODS AND MODELS .....	62
4.2.1 Cluster-model Calculations: .....	62
4.2.2 Periodic DFT: .....	63
4.3 RESULTS AND DISCUSSION .....	64
4.3.1 Mechanism for Methane Activation and Over-Oxidation: .....	64
4.3.2 Formation of Formates: .....	70
4.3.3 Zeolite Confinement Effects: .....	71
4.3.4 Impact of the Exchange-Correlation Density Functional: .....	72
4.4 CONCLUSIONS .....	72
CHAPTER 5. COPPER OXO ACTIVE SITES FOR METHANE C-H ACTIVATION IN ZEOLITES: MOLECULAR UNDERSTANDING OF IMPACT OF METHANE HYDROXYLATION ON UV-VIS SPECTRA .....	77
5.2 METHODOLOGY .....	80
5.2.1 Geometry Optimizations .....	80
5.2.2 Electronic Structure Analysis: .....	80
5.2.3 TD-DFT Calculations .....	80
5.3 RESULTS AND DISCUSSIONS .....	80
5.3.1. Dicopper Mono-Oxo $[\text{Cu}_2\text{O}]^{2+}$ System .....	80
5.3.2. Tricopper Trioxo $[\text{Cu}_3\text{O}_3]^{2+}$ System .....	85
5.4 CONCLUSIONS .....	93
CHAPTER 6. HETEROMETALLIC $[\text{Cu-O-M}]^{2+}$ ACTIVE SITES FOR METHANE C-H ACTIVATION IN ZEOLITES: STABILITY, REACTIVITY, FORMATION MECHANISM AND RELATIONSHIP TO OTHER ACTIVE SITES .....	100
6.1 INTRODUCTION .....	101
6.2 COMPUTATIONAL DETAILS .....	103
6.2.1 Periodic DFT Calculations: .....	103
6.2.2 Formation Reaction .....	104
6.2.3 Decomposition with Oxygen Elimination .....	106
6.2.4 Cluster-model Calculations .....	106
6.3.1 Optimized Structures .....	107
6.3.2 Formation Energies .....	108
6.3.3 Decomposition via Oxygen Elimination .....	110
6.3.4 Reactivity with Methane .....	111

6.3.5 Formation Mechanism of $[\text{Cu}_2\text{O}]^{2+}$ Sites .....	113
6.3.5 Free Energy Corrections and Comparison to other copper-oxo Sites .....	116
6.4 CONCLUSIONS .....	118
CHAPTER 7. SUMMARY AND CONCLUSIONS .....	125
LIST OF PUBLICATIONS .....	127

## LIST OF TABLES

Table 1.1: Electronic configuration of actinide elements and their various oxidation states. ....	2
Table 2.1: Systems studied in this work. ....	24
Table 2.2: Ground state character of the $\text{AnO}_2^{m+}$ species. ....	25
Table 2.3: Comparison of the actinyl bond-lengths from all-electron scalar-relativistic CASPT2 and CCSD(T) calculations with CCSDT results using scalar-relativistic effective core potentials. ....	29
Table 2.4: Deviations (given in kcal/mol) for CASSCF, CCSD(T), MC-PDFT and KS-DFT from CASPT2 for the binding energies of $\text{F}^-$ to $\text{UO}_2^{2+}$ , $\text{NpO}_2^{2+}$ and $\text{PuO}_2^{2+}$ . ....	32
Table 2.5: Deviations ( $\text{cm}^{-1}$ ) of various methods from CASPT2 for the frequencies of the symmetric stretching vibrational mode of $\text{UN}_2$ and actinyl groups. ....	34
Table 2.6: Deviations (given in kcal/mol) for CASSCF, CCSD(T), MC-PDFT and KS-DFT from CASPT2 for the energetics of the water-induced reduction of actinyl groups (reactions 1 and 2). ....	35
Table 2.7: Experimental and calculated adiabatic reduction potentials (eV) for various actinyl species. ....	35
Table 3.1: Comparison of the calculated structural properties of $[(\text{O})\text{U}-\text{N}-\text{U}(\text{O})][\text{OSi}(\text{O}-t\text{-Bu})_3]^-$ and $[(\text{N})\text{U}-\text{N}-\text{U}(\text{N})][\text{N}(\text{SiMe}_3)_2]^-$ to the crystal structure parameters. Bond lengths are given in Å while bond angles are given in $^\circ$ . ....	50
Table 3.2: Calculated reaction energies and enthalpies, kcal/mol, for $\text{H}_2$ capture and hydride transfer by $[(\text{O})\text{U}-\text{N}-\text{U}(\text{O})][\text{OSi}(\text{O}-t\text{-Bu})_3]^-$ and $[(\text{N})\text{U}-\text{N}-\text{U}(\text{N})][\text{N}(\text{SiMe}_3)_2]^-$ . ....	51
Table 3.3: Calculated reaction energies and enthalpies, kcal/mol, for $\text{H}_2$ capture and hydride transfer by $[(\text{O})\text{Np}-\text{N}-\text{Np}(\text{O})][\text{OSi}(\text{O}-t\text{-Bu})_3]^-$ and $[(\text{N})\text{Np}-\text{N}-\text{Np}(\text{N})][\text{N}(\text{SiMe}_3)_2]^-$ . ....	53
Table 4.1: Calculated reaction energies and free-energies, kcal/mol, obtained at the PBE/L1, PBE-D3BJ/def2-TZVPP and B3LYP-D3BJ/def2-TZVPP levels for the first 4 HAA steps. ....	65
Table 4.2: Partial atomic charges and spin densities on the C atom during the first and second HAA steps. ....	66
Table 5.1: Characters of the dominant excitations, in $\text{cm}^{-1}$ , in the TDA-DFT spectrum of $[\text{Cu}_3\text{O}_3]^{2+}$ . ....	90
Table 5.2: Characters of the dominant excitations, in $\text{cm}^{-1}$ , in the TDA-DFT spectrum of 5.5h. ....	93
Table 6.1: Ground state multiplicities ( $2S+1$ ) of the $[\text{Cu}-\text{O}-\text{M}]^{2+}$ active sites in the MOR zeolite. ....	105
Table 6.2: Calculated formation energies for the $[\text{Cu}_2\text{O}]^{2+}$ active site. ....	108
Table 6.3: Energies, kcal/mol, for $\text{O}_2$ elimination from $[\text{Cu}_2\text{O}]^{2+}$ and $[\text{Cu}-\text{O}-\text{M}]^{2+}$ active sites. ....	111
Table 6.4: Relative energies (kcal/mol) of the intermediates formed after methane C-H activation by various $[\text{Cu}-\text{O}-\text{M}]^{2+}$ active sites. The associated transition state barriers are given in parenthesis. ....	112
Table 6.5: Energies, kcal/mol, for formation of $[\text{Cu}_2\text{O}]^{2+}$ , $[\text{Cu}_3\text{O}_3]^{2+}$ , isolated $[\text{Cu}-\text{OH}]^+$ and paired $[\text{Cu}-\text{OH}]^+$ active sites. Temperatures at which $\Delta G$ becomes 0.0 kcal/mol are in $^\circ\text{C}$ . ....	117

## LIST OF FIGURES

Figure 1.1: Different types of excited Slater determinants generated from a HF reference.....	4
Figure 1.2: Modelling a 1s-STO with GTOs. <sup>33</sup> .....	12
Figure 1.3: Schematic description of remaining chapters in this thesis.....	13
Figure 2.1: MADs and RMSDs relative to CASPT2 for bond distances of actinyls.....	28
Figure 2.2: Potential energy curves for $\text{NpO}_2^{3+}$ . Comparison of CASPT2 and CCSDT to (A) KS-DFT functionals, (B) KS-DFT and MC-PDFT functionals, (C) Expanded 165-180° range of A and (D) Expanded 165-180° range of B. The Np-O bond distances were fixed at 1.685 Å.....	30
Figure 2.3: Potential energy curves for the U-F bond of $\text{UO}_2\text{F}^+$ obtained with (A) CASPT2, CCSD(T) and MC-PDFT functionals and (B) CASPT2, CCSD(T) and KS-DFT functionals. ...	32
Figure 2.4: Calculated symmetric stretching vibrational frequencies obtained with various methods. ....	33
Figure 2.5: Mean absolute deviations (A) and signed deviations (B), eV, of KS-DFT, CCSD(T), CASSCF, MC-PDFT and CASPT2 from experimental estimates of the ionization potentials....	36
Figure 3.1: Structures of A. $[(^{\text{Ad,Me}}\text{ArO})_3\text{mes})\text{U}]\cdot\text{OH}_2$ B. $[(^{\text{Ad,Me}}\text{ArNH})_3\text{mes})\text{Np}]\cdot\text{OH}_2$ C. $[(\text{N})\text{U}-\text{N}-\text{U}(\text{N})]^-$ and D. $[(\text{O})\text{U}-\text{N}-\text{U}(\text{O})]^-$ . The ligands are depicted with wireframes for better visibility. A and B are studied for HER while C and D are studied for $\text{H}_2$ capture and hydride transfer.....	45
Figure 3.2: Overall reaction energy profiles for $[(^{\text{Ad,Me}}\text{ArO})_3\text{mes})\text{U}]\cdot\text{OH}_2$ , $[(^{\text{Ad,Me}}\text{ArO})_3\text{mes})\text{Np}]\cdot\text{OH}_2$ and $[(^{\text{Ad,Me}}\text{ArNH})_3\text{mes})\text{Np}]\cdot\text{OH}_2$ . These species are labeled as U-O, Np-O and Np-NH respectively. The results based on electronic energies are shown on the <i>left</i> while those including enthalpic, solvent and spin-orbit corrections are shown on the <i>right</i> . ....	47
Figure 3.3: ( <i>left</i> ) Reaction profiles for $[(^{\text{Ad,Me}}\text{ArO})_3\text{mes})\text{U}]\cdot\text{OH}_2$ , $[(^{\text{Ad,Me}}\text{ArO})_3\text{mes})\text{Np}]\cdot\text{OH}_2$ and $[(^{\text{Ad,Me}}\text{ArNH})_3\text{mes})\text{Np}]\cdot\text{OH}_2$ obtained with the B3LYP-D3BJ functional. ( <i>right</i> ) Reaction profiles obtained for $\text{H}_2$ evolution from water by $[\text{U}(\text{OMe})_3]$ , $[\text{Np}(\text{OMe})_3]$ and $[\text{Np}(\text{NMe}_2)_3]$ obtained with the PBE-D3BJ functional.....	48
Figure 3.4: Calculated pathway for $\text{H}_2$ capture and hydride transfer by $[(\text{N})\text{U}-\text{N}-\text{U}(\text{N})][\text{N}(\text{SiMe}_3)_2]^-$ obtained at the PBE/L1 level of theory.....	52
Figure 3.5: Calculated pathway for $\text{H}_2$ capture and hydride transfer by $[(\text{O})\text{U}-\text{N}-\text{U}(\text{O})][\text{OSi}(\text{O}-t\text{-Bu})_3]^-$ obtained at the PBE/L1 level of theory. ....	53
Figure 3.6: The structure of $[(\text{N})\text{U}-(\text{H})(\text{NH})-\text{U}(\text{N})][(\text{NH})\text{Si}(\text{O}-t\text{-Bu})_3]^-$ is shown on the <i>left</i> . This species is formed after $\text{H}_2$ capture and hydride transfer by $[(\text{N})\text{U}-\text{N}-\text{U}(\text{N})][(\text{NH})\text{Si}(\text{O}-t\text{-Bu})_3]^-$ . The reaction energies for $\text{H}_2$ capture and hydride transfer by various species are shown on the <i>right</i> .....	54
Figure 4.1: Activation of methane C-H bond to methanol by $[\text{Cu}_3\text{O}_3]^{2+}$ active site, steam-facilitated extraction of products and regeneration of the active copper oxo cluster.....	61
Figure 4.2: Models for the $[\text{Cu}_3\text{O}_3]^{2+}$ active site in MOR. (A) Periodic unit cell showing the immediate environment around $[\text{Cu}_3\text{O}_3]^{2+}$ . (B) Rotated view of the unit cell to better visualize the location of the active site at the 8MR. (C) Proton-terminated cluster model. H, O, Al, Si and Cu atoms are represented with white, red, light pink, grey and brown spheres, respectively. ....	63
Figure 4.3: Activation of methane via 4 successive hydrogen atom abstraction (HAA) steps on extra-framework $[\text{Cu}_3\text{O}_3]^{2+}$ in zeolite MOR. ....	64

Figure 4.4: Species involved in the first HAA step. Terminating protons are omitted for better visibility. Energies and barrier, in kcal/mol and green, at the PBE/L1 level are given relative to the reactant complex. ....	66
Figure 4.5: Species involved in the second HAA step. Energies and barrier, in kcal/mol and green, at the PBE/L1 level are given relative to the reactant complex. ....	67
Figure 4.6: Species involved in the third HAA step. The structures of TS-3 and $\mu$ -(O=CH) group are slightly rotated to better depict the HAA. Energies and barrier, in kcal/mol and green, at the PBE/L1 level are given relative to the reactant complex. ....	68
Figure 4.7: Species involved in the fourth HAA step. Energies and barrier, in kcal/mol and green, at the PBE/L1 level are given relative to the reactant complex. ....	69
Figure 4.8: Conversion of the $\mu$ -(O=CH) group to formic acid and formates. Reaction energies, in kcal/mol, at the PBE/L1 level of theory are given relative to the $\mu$ -(O=CH) structure. ....	71
Figure 4.9: Comparison of calculated reaction energies and barriers for the first two HAA steps with cluster-model and periodic DFT calculations. ....	71
Figure 5.1: Optimized structures of the cluster models of $[\text{Cu}_2\text{O}]^{2+}$ . A is the cluster model for the active site. B-E are possible intermediates formed after methane C-H activation. The considered spin states are provided. ....	81
Figure 5.2: Frontier orbitals of the open-shell singlet ground state of the $[\text{Cu}_2\text{O}]^{2+}$ cluster model obtained with the $\omega$ B2LYP functional and cc-pVDZ basis sets. ....	83
Figure 5.3: Frontier orbitals of the open-shell singlet ground state of the $[\text{Cu}_2\text{O}]^{2+}$ active site after methane activation. These were obtained at the $\omega$ B2LYP/cc-pVDZ level. ....	84
Figure 5.4: Calculated spectra obtained at the $\omega$ B2PLYP/cc-pVDZ level for the $[\text{Cu}_2\text{O}]^{2+}$ cluster model and possible intermediates after methane activation. The difference densities between the ground and excited states are shown as insets. ....	84
Figure 5.5: Optimized structures of the cluster models of $[\text{Cu}_3\text{O}_3]^{2+}$ . A is the cluster model for the active site. B-I are possible intermediates formed after methane C-H activation. The ground spin states of these species are provided. ....	86
Figure 5.6: Frontier $\alpha$ -orbitals of the $[\text{Cu}_3\text{O}_3]^{2+}$ cluster model at $\omega$ B2LYP/cc-pVDZ level. ....	87
Figure 5.7: Frontier $\beta$ -orbitals of the $[\text{Cu}_3\text{O}_3]^{2+}$ cluster model at $\omega$ B2LYP/cc-pVDZ level. ....	88
Figure 5.8: Comparison of calculated spectra of $[\text{Cu}_3\text{O}_3]^{2+}$ to several possible intermediates for methane activation, 5.5b-5.5d. ....	89
Figure 5.9: Comparison of calculated spectra of $[\text{Cu}_3\text{O}_3]^{2+}$ to several possible intermediates for methane activation, 5.5e-5.5i. ....	89
Figure 5.10: TDA-DFT spectra of cluster models of 5.5h obtained from AIMD simulations (1-3) are compared to geometry optimized models for 5.5a and 5.5h. ....	91
Figure 5.11: Frontier orbitals of the doublet state of the $[\text{Cu}_3\text{O}_3]^{2+}$ active site after methane activation to form structure 5.5h. These were obtained at the $\omega$ B2LYP/cc-pVDZ level. ....	92
Figure 6.1: Structures of (A) $\text{H}_4\text{MOR}$ , (B) $[\text{Cu}(\text{H}_2\text{O})_6](\text{H}_2\text{MOR})$ and (C) $[\text{Cu}_2\text{O}](\text{H}_2\text{MOR})$ . O, Si, Al and Cu atoms are represented with red, grey, green and blue polyhedra, respectively. Locations of the charge-balancing protons are visible and the aluminates conform to Lowenstein's rule. ....	104

Figure 6.2: Cluster-model structures of (A) $[\text{Cu}_2\text{O}]^{2+}$ and (B) paired $[\text{Cu-OH}]^+$ in MOR. The latter is slightly rotated to allow easy visualization of the copper site. H, O, Si, Al and Cu atoms are represented with white, red, grey, pink and orange spheres, respectively. ....	107
Figure 6.3: Periodic structures of (A) $[\text{Cu}_2\text{O}](\text{H}_2\text{MOR})$ and (B) $[\text{Cu}(\text{H}_2\text{O})_6](\text{H}_2\text{MOR})$ with Al-Si-Si-Al arrangements of the aluminates in the lower 8MR channel. ....	108
Figure 6.4: Formation energies of $[\text{Cu-O-M}](\text{H}_2\text{MOR})$ species from $[\text{Cu}(\text{H}_2\text{O})_6][\text{H}_2\text{MOR}]$ and $[\text{M}(\text{H}_2\text{O})_6][\text{H}_2\text{MOR}]$ species. ....	109
Figure 6.5: Pathway for hexaaquo core of $\text{CuH}_2\text{O}_6\text{H}_2\text{MOR}$ during formation of $[\text{Cu}_2\text{O}]^{2+}$ sites. Reaction energies are given in green and kcal/mol. Barriers are given in red and parenthesis. These are all relative to $\text{CuH}_2\text{O}_6\text{H}_2\text{MOR}$ . The four aluminates of the unit cell are also shown. ....	114
Figure 6.6: Aggregation and dehydration steps during formation of $[\text{Cu}_2\text{O}]^{2+}$ . Reaction energies are given in green and kcal/mol. Barriers are given in red and parenthesis. These are all relative to two $\text{CuH}_2\text{O}_6\text{H}_2\text{MOR}$ reactants. Details of the condensation of $\mu$ -hydroxo groups are shown. ....	115
Figure 6.7: Temperature-dependent free-energy corrections for formation of copper active sites in zeolite MOR. The shaded regions represent $\pm 15$ kcal/mol around the electronic formation energies. ....	118

## CHAPTER 1. INTRODUCTION

### 1.1 Zeolites and their applications

Zeolites are aluminosilicate materials containing aluminate,  $\text{AlO}_4^-$ , and silicate,  $\text{SiO}_4$ , tetrahedra. The excess charge from the aluminate tetrahedra are balanced with positive counterions like protons, ammonium or alkali metals.<sup>1-2</sup> Interestingly, the counterions can be readily exchanged with transition metal ions or transition metal oxide ions.<sup>3-4</sup> The resulting species are called metal-exchanged zeolites. This process of cation exchange enables substitution of the often benign counterions with metal ions that are capable of catalytic transformations.<sup>4-5</sup> There are many different types of zeolitic frameworks, with important differences in the number and sizes of micropores (small, medium or large) as well as the inter-connections between these pores. Additionally, the catalytic properties of zeolites also depend on the composition (Si/Al ratio, nature of charge-balancing ions or extra-framework sites) as well as the size and accessibility of the micropores. Zeolites can also be classified by noting that some, like mordenite (MOR zeolite) and chabazite (CHA zeolite) are naturally occurring and can be mined in different places across the globe; others are synthetic materials, like the pentasil-zeolite (ZSM-5) zeolite with an MFI framework.<sup>6-7</sup>

Zeolites are applied mainly in industry for catalysis, gas separation and ion exchange. They can be used as sieves due to their porous nature, this property enables application in processes like purification and gas separation. Zeolites are very useful as catalysts in several important reactions that involve organic molecules, such as cracking and hydrocarbon synthesis, making zeolites one of the most important catalysts in the petrochemical industry.<sup>8-10</sup>

Importantly, in the direct oxidation of methane-to-methanol, the active sites of methane monooxygenases are mimicked by incorporating transition metals like Cu and Fe into the zeolite framework. These charge-balancing ions are also known as extra-framework species. Metal-exchanged zeolites have been studied extensively over the last few years for their abilities to achieve excellent selectivities for methanol.<sup>11-14</sup> Conversion of methane to methanol using metal exchanged zeolite occurs in a step-wise fashion. The process is sub-stoichiometric and not catalytic as the active site is reduced, resulting in a need for regeneration after production of methanol. The process begins with the formation of the active site, usually at high temperatures. The activation temperature at which this occurs depends on the nature of the active site as well as the zeolite framework. For copper-exchanged zeolites, the temperature for active site formation is usually



around 450 °C. The formation of the active site is followed by the activation of the C-H bond in methane resulting in strongly-bound methoxy groups and consuming the active site. The last process involves regeneration of the active site and methanol release, both concluding the methane-to-methanol conversion (MMC) cycle. In general, the methane activation process is performed at 200 °C while the methanol release and active-site regeneration step is performed at 120-200 °C in copper-exchanged zeolites.<sup>11, 15-18</sup>

In this thesis, we focus on optimizing various stages in the MMC cycle, with the aim of driving the process towards isothermal operation using various quantum-mechanical approaches. Specifically, efforts to understand over-oxidation of methane in Cu-exchanged zeolites, study of hetero-metallic  $[\text{Cu}-\text{O}-\text{M}]^{2+}$  species ( $\text{M} = \text{Ti}-\text{Cu}$ ,  $\text{Zr}-\text{Mo}$  and  $\text{Ru}-\text{Ag}$ ) in zeolite mordenite as well as molecular level understanding of the evolution of Cu species during MMC using UV-Vis spectroscopy.<sup>19-21</sup>

## 1.2 Actinides and their uses

The actinides are the elements on the periodic table with atomic numbers ranging from 89 to 103. Their electronic configuration in the ground state is characterized by partially or fully filled  $5f$  shell, Table 1.1.

**Table 1.1: Electronic configuration of actinide elements and their various oxidation states.**

Element	Configuration	Oxidation states	Element	Configuration	Oxidation states
Actinium	$[\text{Rn}]6d^17s^2$	+3	Berkelium	$[\text{Rn}]5f^97s^2$	+3, +4
Thorium	$[\text{Rn}]6d^27s^2$	+3, +4	Californium	$[\text{Rn}]5f^{10}7s^2$	+2 to +4
Protactinium	$[\text{Rn}]5f^26d^17s^2$	+3 to +5	Einsteinium	$[\text{Rn}]5f^{11}7s^2$	+2, +3
Uranium	$[\text{Rn}]5f^36d^17s^2$	+3 to +6	Fermium	$[\text{Rn}]5f^{12}7s^2$	+2, +3
Neptunium	$[\text{Rn}]5f^46d^17s^2$	+3 to +7	Mendelevium	$[\text{Rn}]5f^{13}7s^2$	+2, +3
Plutonium	$[\text{Rn}]5f^67s^2$	+3 to +7	Nobelium	$[\text{Rn}]5f^{14}7s^2$	+2, +3
Americium	$[\text{Rn}]5f^77s^2$	+3 to +6	Lawrencium	$[\text{Rn}]5f^{14}6d^17s^2$	+3
Curium	$[\text{Rn}]5f^76d^17s^2$	+3 to +5			

Naturally occurring uranium (U), thorium (Th) and protactinium (Pa) are the most abundant actinides on earth, U and Th can undergo radioactive decay to produce Pa. Human activities like nuclear weapon production and nuclear energy production and storage of radioactive wastes, have

increased the distribution of actinides in the environment. It is therefore important to understand the chemistry of these species to enhance utilization.<sup>22-23</sup>

Recent reports by several workers have shown U can catalyze conversion of small molecules like N<sub>2</sub>, H<sub>2</sub>, H<sub>2</sub>O, and CH<sub>4</sub> into useful chemical feedstocks. However, there is not enough understanding of the abilities of trans-uranium complexes to undergo such useful transformations.<sup>24-28</sup> In this thesis, we study the activity of trans-uranium complexes towards catalyzing small-molecule transformations in comparison to their U analogues. Specifically, we study the electrocatalytic evolution of hydrogen from water (HER) using actinide complexes, the actinides of interest are U, neptunium (Np) and plutonium (Pu).<sup>29</sup>

### 1.3 Quantum-Mechanical Methods

#### 1.3.1 Hartree-Fock Theory

Numerous solutions exist to the time-independent Schrödinger equation given in equation 1.1.

$$\hat{H}\Psi = E\Psi \quad (1.1)$$

Some of these solutions are generated without reference to experimental results, i.e. *ab initio*. An essential approximation to solving the Schrödinger equation is the Born-Oppenheimer approximation. This involves neglecting the coupling between the nuclei and electronic motions, allowing the electronic portion to be solved with the nuclear positions as parameters. Despite this approximation, the dynamics for solving a many-electron system can be complicated requiring elaborate computations. One of the simplest solutions is the Hartree-Fock (HF) method, an independent-particle model, i.e. the motion of a given electron is independent of the motions of other electrons in the system. For the HF theory, the interactions between all particles is taken in an average fashion, this is known as the mean-field approximation. Each electron is represented as an orbital and the wavefunction is given by a product of orbitals arranged in a Slater determinant, which is then solved variationally.<sup>30-32</sup>

$$\Phi = \frac{1}{\sqrt{N!}} \begin{bmatrix} \phi_1(\vec{x}_1) & \phi_2(\vec{x}_1) & \cdots & \phi_N(\vec{x}_1) \\ \phi_1(\vec{x}_2) & \phi_2(\vec{x}_2) & \cdots & \phi_N(\vec{x}_2) \\ \vdots & \vdots & \cdots & \vdots \\ \phi_1(\vec{x}_N) & \phi_2(\vec{x}_N) & \cdots & \phi_N(\vec{x}_N) \end{bmatrix} \quad (1.2)$$

Since HF theory employs the mean-field approximation, it only accounts for average electron-electron interaction neglecting electron correlation which is essential for accurate computations. The total HF energy of a single slater determinant, E, can then be given as:

$$E = \sum_i^{N_{elec}} \mathcal{E}_i - \frac{1}{2} \sum_{ij}^{N_{elec}} (J_{ij} - K_{ij}) + V_{nn} \quad (1.3)$$

$$\mathcal{E}_i = \langle \phi_i | F_i | \phi_i \rangle = h_i + \sum_j^{N_{elec}} J_{ij} - K_{ij} \quad (1.4)$$

where  $\mathcal{E}_i$  is the molecular orbital (MO) energy,  $J_{ij}$  and  $K_{ij}$  account for electron-electron repulsion contributions representing the coulomb and exchange terms respectively. To account for electron correlation, methods that generate multi-determinant wave function must be employed.

### 1.3.2 Coupled Cluster

The idea in Coupled cluster method is to improve the wavefunction by including excitations to an infinite order. Starting from the HF wavefunction an excitation operator,  $T$ , is used to generate excited slater determinants as shown below:

$$\Psi_{CC} = e^T \Phi^o \quad (1.5)$$

$$e^T = 1 + T_1 + \left(T_2 + \frac{1}{2}T_1^2\right) + \left(T_3 + T_2T_1 + \frac{1}{6}T_1^3\right) + \dots \quad (1.6)$$

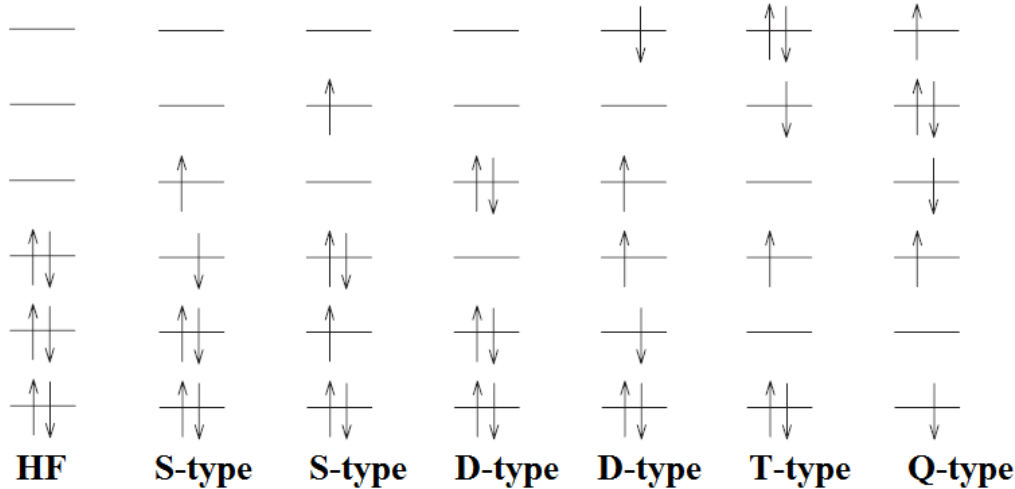


**Figure 1.1: Different types of excited slater determinants generated from a HF reference.<sup>33</sup>**

The final coupled cluster energy,  $E_{CC}$ , can be given as:

$$E_{CC} = E_o + \sum_{i < j}^{occ} \sum_{a < b}^{vir} (t_{ij}^{ab} + t_i^a t_j^b + t_i^b t_j^a) (\langle \phi_i \phi_j | \phi_a \phi_b \rangle - \langle \phi_i \phi_j | \phi_b \phi_a \rangle) \quad (1.7)$$

The cluster operators,  $T_i$ , can be included up to  $T_N$  where  $N$  is the total number of electrons in the system, at this limit coupled cluster will be exact. For this method to be practical,  $T$  has to be truncated at some level due to the exact form being impossible and computationally expensive even for the smallest systems. The lowest level of truncation that provides improvement on the HF

energy is setting  $T = T_2$ , giving rise to the method known as *Coupled Cluster Doubles (CCD)*.<sup>34-35</sup> At this level, accounting for electron correlation energy begins. The next level of truncated coupled cluster is *Coupled Cluster Singles and Doubles (CCSD)* with  $T = T_1 + T_2$ . The truncation progresses in likewise manner with systematic improvement to the wavefunction and energy. In this thesis, CCSD<sup>36</sup> as well as CCSD(T)<sup>36</sup> is employed using MOLCAS code, version 8.1.<sup>37-38</sup>

### 1.3.3 Complete Active Space Self-Consistent Field (CASSCF) Theory

HF and other methods that make use of single Slater determinants fail in the description of multireference systems, that is, systems that require more than a single Slater determinant for accurate description of their wavefunction. The kind of electron correlation dominant in these systems is static, complete active space self-consistent field theory, CASSCF, is an example of multiconfigurational self-consistent field theory, MCSCF, in which full configuration interaction, CI, is carried out for a selected number of orbitals and electrons.<sup>39-42</sup> This selection must be made based on specific considerations, with the most important being the nature of molecular orbitals. Practically, the limit of the active space in CASSCF is about 18 to 24 electrons in 18 to 24 orbitals.<sup>43</sup>

Since CASSCF provides static correlation, to improve the solution, dynamic correlation can be added by coupling CASSCF with second order perturbation theory to yield CASPT2.<sup>44</sup> Both methods are employed in this thesis, as implemented by the MOLCAS code.<sup>37-38</sup>

### 1.3.4 Multiconfiguration Pair Density Functional Theory (MC-PDFT)

In CASPT2, the cost of accounting for dynamical correlation using perturbation theory scales with the system and active space size. To circumvent the scaling difficulty associated with CASPT2, the post-CASSCF calculation can be done using density functional theory, DFT. This leads to a hybrid method, MC-PDFT which captures both static and dynamic electron correlation. The MC-PDFT energy can be given as;

$$E = V_{nn} + 2 \sum_i h_i + 2 \sum_{ij} g_{iijj} + \sum_{vw} h_{vw} D_{vw} + 2 \sum_{i vw} g_{iivw} D_{vw} + \frac{1}{2} \sum_{vwxy} g_{vwxy} D_{vw} D_{xy} + E_{ot}[\rho, \Pi]$$

where  $V_{nn}$  is the nucleus-nucleus repulsion energy,  $h$  and  $g$  represent the one-electron and two-electron integrals respectively,  $D$  is the one-body density matrix.  $i$  and  $j$  are used to denote inactive

orbitals while  $v$ ,  $w$ ,  $x$ , and  $y$  are the active orbitals. The on-top pair-density functional energy,  $E_{ot}[\rho, \Pi]$ , is obtained by ‘*translating*’ existing Kohn-Sham exchange-correlation density functionals of  $\rho$  into new pair-density functionals of the  $\rho$  and  $\Pi$  of a multiconfigurational wavefunction.<sup>45-46</sup> In this thesis, MC-PDFT as implemented in the MOLCAS software is employed. The following functionals were employed in our computations t-LSDA, t-BLYP, t-PBE, ft-LSDA, ft-BLYP and ft-PBE.<sup>47</sup>

### 1.3.5 Kohn-Sham Density Functional Theory (KS-DFT)

Density functional theory (DFT) is another independent-particle model. The major advantage DFT has over other computational methods and models is its favorable computational cost. DFT accounts for dynamic electron correlation at an affordable computational cost, it scales at  $N^3$  where  $N$  is the system size. Initially, DFT was formulated based on the Hohenberg-Kohn theorems, one of which states that the external potential ( $v(r)$ ) and the total energy ( $E_{HK}$ ) is a unique functional of the electron density,  $\rho(r)$ . The second theorem establishes that the ground state energy can be obtained variationally. The true ground state density is one that minimizes the total energy.<sup>48-49</sup>

$$E_{HK}[\rho(r)] = F_{HK}[\rho(r)] + \int n(r) v_{ext}(r) dr \quad (1.9)$$

In the Kohn-Sham (KS) formulation of density functional theory, the many-body effect of electron correlation is modelled by a function of the total energy<sup>50</sup>. The idea in the KS formalism is to divide the kinetic energy into two parts, one which can be calculated correctly and a small correction term. For the kinetic energy portion that can be calculated correctly, a system of non-interacting electrons with the same density as the system of interacting electrons is assumed. The remaining kinetic energy is absorbed into the exchange-correlation term. The general energy expression for KS-DFT can be given as:

$$E_{DFT}[\rho] = T_s[\rho] + E_{ne}[\rho] + J[\rho] + E_{xc}[\rho] \quad (1.10)$$

The exchange correlation term,  $E_{xc}$ , shown in equation 1.10 is made up of the kinetic energy correlation, potential correlation and the exchange energy.<sup>50</sup>

$$E_{xc}[\rho] = (T[\rho] - T_s[\rho]) + (E_{ee}[\rho] - J[\rho]) \quad (1.11)$$

There exists various approximations to the exchange correlation functional, this gives rise to a plethora of density functionals with a somewhat systematic way of ordering then known as the Jacob’s ladder.<sup>51</sup>

### 1.3.5.1 Local Density Approximation (LDA)

LDA is a simple analytical approximation to  $E_{XC}$  based on the assumption that density can be treated as a uniform electron gas, UEG. The exchange energy for the UEG is given by the Dirac's formula shown below;

$$E_X^{LDA}[\rho] = -C_X \int \rho^{\frac{4}{3}}(r) dr \quad (1.12)$$

In cases where there is a difference in  $\alpha$  and  $\beta$  spin densities as observed in open-shell systems, the more acceptable form of LDA is the Local Spin Density Approximation (LSDA).<sup>52-53</sup>

$$E_X^{LSDA}[\rho] = -2^{\frac{1}{3}} C_X \int \left( \rho_{\alpha}^{\frac{4}{3}} + \rho_{\beta}^{\frac{4}{3}} \right) dr \quad (1.13)$$

However, LSDA approximation is effective with systems where slowly varying densities is a valid approximation, as observed in extended systems like metals. Beyond these cases, for molecular systems, LSDA underestimates exchange energy, consequently overestimating electron correlation and bond strengths.<sup>54</sup>

### 1.3.5.2 Generalized Gradient Approximation (GGA)

Improved functionals beyond LSDA must consider a non-uniform electron gas model to include dependence on the derivatives of electron density. This will provide improved performance for molecular systems. In GGA functionals, the first derivative of the electron density is included as a variable in addition to the electron density. One of the earliest and most popular GGA density functionals formulated by A.D. Becke is B88.<sup>55</sup> Other examples of GGA exchange functionals include: OPTX<sup>56</sup> (proposed by Handy and Cohen) and PBE<sup>57</sup> (proposed by Perdew, Burke and Ernzerhof). Similarly, there are various GGA functionals proposed for correlation energy, a popular example is LYP, formulated by Lee, Yang and Parr.<sup>58</sup>

In this thesis, PBE density functional is used extensively due to its accuracy, the parameters in PBE are not obtained from fitting to experimental data.<sup>57</sup> GGA functionals provide improvement over LSDA considering binding and formation energies. However, they tend to over delocalize electrons.

### 1.3.5.3 Meta-Generalized Gradient Approximation (meta-GGA)

Including the second-order derivative of the electron density (Laplacian) to the components of the GGA class of functionals provides improvement, this gives rise to the meta-GGA functionals. In

addition to the variables GGA functionals depend on, meta-GGA functionals also depend on the Laplacian or the orbital kinetic energy density. Density functionals in this class have an explicit dependence on occupied orbitals (as shown in equation 1.14) making them more computationally expensive in comparison to GGA functionals.

$$\tau(r) = \frac{1}{2} \sum_i^{\text{occ}} \mathcal{E}_i |\phi_i(r)|^2 - v_{\text{eff}}(r)\rho(r) + \frac{1}{2} \nabla^2 \rho(r) \quad (1.14)$$

Examples of meta-GGA exchange-correlation functionals include; TPSS<sup>59</sup> and PKZB<sup>60</sup>.

#### 1.3.5.4 Hybrid Functionals

The formulation of hybrid functionals involves including pure HF exchange into existing GGA or meta-GGA functionals to give hybrid GGA or hybrid meta-GGA functionals respectively. Hybrid functionals provide significant improvement in accuracy when compared to GGA and meta-GGA functionals. Previous work has shown that hybrid functionals are suitable for structural properties, reaction energies, and excited state properties of molecular systems and even extended systems like zeolites.<sup>61-62</sup>

In this thesis, B3LYP density functional is used extensively. It is a very popular functional as it is one of the earliest known hybrid functionals. Equation 1.15 shows the general mixing pattern of a 3-parameter hybrid functional, specifically B3LYP.<sup>63</sup>

$$E_{XC}^{B3LYP} = 0.20E_X^{HF} + 0.80E_X^{LSDA} + 0.70\Delta E_X^{B88} + 0.20E_C^{LSDA} + 0.80E_C^{LYP} \quad (1.15)$$

#### 1.3.6 Periodic Density Functional Theory (Periodic DFT)

Majority of the computations in this thesis involve zeolitic materials. Due to the crystalline nature and large size of zeolites, it is necessary to impose periodic boundary conditions using unit cells to ensure accurate and computationally feasible approximations. Using DFT to describe the electronic structure of periodic systems involves an application of Bloch's theorem to the Kohn-Sham wavefunctions. Bloch's theorem ensures that the wavefunction for the entire crystal or periodic system can be obtained by performing calculation on one simulation cell or unit cell.<sup>64</sup>

$$\Psi_{k(r)} = e^{ik \cdot r} u_{k(r)} \quad (1.16)$$

where  $k$  is a point within the Brillouin zone and  $u_{k(r)}$  describes the periodicity of the Bravais lattice. The periodic DFT calculations in this thesis are done using the Quantum Espresso software<sup>65-66</sup> using the GGA functional, PBE.<sup>57</sup>

### 1.3.7 Time Dependent Density Functional Theory (TD- DFT)

In this thesis, TD-DFT was used to simulate the UV-Vis spectra of Cu-oxo active sites to gain a molecular understanding of the impact of methane hydroxylation.<sup>19</sup> Excited state properties like this must be studied using the time-dependent variant, TD-DFT as this provides a solution to the time-dependent Schrödinger equation. TD-DFT is based on the Runge-Gross theorem,<sup>67</sup> this is the equivalent of the Hohenberg-Kohn theorems for stationary DFT. The Runge-Gross theorem (equation 1.17) states that, the time-dependent density is a function of the external potential for a given initial state. Time-dependent potentials,  $v(\mathbf{r}, t)$  and  $v'(\mathbf{r}, t)$ , acting on a system will cause different time-dependent densities  $\rho(\mathbf{r}, t)$  and  $\rho'(\mathbf{r}, t)$  respectively.

$$v(\mathbf{r}, t) \neq v'(\mathbf{r}, t) + c(t) \rightarrow \rho(\mathbf{r}, t) \neq \rho'(\mathbf{r}, t) \quad (1.17)$$

Like KS-DFT, TD-DFT is formally exact, however, it requires approximation to the exchange-correlation functional. In this work,  $\omega$ B2PLYP<sup>68</sup> density functional is employed in our calculations. It is a long-range corrected double-hybrid functional which allows for good treatment of charge-transfer problems and effective description of multi-electron processes. Tamm-Dancoff approximation to TD-DFT (TDA-DFT)<sup>69</sup> as implemented in ORCA v4.2.1 was employed.<sup>70</sup>

### 1.4 Relativistic Effects

The fundamental structure of the Schrödinger equation does not account for relativistic effect. Relativistic effects are normally negligible for lighter atoms, however, beyond the first three rows of elements, relativistic corrections become imperative for geometries and energies especially for lanthanides (fifth row) and actinides (sixth row). For a free electron, the Dirac equation, equation 1.18, was formulated to replace the time-dependent Schrödinger equation.  $\alpha$  and  $\beta$  are 4 X 4 matrices and  $\mathbf{p}$  is the momentum operator.

$$[c\alpha \cdot \mathbf{p} + \beta mc^2]\Psi = i \frac{\partial \Psi}{\partial t} \quad (1.18)$$

$$\alpha = \begin{pmatrix} 0 & \sigma_{x,y,z} \\ \sigma_{x,y,z} & 0 \end{pmatrix} \quad \beta = \begin{pmatrix} I & 0 \\ 0 & -I \end{pmatrix} \quad (1.19)$$

$$\sigma_x = \begin{pmatrix} 0 & 1 \\ 1 & 0 \end{pmatrix} \quad \sigma_y = \begin{pmatrix} 0 & -i \\ i & 0 \end{pmatrix} \quad \sigma_z = \begin{pmatrix} 1 & 0 \\ 0 & -1 \end{pmatrix} \quad I = \begin{pmatrix} 1 & 0 \\ 0 & 1 \end{pmatrix} \quad (1.20)$$

Relativistic effects either involve a mass correction for heavier atoms also known as scalar relativistic or involve electron spin as in spin-orbit coupling. For the computations in this thesis, our major concern was accounting for scalar relativistic effects, this resulted in projecting out the



spin component in the four-component Dirac equation. In modern software codes, scalar relativistic effect is usually accounted for using either the Douglas-Kroll-Hess second-order Hamiltonian (DKH-2)<sup>71-73</sup> or the zeroth-order regular approximation (ZORA)<sup>74-75</sup>. The calculations in this thesis were done using any one of the following software codes; Priroda,<sup>76</sup> ADF<sup>77</sup> and MOLCAS<sup>37-38</sup>. The approximations to the Hamiltonians were coupled with basis sets contracted for relativistic calculations.

### 1.5 Solvation Effects

While most of the calculations in this thesis were computed in the gas phase, some were done in solution phase. The effect of solvent environment can impact the chemistry of species, making accurate description of the solvent environment necessary. Solvation can be implicit or explicit, in this thesis, implicit solvation is employed. Explicit solvation involves the addition of solvent molecules around the chemical species of interest (solute), making computations more expensive as number of solvent molecules increase. For this reason, we employ the implicit solvation model for our computations. The implementation of Minnesota's Solvation Model 12 (SM12)<sup>78</sup> in ADF<sup>77</sup> software suite was used in our work, with tetrahydrofuran (THF) as the solvent of interest.

### 1.6 Dispersion Effects

Dispersion interactions are attractive weak interactions originating from the response of electrons in one region to density fluctuations in another region. Dispersion effects are not incorporated in standard KS-DFT and they play significant role in energetics, electronic excitation and response properties like spectroscopic constants. In addition, for accurate computations in large systems like zeolites, dispersion needs to be properly accounted for. Dispersion effects within the scope of DFT can be divided into the short- and long-range. The electronic density from standard KS-DFT is not asymptotically correct because it is based on the UEG model, making it difficult for standard DFT to account for long-range dispersion. To account for dispersion in DFT, there are various approaches, one of which is adding a non-local correction to the exchange-correlation potential, leading to the vdW-DFT class of density functionals.<sup>79</sup> Another way to account for dispersion is the use of error function, this is the basis of range-separated functionals.<sup>80-82</sup> The method most used in this thesis is the addition of a  $C_6$ -based  $\frac{1}{r^6}$  type correction. Here, damped atom pair-wise potentials are added to the standard KS-DFT result, this is known as the DFT-D method.<sup>83</sup> The

most commonly used form in this thesis is Grimme's DFT-D3 dispersion scheme coupled with the BJ-damping scheme to give DFT-D3BJ.<sup>84</sup>

## 1.7 Basis Sets

To construct the wavefunction,  $\Psi$ , which is made up of molecular orbitals (MOs), basis functions are required to represent the atomic orbitals (AOs). Expanding the MOs using basis functions leads to integrals which can then be solved by various quantum chemical software codes. The ease with which the integrals can be solved depends on the type of basis functions employed. There are two major types of basis functions, Slater type orbitals (STOs) and Gaussian type orbitals (GTOs). The functional form of STOs is shown in equation 1.21.

$$\chi_{\zeta,n,l,m}(r, \theta, \varphi) = N Y_{l,m}(\theta, \varphi) r^{n-1} e^{-\zeta r} \quad (1.21)$$

where  $N$  is the normalization constant and  $Y_{l,m}$  are spherical harmonic functions. STOs are hydrogenic orbitals, they mirror the exact orbitals for the hydrogen atom. STOs have no radial nodes, however nodes can be introduced by making linear combinations of STOs. Despite the accuracy of STOs, it is difficult to use them in calculations that involving four-center integrals, making GTOs a more suitable choice of basis functions.<sup>85-87</sup> Equations 1.22 and 1.23, show the functional form of GTOs in polar and cartesian coordinates respectively.

$$\chi_{\zeta,n,l,m}(r, \theta, \varphi) = N Y_{l,m}(\theta, \varphi) r^{2n-2-l} e^{-\zeta r^2} \quad (1.22)$$

$$\chi_{\zeta,l_x,l_y,l_z}(x, y, z) = N x^{l_x} y^{l_y} z^{l_z} e^{-\zeta r^2} \quad (1.23)$$

While GTOs are somewhat inferior to STOs, the ease with which required integrals can be computed compensate for the inaccuracy. Also, the accuracy of a single STO can be achieved by making a linear combination of about three GTOs, leading to contracted GTOs (CGTOs), Figure 1.2. Basis sets can be classified using the number of basis functions per orbital, with the minimum being a single basis function per orbital. The next improvement will be doubling the basis function leading to a double zeta type basis (DZ), the next step up in size will be a triple zeta (TZ) basis set. To ensure accurate description of chemical bonding, dissociation and some other properties, additional functions like polarization (higher-order angular momentum functions added for describing bonding) and diffuse functions (functions with the same order of angular momentum necessary for interactions at large distances) are added to supplement the standard basis functions. There are tons of basis sets contracted for different methods, the chemistry of the system and method of choice should be examined before making a choice of basis set to be used. In this thesis,

different kinds of basis sets are employed, one of which is the atomic natural orbital basis set, specifically ANO-RCC-VTZP.<sup>88</sup> Other basis set employed include; correlation consistent cc-pVTZ<sup>89</sup>, Ahlrichs and co-worker's split-valence basis set def2-TZVP and doubly-polarized TZ2P basis set.<sup>90</sup>

STOs and GTOs are not suited for modelling extended systems, the more suited type of basis function are plane wave basis functions generally represented as;

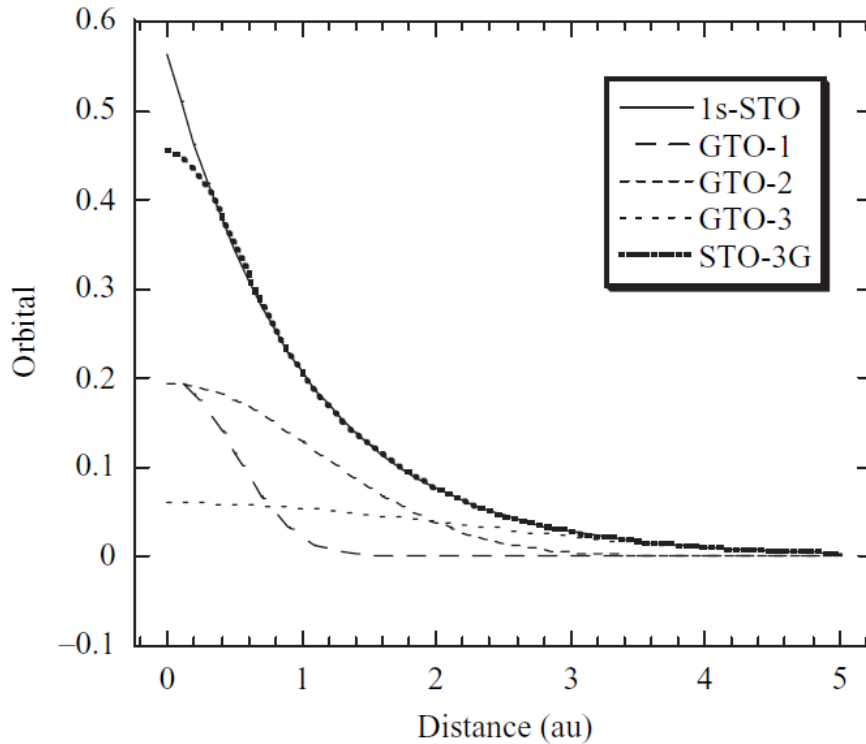


**Figure 1.2: Modelling a 1s-STO with GTOs.**<sup>33</sup>

$$\chi_{\mathbf{k}}(r) = e^{i\mathbf{k} \cdot \mathbf{r}} \quad (1.24)$$

The wave vector,  $\mathbf{k}$ , plays the same role as  $\zeta$  in GTOs, however,  $\mathbf{k}$  does not necessarily depict size for plane waves, the size of plane wave basis sets depends only on the size of the unit cell. The type of plane wave basis employed in this thesis are projector-augmented wave (PAW) pseudopotentials as implemented in Quantum Espresso. PAW is a frozen-core all-electron (AE) pseudopotential proposed by Blöchl, Kresse and Joubert reformulated the PAW energy functional to resemble the pseudopotentials employed in modern periodic codes.<sup>91</sup> The two important cut-offs used to control the waves are the energy and density cut-off which we typically set to 50 and 250 Ry respectively.

## 1.8 Organization of Thesis

Subsequent chapters in this thesis are arranged as shown in Figure 1.3.

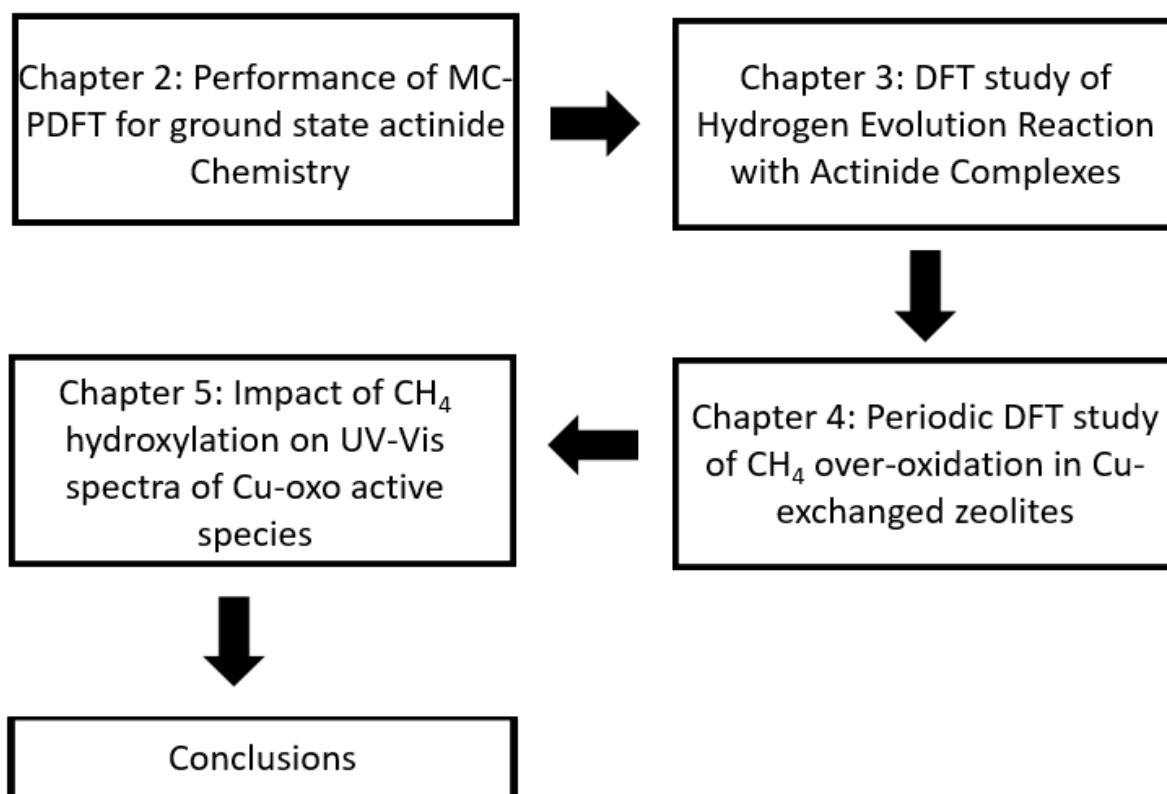


**Figure 1.3: Schematic description of remaining chapters in this thesis.**

## REFERENCES

1. Breck, D. W.; Eversole, W. G.; Milton, R. M.; Reed, T. B.; Thomas, T. L., Crystalline Zeolites. I. The Properties of a New Synthetic Zeolite, Type A. *Journal of the American Chemical Society* **1956**, 78 (23), 5963-5972.
2. Hartmann, M.; Thommes, M.; Schwieger, W., Hierarchically-Ordered Zeolites: A Critical Assessment. *Advanced Materials Interfaces* **2021**, 8 (4), 2001841.
3. Sherry, H. S., The Ion-Exchange Properties of Zeolites. I. Univalent Ion Exchange in Synthetic Faujasite. *The Journal of Physical Chemistry* **1966**, 70 (4), 1158-1168.
4. Armor, J. N., Metal-exchanged zeolites as catalysts. Dedicated to Professor Lovat V.C. Rees in recognition and appreciation of his lifelong devotion to zeolite science and his outstanding achievements in this field. *Microporous and Mesoporous Materials* **1998**, 22 (1), 451-456.
5. Marakatti, V. S.; Halgeri, A. B.; Shanbhag, G. V., Metal ion-exchanged zeolites as solid acid catalysts for the green synthesis of nopol from Prins reaction. *Catalysis Science & Technology* **2014**, 4 (11), 4065-4074.
6. Osuga, R.; Bayarsaikhan, S.; Yasuda, S.; Manabe, R.; Shima, H.; Tsutsuminai, S.; Fukuoka, A.; Kobayashi, H.; Yokoi, T., Metal cation-exchanged zeolites with the location, state, and size of metal species controlled. *Chemical Communications* **2020**, 56 (44), 5913-5916.

7. Król, M., Natural vs. Synthetic Zeolites. *Crystals* **2020**, *10* (7), 622.
8. Shi, J.; Wang, Y.; Yang, W.; Tang, Y.; Xie, Z., Recent advances of pore system construction in zeolite-catalyzed chemical industry processes. *Chemical Society Reviews* **2015**, *44* (24), 8877-8903.
9. Blay, V.; Louis, B.; Miravalles, R.; Yokoi, T.; Peccatiello, K. A.; Clough, M.; Yilmaz, B., Engineering Zeolites for Catalytic Cracking to Light Olefins. *ACS Catalysis* **2017**, *7* (10), 6542-6566.
10. Corma, A., Application of Zeolites in Fluid Catalytic Cracking and Related Processes. In *Studies in Surface Science and Catalysis*, Jacobs, P. A.; van Santen, R. A., Eds. Elsevier: 1989; Vol. 49, pp 49-67.
11. Newton, M. A.; Knorpp, A. J.; Sushkevich, V. L.; Palagin, D.; van Bokhoven, J. A., Active sites and mechanisms in the direct conversion of methane to methanol using Cu in zeolitic hosts: a critical examination. *Chemical Society Reviews* **2020**, *49* (5), 1449-1486.
12. Fickel, D. W.; Lobo, R. F., Copper Coordination in Cu-SSZ-13 and Cu-SSZ-16 Investigated by Variable-Temperature XRD. *The Journal of Physical Chemistry C* **2010**, *114* (3), 1633-1640.
13. Smeets, P. J.; Hadt, R. G.; Woertink, J. S.; Vanelderen, P.; Schoonheydt, R. A.; Sels, B. F.; Solomon, E. I., Oxygen Precursor to the Reactive Intermediate in Methanol Synthesis by Cu-ZSM-5. *Journal of the American Chemical Society* **2010**, *132* (42), 14736-14738.
14. Godiksen, A.; Stappen, F. N.; Vennestrøm, P. N. R.; Giordanino, F.; Rasmussen, S. B.; Lundegaard, L. F.; Mossin, S., Coordination Environment of Copper Sites in Cu-CHA Zeolite Investigated by Electron Paramagnetic Resonance. *The Journal of Physical Chemistry C* **2014**, *118* (40), 23126-23138.
15. Alayon, E. M. C.; Nachtegaal, M.; Ranocchiari, M.; van Bokhoven, J. A., Catalytic Conversion of Methane to Methanol Using Cu-Zeolites. *CHIMIA* **2012**, *66* (9), 668.
16. Alayon, E. M.; Nachtegaal, M.; Ranocchiari, M.; van Bokhoven, J. A., Catalytic conversion of methane to methanol over Cu-mordenite. *Chemical Communications* **2012**, *48* (3), 404-406.
17. Ipek, B.; Lobo, R. F., Catalytic conversion of methane to methanol on Cu-SSZ-13 using N<sub>2</sub>O as oxidant. *Chemical Communications* **2016**, *52* (91), 13401-13404.
18. Arvidsson, A. A.; Zhdanov, V. P.; Carlsson, P.-A.; Grönbeck, H.; Hellman, A., Metal dimer sites in ZSM-5 zeolite for methane-to-methanol conversion from first-principles kinetic modelling: is the [Cu–O–Cu]<sup>2+</sup> motif relevant for Ni, Co, Fe, Ag, and Au? *Catalysis Science & Technology* **2017**, *7* (7), 1470-1477.
19. Adeyiga, O.; Suleiman, O.; Odoh, S. O., Copper-Oxo Active Sites for Methane C–H Activation in Zeolites: Molecular Understanding of Impact of Methane Hydroxylation on UV–Vis Spectra. *Inorganic Chemistry* **2021**, *60* (12), 8489-8499.
20. Adeyiga, O.; Odoh, S. O., Methane Over-Oxidation by Extra-Framework Copper-Oxo Active Sites of Copper-Exchanged Zeolites: Crucial Role of Traps for the Separated Methyl Group. *ChemPhysChem* **2021**, *22* (11), 1101-1109.
21. Adeyiga, O.; Panthi, D.; Odoh, S. O., Heterometallic [Cu–O–M]<sup>2+</sup> active sites for methane C–H activation in zeolites: stability, reactivity, formation mechanism and relationship to other active sites. *Catalysis Science & Technology* **2021**, *11* (16), 5671-5683.
22. Palumbo, C. T.; Barluzzi, L.; Scopelliti, R.; Zivkovic, I.; Fabrizio, A.; Corminboeuf, C.; Mazzanti, M., Tuning the structure, reactivity and magnetic communication of nitride-bridged uranium complexes with the ancillary ligands. *Chemical Science* **2019**, *10* (38), 8840-8849.

23. Merroun, M. L., Actinides, Interactions with Proteins. In *Encyclopedia of Metalloproteins*, Kretsinger, R. H.; Uversky, V. N.; Permyakov, E. A., Eds. Springer New York: New York, NY, 2013; pp 11-16.
24. Falcone, M.; Chatelain, L.; Scopelliti, R.; Živković, I.; Mazzanti, M., Nitrogen reduction and functionalization by a multimetallic uranium nitride complex. *Nature* **2017**, *547* (7663), 332-335.
25. Arnold, P. L.; Turner, Z. R., Carbon oxygenate transformations by actinide compounds and catalysts. *Nature Reviews Chemistry* **2017**, *1* (1), 0002.
26. Barluzzi, L.; Falcone, M.; Mazzanti, M., Small molecule activation by multimetallic uranium complexes supported by siloxide ligands. *Chemical Communications* **2019**, *55* (87), 13031-13047.
27. Panthi, D.; Adeyiga, O.; Dandu, N. K.; Odoh, S. O., Nitrogen Reduction by Multimetallic trans-Uranium Actinide Complexes: A Theoretical Comparison of Np and Pu to U. *Inorganic Chemistry* **2019**, *58* (10), 6731-6741.
28. Halter, D. P.; Heinemann, F. W.; Maron, L.; Meyer, K., The role of uranium–arene bonding in H<sub>2</sub>O reduction catalysis. *Nature Chemistry* **2018**, *10* (3), 259-267.
29. Adeyiga, O.; Panthi, D.; Suleiman, O.; Stetler, D.; Long, R. W.; Odoh, S. O., Activating Water and Hydrogen by Ligand-Modified Uranium and Neptunium Complexes: A Density Functional Theory Study. *Inorganic Chemistry* **2020**, *59* (5), 3102-3109.
30. Slater, J. C., Note on Hartree's Method. *Physical Review* **1930**, *35* (2), 210-211.
31. Slater, J. C., The Self Consistent Field and the Structure of Atoms. *Physical Review* **1928**, *32* (3), 339-348.
32. Slater, J. C., A Simplification of the Hartree-Fock Method. *Physical Review* **1951**, *81* (3), 385-390.
33. Jensen, F., *Introduction to Computational Chemistry*. Second Edition ed.; John Wiley and Sons, New York: 1999.
34. Bartlett, R. J.; Musiał, M., Coupled-cluster theory in quantum chemistry. *Reviews of Modern Physics* **2007**, *79* (1), 291-352.
35. Pople, J. A.; Head-Gordon, M.; Raghavachari, K., Quadratic configuration interaction. A general technique for determining electron correlation energies. *The Journal of Chemical Physics* **1987**, *87* (10), 5968-5975.
36. III, G. D. P.; Bartlett, R. J., A full coupled-cluster singles and doubles model: The inclusion of disconnected triples. *The Journal of Chemical Physics* **1982**, *76* (4), 1910-1918.
37. Aquilante, F.; Autschbach, J.; Carlson, R. K.; Chibotaru, L. F.; Delcey, M. G.; De Vico, L.; Fdez. Galván, I.; Ferré, N.; Frutos, L. M.; Gagliardi, L.; Garavelli, M.; Giussani, A.; Hoyer, C. E.; Li Manni, G.; Lischka, H.; Ma, D.; Malmqvist, P. Å.; Müller, T.; Nenov, A.; Olivucci, M.; Pedersen, T. B.; Peng, D.; Plasser, F.; Pritchard, B.; Reiher, M.; Rivalta, I.; Schapiro, I.; Segarra-Martí, J.; Stenrup, M.; Truhlar, D. G.; Ungur, L.; Valentini, A.; Vancoillie, S.; Veryazov, V.; Vysotskiy, V. P.; Weingart, O.; Zapata, F.; Lindh, R., Molcas 8: New capabilities for multiconfigurational quantum chemical calculations across the periodic table. *Journal of Computational Chemistry* **2016**, *37* (5), 506-541.
38. Aquilante, F.; Autschbach, J.; Baiardi, A.; Battaglia, S.; Borin, V. A.; Chibotaru, L. F.; Conti, I.; Vico, L. D.; Delcey, M.; Galván, I. F.; Ferré, N.; Freitag, L.; Garavelli, M.; Gong, X.; Knecht, S.; Larsson, E. D.; Lindh, R.; Lundberg, M.; Malmqvist, P. Å.; Nenov, A.; Norell, J.; Odelius, M.; Olivucci, M.; Pedersen, T. B.; Pedraza-González, L.; Phung, Q. M.; Pierloot, K.; Reiher, M.; Schapiro, I.; Segarra-Martí, J.; Segatta, F.; Seijo, L.; Sen, S.; Sergentu, D.-C.; Stein,

- C. J.; Ungur, L.; Vacher, M.; Valentini, A.; Veryazov, V., Modern quantum chemistry with [Open]Molcas. *The Journal of Chemical Physics* **2020**, *152* (21), 214117.
39. Roos, B. O.; Taylor, P. R.; Sigbahn, P. E. M., A complete active space SCF method (CASSCF) using a density matrix formulated super-CI approach. *Chemical Physics* **1980**, *48* (2), 157-173.
  40. Per, S.; Anders, H.; Björn, R.; Bernard, L., A Comparison of the Super-CI and the Newton-Raphson Scheme in the Complete Active Space SCF Method. *Physica Scripta* **1980**, *21* (3-4), 323.
  41. Siegbahn, P. E. M.; Almlöf, J.; Heiberg, A.; Roos, B. O., The complete active space SCF (CASSCF) method in a Newton-Raphson formulation with application to the HNO molecule. *The Journal of Chemical Physics* **1981**, *74* (4), 2384-2396.
  42. Roos, B. O., The Complete Active Space Self-Consistent Field Method and its Applications in Electronic Structure Calculations. In *Advances in Chemical Physics*, 1987; pp 399-445.
  43. Levine, D. S.; Hait, D.; Tubman, N. M.; Lehtola, S.; Whaley, K. B.; Head-Gordon, M., CASSCF with Extremely Large Active Spaces Using the Adaptive Sampling Configuration Interaction Method. *Journal of Chemical Theory and Computation* **2020**, *16* (4), 2340-2354.
  44. Finley, J.; Malmqvist, P.-Å.; Roos, B. O.; Serrano-Andrés, L., The multi-state CASPT2 method. *Chemical Physics Letters* **1998**, *288* (2), 299-306.
  45. Li Manni, G.; Carlson, R. K.; Luo, S.; Ma, D.; Olsen, J.; Truhlar, D. G.; Gagliardi, L., Multiconfiguration Pair-Density Functional Theory. *Journal of Chemical Theory and Computation* **2014**, *10* (9), 3669-3680.
  46. Li Manni, G.; Carlson, R. K.; Luo, S.; Ma, D.; Olsen, J.; Truhlar, D. G.; Gagliardi, L., Correction to Multiconfiguration Pair-Density Functional Theory. *Journal of Chemical Theory and Computation* **2016**, *12* (1), 458-458.
  47. Adeyiga, O.; Suleiman, O.; Dandu, N. K.; Odoh, S. O., Ground-state actinide chemistry with scalar-relativistic multiconfiguration pair-density functional theory. *The Journal of Chemical Physics* **2019**, *151* (13), 134102.
  48. Hohenberg, P.; Kohn, W., Inhomogeneous Electron Gas. *Physical Review* **1964**, *136* (3B), B864-B871.
  49. Sahni, V., The Hohenberg-Kohn Theorems and Kohn-Sham Density Functional Theory. In *Quantal Density Functional Theory*, Sahni, V., Ed. Springer Berlin Heidelberg: Berlin, Heidelberg, 2004; pp 99-123.
  50. Kohn, W.; Sham, L. J., Self-Consistent Equations Including Exchange and Correlation Effects. *Physical Review* **1965**, *140* (4A), A1133-A1138.
  51. Perdew, J. P.; Schmidt, K., Jacob's ladder of density functional approximations for the exchange-correlation energy. *AIP Conference Proceedings* **2001**, *577* (1), 1-20.
  52. Dirac, P. A. M., Note on Exchange Phenomena in the Thomas Atom. *Mathematical Proceedings of the Cambridge Philosophical Society* **2008**, *26* (3), 376-385.
  53. Zhao, G. L.; Bagayoko, D.; Williams, T. D., Local-density-approximation prediction of electronic properties of GaN, Si, C, and  $\text{RuO}_2$ . *Physical Review B* **1999**, *60* (3), 1563-1572.
  54. Riley, K. E.; Op't Holt, B. T.; Merz, K. M., Critical Assessment of the Performance of Density Functional Methods for Several Atomic and Molecular Properties. *Journal of Chemical Theory and Computation* **2007**, *3* (2), 407-433.
  55. Becke, A. D., Density-functional exchange-energy approximation with correct asymptotic behavior. *Physical Review A* **1988**, *38* (6), 3098-3100.
  56. Handy, N. C.; Cohen, A. J., Left-right correlation energy. *Molecular Physics* **2001**, *99* (5),

403-412.

57. Perdew, J. P.; Burke, K.; Ernzerhof, M., Generalized Gradient Approximation Made Simple [Phys. Rev. Lett. 77, 3865 (1996)]. *Physical Review Letters* **1997**, 78 (7), 1396-1396.
58. Lee, C.; Yang, W.; Parr, R. G., Development of the Colle-Salvetti correlation-energy formula into a functional of the electron density. *Physical Review B* **1988**, 37 (2), 785-789.
59. Tao, J.; Perdew, J. P.; Staroverov, V. N.; Scuseria, G. E., Climbing the Density Functional Ladder: Nonempirical Meta--Generalized Gradient Approximation Designed for Molecules and Solids. *Physical Review Letters* **2003**, 91 (14), 146401.
60. Perdew, J. P.; Kurth, S.; Zupan, A.; Blaha, P., Accurate Density Functional with Correct Formal Properties: A Step Beyond the Generalized Gradient Approximation. *Physical Review Letters* **1999**, 82 (12), 2544-2547.
61. Tirado-Rives, J.; Jorgensen, W. L., Performance of B3LYP Density Functional Methods for a Large Set of Organic Molecules. *Journal of Chemical Theory and Computation* **2008**, 4 (2), 297-306.
62. Dandu, N. K.; Adeyiga, O.; Panthi, D.; Bird, S. A.; Odoh, S. O., Performance of density functional theory for describing hetero-metallic active-site motifs for methane-to-methanol conversion in metal-exchanged zeolites. *Journal of Computational Chemistry* **2018**, 39 (32), 2667-2678.
63. Stephens, P. J.; Devlin, F. J.; Chabalowski, C. F.; Frisch, M. J., Ab initio calculation of vibrational absorption and circular dichroism spectra using density functional force fields. *The Journal of physical chemistry* **1994**, 98 (45), 11623-11627.
64. Bloch, F., Über die Quantenmechanik der Elektronen in Kristallgittern. *Zeitschrift für Physik* **1929**, 52 (7), 555-600.
65. Giannozzi, P.; Baroni, S.; Bonini, N.; Calandra, M.; Car, R.; Cavazzoni, C.; Ceresoli, D.; Chiarotti, G. L.; Cococcioni, M.; Dabo, I.; Dal Corso, A.; de Gironcoli, S.; Fabris, S.; Fratesi, G.; Gebauer, R.; Gerstmann, U.; Gougoussis, C.; Kokalj, A.; Lazzeri, M.; Martin-Samos, L.; Marzari, N.; Mauri, F.; Mazzarello, R.; Paolini, S.; Pasquarello, A.; Paulatto, L.; Sbraccia, C.; Scandolo, S.; Sclauzero, G.; Seitsonen, A. P.; Smogunov, A.; Umari, P.; Wentzcovitch, R. M., QUANTUM ESPRESSO: a modular and open-source software project for quantum simulations of materials. *Journal of Physics: Condensed Matter* **2009**, 21 (39), 395502.
66. Giannozzi, P.; Andreussi, O.; Brumme, T.; Bunau, O.; Buongiorno Nardelli, M.; Calandra, M.; Car, R.; Cavazzoni, C.; Ceresoli, D.; Cococcioni, M.; Colonna, N.; Carnimeo, I.; Dal Corso, A.; de Gironcoli, S.; Delugas, P.; DiStasio, R. A.; Ferretti, A.; Floris, A.; Fratesi, G.; Fugallo, G.; Gebauer, R.; Gerstmann, U.; Giustino, F.; Gorni, T.; Jia, J.; Kawamura, M.; Ko, H. Y.; Kokalj, A.; Küçükbenli, E.; Lazzeri, M.; Marsili, M.; Marzari, N.; Mauri, F.; Nguyen, N. L.; Nguyen, H. V.; Otero-de-la-Roza, A.; Paulatto, L.; Poncé, S.; Rocca, D.; Sabatini, R.; Santra, B.; Schlipf, M.; Seitsonen, A. P.; Smogunov, A.; Timrov, I.; Thonhauser, T.; Umari, P.; Vast, N.; Wu, X.; Baroni, S., Advanced capabilities for materials modelling with Quantum ESPRESSO. *Journal of Physics: Condensed Matter* **2017**, 29 (46), 465901.
67. Runge, E.; Gross, E. K. U., Density-Functional Theory for Time-Dependent Systems. *Physical Review Letters* **1984**, 52 (12), 997-1000.
68. Casanova-Páez, M.; Dardis, M. B.; Goerigk, L.,  $\omega$ B2PLYP and  $\omega$ B2GPPLYP: The First Two Double-Hybrid Density Functionals with Long-Range Correction Optimized for Excitation Energies. *Journal of Chemical Theory and Computation* **2019**, 15 (9), 4735-4744.
69. Hirata, S.; Head-Gordon, M., Time-dependent density functional theory within the Tamm-Dancoff approximation. *Chemical Physics Letters* **1999**, 314 (3), 291-299.



70. Neese, F.; Wennmohs, F.; Becker, U.; Riplinger, C., The ORCA quantum chemistry program package. *The Journal of Chemical Physics* **2020**, *152* (22), 224108.
71. Hess, B. A., Relativistic electronic-structure calculations employing a two-component no-pair formalism with external-field projection operators. *Physical Review A* **1986**, *33* (6), 3742-3748.
72. Jansen, G.; Hess, B. A., Revision of the Douglas-Kroll transformation. *Physical Review A* **1989**, *39* (11), 6016-6017.
73. Wolf, A.; Reiher, M.; Hess, B. A., The generalized Douglas–Kroll transformation. *The Journal of Chemical Physics* **2002**, *117* (20), 9215-9226.
74. Lenthe, E. v.; Baerends, E. J.; Snijders, J. G., Relativistic regular two-component Hamiltonians. *The Journal of Chemical Physics* **1993**, *99* (6), 4597-4610.
75. Lenthe, E. v.; Snijders, J. G.; Baerends, E. J., The zero-order regular approximation for relativistic effects: The effect of spin–orbit coupling in closed shell molecules. *The Journal of Chemical Physics* **1996**, *105* (15), 6505-6516.
76. Laikov, D. N.; Ustynyuk, Y. A., PRIRODA-04: a quantum-chemical program suite. New possibilities in the study of molecular systems with the application of parallel computing. *Russian Chemical Bulletin* **2005**, *54* (3), 820-826.
77. te Velde, G.; Bickelhaupt, F. M.; Baerends, E. J.; Fonseca Guerra, C.; van Gisbergen, S. J. A.; Snijders, J. G.; Ziegler, T., Chemistry with ADF. *Journal of Computational Chemistry* **2001**, *22* (9), 931-967.
78. Marenich, A. V.; Cramer, C. J.; Truhlar, D. G., Generalized Born Solvation Model SM12. *Journal of Chemical Theory and Computation* **2013**, *9* (1), 609-620.
79. Berland, K.; Cooper, V. R.; Lee, K.; Schröder, E.; Thonhauser, T.; Hyldgaard, P.; Lundqvist, B. I., van der Waals forces in density functional theory: a review of the vdW-DF method. *Reports on Progress in Physics* **2015**, *78* (6), 066501.
80. Chai, J.-D.; Head-Gordon, M., Systematic optimization of long-range corrected hybrid density functionals. *The Journal of Chemical Physics* **2008**, *128* (8), 084106.
81. Vydrov, O. A.; Heyd, J.; Krukau, A. V.; Scuseria, G. E., Importance of short-range versus long-range Hartree-Fock exchange for the performance of hybrid density functionals. *The Journal of Chemical Physics* **2006**, *125* (7), 074106.
82. Yanai, T.; Tew, D. P.; Handy, N. C., A new hybrid exchange–correlation functional using the Coulomb-attenuating method (CAM-B3LYP). *Chemical Physics Letters* **2004**, *393* (1), 51-57.
83. Grimme, S.; Antony, J.; Ehrlich, S.; Krieg, H., A consistent and accurate ab initio parametrization of density functional dispersion correction (DFT-D) for the 94 elements H-Pu. *The Journal of Chemical Physics* **2010**, *132* (15), 154104.
84. Grimme, S.; Ehrlich, S.; Goerigk, L., Effect of the damping function in dispersion corrected density functional theory. *Journal of Computational Chemistry* **2011**, *32* (7), 1456-1465.
85. Rossikhin, V. V.; Kuz'menko, V. V.; Voronkov, E. O.; Zaslavskaya, L. I., Improvement of STO and GTO Basis Set Quality in Calculations of Magnetic Properties by the Coupled and Uncoupled Hartree–Fock Perturbation Theory. *The Journal of Physical Chemistry* **1996**, *100* (51), 19801-19807.
86. Hehre, W. J.; Stewart, R. F.; Pople, J. A., Self-Consistent Molecular-Orbital Methods. I. Use of Gaussian Expansions of Slater-Type Atomic Orbitals. *The Journal of Chemical Physics* **1969**, *51* (6), 2657-2664.
87. Stewart, R. F., Small Gaussian Expansions of Slater-Type Orbitals. *The Journal of Chemical Physics* **1970**, *52* (1), 431-438.

88. Larsson, E. D.; Zobel, J. P.; Veryazov, V., Benchmarking ANO-R basis set for multiconfigurational calculations. *Electronic Structure* **2022**, 4 (1), 014009.
89. Jr., T. H. D., Gaussian basis sets for use in correlated molecular calculations. I. The atoms boron through neon and hydrogen. *The Journal of Chemical Physics* **1989**, 90 (2), 1007-1023.
90. Weigend, F.; Ahlrichs, R., Balanced basis sets of split valence, triple zeta valence and quadruple zeta valence quality for H to Rn: Design and assessment of accuracy. *Physical Chemistry Chemical Physics* **2005**, 7 (18), 3297-3305.
91. Kresse, G.; Joubert, D., From ultrasoft pseudopotentials to the projector augmented-wave method. *Physical Review B* **1999**, 59 (3), 1758-1775.

## CHAPTER 2. GROUND-STATE ACTINIDE CHEMISTRY WITH SCALAR-RELATIVISTIC MULTICONFIGURATION PAIR-DENSITY FUNCTIONAL THEORY

Olajumoke Adeyiga, Olabisi Suleiman, Naveen K. Dandu and Samuel O. Odoh

Department of Chemistry, University of Nevada Reno, 1664 N. Virginia Street, Reno, NV  
89557-0216

“Reprinted from *J Chem Phys*, 2019, 151, 134102 with permission of AIP Publishing”

**ABSTRACT:** We have examined the performance of Multiconfiguration Pair-Density Functional Theory (MC-PDFT) for computing the ground-state properties of actinide species. Specifically, we focused on the properties of UN<sub>2</sub> and various actinyl species. The properties obtained with MC-PDFT at the scalar-relativistic level are compared to Kohn-Sham DFT (KS-DFT), complete active space self-consistent field theory, CASSCF, coupled-cluster theory, CCSD(T) and CCSDT, as well as multireference perturbation theory, (CASPT2). We examine the degree to which MC-PDFT improves over KS-DFT and CASSCF while aligning with CASPT2, CCSD(T) and CCSDT. All properties that we considered were for the CASPT2 electronic ground states. For structural parameters, MC-PDFT confers very little advantage over KS-DFT, especially the B3LYP density functional. For NpO<sub>2</sub><sup>3+</sup>, MC-PDFT and local KS-DFT functionals excessively favor the bent structure whereas CCSDT and CASPT2 predict the bent and linear structures as iso-energetic. For this special case, hybrid KS-DFT functionals like PBE0 and B3LYP provide results closer to CASPT2 and CCSDT than MC-PDFT. On a more positive note, MC-PDFT is very close to CASPT2 and CCSD(T) for the redox potentials, energetics of redox chemical reactions as well as ligand-binding energies. These are encouraging results since MC-PDFT is more affordable. The best MC-PDFT functional is ft-PBE. Our findings suggest that MC-PDFT can be used to study systems and excited states with larger strong electron correlation effects than were considered here. However, for the systems and properties considered here, KS-DFT functionals do well, justifying their usage as the bulwark of computational actinyl chemistry over the last two-three decades.

## 2.1 INTRODUCTION

There has been significant interest in using quantum mechanical calculations for computing the structural, electronic, optical, chemical and magnetic properties of actinide complexes. A significant proportion of these calculations are performed at the scalar-relativistic Kohn-Sham density functional theory (KS-DFT) level.<sup>1-5</sup> The relatively low computational cost and fairly black-box nature of KS-DFT makes it more affordable and appealing than many correlated wavefunction approaches.<sup>6-9</sup> The affordability of KS-DFT comes at the expense of non-trivial dependence of results on the choice of exchange-correlation density functional. As such, many researchers have examined the performance of various KS-DFT functionals for predicting the properties of actinide compounds by comparison with experimental data or by comparison with results obtained from wavefunction approaches like coupled cluster (CC) theory. In general, CC calculations are usually performed at the level of iterative inclusion of single and double excitations and a perturbative treatment of triple excitations, CCSD(T). The results of KS-DFT calculations on actinide species have also been compared to complete active space second order perturbation theory (CASPT2).<sup>1, 10-41</sup> Although KS-DFT performs well for predicting some properties of actinide species, there are instances of strong disagreements with the wavefunction methods.<sup>4, 24, 33, 38</sup> Such disparities are often due to the fact that the partially-filled nature of the *5f* shell of the early actinides (uranium, neptunium and plutonium) confers multiconfigurational character on their atoms, ions and complexes. These static correlation effects are not accurately accounted for within KS-DFT. These effects are however crucial for accurate description of the electronic structures of *5f* complexes as well as quantitative description of their optical, chemical reactivity and magnetic properties.

Although CCSD(T)<sup>42-47</sup> and CASPT2<sup>48-50</sup> are accurate for predicting the properties of actinide species, they are ultimately limited for studying large complexes. The  $N^7$  scaling of conventional implementations of CCSD(T) ensures that it is far more expensive than KS-DFT.<sup>6, 7, 9</sup> Also, CCSD(T) is best suited for studying systems with single-reference character or at worst, modest multireference characters.<sup>45</sup> While there are many ways of identifying systems with multiconfigurational characters, the largest configuration state functions, CSFs, in these systems typically have a weight contribution below 90% of the configuration interaction (CI) expansion.<sup>51-53</sup> For systems with significant multireference character, the Hartree-Fock (HF) wavefunction is no longer a good starting point for CCSD(T) calculations. Indeed, Fang et al. have shown that

using HF solutions in CCSD(T) calculations can lead to fairly large errors in the reaction energies of some actinide compounds.<sup>54</sup> For these systems, it is necessary to employ quantum-mechanical methods designed to handle multireference character. CASPT2 is one such approach that has been used to study actinide species. For CASPT2 calculations, the initial complete active space self-consistent field (CASSCF) step as well as the post-CASSCF perturbation theory step become increasingly unaffordable as the system size and active space are increased. Indeed, most modern CASSCF algorithms can only treat 18-24 electrons in 18-24 orbitals.<sup>55-57</sup> This active space size is not sufficient to adequately account for static and dynamic correlation in many *5f* complexes of interest in catalysis, materials and optics. It is in light of these limitations that several workers have focused on developing approaches that combine DFT with multireference methods.<sup>58-72</sup> We have only cited a few examples. A more exhaustive reference can be found in ref.<sup>68</sup>. In these ‘hybrid’ methods, static correlation energy is recovered with either a multiconfigurational approach like CASSCF or with singlet-paired coupled-cluster (CCD0) theory.<sup>45, 62</sup> Some variant of DFT, is then used to recover the dynamic portion of the electronic correlation energy. The ‘hybrid’ ‘CASSCF/DFT’ methods avoid the scaling difficulties associated with the post-CASSCF step in CASPT2. CCD0/DFT avoids incorporation of higher-order excitations in coupled-cluster theory. Interestingly, there have only been two instances in which CASSCF/DFT and CCD0/DFT methods have been used to study *5f* systems. These studies focused mostly on the structural properties of *f*<sup>0</sup> actinyl systems.<sup>16, 60</sup>

In this work, we examine the structural, redox, ligand bonding and reactivity properties of *f*<sup>0</sup>, *f*<sup>1</sup>, *f*<sup>2</sup>, *f*<sup>3</sup> and *f*<sup>4</sup> actinyl species with the aim of comparing the performance of a recently developed multiconfigurational pair-density functional theory (MC-PDFT<sup>68, 73, 74</sup>) approach with KS-DFT, CASSCF, CASPT2, CCSD(T) and CCSDT<sup>75</sup>. The new approach is called multiconfiguration pair-density functional theory (MC-PDFT).<sup>68, 73, 74</sup> In MC-PDFT, the total energy is obtained by adding the kinetic energy and classical Coulomb energy of any multiconfigurational wavefunction to an “on-top energy contribution” obtained with an “on-top density functional” of the one-electron density,  $\rho$ , and the on-top pair density,  $\Pi$ ,<sup>76-78</sup> of the multiconfigurational wavefunction, 2.1. MC-PDFT is a general ansatz since one can use  $\rho$  and  $\Pi$  from any multiconfigurational solution.<sup>79-81</sup> CAS-PDFT is MC-PDFT when one utilizes a CASSCF solution. This is the only type of MC-PDFT method used in this work. As such we will use CAS-PDFT and MC-PDFT interchangeably, henceforth. For MC-PDFT, the total energy is given by:

$$E = V_{nn} + \langle \psi | \hat{T} + \hat{V}_{ne} | \psi \rangle + V_C[\rho] + E_{ot}[\rho, \Pi] \quad (2.1)$$

$$E = V_{nn} + 2 \sum_i h_{ij} + 2 \sum_{ij} g_{iijj} + \sum_{vw} h_{vw} D_{vw} + 2 \sum_{iivw} g_{iivw} D_{vw} + \frac{1}{2} \sum_{vwxy} g_{vwxy} D_{vw} D_{xy} + E_{ot}[\rho, \Pi] \quad (2.2)$$

where  $V_{nn}$  is the nucleus-nucleus repulsion energy and  $\langle \psi |$  is the multireference wavefunction,  $\hat{T}$  is the kinetic energy operator,  $\hat{V}_{ne}$  is the nucleus-electron attraction energy operator while  $V_C[\rho]$  and  $E_{ot}[\rho, \Pi]$  represent the Coulomb and the on-top pair-density functional energies, respectively. A more detailed breakdown of the CAS-PDFT energy is shown in 2.2, where  $h$  and  $g$  represent the one-electron and two-electron integrals respectively,  $D$  is the one-body density matrix.  $i$  and  $j$  are used to denote inactive orbitals while  $v$ ,  $w$ ,  $x$ , and  $y$  are the active orbitals.<sup>68, 74</sup>

The on-top pair-density functional energy,  $E_{ot}[\rho, \Pi]$  in 2.2, is obtained by ‘*translating*’ or ‘*fully translating*’ existing Kohn-Sham exchange-correlation density functionals of  $\rho$  into new pair-density functionals of the  $\rho$  and  $\Pi$  of a multiconfigurational wavefunction.<sup>68, 73, 74</sup> The *translated* functionals of  $\rho$  and  $\Pi$  are labeled as ‘t-DFT’ (t-PBE, t-LSDA and t-BLYP are examples) while the *fully translated* functionals are labeled as ‘ft-DFT’ (ft-PBE, ft-LSDA and ft-BLYP are examples). The procedures for these translations have been previously discussed.<sup>68, 73, 74</sup> Various tests have shown that MC-PDFT give results in agreement with CASPT2 for predicting the properties of main-group compounds and metal complexes<sup>82-87</sup>, at much lower costs and scaling. There have however been no examination of the relative performance of MC-PDFT to KS-DFT, CASSCF, CASPT2, CCSD(T) and CCSDT for actinide complexes.

The next section presents the details of our computations. We then provide our results and discussion.

## 2.2 COMPUTATIONAL DETAILS

**2.2.1 Basis Set and Relativistic Effects:** With some exceptions, all our CASSCF, CASPT2, MC-PDFT and KS-DFT calculations were performed with ANO-RCC-VTZP basis sets.<sup>88, 89</sup> The primitive functions of the ANO-RCC-VTZP basis sets for the actinide, oxygen/fluorine/nitrogen and hydrogen atoms are contracted to (9s8p6d4f2g1h), (4s3p2d1f) and (3s2p1d), respectively. Scalar-relativistic effects were accounted for with Douglas-Kroll-Hess second-order Hamiltonian (DKH2).<sup>90-92</sup> CCSDT calculations were performed with the actinide atoms described using small-

core Stuttgart effective core potentials (ECPs) and associated valence basis sets.<sup>93</sup> The O and N atoms in these calculations were described with cc-pVTZ basis sets.<sup>94</sup>

**2.2.2 Systems Studied:** The systems and reactions that we studied are summarized in Table 2.1. As a starting point, we computed the structural properties of UN<sub>2</sub> as well as the UO<sub>2</sub><sup>m+</sup> ( $m = 0, 1$  or  $2$ ), NpO<sub>2</sub><sup>m+</sup> ( $m = 1$  or  $2$ ) and PuO<sub>2</sub><sup>m+</sup> ( $m = 1$  or  $2$ ) species. We then computed the adiabatic ionization potentials for these ions. The energies associated with the two-step water-induced reduction of the AnO<sub>2</sub><sup>2+</sup> species (where An = U, Np and Pu) to the corresponding HOAnO<sup>2+</sup> and An(OH)<sub>2</sub><sup>2+</sup> species have also been calculated, Table 2.1.<sup>24, 38</sup> The water-induced reactions are summarized in 2.3 and 2.4.

**Table 2.1: Systems studied in this work.**

Structure	Potential Energy Curves	Reactivity and Binding Energies
UO <sub>2</sub> <sup>2+/+/0</sup>	NpO <sub>2</sub> <sup>3+</sup>	UO <sub>2</sub> F <sup>+</sup> → UO <sub>2</sub> <sup>2+</sup> + F <sup>-</sup>
UN <sub>2</sub>	UO <sub>2</sub> F <sup>+</sup> (U-F bond)	NpO <sub>2</sub> F <sup>+</sup> → NpO <sub>2</sub> <sup>2+</sup> + F <sup>-</sup>
NpO <sub>2</sub> <sup>2+/+</sup>	NpO <sub>2</sub> F <sup>+</sup> (Np-F bond)	PuO <sub>2</sub> F <sup>+</sup> → PuO <sub>2</sub> <sup>2+</sup> + F <sup>-</sup>
PuO <sub>2</sub> <sup>2+/+</sup>	PuO <sub>2</sub> F <sup>+</sup> (Pu-F bond)	UO <sub>2</sub> <sup>2+</sup> + $\frac{1}{2}$ H <sub>2</sub> O → HOUO <sup>2+</sup> + $\frac{1}{4}$ O <sub>2</sub>
	Ionization Potentials	HOUO <sup>2+</sup> + $\frac{1}{2}$ H <sub>2</sub> O → U(OH) <sub>2</sub> <sup>2+</sup> + $\frac{1}{4}$ O <sub>2</sub>
	UO <sub>2</sub> <sup>2+</sup> → UO <sub>2</sub> <sup>+</sup>	NpO <sub>2</sub> <sup>2+</sup> + $\frac{1}{2}$ H <sub>2</sub> O → HONpO <sup>2+</sup> + $\frac{1}{4}$ O <sub>2</sub>
	UO <sub>2</sub> <sup>+</sup> → UO <sub>2</sub>	HONpO <sup>2+</sup> + $\frac{1}{2}$ H <sub>2</sub> O → Np(OH) <sub>2</sub> <sup>2+</sup> + $\frac{1}{4}$ O <sub>2</sub>
	NpO <sub>2</sub> <sup>2+</sup> → NpO <sub>2</sub> <sup>+</sup>	PuO <sub>2</sub> <sup>2+</sup> + $\frac{1}{2}$ H <sub>2</sub> O → HOPuO <sup>2+</sup> + $\frac{1}{4}$ O <sub>2</sub>
	PuO <sub>2</sub> <sup>2+</sup> → PuO <sub>2</sub> <sup>+</sup>	HOPuO <sup>2+</sup> + $\frac{1}{2}$ H <sub>2</sub> O → Pu(OH) <sub>2</sub> <sup>2+</sup> + $\frac{1}{4}$ O <sub>2</sub>
$AnO_2^{2+} + \frac{1}{2}H_2O \rightarrow AnO_2H^{2+} + \frac{1}{4}O_2$		(2.3)
$AnO_2H^{2+} + H_2O \rightarrow AnO_2H_2^{2+} + \frac{1}{4}O_2$		(2.4)

To further examine the abilities of MC-PDFT to yield good potential curves around equilibrium, we studied the Np(VI) species, NpO<sub>2</sub><sup>3+</sup>.<sup>16, 60</sup> Finally, we examined the structure and binding energies of the actinide-ligand interactions in UO<sub>2</sub>F<sup>+</sup>, NpO<sub>2</sub>F<sup>+</sup>, and PuO<sub>2</sub>F<sup>+</sup>, Table 2.1.

**2.2.3 Geometries:** We obtained the geometries of UN<sub>2</sub> and the AnO<sub>2</sub><sup>m+</sup> species at the CASSCF, CASPT2, CCSD(T), CCSDT, MC-PDFT and KS-DFT levels, Table 2.1. This was done by scanning the bond lengths in steps of 0.001 Å. To calculate the adiabatic reduction potentials of the AnO<sub>2</sub><sup>m+</sup> species, Table 2.1, we carried out single-point calculations at the equilibrium

geometries obtained with each method. The ground spin-free states at the CASPT2 level for the  $\text{AnO}_2^{m+}$  species are presented in Table 2.2. The ground states of actinide species are notoriously difficult to accurately determine.<sup>95-97</sup> As such, we have focused on determining the geometries and properties predicted by MC-PDFT at the CASPT2 ground states. It is quite possible that these states are not the MC-PDFT ground states. The ability of MC-PDFT to predict the excited state manifolds of various actinide species will be focus of future reports.

**Table 2.2: Ground state character of the  $\text{AnO}_2^{m+}$  species.**

Ground State Character		Ground State Character	
$\text{UO}_2^{2+}$ and $\text{UN}_2$	$^1\Sigma_g$	$\text{NpO}_2^{2+}$	$^2\Phi_u (\phi^1)$
$\text{UO}_2^+$	$^2\Phi_u (\phi^1)$	$\text{NpO}_2^+$	$^3H_g (\phi^1\delta^1)$
$\text{UO}_2$	$^3\Phi_u (7s^1\phi^1)$	$\text{PuO}_2^{2+}$	$^3H_g (\phi^1\delta^1)$
$\text{NpO}_2^{3+}$	$^1\Sigma_g$	$\text{PuO}_2^+$	$^4\Phi_u (\phi^1\delta^2)$

To compute ligand binding energies as well as the energetics of the water-induced reduction reactions for the  $\text{AnO}_2^{2+}$  species, 2.3 and 2.4, we optimized the structures of the  $\text{AnO}_2^{2+}$ ,  $\text{AnO}_2\text{H}^{2+}$ ,  $\text{AnO}_2\text{H}_2^{2+}$ , and  $\text{AnO}_2\text{F}^+$  species with the B3LYP functional<sup>98,99</sup> while describing the U, Np and Pu atoms with the Stuttgart small-core relativistic effective core potentials and associated valence basis sets.<sup>93</sup> The H, O and F atoms were described with def2-QZVPPD basis sets.<sup>100</sup> Dispersion interactions were accounted for with the D3 correction scheme while utilizing the Becke-Johnson damping approach, D3BJ.<sup>101-103</sup> This combination of DFT functional and basis sets is routinely used for optimizing large actinide complexes.<sup>2, 17-19, 26, 28, 34, 104, 105</sup> We then performed single-point CCSD(T), CASSCF, CASPT2, MC-PDFT and KS-DFT calculations on the optimized geometries.

To describe the region around the equilibrium metal-fluoride (An-F) bond distances of  $\text{UO}_2\text{F}^+$ ,  $\text{NpO}_2\text{F}^+$  and  $\text{PuO}_2\text{F}^+$ , we started from the B3LYP-D3BJ-optimized geometries. The positions of the actinide and oxygen atoms of the actinyl groups were fixed. The An-F bond distances were then varied in steps of 0.005 Å. The three-dimensional potential energy surface (PES) of  $\text{NpO}_2^{3+}$  was obtained in a similar fashion: the bond lengths were scanned in steps of 0.0025 Å from 1.64 to 1.75 Å for every bond angle. The bond angles were scanned in steps of 1.0° from 140° to 180°.

**2.2.4 Vibrational Frequencies:** The symmetric vibrational frequencies of the triatomic molecules were obtained by a sixth-degree polynomial fitting of the curves near the equilibrium geometries.

**2.2.5 Symmetry:** All the calculations in this work were carried out in the  $C_{2v}$  abelian sub-group rather than in the appropriate  $C_{\infty v}$  and  $D_{\infty h}$  groups of most of the studied actinide complexes.



Additional information regarding the use of symmetry and identification of CASPT2 ground states is provided in the Supplementary Material.

## 2.2.6 Multireference Calculations

**2.2.6.1. Complete active space self-consistent field calculations:** Except when otherwise noted, the frontier molecular orbitals formed from the 2p orbitals of the O and N atoms as well as the singly-occupied 5f orbitals of the U, Np and Pu atoms were placed in the CASSCF active space. This results in the following active spaces: (12/12) for  $\text{UO}_2^{2+}$ ,  $\text{NpO}_2^{3+}$  and NUN, (13/13) for  $\text{UO}_2^+$ ,  $\text{UO}_2\text{H}^{2+}$  and  $\text{NpO}_2^{2+}$ , (14/14) for  $\text{UO}_2$ ,  $\text{UO}_2\text{H}_2^{2+}$ ,  $\text{UO}_2\text{F}^+$ ,  $\text{NpO}_2^+$ ,  $\text{NpO}_2\text{H}^{2+}$ , and  $\text{PuO}_2^{2+}$ , (15/15) for  $\text{NpO}_2$ ,  $\text{NpO}_2\text{H}_2^{2+}$ ,  $\text{NpO}_2\text{F}^+$  and  $\text{PuO}_2^+$ , and (16/16) for  $\text{PuO}_2$ ,  $\text{PuO}_2\text{F}^+$  and  $\text{PuO}_2\text{H}_2^{2+}$ . The partitioning of the orbitals into the four representations of the  $C_{2v}$  sub-group are similar to previous reports.<sup>12-14, 37, 104, 105</sup> For  $\text{F}^-$  and  $\text{H}_2\text{O}$ , we used (2/2) and (4/4) complete active spaces, respectively.

**2.2.6.2 Complete active space second order perturbation theory calculations:** We used an empirical ionization-potential–electron-affinity (IPEA) shift<sup>106, 107</sup> of 6.80 eV in the CASPT2 calculations. An imaginary shift of 5.44 eV was used to prevent intruder states.<sup>108, 109</sup>

**2.2.6.3 Complete active space pair-density functional theory calculations:** In the MC-PDFT calculations, we used 3 translated (t-PBE, t-BLYP and t-LSDA) and 3 fully-translated (ft-PBE, ft-BLYP, ft-LSDA) on-top pair density functionals of the CASSCF  $\rho$  and  $\Pi$ .<sup>68, 73, 74</sup>

**2.2.7 Kohn-Sham DFT Calculations:** We studied the actinide species with 5 KS-DFT functionals (BLYP,<sup>99, 110</sup> B3LYP,<sup>98, 99</sup> PBE,<sup>111</sup> PBE0<sup>8, 112</sup> and LSDA<sup>113, 114</sup>). By including B3LYP and PBE0, we are able to compare the improvement of the generalized gradient approximation (GGA) functionals either by adding HF exchange or by using the MC-PDFT ansatz with CASSCF  $\rho$  and  $\Pi$ . t-PBE and ft-PBE have been compared to PBE and PBE0 for various properties.<sup>82, 83, 86, 87, 115,</sup>

116

**2.2.8 Coupled Cluster Calculations:** Coupled cluster calculations were performed at the CCSD(T) and CCSDT levels. All-electron CCSD(T) calculations were performed with the ANO-RCC-TZVP basis sets while employing the DKH2 Hamiltonian.<sup>90-92</sup> In these calculations, the  $1s^2$ - $5d^{10}$  shells of the actinides and the  $1s^2$  shells of O, N and F were kept frozen. As noted earlier,

CCSDT calculations were performed with relativistic ECPs and cc-pVTZ basis sets on the light atoms. 11 core orbitals were frozen during the CCSDT calculations.

**2.2.9 Software:** All-electron KS-DFT, CCSD(T), CASSCF, CASPT2 and MC-PDFT calculations were carried out with MOLCAS 8.1.<sup>117, 118</sup> KS-DFT calculations with relativistic pseudopotentials were performed with *Gaussian* 16.<sup>119</sup> CCSDT calculations were performed with MRCC.<sup>120, 121</sup>

## 2.3. RESULTS AND DISCUSSIONS

All the calculations in this work were performed with symmetry. This makes for faster calculations and allows us to separate degenerate states into different irreducible representations. However, it is interesting to wonder whether MC-PDFT conserves the degeneracy of these states in the absence of symmetry constraints. Tests on  $\text{NpO}_2^{2+}$  indicate that MC-PDFT conserves the degeneracy of the two  $^2\Phi_u$  states in the absence of symmetry, see Supplementary Material. These tests were performed with state-averaged CASSCF and multi-state MC-PDFT. We arrived at the same conclusion when we examined other systems and regardless of the nature of the starting orbitals. In addition, we found similar equilibrium Np-O bond distances for  $\text{NpO}_2^{2+}$  from the MC-PDFT calculations with and without symmetry. This gives us confidence regarding the properties computed with symmetry constraints.

### 2.3.1 Structural Properties of the Actinyl Groups.

The mean absolute deviations (MADs) and root mean squared deviations (RMSDs) from CASPT2 of the calculated bond distances obtained with KS-DFT, MC-PDFT, CASSCF and CCSD(T) of  $\text{UN}_2$  and the  $\text{AnO}_2^{m+}$  (An = U, Np, Pu and  $m$  is any of 0, 1, 2) species are shown in Figure 2.1. These molecules have linear ground state geometries. The dominant CASSCF CSFs have weights of 88.3%, 87.9%, 89.7%, 89.6%, 86.3%, 89.0%, 84.4%, 87.6% at the CASPT2 geometries of  $\text{UN}_2$ ,  $\text{UO}_2^{2+}$ ,  $\text{UO}_2^+$ ,  $\text{UO}_2$ ,  $\text{NpO}_2^{2+}$ ,  $\text{NpO}_2^+$ ,  $\text{PuO}_2^{2+}$  and  $\text{PuO}_2^+$ , respectively. Thus these  $f^0$ ,  $f^1$ ,  $f^2$  and  $f^3$  systems have moderate/appreciable multireference characters.<sup>51-53</sup> The magnitudes of the contributions from the dominant configurations suggest that the perturbative treatment of triple excitations in CCSD(T) will help correct for some of these multiconfigurational effects. We therefore expect that CCSD(T) will give reasonable estimates of the bond distances. As seen in Table 2.3, CASPT2 and CCSD(T) results are always within 0.012 Å of CCSDT. For  $\text{UO}_2$ , these methods are within 0.010 Å of the experimental value of 1.800 Å for the  $^3\Phi_u$  ground state.<sup>122</sup> Our CASPT2 results also agree with previous reports. Gagliardi et al. obtained a U-N bond length of 1.734 Å for  $\text{UN}_2$  and a U-O bond distance of 1.705 Å for  $\text{UO}_2^{2+}$ .<sup>13</sup> These values are within 0.007

Å of our results. Overall, relative to CASPT2, CCSD(T) has a MAD of 0.004 Å and a RMSD of 0.004 Å, Figure 2.1. In contrast, CASSCF yields bond distances that are generally longer than CASPT2. This is understandable given the excessively antibonding character of CASSCF solutions.<sup>50, 123</sup> Of the KS-DFT functionals, B3LYP perform best. This functional is always within 0.010 Å of CASPT2. In contrast, BLYP gives bonds that are far too long (MAD of 0.031 Å) and performs worst of all the methods. PBE0 gives bonds that are too short, underestimating by 0.020 Å. PBE has a MAD of 0.018 Å.

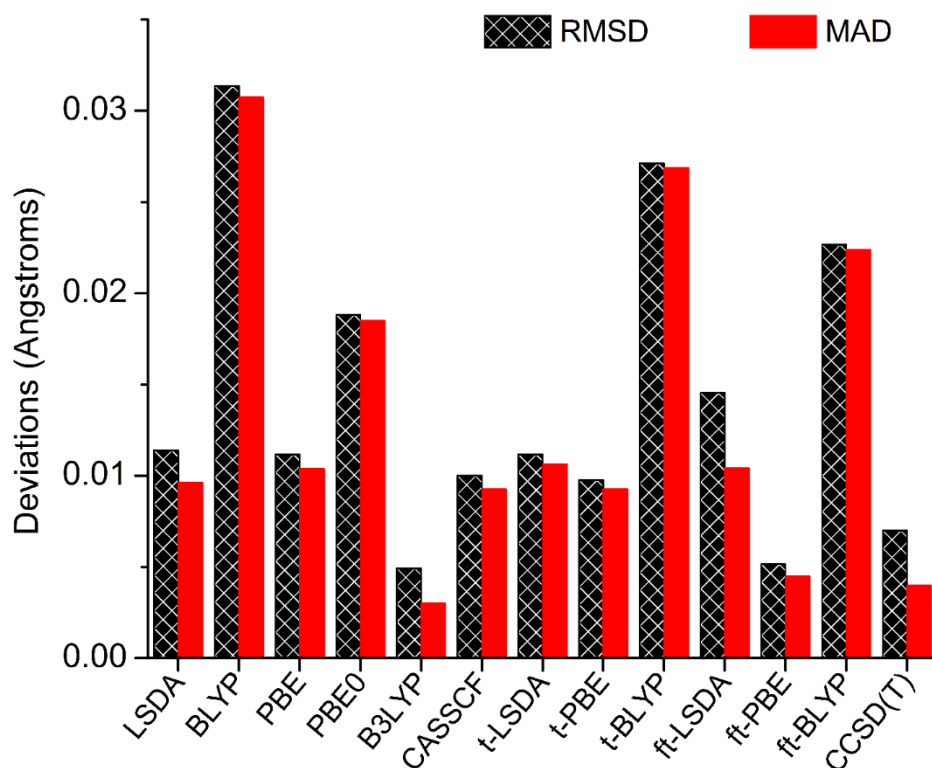


**Figure 2.1: MADs and RMSDs relative to CASPT2 for bond distances of actinyls.**

For MC-PDFT, the *ft*- functionals generally improve slightly over their *t*- counterparts, which already improve over the analogous KS-DFT functionals, Figure 2.1. *ft*-PBE has the lowest MAD and RMSD of all the MC-PDFT methods. It is competitive with B3LYP and CCSD(T), Figure 2.1. Importantly, *ft*-PBE correctly reproduces the trends in the actinyl bond-lengths obtained with CCSD(T), CCSDT and CASPT2. The bond-length elongation as one proceeds from  $\text{AnO}_2$  to  $\text{AnO}_2^+$  and  $\text{AnO}_2^{2+}$  are well reproduced, see Supplementary Material. *ft*-PBE also correctly reproduces the contraction as one moves from the U species to the Np and Pu analogues. However, due to the rather small margins, *ft*-PBE confers little advantages over B3LYP for structure

optimizations, Figure 2.1. Importantly, calculations with B3LYP can be used in a fairly black-box fashion and are cheaper.

**Table 2.3: Comparison of the actinyl bond-lengths from all-electron scalar-relativistic CASPT2 and CCSD(T) calculations with CCSDT results using scalar-relativistic effective core potentials.**

	UO <sub>2</sub> <sup>2+</sup>	UN <sub>2</sub>	UO <sub>2</sub> <sup>+</sup>	UO <sub>2</sub>
CCSDT	1.698	1.726	1.747	1.790
CCSD(T)	+0.002	+0.006	+0.012	+0.007
CASPT2	+0.000	+0.003	+0.009	+0.003
	NpO <sub>2</sub> <sup>2+</sup>	NpO <sub>2</sub> <sup>+</sup>	PuO <sub>2</sub> <sup>2+</sup>	PuO <sub>2</sub> <sup>+</sup>
CCSDT	1.683	1.741	1.684	1.725
CCSD(T)	+0.002	-0.004	-0.003	-0.007
CASPT2	+0.007	-0.008	+0.005	-0.008

### 2.3.2 Potential Energy Curves.

**2.3.2.1. NpO<sub>2</sub><sup>3+</sup>:** Jensen et al. reported that HF, MP2, CASSCF, CASPT2 and CCSD(T) predict NpO<sub>2</sub><sup>3+</sup> as being linear.<sup>60</sup> These approaches contain 100% of the HF exchange energy. In contrast, LSDA, PBE and B3LYP predict NpO<sub>2</sub><sup>3+</sup> as a bent molecule with bond angles of 149-165°. These functionals contain 0-20% of the HF exchange energy with the residual exchange energy in these functionals treated with GGA exchange. Interestingly, Jensen et al have also developed an approach for combining multiconfigurational methods with DFT. They employ a range-separation methodology.<sup>61</sup> Their approach replaces HF exchange with GGA exchange and so favors the bent structure for NpO<sub>2</sub><sup>3+</sup>, just like LSDA, PBE and B3LYP.<sup>60</sup> By contrast, Scuseria et al.'s CCD0/DFT method favors a linear structure for NpO<sub>2</sub><sup>3+</sup>.<sup>16</sup> CCD0/DFT includes all the HF exchange energy. It would thus appear that large amounts of HF exchange is the crucial ingredient for favoring the linear structure of NpO<sub>2</sub><sup>3+</sup>. However, it has been previously suggested that the bending seen with some KS-DFT functionals is due to significant static correlation effects.<sup>124</sup> We find some evidence of this in our results. At the PBE-optimized bent (149°) geometry, the dominant CSF has a weight of 81% while with the linear geometry, the dominant CSF has a weight of 83%. These weights are suggestive of moderate/appreciable nondynamical electron correlation effects. In contrast, the CCSD T1-diagnostics<sup>125</sup> for the bent and linear structures are 0.037 and 0.040 respectively while the largest double excitation amplitudes are 0.14 and 0.10, respectively. The T1 diagnostics are

less than the threshold of 0.050 previously suggested for inorganic species.<sup>51</sup> The double excitation amplitudes are also fairly moderate. The contrasting pictures from the CASSCF CSF weights and the CCSD diagnostics likely indicate that a subtle balance of static and dynamical correlation determine the relative energies of the linear and bent structures of  $\text{NpO}_2^{3+}$ .

The potential energy curves, PESs, obtained for  $\text{NpO}_2^{3+}$  with CCSDT, CASPT2, MC-PDFT and KS-DFT are presented in Figure 2.2. 3D PESs are provided in the Supplementary Material. CASSCF favors the linear structure, albeit with a minor penalty,  $< 1$  kcal/mol, for bending, see Supplementary Material. This is indicative of a flat PES. CCSD(T) also favors the linear structure but with near degeneracy for bent structures with bond angles up to  $169^\circ$ . For CASSCF and CCSD(T), the potential energy curves of  $\text{NpO}_2^{3+}$ , although flat, ultimately have only one minimum (the linear structure). In contrast, with CASPT2, the lowest energy structure is a bent structure (angle of  $174^\circ$ ). This bent structure is iso-energetic with the linear structure (relative energy 0.010

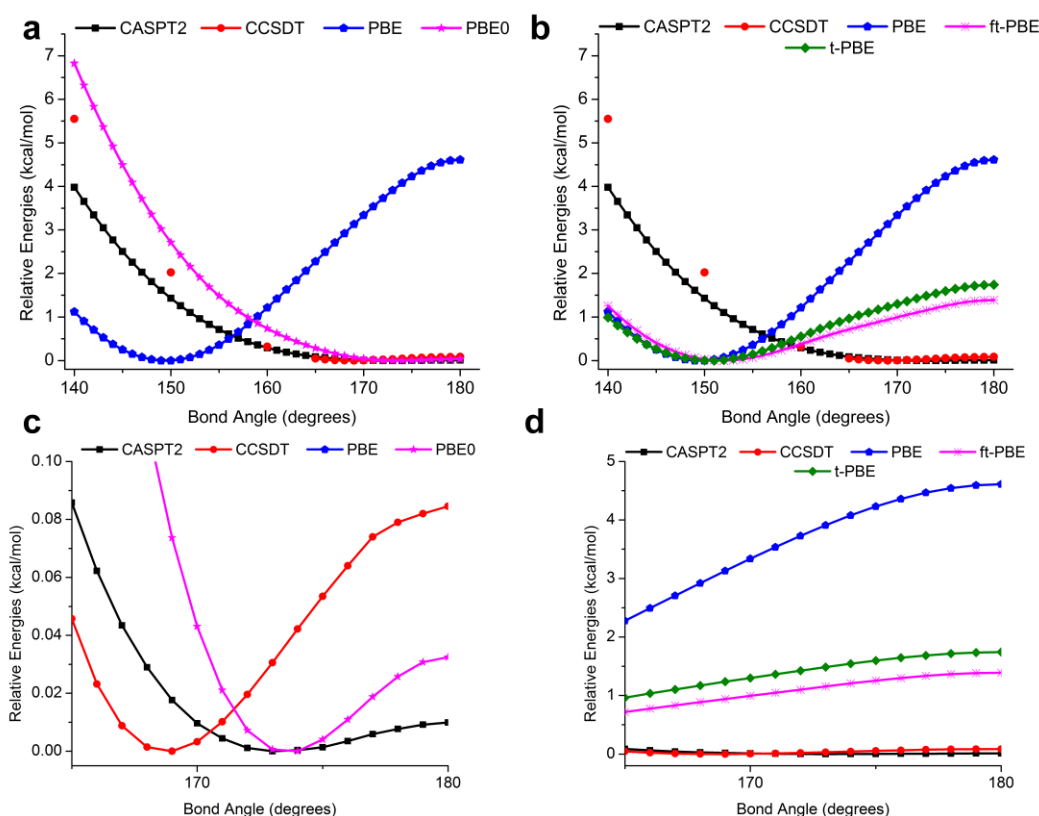


**Figure 2.2: Potential energy curves for  $\text{NpO}_2^{3+}$ .** Comparison of CASPT2 and CCSDT to (A) KS-DFT functionals, (B) KS-DFT and MC-PDFT functionals, (C) Expanded  $165\text{--}180^\circ$  range of A and (D) Expanded  $165\text{--}180^\circ$  range of B. The Np-O bond distances were fixed at  $1.685 \text{ \AA}$ .

kcal/mol), Figure 2.2. CCSDT agrees well with CASPT2. The minimum CCSDT structure has a bond angle of  $169^\circ$ . This bent structure is more stable than the linear structure by just 0.080 kcal/mol, Figure 2.2. From CCSDT and CASPT2, we see that PES of  $\text{NpO}_2^{3+}$  has one minimum (bent structure) with a negligible energy barrier to inversion. Pure KS-DFT calculations favor bending with angles of about  $149^\circ$ , Figure 2.2. These functionals describe the linear structure as a saddle point, 4-5 kcal/mol above the bent structures. Addition of HF exchange to the KS-DFT functionals favors near-degeneracy of the linear and bent structures. With PBE0, the bent structure has an angle of  $175^\circ$  and is 0.02 kcal/mol lower in energy, agreeing with CASPT2 and CCSDT. Interestingly, MC-PDFT favors the bent structure, Figure 2.2, like the pure KS-DFT functionals. Thus, the hybrid KS-DFT functionals provide a better description than MC-PDFT. MC-PDFT however reduces the energy gap between the bent and linear structures. With ft-PBE and t-PBE, the bent structure is more stable by 1-2 kcal/mol, in comparison with 4.7 kcal/mol with PBE, Figure 2.2. In converse, the most stable structures obtained with MC-PDFT have similar bond angles to those from pure KS-DFT. As an example, with ft-PBE and t-PBE, the bond angles are unchanged from PBE,  $149^\circ$ , suggesting that MC-PDFT stabilize the linear structure due to some static correlation energy carried over from CASSCF via the multiconfigurational  $\rho$  and  $\Pi$ . This is however not enough to yield larger O-Np-O angles and degenerate linear and bent structures. We conclude that static correlation is not the only culprit responsible for excessive stabilization of bent  $\text{NpO}_2^{3+}$  by pure KS-DFT and MC-PDFT functionals. The pair-density functionals used in MC-PDFT could be improved with a better balance of GGA and HF exchange.

**2.3.2.2. Actinyl-Ligand Bonds:** Good descriptions of the equilibrium region between actinyl groups and ligands as well as accurate prediction of actinyl-ligand binding energies are crucial for the development of accurate molecular mechanics force field parameters and numerical evaluation of vibrational frequencies.<sup>126, 127</sup> To study actinyl-ligand interactions, we used the fluoride ion,  $\text{F}^-$  and coordinated it to  $\text{UO}_2^{2+}$ ,  $\text{NpO}_2^{2+}$  and  $\text{PuO}_2^{2+}$ . The PESs associated with the U-F bond in  $\text{UO}_2\text{F}^+$  are shown in Figure 2.3. The data for  $\text{NpO}_2\text{F}^+$  and  $\text{PuO}_2\text{F}^+$  is presented in the Supplementary Material. CCSD(T) and CASPT2 give similar curves. In contrast, the near-equilibrium PESs obtained with CASSCF, LSDA, BLYP, t-LSDA and ft-LSDA are quite different from CASPT2. The closest results to CASPT2 were found with t-PBE and ft-PBE. These track CASPT2 quite closely, Figure 2.3. As such, ft-PBE not only accurately describes the actinyl groups but also describes their interactions with environmentally-relevant ligands quite well.

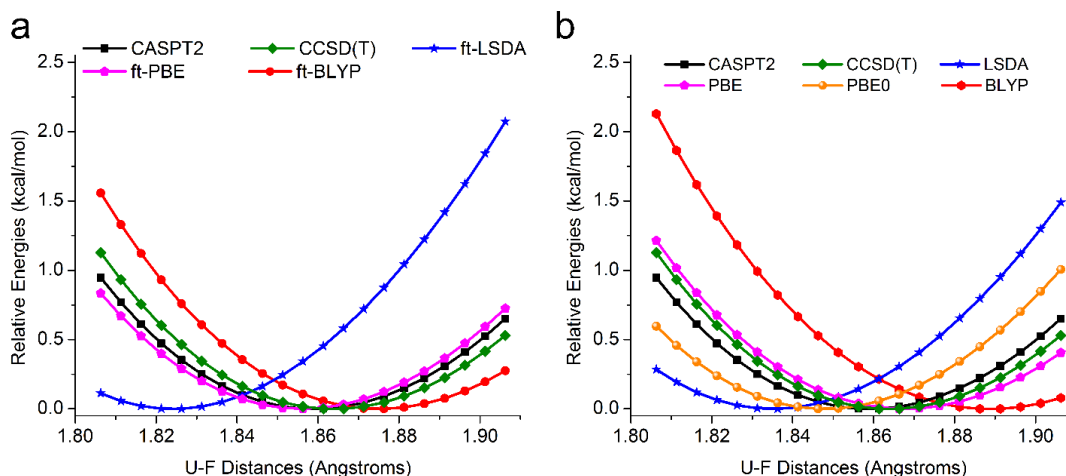


**Figure 2. 3: Potential energy curves for the U-F bond of  $\text{UO}_2\text{F}^+$  obtained with (A) CASPT2, CCSD(T) and MC-PDFT functionals and (B) CASPT2, CCSD(T) and KS-DFT functionals.**

**2.3.2.3 Actinyl-Ligand Bond Dissociation Energies:** We calculated the binding energies of the actinide-fluoride bonds in  $\text{UO}_2\text{F}^+$ ,  $\text{NpO}_2\text{F}^+$  and  $\text{PuO}_2\text{F}^+$ . The deviations of the various methods from CASPT2 are given in Table 2.4. The MSD and MAD of CCSD(T) from CASPT2 are 5.3 and 5.3 kcal/mol, respectively, suggesting that CCSD(T) very slightly over-binds  $\text{F}^-$ , relative to CASPT2. This agrees with the results presented in Figures 2.1 and 2.3. We see similar behavior with ft-BLYP and ft-PBE which have MADs of 1.4 and 4.9 kcal/mol, respectively. These are much more improved over BLYP and PBE which have MADs of 9.9 and 15.8 kcal/mol, respectively. ft-BLYP and ft-PBE also do better than B3LYP and PBE0. The good performance of ft-PBE for the structures of the actinyl moieties, Figure 2.1, as well as the actinide-ligand bond parameters, Figure 2.3, and binding energies, Table 2.4, makes it suitable for the development of high-quality *ab*

**Table 2.4: Deviations (given in kcal/mol) for CASSCF, CCSD(T), MC-PDFT and KS-DFT from CASPT2 for the binding energies of  $\text{F}^-$  to  $\text{UO}_2^{2+}$ ,  $\text{NpO}_2^{2+}$  and  $\text{PuO}_2^{2+}$ .**

	CASSCF	CCSD(T)	MC-PDFT		
			ft-LSDA	ft-BLYP	ft-PBE
Max. deviation	-41.1	5.9	18.4	2.2	6.6
MSD	-40.9	5.3	17.2	0.6	4.9
MAD	40.9	5.3	17.2	1.4	4.9
	KS-DFT				
	LSDA	BLYP	PBE	B3LYP	PBE0
Max. deviation	32.4	11.5	17.3	8.5	10.9
MSD	30.6	9.9	15.8	7.4	10.0
MAD	30.6	9.9	15.8	7.4	10.0

*initio*-derived force-field parameters for actinide complexes. Although B3LYP gives similar accuracy for equilibrium geometries, Figure 2.1, ft-PBE is closer to CASPT2 when used to describe all the properties necessary for molecular mechanics force-field parameterizations. Of the MC-PDFT functionals, ft-LSDA and t-LSDA have the worst performances, with MADs of 17.2 and 15.8 kcal/mol, respectively. These are however still much improved over LSDA, 30.6 kcal/mol, and CASSCF, 40.9 kcal/mol.

**2.3.2.4 Vibrational Frequencies:** We compare the frequencies of the actinyl symmetric stretching vibrational modes obtained with various methods against CASPT2 in Figure 2.4. For  $\text{UO}_2^{2+}$ , we obtained 1029 and 1005  $\text{cm}^{-1}$  at the CCSD(T) and CASPT2 levels, respectively. Gagliardi et al. obtained 1043  $\text{cm}^{-1}$  for this system with CASPT2.<sup>13</sup> For  $\text{UN}_2$ , we obtained 1060 and 1032  $\text{cm}^{-1}$  with CCSD(T) and CASPT2, respectively. These are comparable to 1029 and 999  $\text{cm}^{-1}$  from previous CCSD(T)<sup>105</sup> and CASPT2 calculations.<sup>13</sup> The differences in these results are likely due to disparate fitting procedures. As such, we used the same sixth-order polynomial fitting procedure for all the theoretical methods evaluated in this work. The deviations of the various methods from CASPT2 are examined in Figure 2.4 and Table 2.5. CCSD(T) has a MAD of about 26  $\text{cm}^{-1}$  from CASPT2, Table 2.5. This is quite good. Similarly, CASSCF yields frequencies that are on average

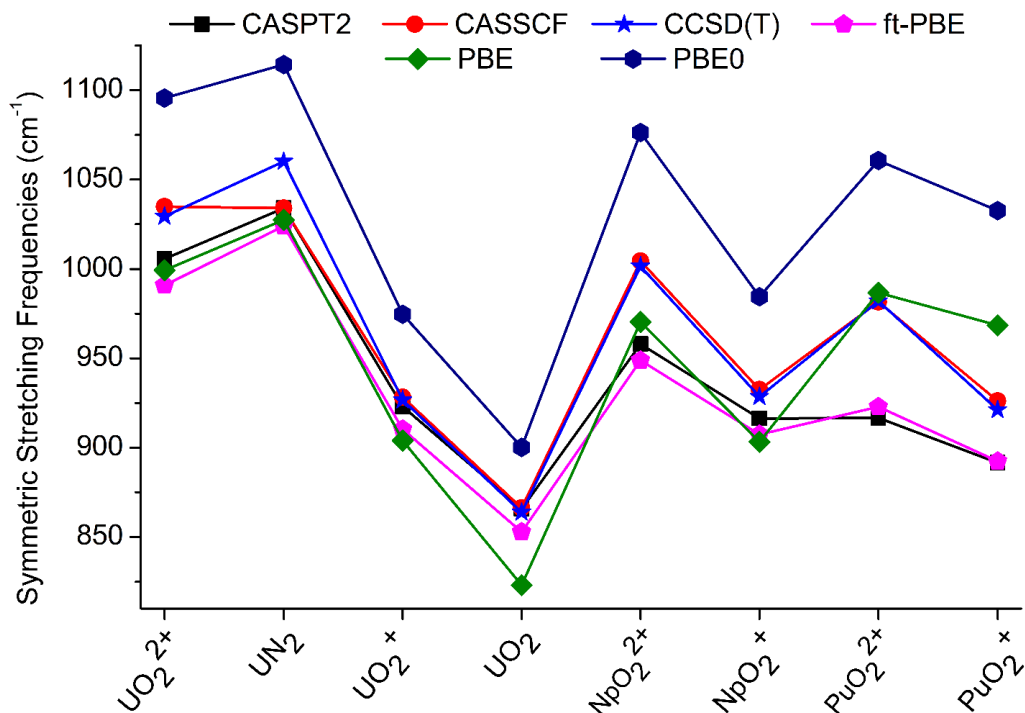


**Figure 2.4:** Calculated symmetric stretching vibrational frequencies obtained with various methods.



**Table 2.5: Deviations ( $\text{cm}^{-1}$ ) of various methods from CASPT2 for the frequencies of the symmetric stretching vibrational mode of  $\text{UN}_2$  and actinyl groups.**

	CASSCF	CCSD(T)	MC-PDFT		
			ft-LSDA	ft-BLYP	ft-PBE
Max. deviation	+65	+65	+44	-54	-8
MSD	+25	+25	+24	-47	-8
MAD	25	26	29	47	9
	KS-DFT				
	LSDA	BLYP	PBE	B3LYP	PBE0
Max. deviation	+109	-61	+77	+127	+144
MSD	+48	-33	+9	+54	+91
MAD	48	41	31	54	91

quite close to CASPT2 with a MAD of  $25 \text{ cm}^{-1}$ . The maximum deviation of CCSD(T) and CASSCF are however somewhat large,  $65 \text{ cm}^{-1}$ . These suggest to us that their performance is a bit uneven. In contrast, the deviations of ft-PBE from CASPT2 are in a narrower range. ft-PBE has a maximum deviation of  $15 \text{ cm}^{-1}$ . Additionally, ft-PBE tracks CASPT2 for all the actinyls and has MAD of only  $9 \text{ cm}^{-1}$ , Figure 2.4 and Table 2.5. The good performance of ft-PBE for the vibrational frequencies is justified given its good performance for structural parameters, Figure 2.1, PESs, Figure 2.3, and the bond dissociation energies, Table 2.4.

### 2.3.3 Reaction Energies.

**2.3.3.1 Water-induced redox processes:** Wahlgren et al. found that for U, CASPT2 predicts that reactions **3** and **4** are both endothermic whereas B3LYP predicts that these reactions are exothermic.<sup>38</sup> They found an overall difference of  $26.2 \text{ kcal/mol}$  between CASPT2 and B3LYP for the energies of these two reactions. This is a substantial difference and it is thus interesting to determine whether other DFT functionals behave in a similar manner and whether MC-PDFT and CCSD(T) can reduce these errors. We are also interested in the trends of these methods for analogous reactions with Np and Pu. The MADs and MSDs of the other methods relative to the CASPT2 benchmark are presented in Table 2.6. CCSD(T) has a MAD of  $4.0 \text{ kcal/mol}$  with a maximum deviation of  $-12.5 \text{ kcal/mol}$ . ft-PBE is competitive with CCSD(T) with a MAD of  $3.0 \text{ kcal/mol}$  and a maximum deviation of  $10.7 \text{ kcal/mol}$  from the CASPT2 benchmark. In contrast, CASSCF has a MAD of  $7.9 \text{ kcal/mol}$ , almost double that ft-PBE and CCSD(T). The pure DFT functionals, LSDA, BLYP and PBE also do very well with MADs around  $3.2\text{-}3.7 \text{ kcal/mol}$  from the benchmark. As to the basic essence of this work, it is encouraging that ft-PBE improves upon

CASSCF and does not destroy the good performance of PBE for these reactions. The individual reaction energies for the U, Np and Pu species are compared in the Supplementary Material.

**Table 2.6: Deviations (given in kcal/mol) for CASSCF, CCSD(T), MC-PDFT and KS-DFT from CASPT2 for the energetics of the water-induced reduction of actinyl groups (reactions 1 and 2).**

	CASSCF	CCSD(T)	MC-PDFT		
			ft-LSDA	ft-BLYP	ft-PBE
Max. deviation	17.9	-12.5	-11.8	-14.1	+10.7
MSD	7.4	-3.2	-3.7	-5.5	-2.7
MAD	7.9	4.0	4.1	5.5	3.0
	KS-DFT				
	LSDA	BLYP	PBE	B3LYP	PBE0
Max. deviation	+6.7	+10.2	-13.2	-8.2	-7.3
MSD	2.3	-3.0	-0.7	-4.7	-3.2
MAD	3.7	3.4	3.2	4.7	3.4

**2.3.3.2 Redox potentials:** The adiabatic ionization potentials of  $\text{UO}_2^+$ ,  $\text{NpO}_2^+$  and  $\text{PuO}_2^+$  as well as  $\text{UO}_2$  obtained at the CASPT2 and CCSD(T) levels are compared to experimental estimates in Table 2.7. The experimental estimates of these species have rather large error bars, up to 0.4 eV. CCSD(T) and CASPT2 are always within the accuracy limits of the experimental data except for  $\text{PuO}_2^{2+}$ .

**Table 2.7: Experimental and calculated adiabatic reduction potentials (eV) for various actinyl species.**

	Experiment	CCSD(T)	CASSCF	CASPT2	ft-PBE
$\text{UO}_2^{2+}$	$14.6 \pm 0.4$	14.2	13.3	14.3	14.8
$\text{NpO}_2^{2+}$	$15.1 \pm 0.4$	15.2	14.3	15.3	15.3
$\text{PuO}_2^{2+}$	$15.1 \pm 0.4$	15.8	14.7	16.0	15.9
$\text{UO}_2^+$	$6.1 \pm 0.003$	6.0	5.2	6.0	6.1

Here CCSD(T) and CASPT2 yield 15.8 and 16.0 eV, respectively, compared to the experimental estimate of  $15.1 \pm 0.4$  eV. KS-DFT and MC-PDFT also yield ionization potentials above 15.8 eV for  $\text{PuO}_2^{2+}$ . CASSCF is the only method within the error margin of the experiment. CASSCF however significantly underestimates the ionization potentials of all the other systems. Indeed, apart from LSDA, t-LSDA ft-LSDA and CASSCF, all the methods do well for  $\text{UO}_2^{2+} \rightarrow \text{UO}_2^+$ ,  $\text{UO}_2^+ \rightarrow \text{UO}_2$  and  $\text{NpO}_2^{2+} \rightarrow \text{NpO}_2^+$ . The experimental estimate for  $\text{PuO}_2^{2+} \rightarrow \text{PuO}_2^+$ , 15.1 eV is far too low, Table 2.7, compared to the theoretical methods. That being said, CASPT2 has a mean absolute error, MAE, of 0.38 eV, from the experimental data. Figure 2.5. This is reasonably in line

with the experimental uncertainties, Table 2.7. CCSD(T), ft-BLYP, ft-PBE, t-BLYP and t-PBE are all competitive with CASPT2, Figure 2.5, with MAEs between 0.27 eV and 0.37 eV. In contrast, CASSCF fails badly with a MAE of 0.86 eV. KS-DFT is better than CASSCF with BLYP, PBE and PBE0 being the best with MAEs of 0.55, 0.56 and 0.53 eV, respectively. It is a success story that t-PBE and ft-PBE perform much better than CASSCF, PBE and PBE0. The performance of the various methods against CASPT2 as the benchmark are discussed in the Supplementary Material.

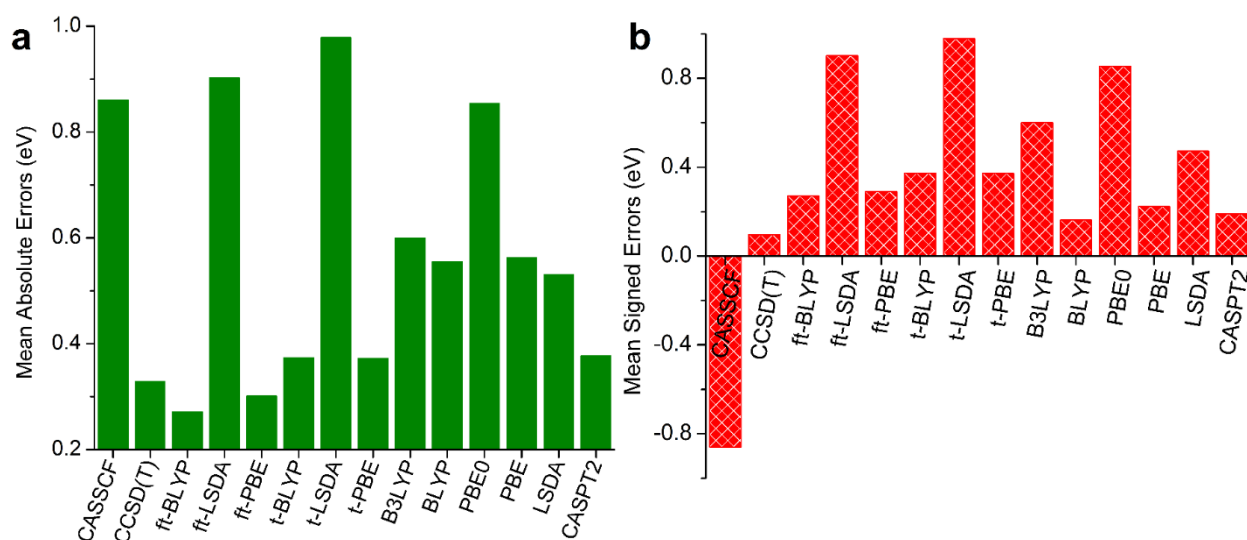


**Figure 2.5:** Mean absolute deviations (A) and signed deviations (B), eV, of KS-DFT, CCSD(T), CASSCF, MC-PDFT and CASPT2 from experimental estimates of the ionization potentials.

## 2.4. CONCLUSIONS

To explore the possibility of using multiconfigurational pair-density functional theory (MC-PDFT) for actinide chemistry, we have examined the structural, electronic and redox properties of various actinyl species. We compare the predictions from MC-PDFT against those from CASPT2, CCSD(T) and CCSDT. We also investigated the extent to which MC-PDFT improves over Kohn-Sham DFT. We investigated the performance of these methods at the scalar-relativistic level, which is at least sufficient to allow for describing the trends in the properties of many actinide complexes. Some of the properties of interest that we considered are equilibrium structures and vibrational frequencies, the potential energy curves of  $\text{NpO}_2^{3+}$ , ligand binding energies as well as redox potentials. In all cases, we considered properties predicted by MC-PDFT, CASSCF, CCSD(T) and KS-DFT at the CASPT2 electronic ground state. Our calculations were performed

with symmetry constraints. Importantly, we confirmed that MC-PDFT conserves the degeneracy of degenerate electronic states when these constraints are lifted.

The ft-PBE MC-PDFT functional does quite well for the structural parameters, ligand binding energies, vibrational frequencies, redox potentials, as well as redox reactivities. This functional supersedes all other MC-PDFT functionals and significantly improves on CASSCF. ft-PBE can be particularly useful for understanding small-molecule activation by trans-uranium complexes. It is also excellently situated for studying systems with significantly greater static electron correlation effects and excited-state properties than those considered in this work. When ft-PBE is compared against PBE, PBE0 and B3LYP, the margins are rather narrow as the KS-DFT functionals do quite well for the systems studied in this work. This further justifies the extensive use of KS-DFT for computational actinide chemistry over the last few decades. The very special case of  $\text{NpO}_2^{3+}$  illustrates a possible direction for improving on extant MC-PDFT functionals, introduction of some Hartree-Fock exchange. To summarize, we recommend the following methods for predicting the properties of actinyl complexes:

- 1) Structure and vibrational properties: ft-PBE
- 2) Ligand binding energies: ft-BLYP, ft-PBE and CCSD(T)
- 3) Redox potentials: ft-PBE and CCSD(T)
- 4) Redox reactivity: PBE, ft-PBE and CCSD(T).

## REFERENCES

1. B. B. Averkiev, M. Mantina, R. Valero, I. Infante, A. Kovacs, D. G. Truhlar and L. Gagliardi, *Theor. Chem. Acc.* **129**, 657-666 (2011).
2. N. Kaltsoyannis, *Chem-Eur. J.* **24**, 2815-2825 (2018).
3. G. Schreckenbach and G. A. Shamov, *Accounts Chem. Res.* **43**, 19-29 (2010).
4. V. Vallet, P. Macak, U. Wahlgren and I. Grenthe, *Theor. Chem. Acc.* **115**, 145-160 (2006).
5. D. Q. Wang, W. F. van Gunsteren and Z. F. Chai, *Chem. Soc. Rev.* **41**, 5836-5865 (2012).
6. K. Capelle, *Braz. J. Phys.* **36**, 1318-1343 (2006).
7. A. J. Cohen, P. Mori-Sanchez and W. T. Yang, *Chem. Rev.* **112**, 289-320 (2012).
8. J. P. Perdew, M. Emzerhof and K. Burke, *J. Chem. Phys.* **105**, 9982-9985 (1996).
9. J. P. Perdew, A. Ruzsinszky, L. A. Constantin, J. W. Sun and G. I. Csonka, *J. Chem. Theory Comput.* **5**, 902-908 (2009).
10. E. R. Batista, R. L. Martin and P. J. Hay, *J. Chem. Phys.* **121**, 11104-11111 (2004).
11. C. Clavaguera-Sarrio, N. Ismail, C. J. Marsden, D. Begue and C. Pouchan, *Chem. Phys.* **302**, 1-11 (2004).
12. C. Clavaguera-Sarrio, V. Vallet, D. Maynau and C. J. Marsden, *J. Chem. Phys.* **121**, 5312-5321 (2004).
13. L. Gagliardi and B. O. Roos, *Chem. Phys. Lett.* **331**, 229-234 (2000).
14. L. Gagliardi, B. O. Roos, P. A. Malmqvist and J. M. Dyke, *J. Phys. Chem. A* **105**, 10602-10606 (2001).
15. M. Garcia-Hernandez, C. Lauterbach, S. Kruger, A. Matveev and N. Rosch, *J. Comput. Chem.* **23**, 834-846 (2002).
16. A. J. Garza, A. G. S. Alencar and G. E. Scuseria, *J. Chem. Phys.* **143**, 244106 (2015).
17. Y. K. Han, *J. Comput. Chem.* **22**, 2010-2017 (2001).
18. Y. K. Han and K. Hirao, *J. Chem. Phys.* **113**, 7345-7350 (2000).
19. N. Iche-Tarrat and C. J. Marsden, *J. Phys. Chem. A* **112**, 7632-7642 (2008).
20. N. Kaltsoyannis, *Inorg. Chem.* **52**, 3407-3413 (2013).
21. A. Kovacs and R. J. M. Konings, *J. Phys. Chem. A* **115**, 6646-6656 (2011).
22. S. A. Kozimor, P. Yang, E. R. Batista, K. S. Boland, C. J. Burns, D. L. Clark, S. D. Conradson, R. L. Martin, M. P. Wilkerson and L. E. Wolfsberg, *J. Am. Chem. Soc.* **131**, 12125-12136 (2009).
23. K. N. Kudin, G. E. Scuseria and R. L. Martin, *Phys. Rev. Lett.* **89**, 266402 (2002).
24. L. V. Moskaleva, S. Kruger, A. Spörl and N. Rosch, *Inorg. Chem.* **43**, 4080-4090 (2004).
25. S. O. Odoh, G. D. Bondarevsky, J. Karpus, Q. Cui, C. He, R. Spezia and L. Gagliardi, *J. Am. Chem. Soc.* **136**, 17484-17494 (2014).
26. S. O. Odoh and G. Schreckenbach, *J. Phys. Chem. A* **114**, 1957-1963 (2010).
27. S. O. Odoh and G. Schreckenbach, *J. Phys. Chem. A* **115**, 14110-14119 (2011).
28. S. O. Odoh and G. Schreckenbach, *Inorg. Chem.* **52**, 5590-5602 (2013).
29. K. Pierloot and E. van Besien, *J. Chem. Phys.* **123**, 204309 (2005).
30. K. Pierloot, E. van Besien, E. van Lenthe and E. J. Baerends, *J. Chem. Phys.* **126**, 194311 (2007).
31. F. Real, A. S. P. Gomes, L. Visscher, V. Vallet and E. Eliav, *J. Phys. Chem. A* **113**, 12504-12511 (2009).
32. F. Real, V. Vallet, C. Marian and U. Wahlgren, *J. Chem. Phys.* **127**, 214302 (2007).
33. B. Schimmelpfennig, T. Privalov, U. Wahlgren and I. Grenthe, *J. Phys. Chem. A* **107**, 9705-9711 (2003).

34. G. Schreckenbach, P. J. Hay and R. L. Martin, *J. Comput. Chem.* **20**, 70-90 (1999).
35. G. A. Shamov and G. Schreckenbach, *J. Phys. Chem. A* **109**, 10961-10974 (2005).
36. G. A. Shamov, G. Schreckenbach, R. L. Martin and P. J. Hay, *Inorg. Chem.* **47**, 1465-1475 (2008).
37. P. Tecmer, A. S. P. Gomes, U. Ekstrom and L. Visscher, *Phys. Chem. Chem. Phys.* **13**, 6249-6259 (2011).
38. V. Vallet, B. Schimmelpfennig, L. Maron, C. Teichteil, T. Leininger, O. Gropen, I. Grenthe and U. Wahlgren, *Chem. Phys.* **244**, 185-193 (1999).
39. E. van Besien, K. Pierloot and C. Gorller-Walrand, *Phys. Chem. Chem. Phys.* **8**, 4311-4319 (2006).
40. V. Vetere, P. Maldivi and C. Adamo, *J. Comput. Chem.* **24**, 850-858 (2003).
41. H. Z. Yu, C. Li, B. H. Chen, C. T. Yang, D. R. Wang, Y. Fu, S. Hu and Z. M. Dang, *RSC Adv.* **4**, 50261-50270 (2014).
42. in *Reviews in Computational Chemistry*.
43. R. J. Bartlett, *Mol. Phys.* **108**, 2905-2920 (2010).
44. R. J. Bartlett and M. Musial, *Rev. Mod. Phys.* **79**, 291-352 (2007).
45. I. W. Bulik, T. M. Henderson and G. E. Scuseria, *J. Chem. Theory Comput.* **11**, 3171-3179 (2015).
46. P. Constans, P. Y. Ayala and G. E. Scuseria, *J. Chem. Phys.* **113**, 10451-10458 (2000).
47. T. D. Crawford and H. F. Schaefer, in *Reviews in Computational Chemistry*, edited by K. B. Lipkowitz and D. B. Boyd (John Wiley & Sons, Inc., Hoboken, NJ, USA), Vol. 14, pp. 33-136.
48. K. Andersson, P. A. Malmqvist and B. O. Roos, *J. Chem. Phys.* **96**, 1218-1226 (1992).
49. K. Andersson, P. A. Malmqvist, B. O. Roos, A. J. Sadlej and K. Wolinski, *J. Phys. Chem.* **94**, 5483-5488 (1990).
50. K. Andersson and B. O. Roos, *Int. J. Quantum Chem.* **45**, 591-607 (1993).
51. W. Y. Jiang, N. J. DeYonker and A. K. Wilson, *J. Chem. Theory Comput.* **8**, 460-468 (2012).
52. J. S. Sears and C. D. Sherrill, *J. Phys. Chem. A* **112**, 6741-6752 (2008).
53. J. S. Sears and C. D. Sherrill, *J. Phys. Chem. A* **112**, 3466-3477 (2008).
54. Z. T. Fang, Z. Lee, K. A. Peterson and D. A. Dixon, *J. Chem. Theory Comput.* **12**, 3583-3592 (2016).
55. W. A. de Jong, E. Bylaska, N. Govind, C. L. Janssen, K. Kowalski, T. Muller, I. M. B. Nielsen, H. J. J. van Dam, V. Veryazov and R. Lindh, *Phys. Chem. Chem. Phys.* **12**, 6896-6920 (2010).
56. P. G. Szalay, T. Muller, G. Gidofalvi, H. Lischka and R. Shepard, *Chem. Rev.* **112**, 108-181 (2012).
57. K. D. Vogiatzis, D. X. Ma, J. Olsen, L. Gagliardi and W. A. de Jong, *J. Chem. Phys.* **147**, 184111 (2017).
58. B. A. Cagg and V. A. Rassolov, *Chem. Phys. Lett.* **543**, 205-207 (2012).
59. M. Filatov and S. Shaik, *J. Phys. Chem. A* **104**, 6628-6636 (2000).
60. E. Fromager, F. Real, P. Wahlin, U. Wahlgren and H. J. A. Jensen, *J. Chem. Phys.* **131**, 054107 (2009).
61. E. Fromager, J. Toulouse and H. J. A. Jensen, *J. Chem. Phys.* **126**, 074111 (2007).
62. A. J. Garza, I. Bulik, A. G. S. Alencar, J. W. Sun, J. P. Perdew and G. E. Scuseria, *Mol. Phys.* **114**, 997-1018 (2016).
63. J. Grafenstein and D. Cremer, *Mol. Phys.* **103**, 279-308 (2005).

64. J. Grafenstein, E. Kraka and D. Cremer, *Chem. Phys. Lett.* **288**, 593-602 (1998).
65. S. Grimme and M. Waletzke, *J. Chem. Phys.* **111**, 5645-5655 (1999).
66. S. Gusarov, P. A. Malmqvist, R. Lindh and B. O. Roos, *Theor. Chem. Acc.* **112**, 84-94 (2004).
67. Y. Kurzweil, K. V. Lawler and M. Head-Gordon, *Mol. Phys.* **107**, 2103-2110 (2009).
68. G. Li Manni, R. K. Carlson, S. J. Luo, D. X. Ma, J. Olsen, D. G. Truhlar and L. Gagliardi, *J. Chem. Theory Comput.* **10**, 3669-3680 (2014).
69. N. O. J. Malcolm and J. J. W. McDouall, *Chem. Phys. Lett.* **282**, 121-127 (1998).
70. B. Miehlich, H. Stoll and A. Savin, *Mol. Phys.* **91**, 527-536 (1997).
71. R. Takeda, S. Yamanaka and K. Yamaguchi, *Chem. Phys. Lett.* **366**, 321-328 (2002).
72. Y. Zhao, B. J. Lynch and D. G. Truhlar, *Phys. Chem. Chem. Phys.* **7**, 43-52 (2005).
73. R. K. Carlson, D. G. Truhlar and L. Gagliardi, *J. Chem. Theory Comput.* **11**, 4077-4085 (2015).
74. L. Gagliardi, D. G. Truhlar, G. Li Manni, R. K. Carlson, C. E. Hoyer and J. W. L. Bao, *Accounts Chem. Res.* **50**, 66-73 (2017).
75. Y. J. Bomble, J. F. Stanton, M. Kallay and J. Gauss, *J. Chem. Phys.* **123**, 054101 (2005).
76. A. D. Becke, A. Savin and H. Stoll, *Theor. Chim. Acta* **91**, 147-156 (1995).
77. F. Moscardó and E. San-Fabián, *Phys. Rev. A* **44**, 1549-1553 (1991).
78. J. P. Perdew, A. Savin and K. Burke, *Phys. Rev. A* **51**, 4531-4541 (1995).
79. S. Ghosh, A. L. Sonnenberger, C. E. Hoyer, D. G. Truhlar and L. Gagliardi, *J. Chem. Theory Comput.* **11**, 3643-3649 (2015).
80. M. Mostafanejad and A. E. DePrince, *J. Chem. Theory Comput.* **15**, 290-302 (2019).
81. S. O. Odoh, G. Li Manni, R. K. Carlson, D. G. Truhlar and L. Gagliardi, *Chem. Sci.* **7**, 2399-2413 (2016).
82. J. J. Bao, L. Gagliardi and D. G. Truhlar, *J. Phys. Chem. Lett.* **10**, 799-805 (2019).
83. J. L. Bao, S. O. Odoh, L. Gagliardi and D. G. Truhlar, *J. Chem. Theory Comput.* **13**, 616-626 (2017).
84. K. Sharkas, L. Gagliardi and D. G. Truhlar, *J. Phys. Chem. A* **121**, 9392-9400 (2017).
85. P. Sharma, D. G. Truhlar and L. Gagliardi, *J. Chem. Theory Comput.* **14**, 660-669 (2018).
86. S. J. Stoneburner, D. G. Truhlar and L. Gagliardi, *J. Chem. Phys.* **148**, 064108 (2018).
87. L. Wilbraham, P. Verma, D. G. Truhlar, L. Gagliardi and I. Ciofini, *J. Phys. Chem. Lett.* **8**, 2026-2030 (2017).
88. B. O. Roos, R. Lindh, P. A. Malmqvist, V. Veryazov and P. O. Widmark, *J. Phys. Chem. A* **108**, 2851-2858 (2004).
89. B. O. Roos, R. Lindh, P. A. Malmqvist, V. Veryazov, P. O. Widmark and A. C. Borin, *J. Phys. Chem. A* **112**, 11431-11435 (2008).
90. B. A. Hess, *Phys. Rev. A* **33**, 3742-3748 (1986).
91. T. Nakajima and K. Hirao, *Chem. Rev.* **112**, 385-402 (2012).
92. A. Wolf, M. Reiher and B. A. Hess, *J. Chem. Phys.* **117**, 9215-9226 (2002).
93. W. Kuchle, M. Dolg, H. Stoll and H. Preuss, *J. Chem. Phys.* **100**, 7535-7542 (1994).
94. T. H. Dunning, *J. Chem. Phys.* **90**, 1007-1023 (1989).
95. L. Gagliardi and B. O. Roos, *Nature* **433**, 848-851 (2005).
96. I. Infante and L. Visscher, *J. Chem. Phys.* **121**, 5783-5788 (2004).
97. S. Knecht, H. J. A. Jensen and T. Saue, *Nature Chem.* **11**, 40-44 (2019).
98. A. D. Becke, *J. Chem. Phys.* **98**, 5648-5652 (1993).
99. C. T. Lee, W. T. Yang and R. G. Parr, *Phys. Rev. B* **37**, 785-789 (1988).

100. D. Rappoport and F. Furche, *J. Chem. Phys.* **133**, 134105 (2010).
101. S. Grimme, J. Antony, S. Ehrlich and H. Krieg, *J. Chem. Phys.* **132**, 154104 (2010).
102. S. Grimme, S. Ehrlich and L. Goerigk, *J. Comput. Chem.* **32**, 1456-1465 (2011).
103. E. R. Johnson and A. D. Becke, *J. Chem. Phys.* **124**, 174104 (2006).
104. B. Vlaisavljevich, P. Miro, C. J. Cramer, L. Gagliardi, I. Infante and S. T. Liddle, *Chem-Eur. J.* **17**, 8424-8433 (2011).
105. F. Wei, G. S. Wu, W. H. E. Schwarz and J. Li, *Theor. Chem. Acc.* **129**, 467-481 (2011).
106. G. Ghigo, B. O. Roos and P. A. Malmqvist, *Chem. Phys. Lett.* **396**, 142-149 (2004).
107. J. P. Zobel, J. J. Nogueira and L. Gonzalez, *Chem. Sci.* **8**, 1482-1499 (2017).
108. N. Forsberg and P. A. Malmqvist, *Chem. Phys. Lett.* **274**, 196-204 (1997).
109. B. O. Roos, K. Andersson, M. P. Fulscher, L. SerranoAndres, K. Pierloot, M. Merchan and V. Molina, *J. Mol. Struct-Theochem* **388**, 257-276 (1996).
110. A. D. Becke, *Phys. Rev. A* **38**, 3098-3100 (1988).
111. J. P. Perdew, K. Burke and M. Ernzerhof, *Phys. Rev. Lett.* **77**, 3865-3868 (1996).
112. C. Adamo and V. Barone, *J. Chem. Phys.* **110**, 6158-6170 (1999).
113. W. Kohn and L. J. Sham, *Phys. Rev.* **140**, 1133-& (1965).
114. S. H. Vosko, L. Wilk and M. Nusair, *Can. J. Phys.* **58**, 1200-1211 (1980).
115. C. E. Hoyer, L. Gagliardi and D. G. Truhlar, *J. Phys. Chem. Lett.* **6**, 4184-4188 (2015).
116. C. E. Hoyer, S. Ghosh, D. G. Truhlar and L. Gagliardi, *J. Phys. Chem. Lett.* **7**, 586-591 (2016).
117. F. Aquilante, J. Autschbach, R. K. Carlson, L. F. Chibotaru, M. G. Delcey, L. De Vico, I. F. Galvan, N. Ferre, L. M. Frutos, L. Gagliardi, M. Garavelli, A. Giussani, C. E. Hoyer, G. Li Manni, H. Lischka, D. X. Ma, P. A. Malmqvist, T. Muller, A. Nenov, M. Olivucci, T. B. Pedersen, D. L. Peng, F. Plasser, B. Pritchard, M. Reiher, I. Rivalta, I. Schapiro, J. Segarra-Marti, M. Stenrup, D. G. Truhlar, L. Ungur, A. Valentini, S. Vancouillie, V. Veryazov, V. P. Vysotskiy, O. Weingart, F. Zapata and R. Lindh, *J. Comput. Chem.* **37**, 506-541 (2016).
118. F. Aquilante, T. B. Pedersen, V. Veryazov and R. Lindh, *WIREs Comput. Mol. Sci.* **3**, 143-149 (2013).
119. M. J. Frisch, et al., (Gaussian Inc. Wallingford CT, Wallingford, CT, 2016).
120. M. Kállay, Z. Rolik, I. Ladjánszki, L. Szegedy, B. Ladoâ&aczk&acaron;ki, J. Csontos and B. Kornis, *J. Chem. Phys.* **139**, 094105 (2013).
121. [www.mrcc.hu](http://www.mrcc.hu).
122. M. F. Zhou, L. Andrews, N. Ismail and C. Marsden, *J. Phys. Chem. A* **104**, 5495-5502 (2000).
123. J. Cullen, *J. Comput. Chem.* **20**, 999-1008 (1999).
124. M. Straka, K. G. Dyall and P. Pyykk&ouml;, *Theor. Chem. Acc.* **106**, 393-403 (2001).
125. T. J. Lee and P. R. Taylor, *Int. J. Quantum Chem.*, 199-207 (1989).
126. K. Newcomb, S. P. Tiwari, N. Rai and E. J. Maginn, *Phys. Chem. Chem. Phys.* **20**, 15753-15763 (2018).
127. S. Pérez-Conesa, F. Torrico, J. M. Martínez, R. R. Pappalardo and E. S. Marcos, *J. Chem. Phys.* **150**, 104504 (2019).



### CHAPTER 3. ACTIVATING WATER AND HYDROGEN BY LIGAND-MODIFIED URANIUM AND NEPTUNIUM COMPLEXES: A DFT STUDY

Olajumoke Adeyiga<sup>#</sup>, Dipak Panthi<sup>#</sup>, Olabisi Suleiman<sup>#</sup>, Dillon Stetler, Ryan W. Long and Samuel O. Odoh<sup>\*</sup>

Department of Chemistry, University of Nevada Reno, 1664 N. Virginia Street, Reno, NV 89557-0216

“Reprinted (adapted) with permission from *Inorganic Chemistry*, 2020, 59, 5, 3102-3109.

Copyright (2020) American Chemical Society”

**ABSTRACT:** Organometallic uranium complexes that can activate small molecules are well known. In contrast, there are no known organometallic trans-uranium species capable of small-molecule transformations. Using density functional theory, we previously showed that changing actinide-ligand bonds from U-O groups to Np-N- (amide/imido) bonds makes redox small-molecule activation more energetically favorable for Np species. Here, we determine how *general* this ligand-modulation strategy is for affecting small-molecule activation in Np species. We focus on two reactions, one involving redox transformation of the actinide(s) and the other involving no change in the oxidation state of the actinide(s). Specifically, we considered the hydrogen evolution reaction (HER) from H<sub>2</sub>O by actinide tris-aryloxide species. We also considered H<sub>2</sub> capture and hydride transfer by actinide siloxide and silylamide complexes. For the HER, the barriers for Np(III) systems are much higher than those of U(III). The overall reaction energies are also much worse. An-O → An-N substitutions marginally improve the barriers by 1-4 kcal/mol and more substantially improve the reaction energies by 9-15 kcal/mol. For H<sub>2</sub> capture and hydride transfer, the reaction energies for the U and Np species are similar. For both actinides, *like-for-like* An-O → An-N substitutions lead to improved reaction energies. Interestingly, in a recent report, it seemingly appears that U-O (siloxide) → U-N (silylamide) leads to complete shutdown of reactivity for H<sub>2</sub> capture and hydride transfer. This observation is reproduced and explained with calculations. The ligand environments of the siloxide and silylamide that were compared are vastly different. The steric environment of the siloxide is conducive for reactivity while the particular silylamide is not. We conclude that small-molecule activation with organometallic neptunium species is achievable with a guided choice of ligands. Additional emphasis should be placed on ligands that can allow for improved transition state barriers.

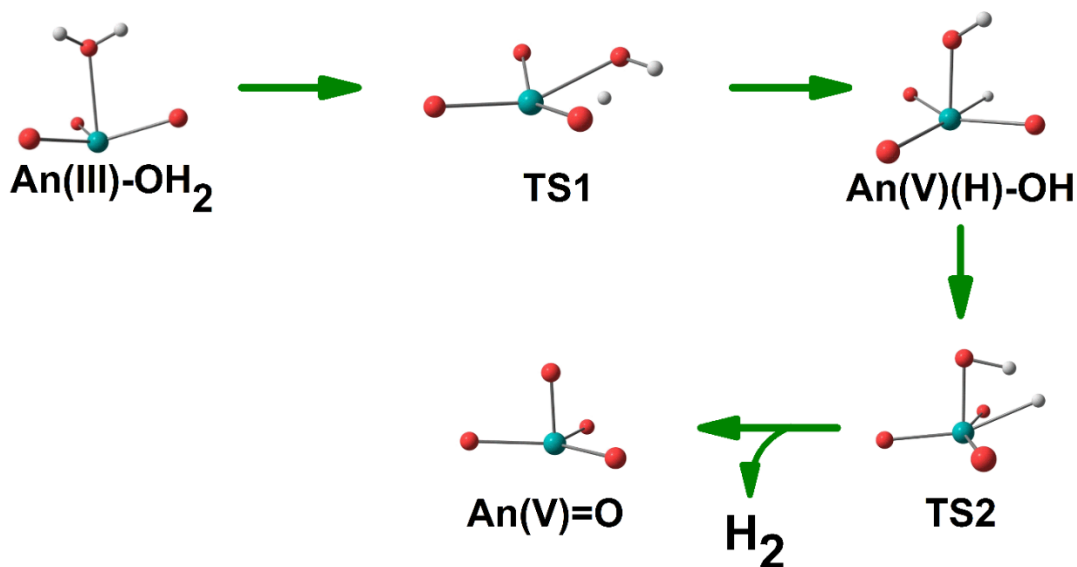
### 3.1 INTRODUCTION

Approaches to activate small molecules like  $\text{N}_2$ ,  $\text{H}_2\text{O}$ ,  $\text{CH}_4$  and  $\text{CO}_2$  in order to generate energy and industrially-important chemical feedstocks are at the cutting edge of research in inorganic, organometallic and materials chemistry. These molecules are often activated with transition metal complexes and surfaces. Recent investigations have however shown that uranium (U) can also effect small-molecule transformations. U complexes can activate  $\text{H}_2$ ,  $\text{CH}_4$ ,  $\text{H}_2\text{O}$ ,  $\text{CO}$ ,  $\text{NO}$  and  $\text{N}_2$ .<sup>1-20</sup> Although many of these transformations are stoichiometric reactions, they remain important nonetheless. A detailed understanding of the thermodynamics, mechanisms, and kinetics of these transformations can provide insights towards the design of catalytic platforms. Additionally, catalytic transformations of small-molecules with U species have the potential to alter the use, separation, storage and public perception of nuclear waste materials. Nuclear waste forms also contain trans-uranium elements like neptunium (Np), plutonium (Pu) and americium (Am). However, there are no reports on the ability of trans-uranium complexes to effect small-molecule redox transformations.<sup>21,22</sup> Thus, there is interest in the development of trans-uranium complexes that can activate small molecules in a similar manner to their U analogues.

Recently, it was shown using density functional theory (DFT) calculations that, while a U complex could perform a four-electron reduction of  $\text{N}_2$ ,  $\text{N}_2 \rightarrow \text{N}_2^{4-}$ , analogous Np and Pu species could not. The Np and Pu analogues could not effect this transformation due to a shift in the balance of redox potentials.<sup>17</sup> The U complex was initially synthesized and characterized by Falcone et al. They also characterized its ability to activate  $\text{N}_2$  to  $\text{N}_2^{4-}$ .<sup>9</sup> We showed that modulation of the actinide-ligand bonds as well as the ligand framework can be used to make  $\text{N}_2 \rightarrow \text{N}_2^{4-}$  favorable for the Np analogue. Specifically, changing the Np-O bonds to metal-imido Np-NH groups favored  $\text{N}_2 \rightarrow \text{N}_2^{4-}$ .<sup>17</sup> Herein, we examine whether Np-O  $\rightarrow$  Np-N substitution is useful in the activation of *other* small molecules.

In this work, we use DFT computations to study the electrocatalytic evolution of hydrogen ( $\text{H}_2$ ) from water by actinide complexes, Scheme 3.1. We considered systems that are based on the previously reported U(III) trisaryloxo complex,  $[(^{\text{Ad,Me}}\text{ArO})_3\text{mes})\text{U}]$  where *mes* = mesityl, *Ad* = adamantyl and *Me* = methyl.  $[(^{\text{Ad,Me}}\text{ArO})_3\text{mes})\text{U}]$  evolves  $\text{H}_2$  from water with a turnover frequency comparable to state-of-the-art transition-metal systems.<sup>12,13</sup> The mechanism for  $\text{H}_2$  evolution from water by this U complex involves two hydrogen atom abstraction steps as well as rare terminal pentavalent  $\text{U}=\text{O}$  and  $\text{U}-\text{OH}$  complexes, Scheme 3.1.<sup>23-27</sup> This reaction mechanism

is quite similar to the one previously reported by Meyer et al.<sup>12,13</sup> The pentavalent U=O complex comproportionates with  $[(^{\text{Ad,Me}}\text{ArO})_3\text{mes}]\text{U}.\text{OH}_2$  to yield a tetravalent U-OH species which is then electrocatalytically reduced in the experiments setup. We compare the stoichiometric process for  $\text{H}_2$  evolution via the intramolecular insertion mechanism, Scheme 3.1, by  $[(^{\text{Ad,Me}}\text{ArO})_3\text{mes}]\text{U}$ ,  $[(^{\text{Ad,Me}}\text{ArNH})_3\text{mes}]\text{U}$ ,  $[(^{\text{Ad,Me}}\text{ArO})_3\text{mes}]\text{Np}$  and  $[(^{\text{Ad,Me}}\text{ArNH})_3\text{mes}]\text{Np}$  species.



**Scheme 3.1:** Mechanism for hydrogen evolution from water by  $\text{An}^{3+}$  trisaryloxy species. The ligands are not shown to allow for clarity.

Additionally, a recent experimental report has revealed interesting insights into small-molecule activation by uranium amide ( $\text{U-NR}_2$ ) complexes. Specifically, reactivity with small molecules ( $\text{CO}$ ,  $\text{CO}_2$  and  $\text{H}_2$ ) was demonstrated by the siloxide complex while the silylamide species showed no reactivity.<sup>16</sup> These results would suggest that  $\text{An-O} \rightarrow \text{An-N}$  ligand substitution may not always lead to improved reactivities. However, close examination indicates that the ligand environments of these species are quite different. Specifically, there is a  $\text{U-O-Si}$  spacer between U and the  $\text{O-}t\text{-Bu}$  groups in the siloxide whereas the  $\text{N}(\text{SiMe}_3)_2$  ligands are rather close-in on the U center in the case of silylamide, Figure 3.1. It is thus important that we ascertain that our computational protocol can adequately distinguish between cases in which significant ligand modification leads to improved or diminished reactivities. We also seek to determine whether a *like-for-like*  $\text{O} \rightarrow \text{NH}$  substitution in  $\text{U-OSi(O-}t\text{-Bu)}_3$  framework (to  $\text{U-N(H)Si(O-}t\text{-Bu)}_3$ ) would restore reactivity with  $\text{H}_2$ . These questions are also explored for the analogous Np species. To this end, we have considered  $\text{H}_2$  capture and hydride transfer by bis-uranium nitride ( $\text{U-N-U}$ ) siloxide or silylamide complexes that were characterized by Palumbo et al., Figure 3.1.<sup>16</sup> The two U centers in these

complexes are in the +4 oxidation state, bridged by a nitride and are coordinated to three siloxide/silylamide groups, with the total charge balanced by a tetrabutyl-ammonium cation,  $\text{NBu}_4^+$ . We studied the anionic forms of these complexes, without  $\text{NBu}_4^+$ . These are labelled as  $[(\text{O})\text{U}-\text{N}-\text{U}(\text{O})]^-$  (for the siloxide,  $\text{OSi}(\text{O}-t\text{-Bu})_3$ ) and  $[(\text{N})\text{U}-\text{N}-\text{U}(\text{N})]^-$  (for the silylamide,  $\text{N}(\text{SiMe}_3)_2$ ), for simplicity, Figure 3.1. We emphasize again that the ligand frameworks of the siloxide and silylamide are quite different, Figure 3.1.

### 3.2 COMPUTATIONAL DETAILS

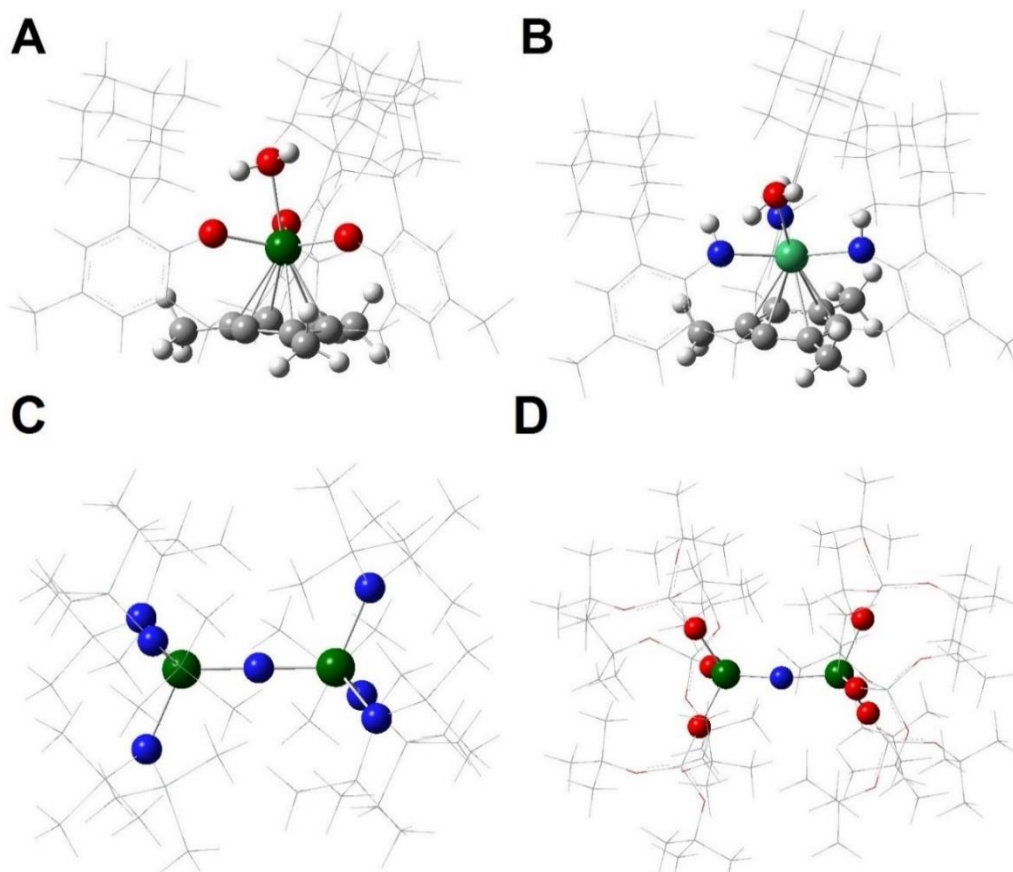


**Figure 3.1: Structures of A.  $[(\text{Ad,MeArO})_3\text{mes}]\text{U}.\text{OH}_2$  B.  $[(\text{Ad,MeArNH})_3\text{mes}]\text{Np}.\text{OH}_2$  C.  $[(\text{N})\text{U}-\text{N}-\text{U}(\text{N})]^-$  and D.  $[(\text{O})\text{U}-\text{N}-\text{U}(\text{O})]^-$ . The ligands are depicted with wireframes for better visibility. A and B are studied for HER while C and D are studied for  $\text{H}_2$  capture and hydride transfer.**

We optimized the structures of the tris-aryloxide and bis-actinide nitride complexes, Figure 3.1, in the gas phase with all-electron L1 (double- $\zeta$ ) extended basis sets at the scalar relativistic level with the Priroda code. These calculations were performed with the PBE functional. The description of the basis sets and scalar-relativistic approach have been previously described.<sup>28-30</sup> Single-point calculations accounting for spin-orbit coupling and/or solvent effects were subsequently

performed with the ADF code.<sup>31,32</sup> We used Slater-type triple- $\zeta$  basis sets with two polarization functions, TZ2P, and the PBE generalized gradient approximation exchange-correlation DFT functional.<sup>33,34</sup> This functional provides accurate results for predicting the redox reactivity and ionization potentials of actinide species.<sup>35-41</sup> Dispersion effects were included in these calculations with the DFT-D3 scheme<sup>42,43</sup> supplemented with the Becke-Johnson damping scheme, DFT-D3(BJ).<sup>44</sup> Scalar-relativistic effects were accounted for with the zeroth order regular approximation (ZORA) approach.<sup>45</sup> The TZ2P basis sets used were adapted for use with ZORA.<sup>46,47</sup> The actinide tris-aryloxides were studied for the HER experiments which were performed in solution (THF). In contrast, the bis-actinide-nitride species were studied for H<sub>2</sub> capture and were studied in the gas phase, in accordance with the experiments of Palumbo et al.<sup>16</sup> The spin-orbit DFT calculations were performed in the non-collinear unrestricted fashion at the PBE-D3(BJ)/TZ2P level while still employing the ZORA approach. Calculations in the solvent phase, specifically in THF were carried out with the SM12 implicit solvation model.<sup>48,49</sup> This is reasonable as the electrocatalytic experiments of Halter et al. were performed in THF.<sup>12,13</sup> The dielectric constant of THF was taken as 7.58 while the radius of the solvent molecules was taken as 3.18 Å. Unless otherwise stated, our discussions are based on calculations at the PBE-D3BJ/TZ2P level.

### 3.3 RESULTS AND DISCUSSION

**3.3.1 Hydrogen Evolution from Water:** The mechanism for H<sub>2</sub> evolution from the aquo ligand in  $[(^{Ad,Me}ArO)_3mes)U].OH_2$ ,  $[(^{Ad,Me}ArO)_3mes)Np].OH_2$  and  $[(^{Ad,Me}ArNH)_3mes)Np].OH_2$  are compared in Figure 3.2. The mechanistic steps are similar to those reported by Meyer et al.<sup>12,13</sup> Interestingly, our calculation shows that the first hydrogen-atom abstraction step is the rate-determining step (RDS) for  $[(^{Ad,Me}ArO)_3mes)U].OH_2$ . This is in contrast to Meyer et al. who predicted the second transition state, TS2, as the rate-limiting barrier. They found that TS2 is 24.6 kcal/mol above the starting complex,  $[(^{Ad,Me}ArO)_3mes)U].OH_2$ . This is rather high for a reaction that occurs at room temperature. It is possible that the differences between our results and those of Meyer et al. are due to the use of different DFT functionals. We used the PBE-D3BJ functional and have recently shown that PBE provides good agreement with high-accuracy wave-function theory methods for the structures, redox reactivities and energetics of actinide species.<sup>35</sup> With our protocol, the rate-determining barrier is 18.7 kcal/mol, indicating that the overall reaction is feasible at room temperature for  $[(^{Ad,Me}ArO)_3mes)U].OH_2$ . To examine the impact of Np-O  $\rightarrow$

Np-N ligand modulation on the profile of the HER reaction, the actinide-oxo groups in  $[((^{\text{Ad,Me}}\text{ArO})_3\text{mes})\text{Np}]\cdot\text{OH}_2$  are converted to actinide-imido groups in  $[((^{\text{Ad,Me}}\text{ArNH})_3\text{mes})\text{Np}]\cdot\text{OH}_2$  rather than actinide-amide interactions to avoid steric clashes. From an electronic structure perspective, we find that the Mayer bond order of the activated O-H bond in  $[((^{\text{Ad,Me}}\text{ArNH})_3\text{mes})\text{Np}]\cdot\text{OH}_2$  is 1.3% smaller than the bond order of the similar bond in  $[((^{\text{Ad,Me}}\text{ArO})_3\text{mes})\text{Np}]\cdot\text{OH}_2$ .<sup>50</sup> The decrease in the covalency is confirmed by topological analysis with the quantum theory of atoms in molecules, see Supporting Information.<sup>51,52</sup>

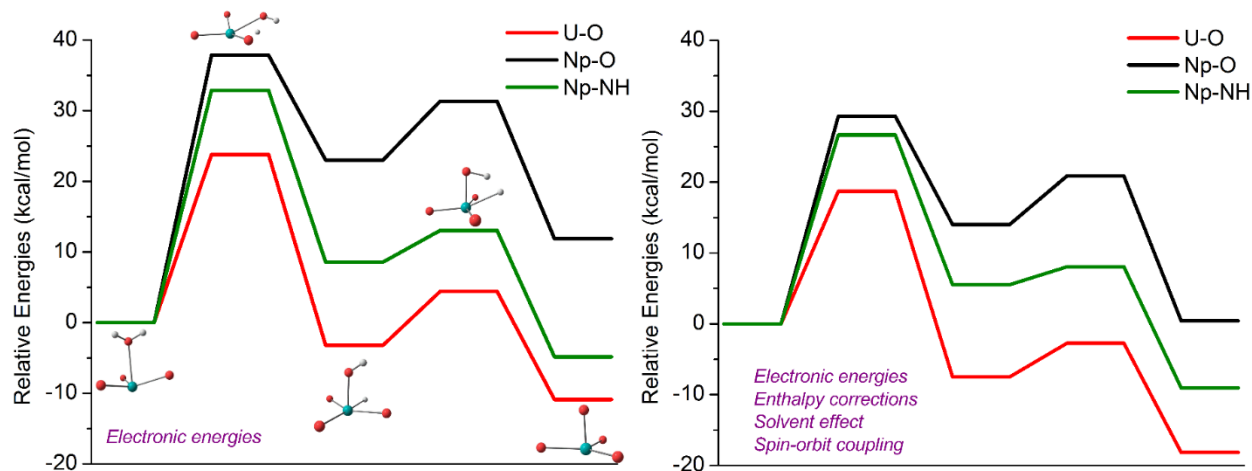


**Figure 3.2:** Overall reaction energy profiles for  $[((^{\text{Ad,Me}}\text{ArO})_3\text{mes})\text{U}]\cdot\text{OH}_2$ ,  $[((^{\text{Ad,Me}}\text{ArO})_3\text{mes})\text{Np}]\cdot\text{OH}_2$  and  $[((^{\text{Ad,Me}}\text{ArNH})_3\text{mes})\text{Np}]\cdot\text{OH}_2$ . These species are labeled as U-O, Np-O and Np-NH respectively. The results based on electronic energies are shown on the left while those including enthalpic, solvent and spin-orbit corrections are shown on the right.

We can thus conclude that the activated O-H bond is slightly stronger in the Np-O complex than in the Np-NH complex. Interestingly, the RDS barrier is 2.6 kcal/mol lower for the Np-NH complex than for  $[((^{\text{Ad,Me}}\text{ArO})_3\text{mes})\text{Np}]\cdot\text{OH}_2$ , Figure 3.2. The RDS barrier for the Np-NH complex is 26.7 kcal/mol, to be compared with 29.3 kcal/mol for the Np-O species and 18.7 kcal/mol for the U-O complex. Based on these results, the HER would be significantly faster for U than for the Np species. We also conclude that Np-O  $\rightarrow$  Np-N ligand modulation provides a marginal improvement in the RDS barrier. We see a similar degree of improvement for the barrier of the second proton abstraction step, Figure 3.2. For  $[((^{\text{Ad,Me}}\text{ArO})_3\text{mes})\text{Np}]\cdot\text{OH}_2$ , the TS2 barrier is 6.8 kcal relative to the intermediate complex, while for  $[((^{\text{Ad,Me}}\text{ArNH})_3\text{mes})\text{Np}]\cdot\text{OH}_2$ , this barrier is only 2.5 kcal/mol. This is an improvement of 4.3 kcal/mol. The magnitude of this improvement remains largely unchanged when we considered only electronic energies, 3.8 kcal/mol, Figure 3.2.

The TS2 barriers for these Np species are to be compared to 4.8 kcal/mol for  $[(^{Ad,Me}ArO)_3mes)U].OH_2$ .

The energies for the first proton abstraction step and the overall reaction are however strongly improved with ligand modulation. The first proton abstraction is exothermic for  $[(^{Ad,Me}ArO)_3mes)U].OH_2$ , -7.5 kcal/mol, but endothermic for  $[(^{Ad,Me}ArO)_3mes)Np].OH_2$ , 14.0 kcal/mol, and  $[(^{Ad,Me}ArNH)_3mes)Np].OH_2$ , 5.5 kcal/mol. This shows that Np-O  $\rightarrow$  Np-N ligand modulation improves the reaction energy by 8.5 kcal/mol. In a similar manner, the overall reaction energy is improved from +0.4 kcal/mol (endothermic) to -9.0 kcal/mol (exothermic) after Np-O  $\rightarrow$  Np-N ligand substitution. This is again an improvement of about 8.5 kcal/mol. We emphasize that the improvement in the reaction energies after Np-O  $\rightarrow$  Np-N substitution is even larger, 16.7 kcal/mol, when we considered only electronic energies. We therefore conclude that Np-O  $\rightarrow$  Np-N substitution is a valuable approach for improving the reaction energies for the HER by Np species. The overall reaction energies for these Np species are to be compared to -18.2 kcal/mol for  $[(^{Ad,Me}ArO)_3mes)U].OH_2$ .

**3.3.1.1. Confirmation of trends for the HER:** The calculated trends for  $[(^{Ad,Me}ArO)_3mes)U].OH_2$ ,  $[(^{Ad,Me}ArO)_3mes)Np].OH_2$  and  $[(^{Ad,Me}ArNH)_3mes)Np].OH_2$  are confirmed in two ways. First, we performed single-point scalar-relativistic DFT calculations with the hybrid B3LYP-D3BJ functional. With this functional, the reaction barriers are larger and the overall HER is less exothermic. Indeed, for  $[(^{Ad,Me}ArO)_3mes)U].OH_2$ , the RDS barrier is 37.2 kcal/mol, Figure 3.3.

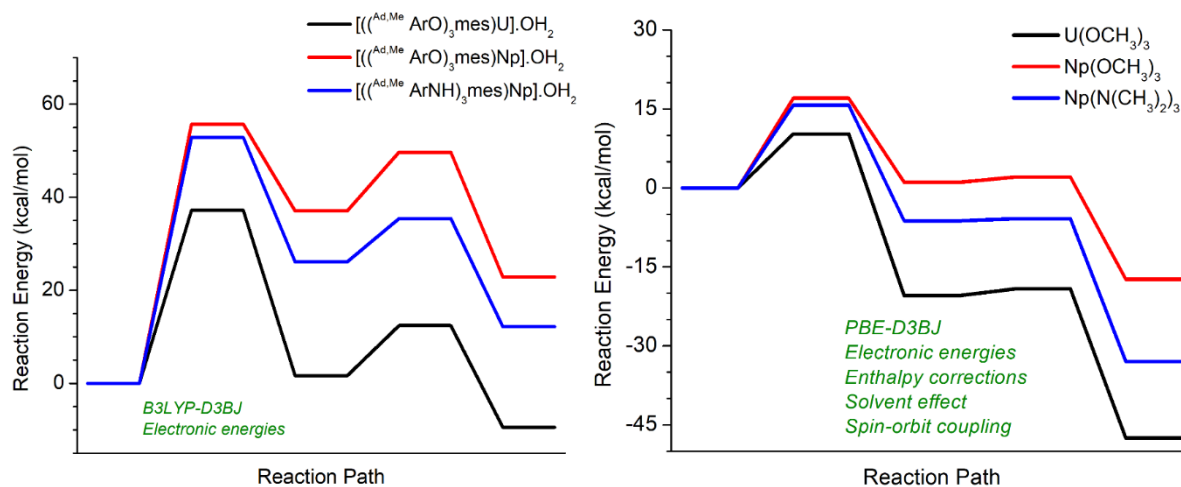


**Figure 3.3:** (left) Reaction profiles for  $[(^{Ad,Me}ArO)_3mes)U].OH_2$ ,  $[(^{Ad,Me}ArO)_3mes)Np].OH_2$  and  $[(^{Ad,Me}ArNH)_3mes)Np].OH_2$  obtained with the B3LYP-D3BJ functional. (right) Reaction profiles obtained for  $H_2$  evolution from water by  $[U(OMe)_3]$ ,  $[Np(OMe)_3]$  and  $[Np(NMe_2)_3]$  obtained with the PBE-D3BJ functional.

This is quite high for a reaction that proceeds under ambient conditions. Most importantly however, B3LYP-D3BJ reproduces the improvement in the RDS barrier and overall reaction energies after Np-O  $\rightarrow$  Np-N substitution. Second, the tris-aryloxide ligands are truncated to methyl groups. For the small tris-methyl complexes, we find that the first hydrogen atom abstraction reaction is still the RDS. Also, the barriers and reaction energies are much favorable for the U complex than for the Np species. Most importantly, Np-O  $\rightarrow$  Np-N ligand substitution improves the RDS barrier by 1.3 kcal/mol. Also, the overall reaction energy is also improved by 15.6 kcal/mol, Figure 3.3. These results give us confidence regarding the accuracy of the results presented in Figure 3.2.

**3.3.2 Hydrogen Capture and Hydride Transfer by Bis-Uranium Nitrides:** As noted earlier Palumbo et al. recently compared small-molecule activation by bis-uranium nitride complexes, Figure 3.1.<sup>16</sup> They compared  $[\text{NBu}_4][(\text{O})\text{U}-\text{N}-\text{U}(\text{O})]^-$  with a  $\text{OSi}(\text{O}-t\text{-Bu})_3$  ligand framework, where  $t\text{-Bu}$  = *tert*-butyl, and  $[\text{NBu}_4][(\text{N})\text{U}-\text{N}-\text{U}(\text{N})]^-$  with a  $\text{N}(\text{SiMe}_3)_2$  ligand framework. Specifically, they examined the reactivities of these species with  $\text{H}_2$ , CO and  $\text{CO}_2$ . They found that the silylamide,  $[\text{NBu}_4][(\text{N})\text{U}-\text{N}-\text{U}(\text{N})]^-$ , was unreactive towards  $\text{H}_2$  while  $[\text{NBu}_4][(\text{O})\text{U}-\text{N}-\text{U}(\text{O})]^-$ , the siloxide, was able to effect  $\text{H}_2$  capture and hydride transfer to yield  $[\text{NBu}_4][(\text{O})\text{U}-\text{NH}(\text{H})-\text{U}(\text{O})]^-$ . It thus appears that the empirical observations contradict our computational results that have indicated that An-O  $\rightarrow$  An-N substitutions and ligand modifications leads to improved reactivities for HER and  $\text{N}_2$  activation.<sup>17</sup> As such, we have studied  $[(\text{N})\text{U}-\text{N}-\text{U}(\text{N})][\text{N}(\text{SiMe}_3)_2]^-$  and  $[(\text{O})\text{U}-\text{N}-\text{U}(\text{O})][\text{OSi}(\text{O}-t\text{-Bu})_3]^-$ . These are the anionic moieties in the silylamide and siloxide complexes, respectively. We consider the structural properties of these moieties as well as their reactivities towards  $\text{H}_2$ .

**3.3.2.1. Structural and electronic properties:** The calculated structural properties of the high-spin quintet ( $S=2$ ) and open-shell singlet, OSS, ( $S=0$ ) states of  $[(\text{O})\text{U}-\text{N}-\text{U}(\text{O})][\text{OSi}(\text{O}-t\text{-Bu})_3]^-$  and  $[(\text{N})\text{U}-\text{N}-\text{U}(\text{N})][\text{N}(\text{SiMe}_3)_2]^-$  are compared to parameters from crystal structures in Table 3.1. The bond distances in the OSS states are longer than those of the quintet states by 0.006-0.023 Å. In contrast, the structural parameters of the quintet states are closer to the parameters from the crystal structures. For the high-spin states, the bond lengths are on average within 0.020 Å of the experiment whereas the bond angles are within 1-4°. This level of agreement gives us good confidence in our computational protocol. The importance of the structural parameters is illustrated by comparing the calculated U-N-U bond angles of  $[(\text{O})\text{U}-\text{N}-\text{U}(\text{O})][\text{OSi}(\text{O}-t\text{-Bu})_3]^-$  to



experimental data. For the OSS state, the U-N-U angle is almost linear,  $179.2^\circ$ , whereas for the quintet state, we obtained  $168.3^\circ$ , in decent agreement with the experiment. At the level of theory used in this work, we find that the OSS and quintet states of  $[(\text{O})\text{U}-\text{N}-\text{U}(\text{O})][\text{OSi}(\text{O}-t\text{-Bu})_3]^-$  and  $[(\text{N})\text{U}-\text{N}-\text{U}(\text{N})][\text{N}(\text{SiMe}_3)_2]^-$  are isoenergetic, 0.1-0.8 kcal/mol. This conforms with the results of Palumbo et al. who used the M06-L and B3LYP functionals.<sup>16</sup> In all cases, we found that the quintet states are more stable than the OSS.

**Table 3.1: Comparison of the calculated structural properties of  $[(\text{O})\text{U}-\text{N}-\text{U}(\text{O})][\text{OSi}(\text{O}-t\text{-Bu})_3]^-$  and  $[(\text{N})\text{U}-\text{N}-\text{U}(\text{N})][\text{N}(\text{SiMe}_3)_2]^-$  to the crystal structure parameters. Bond lengths are given in Å while bond angles are given in  $^\circ$ .**

	$[(\text{N})\text{U}-\text{N}-\text{U}(\text{N})][\text{N}(\text{SiMe}_3)_2]^-$		
	OSS	Quintet	Experiment <sup>16</sup>
U-N <sub>nitride</sub>	2.106, 2.107	2.099, 2.090	2.076, 2.083
U-N <sub>amide</sub>	2.373	2.363	2.35
U-U	4.212	4.189	4.159
U-N-U	177.5	177.8	179.0
	$[(\text{O})\text{U}-\text{N}-\text{U}(\text{O})][\text{OSi}(\text{O}-t\text{-Bu})_3]^-$		
	OSS	Quintet	Experiment <sup>16</sup>
U-N <sub>nitride</sub>	2.062, 2.071	2.058, 2.073	2.032, 2.067
U-O <sub>siloxide</sub>	2.176	2.179	2.200
U-U	4.133	4.110	4.090
U-N-U	179.2	168.3	172.2

**3.3.2.2. Reaction energies for H<sub>2</sub> capture and hydride transfer:** The reaction energies for H<sub>2</sub> capture and hydride transfer by  $[(\text{O})\text{U}-\text{N}-\text{U}(\text{O})][\text{OSi}(\text{O}-t\text{-Bu})_3]^-$  and  $[(\text{N})\text{U}-\text{N}-\text{U}(\text{N})][\text{N}(\text{SiMe}_3)_2]^-$  are presented in Table 3.2. For  $[(\text{N})\text{U}-\text{N}-\text{U}(\text{N})][\text{N}(\text{SiMe}_3)_2]^-$ , the reaction energy and enthalpy are +10.0 and +12.6 kcal/mol, respectively, at the PBE/L1 level. Single-point calculations with all-electron TZ2P basis sets and the ZORA approach yields reaction energies of +6.0 and +8.3 kcal/mol at the scalar-relativistic and spin-orbit coupling levels, respectively. As such, we conclude that this silylamide will not capture H<sub>2</sub> and initiate hydride transfer. In contrast, for  $[(\text{O})\text{U}-\text{N}-\text{U}(\text{O})][\text{OSi}(\text{O}-t\text{-Bu})_3]^-$ , the reaction energies and enthalpies are negative. This indicates that this siloxide complex would be capable of capturing H<sub>2</sub> and initiating hydride transfer. The difference between the reactivities of the siloxide and the silylamide towards H<sub>2</sub> conforms well with the

experimental observations.<sup>16</sup> Our computational protocol is able to distinguish cases where ligand substitution leads to improved reaction energies (activation of H<sub>2</sub>O and N<sub>2</sub>) and situations ligand substitution leads to diminished reactivities, H<sub>2</sub> capture and hydride transfer by [(O)U-N-U(O)][OSi(O-*t*-Bu)<sub>3</sub>]<sup>-</sup> and [(N)U-N-U(N)][N(SiMe<sub>3</sub>)<sub>2</sub>]<sup>-</sup>.

**Table 3.2: Calculated reaction energies and enthalpies, kcal/mol, for H<sub>2</sub> capture and hydride transfer by [(O)U-N-U(O)][OSi(O-*t*-Bu)<sub>3</sub>]<sup>-</sup> and [(N)U-N-U(N)][N(SiMe<sub>3</sub>)<sub>2</sub>]<sup>-</sup>.**

	[(N)U-N-U(N)][N(SiMe <sub>3</sub> ) <sub>2</sub> ] <sup>-</sup>		[(O)U-N-U(O)][OSi(O- <i>t</i> -Bu) <sub>3</sub> ] <sup>-</sup>	
	ΔE	ΔH	ΔE	ΔH
Scalar-relativistic				
PBE/L1	+10.0	+12.6	-11.0	-7.0
PBE-D3BJ/TZ2P	+6.0		-16.1	
Spin-orbit coupling				
PBE-D3BJ/TZ2P	+8.3		-18.2	

To explain the disparity between the siloxide and silylamide species, we consider a pathway that starts with an adduct of H<sub>2</sub> to the U-N-U core, Figure 3.4. This is followed by dissociation of H<sub>2</sub>, transfer of a proton to the nitrido and an hydride to a U center. The intermediate HU-NH-U species has a near-linear U-N-U angle. This species then undergoes structural re-organization to form the final U-(H)(NH)-U product with a bent U-N-U angle, Figure 3.4. The adduct between H<sub>2</sub> and [(N)U-N-U(N)][N(SiMe<sub>3</sub>)<sub>2</sub>]<sup>-</sup> is uphill by 8.1 kcal/mol, due to steric constraints. Formation of the intermediate is uphill by an additional 2.2 kcal/mol. Interestingly, re-organization to final product is downhill by just -0.3 kcal/mol. These results show that the reaction energy of [(N)U-N-U(N)][N(SiMe<sub>3</sub>)<sub>2</sub>]<sup>-</sup> is dominated by the repulsive interactions with H<sub>2</sub> in the adduct. During reorganization of the intermediate, the U-N-U core is not sufficiently flexible to account for the repulsive nature of the first phase, Figure 3.4. We now examine a similar path for [(O)U-N-U(O)][OSi(O-*t*-Bu)<sub>3</sub>]<sup>-</sup>. Here, formation of the adduct is uphill by only 0.6 kcal/mol, Figure 3.5. This conforms with the fact that the environment around the bis-uranium nitride core of [(O)U-N-U(O)][OSi(O-*t*-Bu)<sub>3</sub>]<sup>-</sup> is less confining than that of [(N)U-N-U(N)][N(SiMe<sub>3</sub>)<sub>2</sub>]<sup>-</sup>. As started earlier, the Si(Me)<sub>3</sub> groups are rather close-in to the U-N-U core of the silylamide, whereas the siloxide has a Si-O spacer between the U-N-U core and *t*-Bu groups.<sup>16</sup> Formation of the intermediate is uphill by 0.6 kcal for [(O)U-N-U(O)][OSi(O-*t*-Bu)<sub>3</sub>]<sup>-</sup>, compared to 2.2 kcal/mol for the silylamide. However, reorganization of the intermediate is downhill by -11.5 kcal/mol for the siloxide, to be contrasted with only -0.3 kcal/mol for the silylamide. The U-N-U core in the

intermediate species of the siloxide is thus sufficiently flexible to drive the whole reaction towards exothermicity.

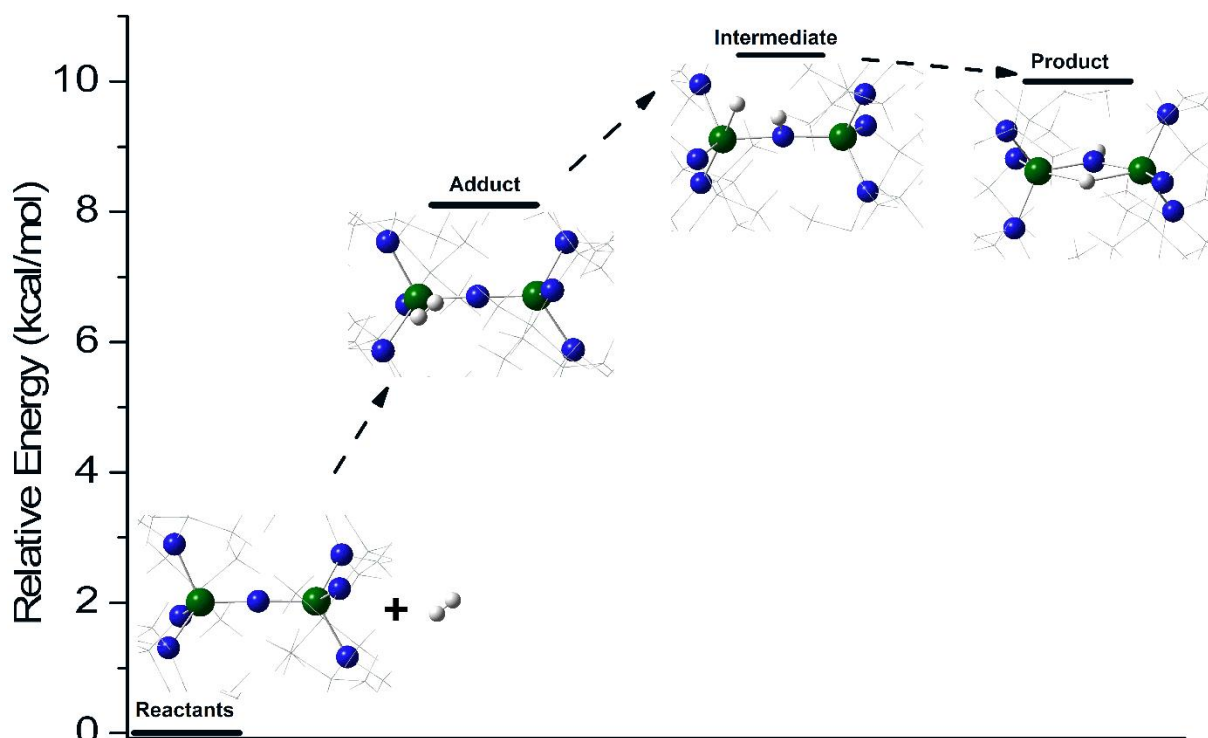


**Figure 3.4:** Calculated pathway for H<sub>2</sub> capture and hydride transfer by [(N)U-N-U(N)][N(SiMe<sub>3</sub>)<sub>2</sub>]<sup>-</sup> obtained at the PBE/L1 level of theory.

**3.3.2.3. H<sub>2</sub> capture and hydride transfer by Np analogues:** The reaction energies for H<sub>2</sub> capture by [(O)Np-N-Np(O)][OSi(O-*t*-Bu)<sub>3</sub>]<sup>-</sup> and [(N)Np-N-Np(N)][N(SiMe<sub>3</sub>)<sub>2</sub>]<sup>-</sup> are shown in Table 3.3. Overall, the reaction energies for the Np species are very similar to those of their U analogues, Table 3.2. This contrasts greatly with the results obtained for the HER where the barriers and reaction energies were more favorable for U. Crucially, for the HER, the oxidation states of the actinides are changed from +3 to +5. In contrast, for H<sub>2</sub> capture the actinide oxidation states are unchanged from +4. Thus Np behaves in a similar manner as U for small-molecule activation reactions that do not involve redox transformation of the actinide center.

**3.2.4. Like-for-like ligand transformation:** The reaction energies for H<sub>2</sub> capture and hydride transfer by [(N)U-N-U(N)][(HN)Si(O-*t*-Bu)<sub>3</sub>]<sup>-</sup> are compared to those of [(O)U-N-U(O)][OSi(O-*t*-Bu)<sub>3</sub>]<sup>-</sup> in Figure 3.6. In [(N)U-N-U(N)][(NH)Si(O-*t*-Bu)<sub>3</sub>]<sup>-</sup>, the U-O bonds of [(O)U-N-U(O)][OSi(O-*t*-Bu)<sub>3</sub>]<sup>-</sup> are transformed into U-NH groups. Comparison of the reaction energies for these molecules allows a *like-for-like* comparison of the impact of An-O → An-NH actinide-

ligand modulation. The steric environments in these two species are largely similar. The results for the Np analogues are also presented.

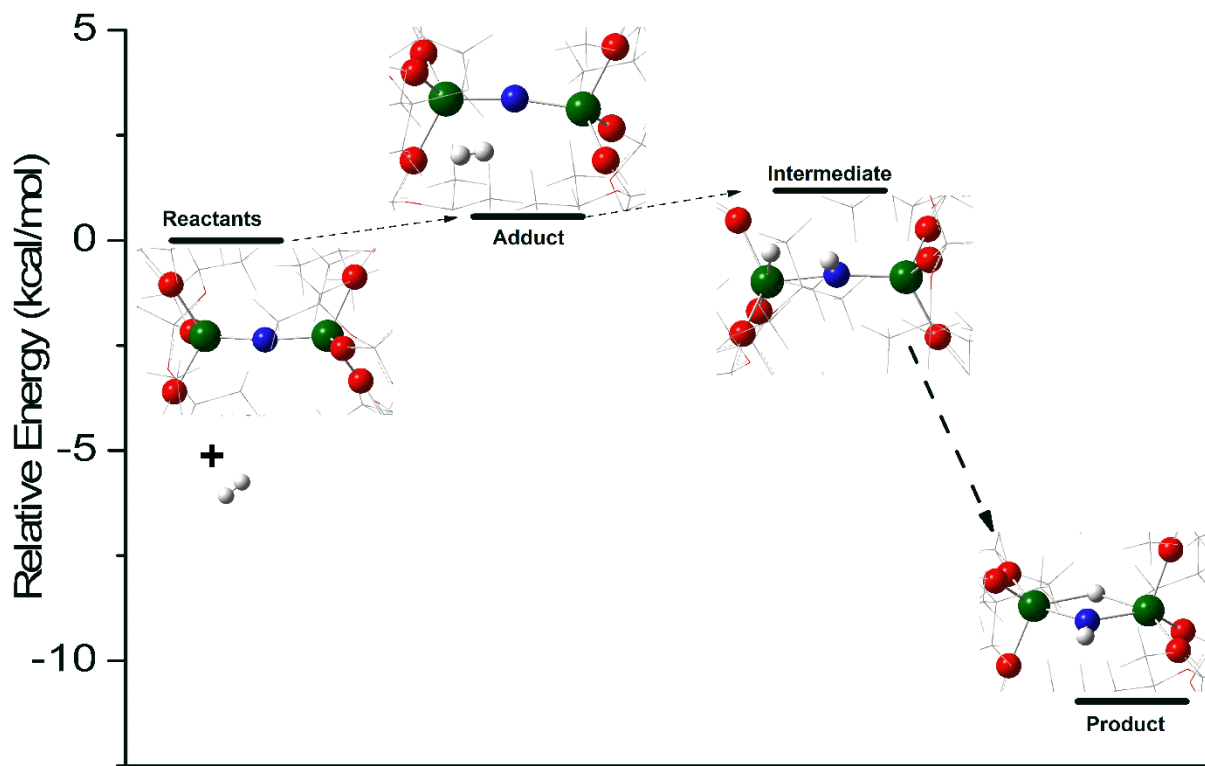


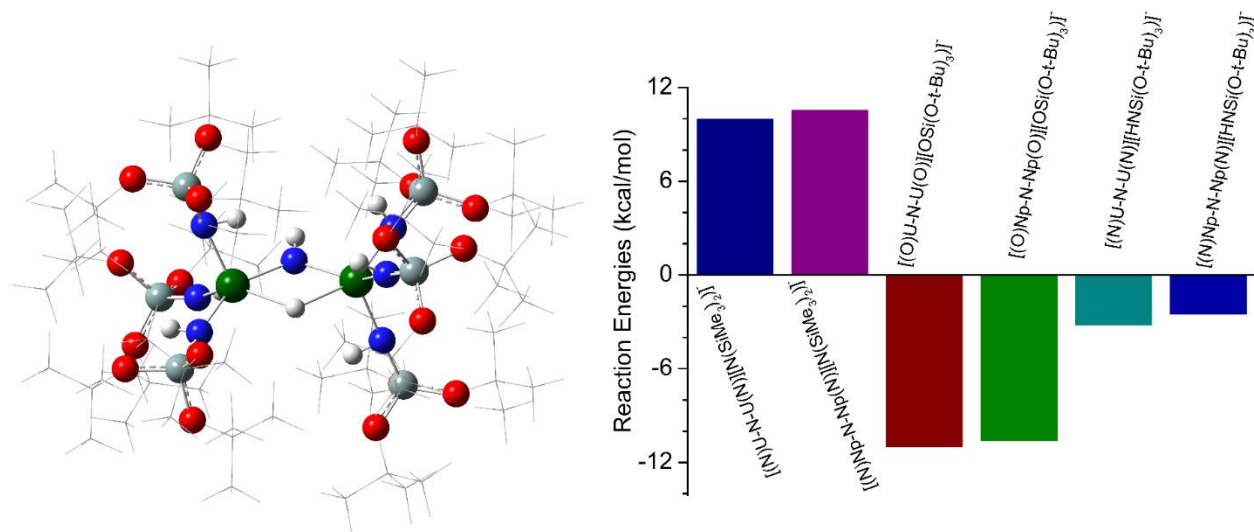
**Figure 3. 5:** Calculated pathway for  $\text{H}_2$  capture and hydride transfer by  $[(\text{O})\text{U}-\text{N}-\text{U}(\text{O})][\text{OSi}(\text{O}-t\text{-Bu})_3]^-$  obtained at the PBE/L1 level of theory.

**Table 3.3:** Calculated reaction energies and enthalpies, kcal/mol, for  $\text{H}_2$  capture and hydride transfer by  $[(\text{O})\text{Np}-\text{N}-\text{Np}(\text{O})][\text{OSi}(\text{O}-t\text{-Bu})_3]^-$  and  $[(\text{N})\text{Np}-\text{N}-\text{Np}(\text{N})][\text{N}(\text{SiMe}_3)_2]^-$ .

	$[(\text{N})\text{Np}-\text{N}-\text{Np}(\text{N})][\text{N}(\text{SiMe}_3)_2]^-$		$[(\text{O})\text{Np}-\text{N}-\text{Np}(\text{O})][\text{OSi}(\text{O}-t\text{-Bu})_3]^-$	
	$\Delta E$	$\Delta H$	$\Delta E$	$\Delta H$
Scalar-relativistic				
PBE/L1	+10.5	+14.3	-10.6	-8.7
PBE-D3BJ/TZ2P	+6.2		-13.6	
Spin-orbit coupling				
PBE-D3BJ/TZ2P	+5.2		-15.3	

The calculated reaction energies for  $[(\text{N})\text{U}-\text{N}-\text{U}(\text{N})][\text{N}(\text{SiMe}_3)_2]^-$  and its Np analogue are -3.2 and -2.5 kcal/mol, respectively. These are exothermic and are to be compared with  $[(\text{N})\text{U}-\text{N}-\text{U}(\text{N})][\text{N}(\text{SiMe}_3)_2]^-$  and  $[(\text{N})\text{Np}-\text{N}-\text{Np}(\text{N})][\text{N}(\text{SiMe}_3)_2]^-$ , for which  $\text{H}_2$  capture and hydride transfer is endothermic, Figure 3.6. This confirms that  $[(\text{N})\text{U}-\text{N}-\text{U}(\text{N})][\text{N}(\text{SiMe}_3)_2]^-$  and  $[(\text{N})\text{Np}-\text{N}-\text{Np}(\text{N})][\text{N}(\text{SiMe}_3)_2]^-$  can not capture  $\text{H}_2$  due to the steric confinement of their ligand frameworks. The inability of these species to capture  $\text{H}_2$  is not due to the presence of the actinide-

amide bonds. By comparing  $[(\text{N})\text{U}-\text{N}-\text{U}(\text{N})][(\text{NH})\text{Si}(\text{O}-t\text{-Bu})_3]^-$  and  $[(\text{O})\text{Np}-\text{N}-\text{Np}(\text{O})][\text{OSi}(\text{O}-t\text{-Bu})_3]^-$ , we see that the U-O-Si-O group is more conducive for reorganization than the U-NH-Si-



O moiety. As we have previously shown for N<sub>2</sub> activation, we expect that H<sub>2</sub> capture would be even more facile for species containing U-NH-Si-NH groups.<sup>17</sup>

**Figure 3.6:** The structure of  $[(\text{N})\text{U}-(\text{H})(\text{NH})-\text{U}(\text{N})][(\text{NH})\text{Si}(\text{O}-t\text{-Bu})_3]^-$  is shown on the left. This species is formed after H<sub>2</sub> capture and hydride transfer by  $[(\text{N})\text{U}-\text{N}-\text{U}(\text{N})][(\text{NH})\text{Si}(\text{O}-t\text{-Bu})_3]^-$ . The reaction energies for H<sub>2</sub> capture and hydride transfer by various species are shown on the right.

### 3.4 CONCLUSIONS

Using scalar-relativistic and spin-orbit coupling DFT calculations, we have investigated small-molecule activation by organometallic uranium (U) and neptunium (Np) complexes. We focus on the impact of An-O → An-N ligand substitution on the reactivities of actinide complexes towards small molecules. An-O depicts actinide-oxo bonds whereas An-N depicts actinide-imido/amide interactions. Specifically we have examined two reactions: *First*, we examined the reaction pathway of the hydrogen evolution reaction (HER) from water. This is motivated by recent work showing that An-O → An-N ligand substitution leads to improved reactivities for neptunium complexes in the four-electron reduction of N<sub>2</sub>. Herein, we aim to determine if this trend extends to reactivity with water. *Second*, we compare H<sub>2</sub> capture and hydride transfer by various bis-actinide silylamide and siloxide complexes. Recent experimental work has shown that while the siloxides are reactive towards H<sub>2</sub>, the silylamides are not, suggesting that An-O → An-N ligand substitution does not lead to improved reactivities. This seemingly conflicts with our previous results. Thus, we sought to explain the discrepancy and also determine whether our computational

protocol could differentiate situations in which ligand substitution leads to improved or diminished reactivities.

For the electrocatalytic reduction of water, HER, we considered U and Np tris-aryloxide complexes. A previous experimental report demonstrated that the U complex,  $[((^{Ad,Me}ArO)_3mes)U].OH_2$ , can effect the HER. This is supported by our calculated reaction energies and barriers. The rate-determining step barrier is on the order of 18.7 kcal/mol for this complex. By contrast, the reaction barriers are significantly higher for  $[((^{Ad,Me}ArO)_3mes)Np].OH_2$ . Additionally, the overall reaction is endothermic for the neptunium complex. We find that  $Np-O \rightarrow An-NH$  ligand substitution leads to marginally lower barriers (1-4 kcal/mol) and improved reaction energies (more exothermic by 9-15 kcal/mol). The trends in the barriers and reaction energies seem to be slightly correlated with the Mayer bond order of the activated O-H bonds of water.

For  $H_2$  capture, our computational protocol sufficiently reproduces the experimental structural properties of the bis-uranium nitride, U-N-U, complexes with silylamide,  $[(N)U-N-U(N)][N(SiMe_3)_2]^-$ , or siloxide,  $[(O)U-N-U(O)][OSi(O-*t*-Bu)_3]^-$ , ligands.  $H_2$  capture by  $[(O)U-N-U(O)][OSi(O-*t*-Bu)_3]^-$  is significantly exothermic while it is strongly endothermic for the  $[(N)U-N-U(N)][N(SiMe_3)_2]^-$ . Based on these results, we expect that reactivity for  $H_2$  capture and hydride transfer will occur for the former and not for the latter. This conclusion agrees with the experimental observations. We found that the reactivities of the Np analogues are very similar to those of the U complex. This contrasts to the situation observed for water activation. We rationalize this as due to the fact that water activation involves redox transformation of the actinide sites ( $+3 \rightarrow +5$  oxidation states) while the oxidation states of the actinides remain unchanged during  $H_2$  capture.

We however emphasize that the ligand environments of  $[(N)U-N-U(N)][N(SiMe_3)_2]^-$  and  $[(O)U-N-U(O)][OSi(O-*t*-Bu)_3]^-$  are significantly different. The ligand environment around the U-N-U core of this silylamide is more crowded. This leads to far greater repulsive interactions with  $H_2$  than in the  $[(O)U-N-U(O)][OSi(O-*t*-Bu)_3]^-$ . Additionally, the final reorganization step is more downhill for the siloxide than for the silylamide. We find that if we simply replaced the U-O bonds in  $[(O)U-N-U(O)][OSi(O-*t*-Bu)_3]^-$  with U-NH bonds, reactivity towards  $H_2$  is established. This confirms that  $[(N)U-N-U(N)][N(SiMe_3)_2]^-$  is un-reactive towards  $H_2$ , not because of  $An-O \rightarrow An-N$  ligand substitution, but because the ligand framework is uncondusive for this reaction.

For Np complexes, small-molecule activation processes involving redox transformation of the

metal site are generally associated with high transition state barriers and endothermicity. Our computations suggest that An-O  $\rightarrow$  An-N ligand substitution provides an opportunity for modest gains in the kinetics as well as substantial gains in the overall reaction energies. There is thus an opportunity for large-scale computational screening of Np complexes that can be useful for catalytic activation of various small molecules. Emphasis should be placed on ligands that can furnish lower activation barriers.

## REFERENCES

- (1) Arnold, P. L. Uranium-mediated activation of small molecules. *Chem. Commun.* **2011**, 47, 9005.
- (2) Arnold, P. L.; Turner, Z. R. Carbon oxygenate transformations by actinide compounds and catalysts. *Nat. Rev. Chem.* **2017**, 1, 0002.
- (3) Arnold, P. L.; Turner, Z. R.; Germeroth, A. I.; Casely, I. J.; Nichol, G. S.; Bellabarba, R.; Tooze, R. P. Carbon monoxide and carbon dioxide insertion chemistry of f-block N-heterocyclic carbene complexes. *Dalton T.* **2013**, 42, 1333.
- (4) Barluzzi, L.; Falcone, M.; Mazzanti, M. Small molecule activation by multimetallic uranium complexes supported by siloxide ligands. *Chem. Commun.* **2019**, 55, 13031.
- (5) Bart, S. C.; Anthon, C.; Heinemann, F. W.; Bill, E.; Edelstein, N. M.; Meyer, K. Carbon dioxide activation with sterically pressured mid- and high-valent uranium complexes. *J. Am. Chem. Soc.* **2008**, 130, 12536.
- (6) Castro-Rodriguez, I.; Meyer, K. Small molecule activation at uranium coordination complexes: control of reactivity via molecular architecture. *Chem. Commun.* **2006**, 1353.
- (7) Falcone, M.; Barluzzi, L.; Andrez, J.; Fadaei Tirani, F.; Zivkovic, I.; Fabrizio, A.; Corminboeuf, C.; Severin, K.; Mazzanti, M. The role of bridging ligands in dinitrogen reduction and functionalization by uranium multimetallic complexes. *Nat. Chem.* **2019**, 11, 154.
- (8) Falcone, M.; Chatelain, L.; Scopelliti, R.; Mazzanti, M. CO cleavage and CO<sub>2</sub> functionalization under mild conditions by a multimetallic CsU<sub>2</sub> nitride complex. *Chimia* **2017**, 71, 209.
- (9) Falcone, M.; Chatelain, L.; Scopelliti, R.; Zivkovic, I.; Mazzanti, M. Nitrogen reduction and functionalization by a multimetallic uranium nitride complex. *Nature* **2017**, 547, 332.
- (10) Falcone, M.; Poon, L. N.; Tirani, F. F.; Mazzanti, M. Reversible dihydrogen activation and hydride transfer by a uranium nitride complex. *Angew. Chem. Int. Edit.* **2018**, 57, 3697.
- (11) Franke, S. M.; Tran, B. L.; Heinemann, F. W.; Hieringer, W.; Mindiola, D. J.; Meyer, K. Uranium(III) Complexes with Bulky Aryloxide Ligands Featuring Metal-Arene Interactions and Their Reactivity Toward Nitrous Oxide. *Inorg. Chem.* **2013**, 52, 10552.
- (12) Halter, D. P.; Heinemann, F. W.; Bachmann, J.; Meyer, K. Uranium-mediated electrocatalytic dihydrogen production from water. *Nature* **2016**, 530, 317.
- (13) Halter, D. P.; Heinemann, F. W.; Maron, L.; Meyer, K. The role of uranium-arene bonding in H<sub>2</sub>O reduction catalysis. *Nat. Chem.* **2018**, 10, 259.
- (14) La Pierre, H. S.; Meyer, K. In "Activation of small molecules by molecular uranium complexes" *Progress in Inorganic Chemistry*, Vol 58; Karlin, K. D., Ed. 2014; Vol. 58, p 303.
- (15) Lam, O. P.; Meyer, K. Uranium-mediated carbon dioxide activation and functionalization. *Polyhedron* **2012**, 32, 1.

- (16) Palumbo, C. T.; Barluzzi, L.; Scopelliti, R.; Zivkovic, I.; Fabrizio, A.; Corminboeuf, C.; Mazzanti, M. Tuning the structure, reactivity and magnetic communication of nitride-bridged uranium complexes with the ancillary ligands. *Chem. Sci.* **2019**, *10*, 8840.
- (17) Panthi, D.; Adeyiga, O.; Dandu, N. K.; Odoh, S. O. Nitrogen reduction by multimetallic trans-uranium actinide complexes: A theoretical comparison of Np and Pu to U. *Inorg. Chem.* **2019**, *58*, 6731.
- (18) Schmidt, A. C.; Heinemann, F. W.; Kefalidis, C. E.; Maron, L.; Roesky, P. W.; Meyer, K. Activation of SO<sub>2</sub> and CO<sub>2</sub> by trivalent uranium leading to sulfite/dithionite and carbonate/oxalate complexes. *Chem.-Eur. J.* **2014**, *20*, 13501.
- (19) Summerscales, O. T.; Cloke, F. G. N. In *Organometallic and Coordination Chemistry of the Actinides*; Albrecht-Schmitt, T. E., Ed. 2008; Vol. 127, p 87.
- (20) Zhang, L.; Zhang, C. C.; Hou, G. H.; Zi, G. F.; Walter, M. D. Small-molecule activation mediated by a uranium bipyridyl metallocene. *Organometallics* **2017**, *36*, 1179.
- (21) Arnold, P. L.; Dutkiewicz, M. S.; Walter, O. Organometallic neptunium chemistry. *Chem. Rev.* **2017**, *117*, 11460.
- (22) Dutkiewicz, M. S.; Farnaby, J. H.; Apostolidis, C.; Colineau, E.; Walter, O.; Magnani, N.; Gardiner, M. G.; Love, J. B.; Kaltsoyannis, N.; Caciuffo, R.; Arnold, P. L. Organometallic neptunium(III) complexes. *Nat. Chem.* **2016**, *8*, 797.
- (23) Arnold, P. L.; Hollis, E.; Nichol, G. S.; Love, J. B.; Griveau, J. C.; Caciuffo, R.; Magnani, N.; Maron, L.; Castro, L.; Yahia, A.; Odoh, S. O.; Schreckenbach, G. Oxo-functionalization and reduction of the uranyl ion through lanthanide-element bond homolysis: Synthetic, structural, and bonding analysis of a series of singly reduced uranyl-rare earth 5f(1)-4f(n) complexes. *J. Am. Chem. Soc.* **2013**, *135*, 3841.
- (24) Faizova, R.; White, S.; Scopelliti, R.; Mazzanti, M. The effect of iron binding on uranyl(v) stability. *Chem. Sci.* **2018**, *9*, 7520.
- (25) Lewis, A. J.; Mullane, K. C.; Nakamaru-Ogiso, E.; Carroll, P. J.; Schelter, E. J. The inverse trans influence in a family of pentavalent uranium complexes. *Inorg. Chem.* **2014**, *53*, 6944.
- (26) Lewis, A. J.; Nakamaru-Ogiso, E.; Kikkawa, J. M.; Carroll, P. J.; Schelter, E. J. Pentavalent uranium trans-dihalides and -pseudohalides. *Chem. Commun.* **2012**, *48*, 4977.
- (27) Odoh, S. O.; Schreckenbach, G. DFT Study of oxo-functionalized pentavalent dioxouranium complexes: Structure, bonding, ligand exchange, dimerization, and U(V)/U(IV) reduction of OUOH and OUOSiH<sub>3</sub> complexes. *Inorg. Chem.* **2013**, *52*, 245.
- (28) Laikov, D. N. A new class of atomic basis functions for accurate electronic structure calculations of molecules. *Chem. Phys. Lett.* **2005**, *416*, 116.
- (29) Laikov, D. N. Neglect of four- and approximation of one-, two-, and three-center two-electron integrals in a symmetrically orthogonalized basis. *J. Comput. Chem.* **2007**, *28*, 698.
- (30) Laikov, D. N.; Ustynyuk, Y. A. PRIRODA-04: a quantum-chemical program suite. New possibilities in the study of molecular systems with the application of parallel computing. *Russ. Chem. B+* **2005**, *54*, 820.
- (31) Baerends, E. J.; Ziegler, T.; Atkins, A. J.; Autschbach, J.; Bashford, D.; Baseggio, O.; Bércecs, A.; Bickelhaupt, F. M.; Bo, C.; Boerritger, P. M.; Cavallo, L.; Daul, C.; Chong, D. P.; Chulhai, D. V.; Deng, L.; Dickson, R. M.; Dieterich, J. M.; Ellis, D. E.; van Faassen, M.; Ghysels, A.; Giammona, A.; van Gisbergen, S. J. A.; Goetz, A.; Götz, A. W.; Gusarov, S.; Harris, F. E.; van den Hoek, P.; Hu, Z.; Jacob, C. R.; Jacobsen, H. *et al.*
- (32) te Velde, G.; Bickelhaupt, F. M.; Baerends, E. J.; Guerra, C. F.; Van Gisbergen, S. J. A.; Snijders, J. G.; Ziegler, T. Chemistry with ADF. *J. Comput. Chem.* **2001**, *22*, 931.



- (33) Perdew, J. P.; Burke, K.; Ernzerhof, M. Generalized gradient approximation made simple. *Phys. Rev. Lett.* **1996**, *77*, 3865.
- (34) Van Lenthe, E.; Baerends, E. J. Optimized slater-type basis sets for the elements 1-118. *J. Comput. Chem.* **2003**, *24*, 1142.
- (35) Adeyiga, O.; Suleiman, O.; Dandu, N. K.; Odoh, S. O. Ground-state actinide chemistry with scalar-relativistic multiconfiguration pair-density functional theory. *J. Chem. Phys.* **2019**, *151*, 134102.
- (36) Clavaguera-Sarrio, C.; Vallet, V.; Maynau, D.; Marsden, C. J. Can density functional methods be used for open-shell actinide molecules? Comparison with multiconfigurational spin-orbit studies. *J. Chem. Phys.* **2004**, *121*, 5312.
- (37) Iche-Tarrat, N.; Marsden, C. J. Examining the performance of DFT methods in uranium chemistry: Does core size matter for a pseudopotential? *J. Phys. Chem. A* **2008**, *112*, 7632.
- (38) Odoh, S. O.; Schreckenbach, G. Performance of relativistic effective core potentials in DFT calculations on actinide compounds. *J. Phys. Chem. A* **2010**, *114*, 1957.
- (39) Odoh, S. O.; Schreckenbach, G. Theoretical study of the structural properties of plutonium(IV) and (VI) complexes. *J. Phys. Chem. A* **2011**, *115*, 14110.
- (40) Schreckenbach, G.; Hay, P. J.; Martin, R. L. Density functional calculations on actinide compounds: Survey of recent progress and application to  $\text{UO}_2\text{X}_4^{2-}$  ( $\text{X} = \text{F}, \text{Cl}, \text{OH}$ ) and  $\text{AnF}_6$  ( $\text{An} = \text{U}, \text{Np}, \text{Pu}$ ). *J. Comput. Chem.* **1999**, *20*, 70.
- (41) Schreckenbach, G.; Shamov, G. A. Theoretical Actinide Molecular Science. *Accounts Chem. Res.* **2010**, *43*, 19.
- (42) Grimme, S.; Antony, J.; Ehrlich, S.; Krieg, H. A consistent and accurate ab initio parametrization of density functional dispersion correction (DFT-D) for the 94 elements H-Pu. *J. Chem. Phys.* **2010**, *132*, 154104.
- (43) Grimme, S.; Ehrlich, S.; Goerigk, L. Effect of the damping function in dispersion corrected density functional theory. *J. Comput. Chem.* **2011**, *32*, 1456.
- (44) Johnson, E. R.; Becke, A. D. A post-Hartree-Fock model of intermolecular interactions: Inclusion of higher-order corrections. *J. Chem. Phys.* **2006**, *124*, 174104.
- (45) Van Lenthe, E.; Snijders, J. G.; Baerends, E. J. The zero-order regular approximation for relativistic effects: The effect of spin-orbit coupling in closed shell molecules. *J. Chem. Phys.* **1996**, *105*, 6505.
- (46) Chong, D. P. Augmenting basis set for time-dependent density functional theory calculation of excitation energies: Slater-type orbitals for hydrogen to krypton. *Mol. Phys.* **2005**, *103*, 749.
- (47) Chong, D. P.; Van Lenthe, E.; Van Gisbergen, S.; Baerends, E. J. Even-tempered slater-type orbitals revisited: From hydrogen to krypton. *J. Comput. Chem.* **2004**, *25*, 1030.
- (48) Marenich, A. V.; Cramer, C. J.; Truhlar, D. G. Generalized Born Solvation Model SM12. *J. Chem. Theory Comput.* **2013**, *9*, 609.
- (49) Peeples, C. A.; Schreckenbach, G. Implementation of the SM12 Solvation Model into ADF and comparison with COSMO. *J. Chem. Theory Comput.* **2016**, *12*, 4033.
- (50) Mayer, I. Bond order and valence indices: A personal account. *J. Comput. Chem.* **2007**, *28*, 204.
- (51) Bader, R. F. W. A quantum theory of molecular structure and its applications. *Chem. Rev.* **1991**, *91*, 893.
- (52) Kaltsoyannis, N. Does Covalency Increase or Decrease across the Actinide Series? Implications for Minor Actinide Partitioning. *Inorg. Chem.* **2013**, *52*, 3407.

## CHAPTER 4. METHANE OVER-OXIDATION BY EXTRA-FRAMEWORK COPPER-OXO ACTIVE SITES OF COPPER-EXCHANGED ZEOLITES: CRUCIAL ROLE OF TRAPS FOR THE SEPARATED METHYL GROUP

Olajumoke Adeyiga and Samuel O. Odoh\*

Department of Chemistry, University of Nevada Reno, 1664 N. Virginia Street, Reno, NV  
89557-0216

“Reprinted (adapted) with permission from *ChemPhysChem*, 2021, 22, 11, 1101-1109.

Copyright (2021) John Wiley and Sons”

**ABSTRACT:** Copper-exchanged zeolites are useful for stepwise conversion of methane to methanol at moderate temperatures. This process also generates some over-oxidation products like CO and CO<sub>2</sub>. However, mechanistic pathways for methane over-oxidation by copper-oxo active sites in these zeolites have not been previously described. Adequate understanding of methane over-oxidation is useful for developing systems with higher methanol yields and selectivities. Here, we use density functional theory (DFT) to examine methane over-oxidation by [Cu<sub>3</sub>O<sub>3</sub>]<sup>2+</sup> active sites in zeolite mordenite MOR. The methyl group formed after activation of a methane C-H bond can be stabilized at a μ-oxo atom of the active site. This μ-(O-CH<sub>3</sub>) intermediate can undergo sequential hydrogen atom abstractions till eventual formation of a copper-monocarbonyl species. Adsorbed formaldehyde, water and formates are also formed during this process. The overall mechanistic path is exothermic and all intermediate steps are facile at 200 °C. Release of CO from the copper-monocarbonyl costs only 3.4 kcal/mol. Thus, for high methanol selectivities, the methyl group from the first hydrogen atom abstraction step *must be* stabilized *away* from copper-oxo active sites. Indeed, it must be quickly trapped at an unreactive site (short diffusion lengths) while avoiding copper-oxo species (large paths between active sites). This stabilization of the methyl group away from the active sites is central to the high methanol selectivities obtained with stepwise methane-to-methanol conversion.

## 4.1 INTRODUCTION

Natural gas consists mainly of methane and is a cleaner source of energy than coal or petroleum. It is also a valuable source of value-added intermediates. However, transportation of natural gas to points of end-use is fairly expensive. As such, there is great interest in the development of cheap, efficient and environmentally friendly approaches for converting methane to methanol.<sup>[1]</sup> Methanol is a liquid and can be transported with existing infrastructure. Currently, large-scale methane-to-methanol conversion, MMC, is carried out via steam reforming and combustion.<sup>[2-3]</sup> Direct oxidation of methane to methanol at moderate temperatures and pressures, while desirable, is fairly problematic. This is because the products of full combustion of methane, like CO and CO<sub>2</sub>, are more stable than methanol. As such, at high temperatures methane is readily over-oxidized to CO and CO<sub>2</sub>. Selectivity for methanol is poor under these conditions, despite high conversion. By contrast, at low temperatures methane conversion is not economically viable although it is often easier to achieve high kinetic selectivities for methanol.<sup>[4-5]</sup> Thus, there is significant interest in development of platforms that can provide economically viable yields under mild operating conditions, are highly selective for methanol, and/or lead to the formation of products resistant to further oxidation.

Over the years, there has been strong interest in metal-exchanged, especially copper-exchanged, zeolites due to their ability to facilitate MMC with fairly high selectivities under mild conditions. These systems have been studied with various experimental and theoretical methods.<sup>[6-25]</sup> However, the step-wise process for MMC in these zeolites is stoichiometric. Thus there is a need to regenerate the copper-oxo active sites after each cycle. Indeed MMC in these zeolites involve 3 steps, Figure 4.1. Typically, methane is converted to strongly-bound methoxy species by the active copper-oxo sites.<sup>[26]</sup> Methanol is then released with steam. This steam-facilitated process also releases dimethyl ether, DME, as well as over-oxidation products like CO and CO<sub>2</sub>. The active sites are subsequently regenerated with oxidants like atmospheric oxygen in a last step. These 3 steps, as well as the initial formation of the active sites, are performed at different temperatures. Thus, a way to improve step-wise MMC by zeolites involves using active sites that can be used in an isothermal or near-isothermal fashion.<sup>[27]</sup> Additionally, there has been interest in optimizing the copper-exchanged zeolites for improved methanol selectivities and yield. To this end, a detailed mechanistic understanding of the pathways leading to over-oxidation products is necessary.

However, a detailed search of the literature reveals little theoretical investigations of the mechanism of methane over-oxidation at the copper-oxo active sites of copper-exchanged zeolites.

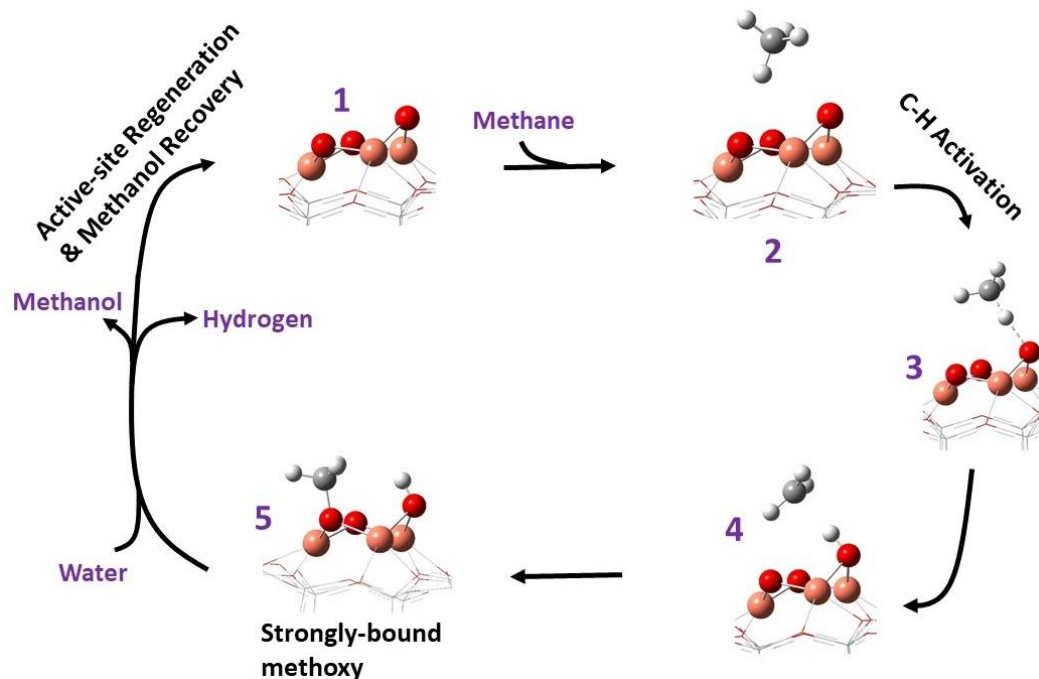


**Figure 4.1: Activation of methane C-H bond to methanol by  $[\text{Cu}_3\text{O}_3]^{2+}$  active site, steam-facilitated extraction of products and regeneration of the active copper oxo cluster.**

Interestingly, the natures of the active sites responsible for MMC in copper-exchanged zeolites remain under some debate. Various active site models have been proposed. It appears that the dominant copper-oxo active sites in each zeolite depend on the composition of the zeolite precursors as well as the preparation and reaction conditions. On the whole,  $[\text{Cu}_2\text{O}]^{2+}$  and  $[\text{Cu}_3\text{O}_3]^{2+}$  are considered as highly reactive for methane activation. MMC by these species have been examined and discussed by various workers.<sup>[12, 16-17, 19, 21, 23, 28-30]</sup> In a complementary fashion, quantum-mechanical computations have been used to study the MMC mechanism on these active sites. More recently, the spectroscopic properties of these active sites during MMC have been described with theoretical calculations.<sup>[31-33]</sup> Most of these computations have used cluster-model or periodic density functional theory, DFT.<sup>[34-36]</sup> For this reason, it is judicious to examine the mechanisms for methane over-oxidation by the copper-oxo active sites with DFT.

Towards this end, we use cluster-model DFT calculations to probe methane over-oxidation at the  $[\text{Cu}_3\text{O}_3]^{2+}$  active site in zeolite mordenite, MOR.<sup>[37-38]</sup> We chose the  $[\text{Cu}_3\text{O}_3]^{2+}$  site as it possesses several oxidizing  $\mu$ -oxo atoms. This allows us to consider methane over-oxidation via multiple hydrogen atom abstraction (HAA) steps between methane and these  $\mu$ -oxo atoms. It is quite likely

that over-oxidation via multiple HAA steps can also occur in zeolites with  $[\text{Cu}_2\text{O}]^{2+}$  active sites. In this situation, HAA will require diffusion of  $\text{CH}_x$  ( $x = 4-0$ ) moieties within the framework to other  $[\text{Cu}_2\text{O}]^{2+}$  sites. We chose the zeolite MOR as it has been shown to provide some of the highest methanol yields and has been extensively characterized with spectroscopic techniques.<sup>[9-10, 15, 21-22, 28, 31, 39-46]</sup> Simply speaking, if  $[\text{Cu}_3\text{O}_3]^{2+}$  can over-oxidize methane, then typical experimental setups (moderate temperature and absence of molecular oxygen) for methane activation must contain scavengers that rapidly trap the methyl intermediate away from copper-oxo sites. These scavengers function by helping to avoid formation of **5** in Figure 4.1.

## 4.2 COMPUTATIONAL METHODS AND MODELS

**4.2.1 Cluster-model Calculations:** Geometry optimizations, transition state searches and vibrational frequency analyses were carried out in the gas phase with all-electron (AE) basis sets and DFT while using a cluster model for the eight-membered ring (8MR) of MOR. This cluster model has been used previously by several workers.<sup>[9-10, 22, 31]</sup> It reflects location of the  $[\text{Cu}_3\text{O}_3]^{2+}$  active site in the 8MR of MOR, Figure 4.2. The edges of this cluster model are terminated with protons. The positions of these protons were initially optimized and then fixed during all other subsequent optimizations.

DFT calculations were performed at the scalar relativistic level with the Priroda code.<sup>[47-48]</sup> We used the Perdew-Burke-Ernzerhof (PBE) generalized gradient approximation (GGA) and B3LYP hybrid functionals in these calculations.<sup>[49-53]</sup> PBE yields good structural parameters for copper-oxo active sites in copper-exchanged zeolites. For these calculations, we employed AE basis sets labelled previously as L1 and of double- $\zeta$ -polarized quality for the large component and appropriate kinetically balanced basis sets for the small components.<sup>[54-55]</sup> The Al and Si atoms were described with 15s11p2d (contracted to 4s3p1d) while the C and O atoms were described with 12s7p2d (contracted to 3s2p1d). Hydrogen atoms were described with 6s2p (contracted to 2s1p). Cu atoms were described with 19s15p10d3f (contracted to 6s5p3d1f). In the scalar-relativistic approach of Priroda, spin-orbit terms are projected out and neglected from the Dirac equation, as described previously.<sup>[56]</sup> Vibrational frequency analyses were carried out with the harmonic approximation. This allows us to characterize all reactants, intermediates and products as local minima structures. Transition state species were characterized with one imaginary vibrational mode. Unless otherwise stated, all our calculations were for the doublet spin state,  $S = 1/2$ . Generally, the doublet species are more stable than the quartet species.

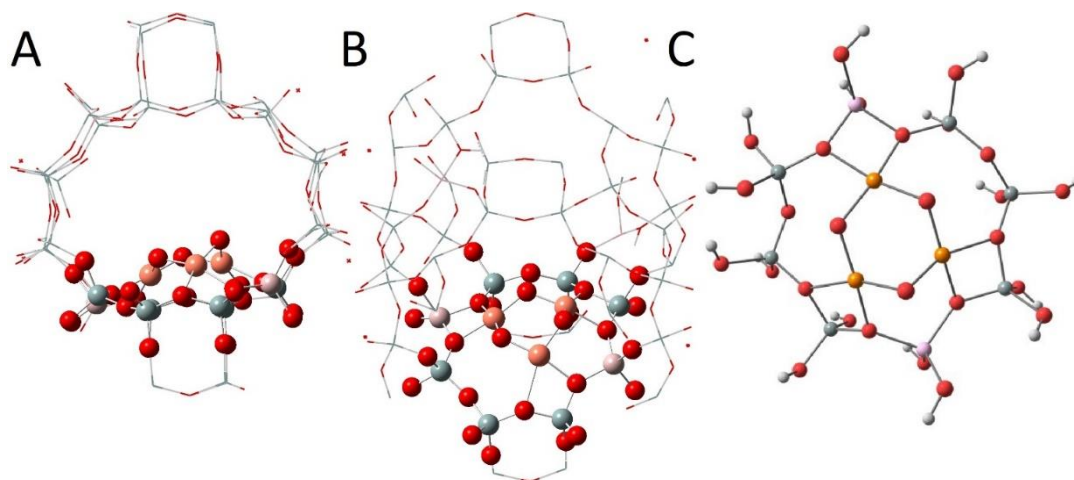


**Figure 4.2: Models for the  $[\text{Cu}_3\text{O}_3]^{2+}$  active site in MOR.** (A) Periodic unit cell showing the immediate environment around  $[\text{Cu}_3\text{O}_3]^{2+}$ . (B) Rotated view of the unit cell to better visualize the location of the active site at the 8MR. (C) Proton-terminated cluster model. H, O, Al, Si and Cu atoms are represented with white, red, light pink, grey and brown spheres, respectively.

The optimized geometries at the PBE/L1 and B3LYP/L1 levels were used for single-point calculations in the Gaussian 16 software package.<sup>[57]</sup> The single-point calculations were performed at the PBE-D3BJ/def2-TZVPP and B3LYP-D3BJ/def2-TZVPP level while using PBE<sup>[51]</sup>/L1- and B3LYP/L1-optimized structures, respectively.<sup>[58-60]</sup> Most reports on copper-exchanged zeolites have used GGA functionals. However, a truncated cluster-model like ours allow us to use the hybrid DFT functionals.<sup>[9-10, 22, 31]</sup>

**4.2.2 Periodic DFT:** The unit cells of the  $[\text{Cu}_3\text{O}_3](\text{H}_2\text{MOR})$  species were initially optimized with Quantum Espresso 6.4.1.<sup>[61-62]</sup> In this structure, two protons from precursor  $\text{H}_4\text{MOR}$  zeolite were replaced with a  $[\text{Cu}_3\text{O}_3]^{2+}$  active site cluster. As noted earlier, this copper-oxo species is placed at the mouth of the 8MR, Figure 4.2. Overall, the  $[\text{Cu}_3\text{O}_3](\text{H}_2\text{MOR})$  structure has a Si/Al ratio of 11. This is very similar to the Si/Al ratio used in several experiments.<sup>[11-12, 14, 40]</sup> All geometry optimizations with periodic DFT were performed by sampling the Brillouin zone at the  $\Gamma$  point while using PBE functional and the D3 dispersion scheme, PBE-D3.<sup>[63]</sup> The ion-core electrons of the computed atoms are described with scalar-relativistic Projector Augmented Wave (PAW) pseudopotentials. Further details of these pseudopotentials and plane wave basis sets are provided in the Supporting Information. We used a kinetic cut-off of 50.0 Ry and a charge density cut-off of 350.0 Ry. Geometries and energies were considered as converged at  $10^{-3}$  Ry/Bohr and  $10^{-6}$  Ry thresholds, respectively. To obtain transition states, we used the climbing-image nudged-elastic

band, CI-NEB method.<sup>[64-65]</sup> 10 images were used between the reactants and products for these reaction steps.

### 4.3 RESULTS AND DISCUSSION

**4.3.1 Mechanism for Methane Activation and Over-Oxidation:** The mechanism for direct HAA from methane by the  $[\text{Cu}_3\text{O}_3]^{2+}$  active site is shown in Figure 4.3. This mechanism progresses via

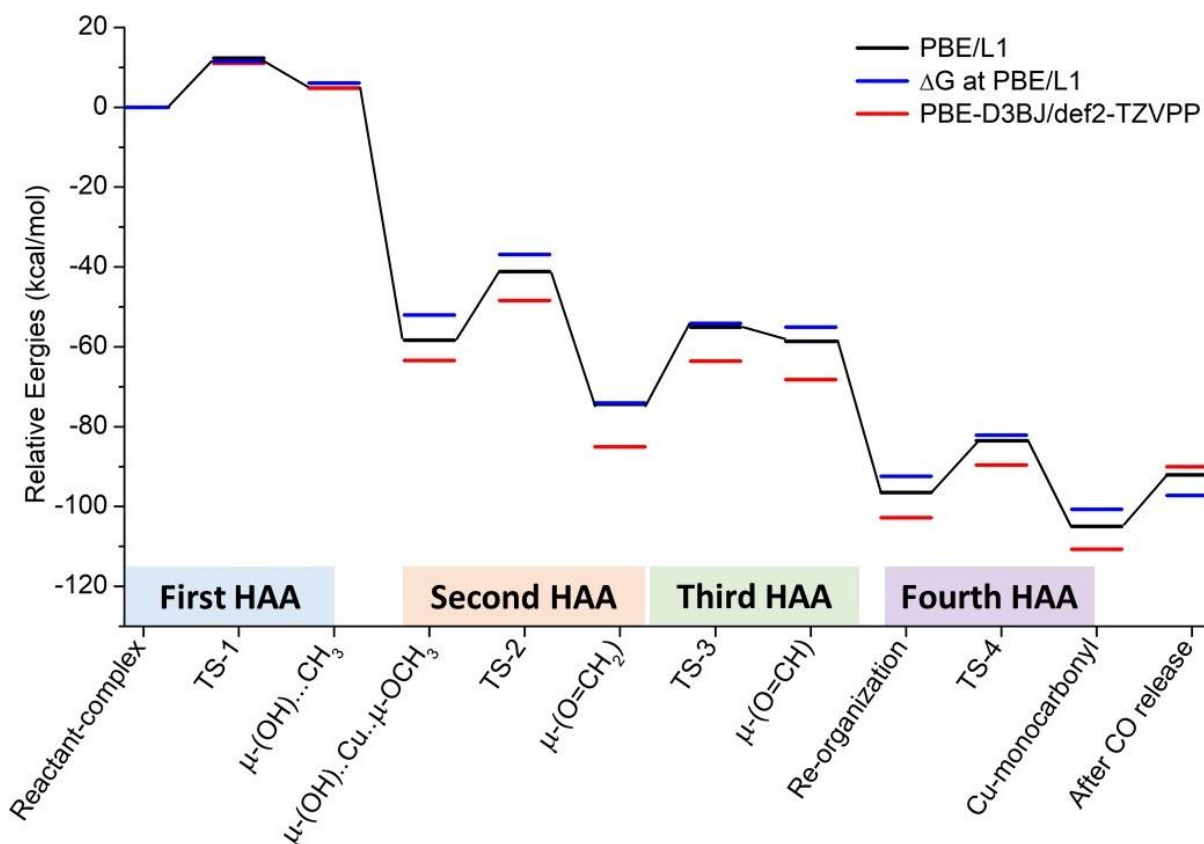


**Figure 4.3: Activation of methane via 4 successive hydrogen atom abstraction (HAA) steps on extra-framework  $[\text{Cu}_3\text{O}_3]^{2+}$  in zeolite MOR.**

a radical-like transition state structure with  $\mu\text{-oxo}\dots\text{H}\dots\text{CH}_3$  character. After activation of the C-H bond, a  $\mu\text{-(OH)}\dots\text{CH}_3$  moiety is formed. At the PBE/L1 level, the barrier for this step is 12.3 kcal/mol. Addition of free-energy corrections bring the barrier to 11.5 kcal/mol. Additionally, formation of the  $\mu\text{-(OH)}\dots\text{CH}_3$  moiety is endothermic by 4.8 kcal/mol based on the electronic energies, or 6.2 kcal/mol based on Gibbs free-energies. The magnitude of the calculated transition state barriers indicate that methane activation is highly facile at the  $[\text{Cu}_3\text{O}_3]^{2+}$  active site. When the results at the PBE/L1 level are compared to those at the PBE- D3BJ/def2-TZVPP level, we see that dispersion effects on the calculated barriers and reaction energies are minor. The barrier for

activation of a methane C-H bond is 11.0 kcal/mol at the PBE-D3BJ/def2-TZVPP level, within 1.3 kcal/mol of the results at the PBE/L1 level. Additionally, the reaction energy for this step is 4.7 kcal/mol at the PBE-D3BJ/def2-TZVPP level, comparable to 4.8 kcal/mol at the PBE/L1 level. The PBE-D3BJ/def2-TZVPP results are presented in Table 4.1. Prior to activation of a C-H bond, methane is only weakly bound to the  $[\text{Cu}_3\text{O}_3]^{2+}$  active site. Indeed, the distance between the H atom of methane and the most reactive  $\mu$ -oxo atom is 2.464 Å, Figure 4.4. The C-H bonds of methane in this weakly-bound complex are 1.101 Å long, same as that of isolated methane, 1.100 Å at the PBE/L1 level. Also, the distances between the nearest copper, Cu, atoms to the  $\mu$ -oxo atom are 1.829 and 1.808 Å. At the transition state, the activated C...H bond is 1.271 Å. This concurs with the direct HAA mechanism and is similar to values obtained for other active site motifs.<sup>[66-68]</sup> The 3 remaining C-H bonds are 1.097 Å long, essentially unchanged from before the reaction. Interestingly the Cu to  $\mu$ -oxo bond distances are now elongated to 1.901 and 1.898 Å. After formation of the methyl radical, the hydrogen atom is directly bound to the  $\mu$ -oxo atom, bond length of 0.995 Å.

**Table 4.1: Calculated reaction energies and free-energies, kcal/mol, obtained at the PBE/L1, PBE-D3BJ/def2-TZVPP and B3LYP-D3BJ/def2-TZVPP levels for the first 4 HAA steps.**

	First HAA			Second HAA		
	TS-1			TS-2		
PBE/L1 $\Delta E$	0.0	12.3	4.8	-58.3	-41.2	-74.3
PBE/L1 $\Delta G$	0.0	11.5	6.1	-52.0	-36.9	-74.1
PBE-D3BJ $\Delta E$	0.0	11.0	4.7	-63.4	-48.4	-85.0
B3LYP-D3BJ $\Delta E$	0.0	4.7	-9.1	-89.1	-63.2	-110.5
	Third HAA			Fourth HAA		
	TS-3			TS-4		
PBE/L1 $\Delta E$	-74.3	-55.1	-58.6	-96.5	-83.5	-105.0
PBE/L1 $\Delta G$	-74.1	-53.1	-55.1	-92.4	-82.1	-100.8
PBE-D3BJ $\Delta E$	-85.0	-63.5	-68.2	-102.8	-89.6	-100.7
B3LYP-D3BJ $\Delta E$	-110.5	-86.0	-101.5	-120.9	-104.0	-131.3

Additionally, the Cu to  $\mu$ -oxo bond distances are now 1.951 and 1.959 Å. These results suggest that methane C-H activation is associated with significant structural changes in the active site. This concurs with the fact that the spin density on the C atom of methane is 0.00, -0.30 and -0.73,



respectively, before C-H activation, at the transition state and in the  $\mu\text{-(OH)}\dots\text{CH}_3$  moiety, Table 4.2. Additionally, the atomic partition of the density<sup>[69-70]</sup> shows that the partial atomic charge on the C atom is -0.16, -0.10 and -0.07 across the C-H activation reaction path. This is consistent with charge transfer between the  $\mu\text{-oxo}$ , C and H atoms involved in the reaction step.

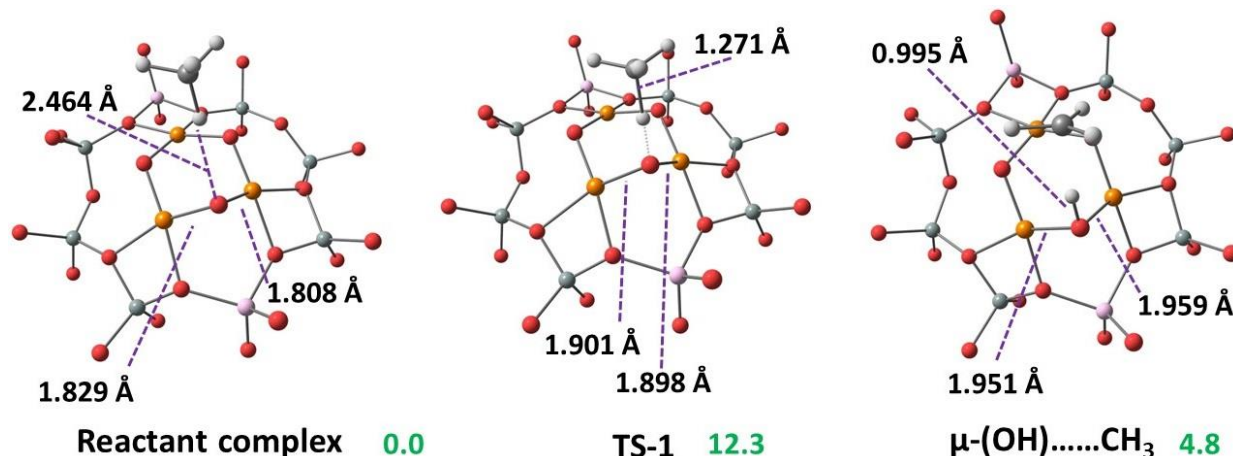


**Figure 4.4:** Species involved in the first HAA step. Terminating protons are omitted for better visibility. Energies and barrier, in kcal/mol and green, at the PBE/L1 level are given relative to the reactant complex.

**Table 4.2:** Partial atomic charges and spin densities on the C atom during the first and second HAA steps.

First HAA Step			
	Reactant Complex	TS-1	$\mu\text{-(OH)}\dots\text{CH}_3$
Charge	-0.16	-0.10	-0.07
Spin density	0.00	-0.30	-0.73
Second HAA Step			
	$\mu\text{-(OH)-Cu-}\mu\text{-(OCH}_3\text{)}$	TS-2	$\mu\text{-(O=CH)}$
Charge	-0.25	-0.02	0.09
Spin density	0.00	0.08	-0.01

As noted earlier, the methyl group of the  $\mu\text{-(OH)}\dots\text{CH}_3$  species is unstable and needs to be stabilized. For the  $[\text{Cu}_3\text{O}_3]^{2+}$  active site, there remains 2 free  $\mu\text{-oxo}$  atoms after methane C-H activation. The dangling methyl group can rebound to either of these. For smaller copper-oxo motifs, like  $[\text{Cu}_2\text{O}]^{2+}$  or  $[\text{Cu-OH}]^+$ , the methyl group will stabilize at other active sites. This would especially be possible at low methane pressures. In Figure 4.3, we show that rebound of the methyl group to a neighboring  $\mu\text{-oxo}$  atom provides a stabilization energy of -63.1 kcal/mol at the PBE/L1 level. At the PBE-D3BJ/def2-TZVPP level, this stabilization energy is -68.2 kcal/mol. Based on these values, it is easy to assume that the  $\mu\text{-(OH)-Cu-}\mu\text{-(OCH}_3\text{)}$  species is highly stable, unreactive

and long-living. This species is significantly more stable than the structures formed when the methyl group rebounds to a copper center.

Interestingly, in Figure 4.5, there remains 1 free  $\mu$ -oxo atom in the  $\mu$ -(OH)-Cu- $\mu$ -(OCH<sub>3</sub>) species.

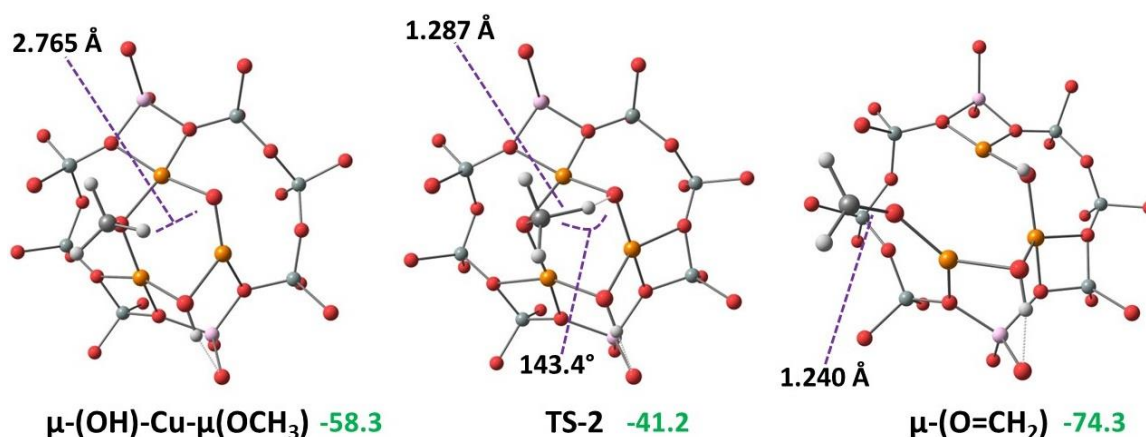


**Figure 4.5:** Species involved in the second HAA step. Energies and barrier, in kcal/mol and green, at the PBE/L1 level are given relative to the reactant complex.

This atom is within 3.221 Å of the carbon atom of the  $\mu$ -(OCH<sub>3</sub>) group. A proton of the  $\mu$ -(OCH<sub>3</sub>) group is within 2.765 Å of the free  $\mu$ -oxo atom. It is thus conceivable that the latter can abstract a hydrogen atom from the  $\mu$ -(OCH<sub>3</sub>) group. This HAA step will lead to the formation of a  $\mu$ -(O=CH<sub>2</sub>) moiety. The  $\mu$ -(O=CH<sub>2</sub>) moiety is reminiscent of adsorbed formaldehyde. Indeed, recent NMR spectroscopic characterizations have revealed the presence of formaldehyde during activation of methane by extra-framework Cu<sup>2+</sup>-based active sites in zeolites.<sup>[71]</sup> At the PBE/L1 level of theory, the barrier for the second HAA step is 17.1 kcal/mol, Figure 4.3. After inclusion of free-energy corrections, this barrier is only 15.1 kcal/mol. At the PBE-D3BJ/def2-TZVPP level, the electronic reaction barrier is also 15.1 kcal/mol. One would expect that this process proceeds rapidly at 200 °C, where methane is generally contacted with zeolites. The only way to avoid this fate would be to stabilize the methyl group as an entity other than the  $\mu$ -(OH)-Cu- $\mu$ -(OCH<sub>3</sub>) species. We also find that this reaction step is strongly exothermic; -16.0 and -21.6 kcal/mol electronic reaction energies at the PBE/L1 and PBE-D3BJ/def2-TZVPP levels respectively; -22.2 kcal/mol Gibbs free-energy at the PBE/L1 level, Figure 4.3. This is likely because of the strong bond between the  $\mu$ -oxo atom and the CH<sub>2</sub> group. Indeed, the O-C bond of the  $\mu$ -(O=CH<sub>2</sub>) moiety is 1.240 Å long. This is compared with 1.444 Å in the  $\mu$ -(OCH<sub>3</sub>) group, prior to the second HAA. Interestingly, the second HAA step results in cleavage of a Cu-O bond, revealing that over-oxidation likely leads to significant disorder in the [Cu<sub>3</sub>O<sub>3</sub>]<sup>2+</sup> active site, Figure 4.5.

At the transition state, the separated C...H bond is 1.287 Å long, similar to the first HAA step. The C...H...μ-oxo bond angle is 143.4°. This is significantly more obtuse than for the first HAA, 177.4 ° in Figure 4.4. Indeed, there is a need for greater structural deformation in order to reach the transition state for the second HAA step than for the first. This likely explains why the barrier for the second HAA is 3.6-4.8 kcal/mol higher than for the first HAA.

By a similar token, the CH<sub>2</sub> group formed after the second HAA can be further oxidized via subsequent HAA steps. In a real zeolite, there are likely other μ-oxo atoms at nanometric copper-oxo sites for these HAA steps. And it is likely that subsequent HAA steps will have similar apparent activation energies as the first two. However, in our [Cu<sub>3</sub>O<sub>3</sub>]<sup>2+</sup> cluster model, there are no more μ-oxo atoms, Figure 4.5. Indeed, after the first 2 HAA steps, we are left with 2 μ-OH groups. For this reason, we considered HAA from the μ-(O=CH<sub>2</sub>) moiety to a μ-OH group. The third HAA step leads to the formation of a μ-(O=CH) group as well as adsorbed water, Figure 4.6. The calculated activation energy for this third HAA step is 19.3 kcal/mol at the PBE/L1 level and 21.5 kcal/mol at the PBE-D3BJ/def2-TZVPP level.

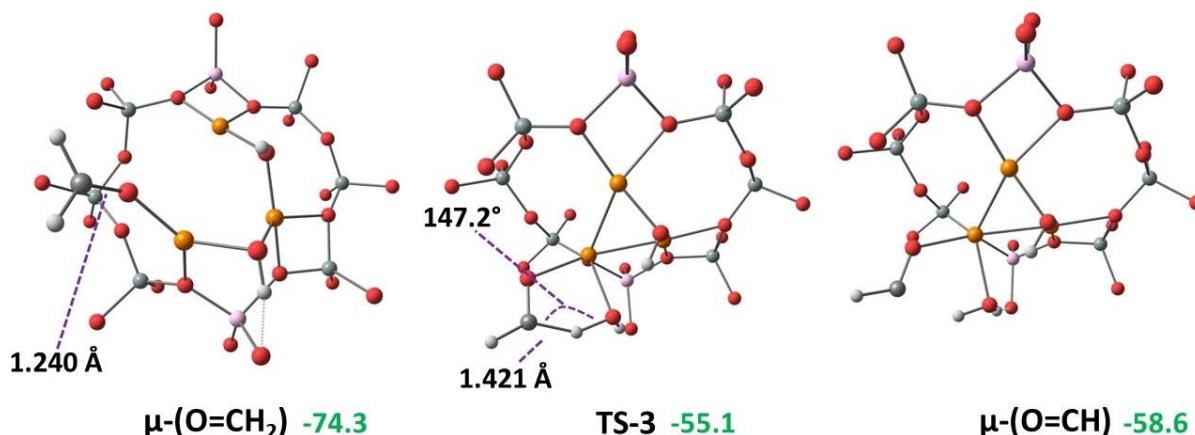


**Figure 4.6: Species involved in the third HAA step. The structures of TS-3 and μ-(O=CH) group are slightly rotated to better depict the HAA. Energies and barrier, in kcal/mol and green, at the PBE/L1 level are given relative to the reactant complex.**

The activation Gibbs free energy is 18.3 kcal/mol at the PBE/L1 level, Figure 4.3. The magnitude of this barrier suggests rapid conversion of the μ-(O=CH<sub>2</sub>) moiety to the μ-(O=CH) group at 200 °C. However, this step is endothermic by 16.3 kcal/mol at the PBE/L1 level, Figure 4.3. In any case, the μ-(oxo=CH) group is 58.6 kcal/mol more stable than the starting reactant complex at the PBE/L1 level, Figure 4.3. The separated C...H distance at the transition state of the third HAA is 1.421 Å, significantly longer than the cases for the first and second HAA steps. The C...H...μ-

OH angle is  $147.2^\circ$ , close to that of the second HAA step. However, examination of the partial atomic charges and spin densities reveals no change across the third HAA step. This is clearly different from the first 2 HAA steps. These differences suggest that the third HAA step has a much later transition state with greater  $\text{H}\cdots\mu\text{-O}$  character than the first two steps. As such, the barrier for the third HAA step is higher than the first two.

It is interesting to examine closely the structure of the  $\mu\text{-(O=CH)}$  group formed after the third HAA step. The first coordination spheres of the C and O atoms in this group are not fully satisfied, Figure 4.6. Based on this, a reorganization can occur to satisfy the coordination for C, Figure 4.7. At the PBE/L1 level, this reorganization stabilizes the whole system by 37.9 kcal/mol. The structure formed from this reorganization has a  $\mu\text{-C(H)=O}$  character, Figure 4.7, and is 96.5 kcal/mol more stable than the reactant complex at the PBE/L1 level, Figure 4.3. Additionally, this structure is primed for a fourth HAA transfer to the adjacent  $\mu\text{-OH}$  group. This is because the distance between the proton of the CH moiety and the  $\mu\text{-OH}$  group is 2.280 Å, significantly shorter than the situations for the initial 3 steps. Indeed, the fourth HAA step has a barrier of only 13.0 and 13.2 kcal/mol at the PBE/L1 and PBE-D3BJ/def2-TZVPP levels, respectively.

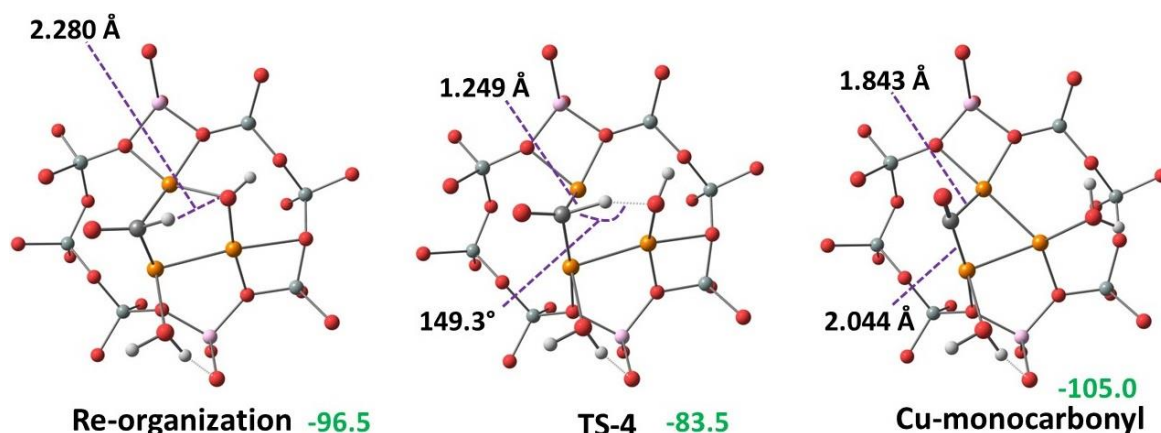


**Figure 4.7: Species involved in the fourth HAA step. Energies and barrier, in kcal/mol and green, at the PBE/L1 level are given relative to the reactant complex.**

The Gibbs free-energy barrier is 10.2 kcal/mol at the PBE/L1 level, Figure 4.3. At the transition state, the separated  $\text{C}\cdots\text{H}$  bond is 1.249 Å long, commensurate with the first 2 HAA steps. The  $\text{C}\cdots\text{H}\cdots\mu\text{-OH}$  bond angle is  $149.3^\circ$ , similar to those of the second and third HAA steps. This reaction step is also exothermic by 8.3 kcal/mol. The 4 HAA steps bring the overall reaction energy to -105.0 and -110.7 kcal/mol at the PBE/L1 and PBE-D3BJ/def2-TZVPP levels respectively. At

the PBE/L1 level, the Gibbs free-energy for all 4 steps is -100.7 kcal/mol. Lastly, these HAA steps lead to the formation of a CO moiety bound to Cu centers, Figure 4.7. Thus, formation of Cu-monocarbonyls is an outcome of methane over-oxidation, according to the mechanism presented in Figure 4.3.

The Cu-C distances in the monocarbonyl species are 1.843 and 2.044 Å, Figure 4.7. Interestingly, calculations at the PBE/L1 level show that release of CO from the Cu-monocarbonyl species costs 12.9 kcal/mol, Figure 4.3. Indeed, the Gibbs free-energy for CO release is only 3.4 kcal/mol. Overall, the mechanism in Figure 4.3 describes the formation of adsorbed formaldehyde, adsorbed water, Cu-monocarbonyls and gaseous CO.

**4.3.2 Formation of Formates:** In this section, we consider the pathway to formation of formates. We start at the  $\mu$ -(O=CH) species, Figure 4.6. In forming the Cu-monocarbonyl, this group reorganizes such that the C atom becomes bonded to two Cu centers, Figure 4.7. There is however an alternative path towards stabilization for the  $\mu$ -(O=CH) species. The  $\mu$ -(O=CH) moiety can simply be rotated to be close to the adjacent  $\mu$ -(OH) group. This gives 2 possibilities. The first involves formation of molecularly-adsorbed formic acid bound to a Cu center in a monodentate fashion, Figure 4.8. Notably, desorption of formic acid from the Cu cluster costs 11.9 kcal/mol at the PBE/L1 level. However, the Gibbs free energy for formic acid desorption is -2.6 kcal/mol. This indicates that formic acid can be easily desorbed from the monodentate species shown in Figure 4.8. The second option resembles a bidentate formate.

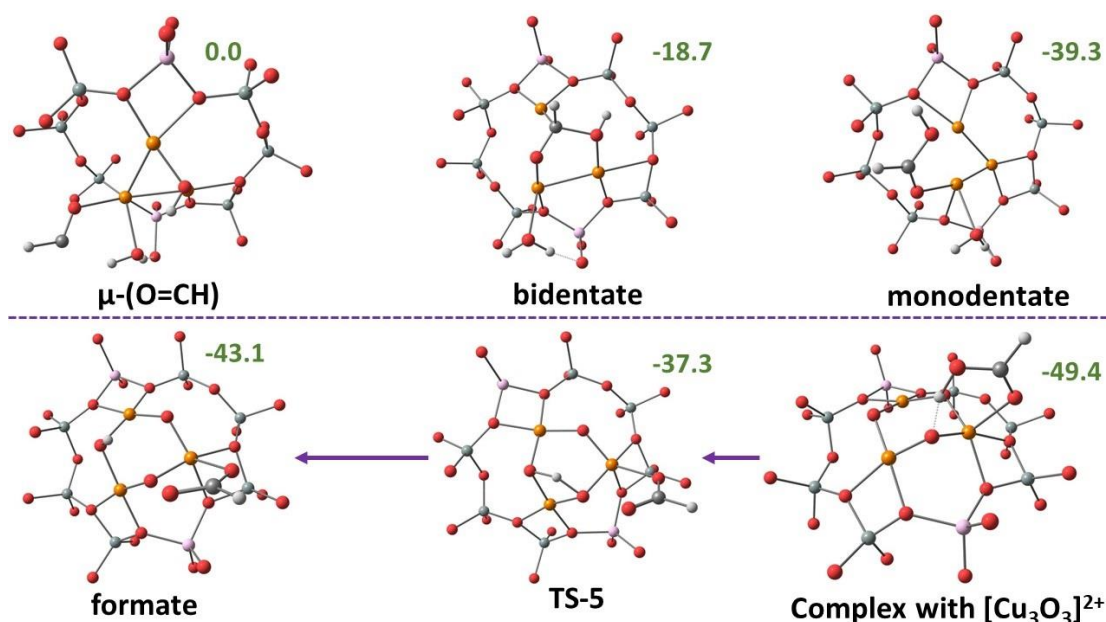




**Figure 4.8: Conversion of the  $\mu$ -(O=CH) group to formic acid and formates. Reaction energies, in kcal/mol, at the PBE/L1 level of theory are given relative to the  $\mu$ -(O=CH) structure.**

The desorbed formic acid can be adsorbed at another  $[\text{Cu}_3\text{O}_3]^{2+}$  site, Figure 4.8. The binding energy is -22.0 kcal/mol and the binding Gibbs free energy is -10.0 kcal/mol, both at the PBE/L1 level. Interestingly, the conformation for the adsorbed formic acid is such that a proton can be readily abstracted by a  $\mu$ -oxo atom of  $[\text{Cu}_3\text{O}_3]^{2+}$ . Thus, adsorbed formic acid is likely a precursor to formation of  $\text{CO}_2$ . A first HAA step leads to formation of a Cu-bound monodentate formate moiety. The transition state barrier for this step is 12.0 kcal/mol and the reaction energy is +6.2 kcal/mol.

**4.3.3 Zeolite Confinement Effects:** Several reports have indicated that confinement effects from the zeolite framework can significantly affect the methane C-H activation energy.<sup>[72-73]</sup> In general, most of these reports have shown that the framework contributes to reducing the activation energy. Towards this end, we examined the first 2 HAA steps with periodic DFT using unit cells of MOR. The calculated path for these HAA steps from periodic DFT are compared to results of our cluster model in Figure 4.9.

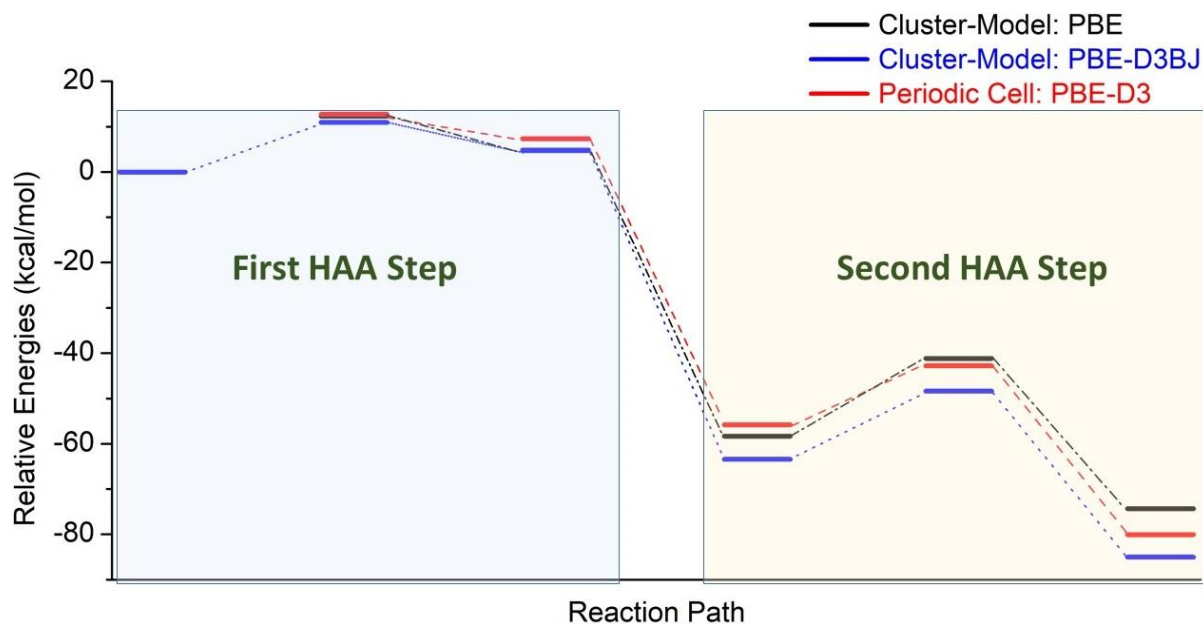


**Figure 4.9: Comparison of calculated reaction energies and barriers for the first two HAA steps with cluster-model and periodic DFT calculations.**

The barrier for the first HAA step is 12.7 kcal/mol from periodic DFT calculations with PBE-D3, Figure 4.9. This agrees quite well with 12.3 and 11.0 kcal/mol from cluster-model calculations

with PBE and PBE-D3BJ, respectively, Figure 4.3. For the second HAA step, the barriers from the cluster-model calculations are 17.1 and 15.1 kcal/mol with PBE and PBE-D3BJ, respectively. These are to be compared with 13.0 kcal/mol from the periodic DFT calculations. Overall, the cluster-model calculations provide a similar qualitative picture as the calculations with periodic boundary conditions. The magnitude of the barriers computed at both levels indicate that the HAA steps will be facile at 200 °C. The confinement effects due to the zeolite framework appear to be smaller than the effects due to choice of dispersion effects and basis sets. This makes sense as our cluster model includes the first and second-coordination spheres around the  $[\text{Cu}_3\text{O}_3]^{2+}$  active site, ensuring adequate description of its reactivity.

**4.3.4 Impact of the Exchange-Correlation Density Functional:** Thus far, we have seen how sequential HAA steps lead to formation of adsorbed formaldehyde, Cu-monocarbonyls, adsorbed water, formates and gaseous CO. These reaction steps were examined with structures optimized with the PBE functional. We also have described the impact of dispersion effects, PBE-D3BJ, on the calculated results, Figures 4.3 and 4.9. However, one could readily question the dependence of the reaction energies and barriers on the choice of exchange-correlation functional. In Table 4.1, we present results obtained at the PBE-D3BJ/def2-TZVPP and B3LYP-D3BJ/def2-TZVPP levels. We show all relative energies from the reactant complex to formation of the Cu-monocarbonyl. In comparing PBE-D3BJ and B3LYP-D3BJ, we see that the barrier for the first HAA is rather low for the latter. Thus, B3LYP-D3BJ provides a rather unusual stability for the TS-1 structure. At TS-1, the activated C....H bond is 1.271 Å in the PBE structure but 1.204 Å in the B3LYP structure. Similarly, the  $\mu\text{-O} \cdots \text{H}$  distance is 1.288 Å with PBE but 1.370 Å with B3LYP. Thus, structural differences cause massive differences when comparing reaction energies and barriers provided by GGA and hybrid DFT functionals. With PBE-D3BJ, the highest barrier is 21.5 kcal/mol, for the third HAA step. Thus, PBE-D3BJ predicts that all 4 HAA steps are facile at 200 °C. However, with B3LYP-D3BJ, the highest barrier is 25.9 kcal/mol, for the second HAA step. Notably, the Gibbs free-energy correction for this step is about -1.1 kcal/mol at 200 °C. This would suggest reasonable rates for all methane over-oxidation steps at 200 °C. Thus to avoid these facile over-oxidation steps, Figures 4.3 and 4.8, copper-exchanged zeolites must contain traps or scavengers that rapidly stabilize the methyl group away from the active sites.

## 4.4 CONCLUSIONS

Extra-framework  $[\text{Cu}_3\text{O}_3]^{2+}$  is one of the active site motifs invoked to describe direct conversion

of methane to methanol in copper-exchanged zeolites. In the step-wise methane-to-methanol conversion (MMC) process, methane is reacted with these copper-oxo sites to form kinetically-trapped methoxy groups which are subsequently extracted as methanol with solvents. However, recent experimental investigations indicate that the methoxy groups are located at the zeolite framework, rather than at the copper-oxo active sites. These observations necessitate a quantitative understanding of why the methoxy groups are not located at the copper-oxo sites. To rationalize these findings, we used density functional theory (DFT) calculations to show how methane over-oxidation at copper-oxo active sites leads to various oxygenate species (in the absence of molecular oxygen).

Overall, we:

- 1) Used the  $[\text{Cu}_3\text{O}_3]^{2+}$  model as it presents several  $\mu$ -oxo atoms for interaction with methane. If we had used smaller copper-oxo clusters, like  $[\text{Cu}_2\text{O}]^{2+}$  or  $[\text{Cu-OH}]^+$ , it would have been necessary to consider hydrogen atom abstraction, HAA, at multiple active sites. This would require adequate description of the diffusion of  $\text{CH}_x$  ( $x = 1-4$ ) species between active sites. The choice of  $[\text{Cu}_3\text{O}_3]^{2+}$  notwithstanding, we expect our general conclusions to be relevant for all copper-oxo active sites.
- 2) Found that activation of a methane C-H bond at a  $\mu$ -oxo atom of  $[\text{Cu}_3\text{O}_3]^{2+}$  is quite facile. This direct HAA step leads to the formation of a  $\mu$ -(OH)... $\text{CH}_3$  moiety. The separated methyl group can be stabilized at the active site or away from the active site in the zeolite framework. Our calculations reveal that over-oxidation occurs if the methyl is stabilized at the active site. The intermediate reaction steps in the over-oxidation pathway are all facile and are nearly all exothermic. Over-oxidation leads to copper-bound monocarbonyls, gaseous CO, adsorbed formaldehyde, adsorbed water and formates.
- 3) Conclude that although the step-wise process of MMC spatially and temporally separates methane activation and active site regeneration, some over-oxidation is bound to happen. The oxo-sites of copper-oxo clusters are quite capable of over-oxidizing methane. As such, methanol selectivity cannot reach 100%. Our results also show that high methanol selectivities in MMC are made possible only by the presence of scavengers that trap the methyl group formed during the first HAA step. Without such scavengers, copper-oxo sites will actively over-oxidize methane. Recent experimental results suggest that Brønsted acid sites are the traps needed to avoid such over-oxidation. Indeed, short diffusion paths between these traps and



copper-oxo sites would be beneficial for methanol selectivity. Additionally, the necessity for high copper content must be balanced with necessity of large diffusion paths between the nanometric active sites. These findings also allow us to conclude that methanol selectivity for  $[\text{Cu}_3\text{O}_3]^{2+}$  will always be substantially lower than those of  $[\text{Cu}_2\text{O}]^{2+}$  or  $[\text{Cu-OH}]^+$ .

## REFERENCES

- [1] J. H. Lunsford, *Catal. Today* **2000**, *63*, 165-174.
- [2] H. Schulz, *Appl. Catal. A-Gen.* **1999**, *186*, 3-12.
- [3] M. H. Mahyuddin, R. V. Belosludov, M. Khazaei, H. Mizuseki, Y. Kawazoe, *J. Phys. Chem. C* **2011**, *115*, 23893-23901.
- [4] T. Sheppard, C. D. Hamill, A. Goguet, D. W. Rooney, J. M. Thompson, *Chem. Commun.* **2014**, *50*, 11053-11055.
- [5] G. A. Olah, *Angew. Chem. Int. Edit.* **2005**, *44*, 2636-2639.
- [6] E. M. C. Alayon, M. Nachtegaal, A. Bodi, M. Ranocchiari, J. A. van Bokhoven, *Phys. Chem. Chem. Phys.* **2015**, *17*, 7681-7693.
- [7] A. A. Arvidsson, V. P. Zhdanov, P. A. Carlsson, H. Gronbeck, A. Hellman, *Catal. Sci. Technol.* **2017**, *7*, 1470-1477.
- [8] L. Burnett, M. Rysakova, K. Wang, J. Gonzalez-Carballo, R. P. Tooze, F. R. Garcia-Garcia, *Appl. Catal. A-Gen.* **2019**, *587*, 117272.
- [9] N. K. Dandu, O. Adeyiga, D. Panthi, S. A. Bird, S. O. Odoh, *J. Comput. Chem.* **2018**, *39*, 2667-2678.
- [10] N. K. Dandu, J. A. Reed, S. O. Odoh, *J. Phys. Chem. C* **2018**, *122*, 1024-1036.
- [11] S. Grundner, W. Luo, M. Sanchez-Sanchez, J. A. Lercher, *Chem. Commun.* **2016**, *52*, 2553-2556.
- [12] S. Grundner, M. A. C. Markovits, G. Li, M. Tromp, E. A. Pidko, E. J. M. Hensen, A. Jentys, M. Sanchez-Sanchez, J. A. Lercher, *Nat. Commun.* **2015**, *6*, 7546.
- [13] C. Hammond, M. M. Forde, M. H. Ab Rahim, A. Thetford, Q. He, R. L. Jenkins, N. Dimitratos, J. A. Lopez-Sanchez, N. F. Dummer, D. M. Murphy, A. F. Carley, S. H. Taylor, D. J. Willock, E. E. Stangland, J. Kang, H. Hagen, C. J. Kiely, G. J. Hutchings, *Angew. Chem. Int. Edit.* **2012**, *51*, 5129-5133.
- [14] T. Ikuno, S. Grundner, A. Jentys, G. N. Li, E. Pidko, J. Fulton, M. Sanchez-Sanchez, J. A. Lercher, *J. Phys. Chem. C* **2019**, *123*, 8759-8769.
- [15] B. Ipek, R. F. Lobo, *Chem. Commun.* **2016**, *52*, 13401-13404.
- [16] A. R. Kulkarni, Z. J. Zhao, S. Siahrostami, J. K. Norskov, F. Studt, *Catal. Sci. Technol.* **2018**, *8*, 114-123.
- [17] G. N. Li, P. Vassilev, M. Sanchez-Sanchez, J. A. Lercher, E. J. M. Hensen, E. A. Pidko, *J. Catal.* **2016**, *338*, 305-312.
- [18] M. H. Mahyuddin, A. Staykov, Y. Shiota, K. Yoshizawa, *ACS Catal.* **2016**, *6*, 8321-8331.
- [19] K. Narsimhan, K. Iyoki, K. Dinh, Y. Roman-Leshkov, *ACS Cent. Sci.* **2016**, *2*, 424-429.
- [20] M. B. Park, E. D. Park, W. S. Ahn, *Front. Chem.* **2019**, *7*, 514.
- [21] B. E. R. Snyder, M. L. Bols, R. A. Schoonheydt, B. F. Sels, E. I. Solomon, *Chem. Rev.* **2018**, *118*, 2718-2768.
- [22] K. D. Vogiatzis, G. N. Li, E. J. M. Hensen, L. Gagliardi, E. A. Pidko, *J. Phys. Chem. C* **2017**, *121*, 22295-22302.

- [23] J. S. Woertink, P. J. Smeets, M. H. Groothaert, M. A. Vance, B. F. Sels, R. A. Schoonheydt, E. I. Solomon, *P Natl. Acad. Sci. USA* **2009**, *106*, 18908-18913.
- [24] Z. J. Zhao, A. Kulkarni, L. Vilella, J. K. Norskov, F. Studt, *ACS Catal.* **2016**, *6*, 3760-3766.
- [25] A. V. Kucherov, A. A. Slinkin, *Zeolites* **1986**, *6*, 175-180.
- [26] M. Dyballa, K. Thorshaug, D. K. Pappas, E. Borfecchia, K. Kvande, S. Bordiga, G. Berlier, A. Lazzarini, U. Olsbye, P. Beato, S. Svelle, B. Arstad, *ChemCatChem* **2019**, *11*, 5022-5026.
- [27] P. Tomkins, M. Ranocchiari, J. A. van Bokhoven, *Accounts Chem. Res.* **2017**, *50*, 418-425.
- [28] G. Brezicki, J. D. Kammert, T. B. Gunnoe, C. Paolucci, R. J. Davis, *ACS Catal.* **2019**, *9*, 5308-5319.
- [29] M. H. Groothaert, P. J. Smeets, B. F. Sels, P. A. Jacobs, R. A. Schoonheydt, *J. Am. Chem. Soc.* **2005**, *127*, 1394-1395.
- [30] D. K. Pappas, A. Martini, M. Dyballa, K. Kvande, S. Teketel, K. A. Lomachenko, R. Baran, P. Glatzel, B. Arstad, G. Berlier, C. Lamberti, S. Bordiga, U. Olsbye, S. Svelle, P. Beato, E. Borfecchia, *J. Am. Chem. Soc.* **2018**, *140*, 15270-15278.
- [31] K. Curtis, D. Panthi, S. O. Odoh, *Inorg. Chem.* **2021**, *60*, 1149-1159.
- [32] A. A. Kolganov, A. A. Gabrienko, I. Y. Chernyshov, A. G. Stepanov, E. A. Pidko, *Phys. Chem. Chem. Phys.* **2020**, *22*, 24004-24013.
- [33] A. A. Kolganov, A. A. Gabrienko, S. A. Yashnik, E. A. Pidko, A. G. Stepanov, *J. Phys. Chem. C* **2020**, *124*, 6242-6252.
- [34] K. Capelle, *Braz. J. Phys.* **2006**, *36*, 1318-1343.
- [35] A. J. Cohen, P. Mori-Sanchez, W. T. Yang, *Chem. Rev.* **2012**, *112*, 289-320.
- [36] J. P. Perdew, A. Ruzsinszky, L. A. Constantin, J. W. Sun, G. I. Csonka, *J. Chem. Theory Comput.* **2009**, *5*, 902-908.
- [37] W. M. Meier, *Zeitschrift für Kristallographie* **1961**, *115*, 439-450.
- [38] A. Alberti, P. Davoli, G. Vezzolini, *Zeitschrift für Kristallographie - Crystalline Materials* **1986**, *175*, 249-256.
- [39] M. Dyballa, D. K. Pappas, K. Kvande, E. Borfecchia, B. Arstad, P. Beato, U. Olsbye, S. Svelle, *ACS Catal.* **2019**, *9*, 365-375.
- [40] Y. Kim, T. Y. Kim, H. Lee, J. Yi, *Chem. Commun.* **2017**, *53*, 4116-4119.
- [41] M. H. Mahyuddin, T. Tanaka, Y. Shiota, A. Staykov, K. Yoshizawa, *ACS Catal.* **2018**, *8*, 1500-1509.
- [42] M. H. Mahyuddin, T. Tanaka, A. Staykov, Y. Shiota, K. Yoshizawa, *Inorg. Chem.* **2018**, *57*, 10146-10152.
- [43] M. A. Newton, A. J. Knorpp, V. L. Sushkevich, D. Palagin, J. A. van Bokhoven, *Chem. Soc. Rev.* **2020**, *49*, 1449-1486.
- [44] M. B. Park, S. H. Ahn, A. Mansouri, M. Ranocchiari, J. A. van Bokhoven, *ChemCatChem* **2017**, *9*, 3705-3713.
- [45] V. L. Sushkevich, J. A. van Bokhoven, *Catal. Sci. Technol.* **2020**, *10*, 382-390.
- [46] J. Zheng, I. Lee, E. Khramenkova, M. Wang, B. Peng, O. Y. Gutierrez, J. L. Fulton, D. M. Camaioni, R. Khare, A. Jentys, G. L. Haller, E. A. Pidko, M. Sanchez-Sanchez, J. A. Lercher, *Chem-Eur. J.* **2020**, *26*, 7563-7567.
- [47] D. N. Laikov, *Chem. Phys. Lett.* **2005**, *416*, 116-120.
- [48] D. N. Laikov, Y. A. Ustynyuk, *Russ. Chem. Bull.* **2005**, *54*, 820-826.
- [49] A. D. Becke, *J. Chem. Phys.* **1993**, *98*, 5648-5652.
- [50] C. T. Lee, W. T. Yang, R. G. Parr, *Phys. Rev. B* **1988**, *37*, 785-789.

- [51] J. P. Perdew, K. Burke, M. Ernzerhof, *Phys. Rev. Lett.* **1996**, 77, 3865-3868.
- [52] P. J. Stephens, F. J. Devlin, C. F. Chabalowski, M. J. Frisch, *J. Phys. Chem.* **1994**, 98, 11623-11627.
- [53] A. D. Becke, *Physical Review A* **1988**, 38, 3098-3100.
- [54] D. N. Laikov, *Theor. Chem. Acc.* **2019**, 138, 40.
- [55] D. N. Laikov, *J. Chem. Phys.* **2020**, 153, 114121.
- [56] K. G. Dyall, *J. Chem. Phys.* **1994**, 100, 2118-2127.
- [57] M. J. T. Frisch, G.W.; Schlegel, H.B.; Scuseria, G.E.; Robb, M.A.; Cheeseman, J.R.; Scalmani, G.; Barone, V.; Petersson, G. A.; Nakatsuji, H. , et al. Gaussian, Inc. , Wallingford, CT, **2016**.
- [58] A. D. Becke, E. R. Johnson, *J. Chem. Phys.* **2005**, 123, 154101.
- [59] S. Grimme, S. Ehrlich, L. Goerigk, *J. Comput. Chem.* **2011**, 32, 1456-1465.
- [60] E. R. Johnson, A. D. Becke, *J. Chem. Phys.* **2005**, 123, 174104.
- [61] P. Giannozzi, O. Andreussi, T. Brumme, O. Bunau, M. Buongiorno Nardelli, M. Calandra, R. Car, C. Cavazzoni, D. Ceresoli, M. Cococcioni, N. Colonna, I. Carnimeo, A. Dal Corso, S. de Gironcoli, P. Delugas, R. A. DiStasio, A. Ferretti, A. Floris, G. Fratesi, G. Fugallo, R. Gebauer, U. Gerstmann, F. Giustino, T. Gorni, J. Jia, M. Kawamura, H. Y. Ko, A. Kokalj, E. Küçükbenli, M. Lazzeri, M. Marsili, N. Marzari, F. Mauri, N. L. Nguyen, H. V. Nguyen, A. Otero-de-la-Roza, L. Paulatto, S. Poncé, D. Rocca, R. Sabatini, B. Santra, M. Schlipf, A. P. Seitsonen, A. Smogunov, I. Timrov, T. Thonhauser, P. Umari, N. Vast, X. Wu, S. Baroni, *J. Phys-Condens. Mat.* **2017**, 29, 465901.
- [62] P. Giannozzi, S. Baroni, N. Bonini, M. Calandra, R. Car, C. Cavazzoni, D. Ceresoli, G. L. Chiarotti, M. Cococcioni, I. Dabo, A. Dal Corso, S. de Gironcoli, S. Fabris, G. Fratesi, R. Gebauer, U. Gerstmann, C. Gougoussis, A. Kokalj, M. Lazzeri, L. Martin-Samos, N. Marzari, F. Mauri, R. Mazzarello, S. Paolini, A. Pasquarello, L. Paulatto, C. Sbraccia, S. Scandolo, G. Sclauzero, A. P. Seitsonen, A. Smogunov, P. Umari, R. M. Wentzcovitch, *J. Phys-Condens. Mat.* **2009**, 21, 395502.
- [63] S. Grimme, J. Antony, S. Ehrlich, H. Krieg, *J. Chem. Phys.* **2010**, 132, 154104.
- [64] G. Henkelman, B. P. Uberuaga, H. Jónsson, *J. Chem. Phys.* **2000**, 113, 9901-9904.
- [65] H. Jónsson, G. Mills, K. W. Jacobsen, in *Classical and Quantum Dynamics in Condensed Phase Simulations*, pp. 385-404.
- [66] J. T. Groves, G. A. McClusky, *J. Am. Chem. Soc.* **1976**, 98, 859-861.
- [67] J. T. Groves, M. Vanderpuy, *J. Am. Chem. Soc.* **1976**, 98, 5290-5297.
- [68] M. H. Mahyuddin, Y. Shiota, A. Staykov, K. Yoshizawa, *Inorg. Chem.* **2017**, 56, 10370-10380.
- [69] I. Mayer, *Simple theorems, proofs, and derivations in quantum chemistry*, Kluwer Academic/Plenum Publishers, New York, **2003**.
- [70] I. Mayer, *J. Comput. Chem.* **2007**, 28, 204-221.
- [71] V. L. Sushkevich, R. Verel, J. A. van Bokhoven, *Angew. Chem. Int. Edit.* **2020**, 59, 910-918.
- [72] F. Goltl, C. Michel, P. C. Andrikopoulos, A. M. Love, J. Hafner, I. Hermans, P. Sautet, *ACS Catal.* **2016**, 6, 8404-8409.
- [73] M. H. Mahyuddin, A. Staykov, Y. Shiota, M. Miyanishi, K. Yoshizawa, *ACS Catal.* **2017**, 7, 3741-3751.

## CHAPTER 5. COPPER OXO ACTIVE SITES FOR METHANE C-H ACTIVATION IN ZEOLITES: MOLECULAR UNDERSTANDING OF IMPACT OF METHANE HYDROXYLATION ON UV-VIS SPECTRA

Olajumoke Adeyiga, Olabisi Suleiman and Samuel O. Odoh\*

Department of Chemistry, University of Nevada Reno, 1664 N. Virginia Street, Reno, NV  
89557-0216

“Reprinted (adapted) with permission from *Inorganic Chemistry*, 2021, 60, 12, 8489-8499.

Copyright (2021) American Chemical Society”

**ABSTRACT:** Here, we analyze changes in the optical spectra of activated copper-exchanged zeolites during methane activation with Tamm-Dancoff time-dependent density functional theory, TDA-DFT, while using the  $\omega$ B2PLYP functional. Two active sites,  $[\text{Cu}_2\text{O}]^{2+}$  and  $[\text{Cu}_3\text{O}_3]^{2+}$ , were studied. For  $[\text{Cu}_2\text{O}]^{2+}$ , the  $22700\text{ cm}^{-1}$  peak is associated with  $\mu$ -oxo  $2p \rightarrow \text{Cu } 3d/4s$  charge transfer. Of the  $[\text{Cu}_2\text{O}]^{2+}$  methane C-H activation intermediates that we examined, only  $[\text{Cu}-\text{O}(\text{H})(\text{H})-\text{Cu}]$  and  $[\text{Cu}-\text{O}(\text{H})(\text{CH}_3)-\text{Cu}]$  have spectra that match experimental observations. After methane activation, the  $\mu$ -oxo  $2p$  orbitals lose two electrons and become hybridized with methanol C  $2p$  orbitals and/or H  $1s$  orbitals. The frontier unoccupied orbitals become more Cu  $4s/4p$  Rydberg-like, reducing overlap with occupied orbitals. These effects cause the disappearance of the  $22700\text{ cm}^{-1}$  peak. For  $[\text{Cu}_3\text{O}_3]^{2+}$ , the exact structures of the species formed after methane activation are unknown. Thus, we considered 8 possible structures. Several of these provide significant decrease in intensity near  $23000\text{--}38000\text{ cm}^{-1}$ , as seen experimentally. Notably, these species involve either rebound of the separated methyl to a  $\mu$ -oxo atom or its remote stabilization at a Brønsted acid site in exchange for the acidic proton. These spectral changes are caused by the same mechanism seen in  $[\text{Cu}_2\text{O}]^{2+}$  and are likely responsible for the observed reduced intensities near  $23000\text{--}38000\text{ cm}^{-1}$ . Thus, TDA-DFT calculations with  $\omega$ B2PLYP provide molecular-level understanding of the evolution of copper-oxo active sites during methane-to-methanol conversion.

## 5.1 INTRODUCTION

Methane in natural gas is a source of energy and a starting point for making various chemical intermediates.<sup>1,2</sup> However, due to the expensive nature of storing and transporting natural gas, there is great interest in the development of cheap and environmentally friendly approaches to convert methane to methanol.<sup>3</sup> This conversion of methane to a liquid derivative is one of the holy grails of hydrocarbon chemistry and chemical catalysis. A critical challenge is balancing the requirement of high temperatures or highly reactive substrates to activate the stable methane C-H bond while preventing over-oxidation to species like CO<sub>2</sub> or CO. Interestingly, copper-exchanged zeolites are one of the most exciting species for achieving this conversion at moderate temperatures, albeit in a stoichiometric, rather than catalytic fashion.<sup>4-7</sup> Thus, there has been great interest in understanding the properties of these zeolites. Specifically, there is interest in understanding the nature of the copper-oxo active sites as well as the impact of the zeolite framework's second coordination sphere on methane-to-methanol conversion.<sup>8,9</sup> This has led to many detailed experimental characterizations of the copper-exchanged zeolites, with great interest in the evolution of their properties during the step-wise conversion of methane to methanol. Spectroscopic techniques like X-ray diffraction, NMR, EPR, IR and resonant Raman have been extensively used to study copper-exchanged zeolites. Additionally, UV-Vis/NIR spectroscopy has been used to study the evolution of the copper-oxo active sites during their activation and reaction with methane.<sup>10-26</sup> By activation, we mean high-temperature processes for forming the copper-oxo active sites from Cu<sup>2+</sup> ions that are typically introduced into the zeolite by ion-exchange methods. In many areas of advanced chemistry, it is common to use quantum-mechanical computational analysis to provide insights and support for experimental spectroscopic data.<sup>27</sup> However, interpretation of the UV-Vis/NIR spectra of copper-exchanged zeolites has not been widespread. This is partly because of the size of the zeolitic systems, necessitating the use of periodic boundary conditions or large cluster models. This limits one's ability to use the highest quality computational methods to study these systems. For this reason, most studies on the optical spectra of copper-exchanged zeolites have used time-dependent linear-response density functional theory (TD-DFT)<sup>28</sup> or Hartree-Fock theory (TD-HF).<sup>29</sup> As examples, Woertink et al. showed that the observed peak at 22700 cm<sup>-1</sup> in the optical spectrum of the mono-(μ-oxo) dicopper [Cu<sub>2</sub>O]<sup>2+</sup> active site within zeolite ZSM-5 can be reproduced well with TD-DFT calculations while using the B3LYP functional.<sup>30</sup> Li et al. used a combination of ab initio molecular dynamics and TD-DFT to

show the importance of exchange-site heterogeneity and dynamics on the UV-Vis spectrum of copper-oxo dimers and polynuclear species in the SSZ-13 zeolite.<sup>31</sup> Göttl et al. used a novel, parameterized TD-HF-type approach to compute the absorption and photoluminescence spectra of Cu(I) sites in the SSZ-13 zeolite.<sup>32</sup> Also recently, Ipek et al. used Green functions-based methods as well as the Bethe-Salpeter equation<sup>33,34</sup> to compute the optical spectra of the  $\mu$ -( $\eta^2$ : $\eta^2$ ) bent-peroxo dicopper  $[\text{Cu}_2\text{O}_2]^{2+}$  in the SSZ zeolite.<sup>35</sup> Interestingly, TD-DFT is far cheaper than the approaches used by Ipek et al. However, TD-DFT calculations on transition metal species are often problematic due to static correlation effects as well as other deficiencies in approximate Kohn-Sham density functionals.<sup>36-38</sup> Some other deficiencies include the presence of ghost excitations, incorrect treatment of charge-transfer effects as well as difficulties associated with handling systems with broken-symmetry open-shell singlet wavefunctions.<sup>28,39,40</sup> Fortunately, there have been significant advances in practical TD-DFT over the last few decades. As such, some of these problems already have some practical solutions.<sup>41</sup> Towards this end, some of us recently reported that a fairly new density functional,  $\omega$ B2PLYP,<sup>42-44</sup> can provide excellent accuracies for predicting the spectra of several copper-oxo active site motifs implicated in methane-to-methanol conversion, MMC.<sup>45</sup> This functional is a long-range corrected double-hybrid functional. It uses a previously-described configuration-interaction singles and double, CIS(D)-style<sup>42,46,47</sup> scheme to predict electronic transitions, when used for computing absorption spectra.<sup>42-44</sup> The long-range correction allows for good treatment of charge-transfer problems while the corrections for CIS(D)-style scheme might be useful for multi-electron processes. Interestingly, despite the various advances within TD-DFT, there has been no detailed quantum-mechanical description of the changes in the UV-Vis spectra of copper-exchanged zeolites during methane activation.

Here, we use TD-DFT calculations with  $\omega$ B2PLYP to probe UV-Vis spectra of the mono-( $\mu$ -oxo) dicopper  $[\text{Cu}_2\text{O}]^{2+}$  and tris-( $\mu$ -oxo) tricopper  $[\text{Cu}_3\text{O}_3]^{2+}$  active sites. Specifically, we report the calculated spectra for these species, before and after reaction with methane. We provide quantum-mechanical insights into how methane activation causes the disappearance of some signature peaks:  $22700\text{ cm}^{-1}$  for  $[\text{Cu}_2\text{O}]^{2+}$  and  $30000\text{-}38000\text{ cm}^{-1}$  for  $[\text{Cu}_3\text{O}_3]^{2+}$ .<sup>9,48</sup> This is important for identifying intermediate species involved during stepwise stoichiometric methane activation. Electronic structure understanding of the spectral changes provides a formal description of the evolution of the copper-oxo active sites. Additionally, it is important to ascertain the utility of

$\omega$ B2PLYP during methane activation as well as during active site formation and regeneration. This is likely to be very useful in future spectroscopic characterizations of novel active site motifs.

## 5.2 METHODOLOGY

**5.2.1 Geometry Optimizations:** All cluster models in this work were optimized with the B3LYP<sup>49-51</sup> functional while accounting for dispersion effects with the D3BJ scheme.<sup>52-55</sup> Due to the large number and sizes of the complexes, Figures 5.1 and 5.2, we used the def2-SVP basis sets<sup>56</sup> for all atoms. For  $[\text{Cu}_2\text{O}]^{2+}$  and  $[\text{Cu}_3\text{O}_3]^{2+}$  as well as their intra-zeolite methoxy intermediates, we separately optimized the high- and low-spin states. Energies were considered to be converged after reaching  $1 \times 10^{-8}$  a.u. thresholds. These geometry optimizations were performed with the ORCA v4.2.1 software code.<sup>57</sup> Vibrational frequency analyses were carried out analytically to ensure that the optimized structures corresponded to local minima. Most of our optimized structures had only positive vibrational frequencies. In a few cases with imaginary frequencies (less than  $200 \text{ cm}^{-1}$ ), we ascertained that these motions were centered on the terminating protons of the cluster models.

**5.2.2 Electronic Structure Analysis:** To analyze the characteristics of the molecular orbitals of the  $[\text{Cu}_2\text{O}]^{2+}$  and  $[\text{Cu}_3\text{O}_3]^{2+}$  cluster models, we considered the Löwdin orbital populations. This maintains the features of Mulliken analysis, without the heavy basis set dependence.

**5.2.3 TD-DFT Calculations:** Using the ORCA v4.2.1<sup>57</sup> software code and the Tamm-Dancoff approximation,<sup>58</sup> TDA-DFT, we computed the UV-Vis spectra of all species in Figures 5.1 and 5.2 with the  $\omega$ B2PLYP functional.<sup>42</sup> These calculations were performed with the cc-pVDZ<sup>59-61</sup> basis set. We have shown that TDA-DFT spectra of copper oxo species are largely independent of basis set size.<sup>45</sup> We used the resolution of identity and chain-of-spheres approximation, RIJCOSX,<sup>62</sup> with def2-TZVP<sup>63</sup> auxiliary correlation basis sets. We requested 100-200 states during all TDA-DFT calculations. TDA-DFT spectra for the  $[\text{Cu}_2\text{O}]^{2+}$  and  $[\text{Cu}_3\text{O}_3]^{2+}$  species were fitted with a Lorentzian functions<sup>64</sup> with full widths at half maxima of  $1200$  and  $3500 \text{ cm}^{-1}$ , respectively.

## 5.3 RESULTS AND DISCUSSIONS

### 5.3.1. Dicopper Mono-Oxo $[\text{Cu}_2\text{O}]^{2+}$ System:

*5.3.1.1. Cluster models:* To create a cluster model for  $[\text{Cu}_2\text{O}]^{2+}$ , we took this active site and achieved charge neutrality by adding two aluminate tetrahedra to the metal centers. We then added silicate tetrahedra, ensuring a good description of the second-coordination spheres around the

metals, Figure 5.1. We constructed this model from an optimized unit cell of ZSM-5.<sup>7,12,65,66</sup> The model was extracted from an optimized unit cell with Al atoms placed at the crossing of the straight and sinusoidal pores. There are two T-sites between the Al atoms. Cu centers were arranged near the aluminate tetrahedra in accordance with the descriptions of Tsai et al.<sup>67</sup> and Arvidsson et al.<sup>66</sup> Cu-ZSM-5 has been demonstrated for stepwise and continuous catalytic MMC. The spectroscopic properties of the  $[\text{Cu}_2\text{O}]^{2+}$  active site in this zeolite have also been investigated.

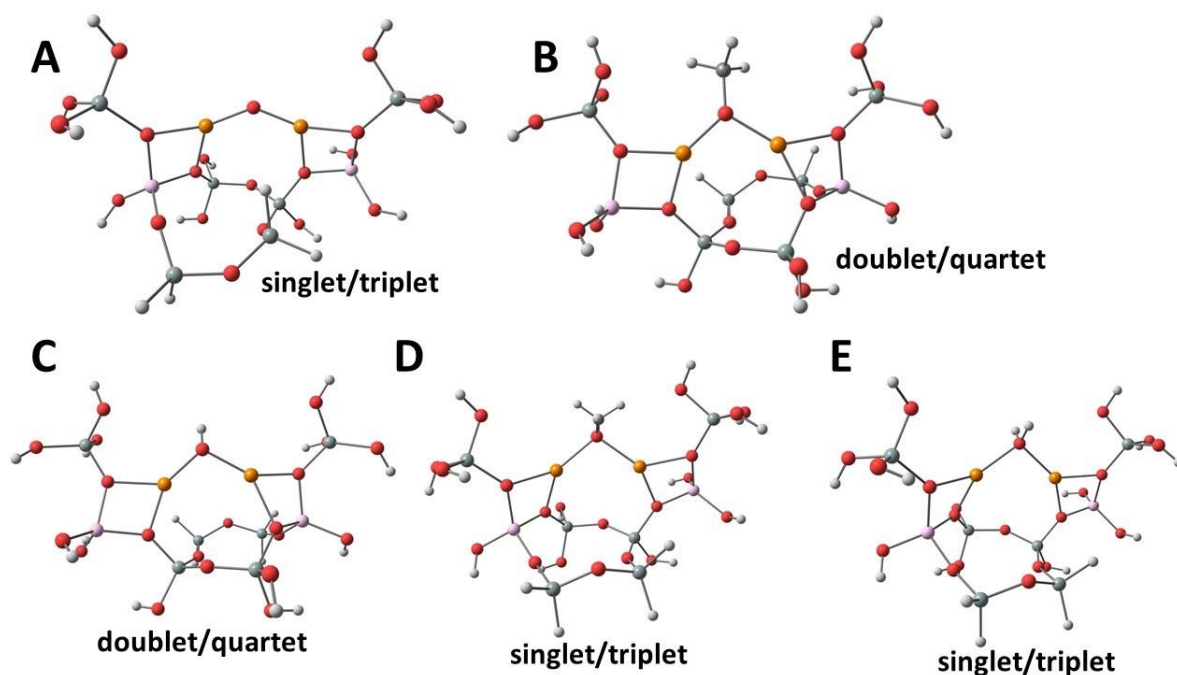


**Figure 5.1: Optimized structures of the cluster models of  $[\text{Cu}_2\text{O}]^{2+}$ . A is the cluster model for the active site. B-E are possible intermediates formed after methane C-H activation. The considered spin states are provided.**

To examine the impact of methane activation on the spectra of  $[\text{Cu}_2\text{O}]^{2+}$ , we considered strongly-bound methanol at the active site. This makes sense as Oord et al.<sup>68</sup> have demonstrated that methane reaction with copper oxo sites is accompanied by detection of vibrational overtones due to  $\text{Cu}(\text{CH}_3)(\text{H}_2\text{O})$  or  $\text{Cu}(\text{CH}_3)(\text{OH})$  species.<sup>69</sup> For  $[\text{Cu}_2\text{O}]^{2+}$ , the methyl group and proton from methane are bound to the  $\mu$ -oxo atom, Figure 5.1. This concurs with the mechanism described by several workers.<sup>66,69-73</sup> Alayon et al. have also proposed the formation of  $[\text{Cu}-\text{O}(\text{CH}_3)-\text{Cu}]^{2+}$  and  $[\text{Cu}-\text{O}(\text{H})-\text{Cu}]^{2+}$  species with the separated methyl group migrating to another active site, Figure 5.1b and 5.1c, respectively.  $[\text{Cu}-\text{O}(\text{H})-\text{Cu}]^{2+}$  is also relevant if the separated methyl group becomes stabilized at a Brønsted acid site, BAS. Stabilization of the methyl group could also occur with exchange with an acidic proton. This leads to  $[\text{Cu}-\text{O}(\text{H}_2)-\text{Cu}]^{2+}$  as shown in Figure 5.1e.



*5.3.1.2. Spin state of  $[\text{Cu}_2\text{O}]^{2+}$  active site:* Single point calculations on the optimized structures of the singlet and triplet states of the  $[\text{Cu}_2\text{O}]^{2+}$  cluster model, Figure 5.1a, reveals that the singlet state is more stable. Indeed with B3LYP, CAM-B3LYP<sup>74</sup> and  $\omega$ B2LYP, we found that the singlet state is favored over the triplet state by 2.8, 3.0 and 2.6 kcal/mol, respectively. Based on these relative energies, the triplet state will contribute less than 1.2% of the population for the  $[\text{Cu}_2\text{O}]^{2+}$  active site, assuming a Boltzmann population distribution. This agrees very well with the absence of any EPR signal in experiments on copper-loaded ZSM-5 by Groothaert et al.<sup>13</sup> As such, we shall focus most of our discussions on the singlet state.

*5.3.1.3. Ground state electronic structure:* The frontier orbitals of the singlet state of the  $[\text{Cu}_2\text{O}]^{2+}$  cluster model are shown in Figure 5.2. The highest singly occupied molecular orbitals (HSOMOs) are largely made up of  $\mu$ -oxo 2p atomic orbitals (AOs), albeit with appreciable contributions from Cu 3d AOs. Specifically, in the  $\alpha$ -electron manifold, the HSOMO has 72.2%  $\mu$ -oxo 2p and 12.4% Cu 3d AO contributions. Similarly, the HSOMO in the  $\beta$ -electron manifold is made of 71.5% AO from the  $\mu$ -oxo 2p and 12.5% from the Cu 3d. We see the same behavior in the next highest SOMOs, HSOMO-1s. In the  $\alpha$ -electron manifold, the HSOMO-1 is made up of 38.6% from the  $\mu$ -oxo 2p, 30.3% from the  $\mu$ -oxo 2p and 13.8% from the Cu 3d AOs. And in the  $\beta$ -electron manifold, there is 55.6% from the  $\mu$ -oxo 2p, 11.1% from the  $\mu$ -oxo 2p and 14.5% from the Cu 3d AOs, Figure 5.2. On the other hand, the lowest unoccupied molecular orbitals (LUMO) of the  $[\text{Cu}_2\text{O}]^{2+}$  cluster model are largely localized on the Cu centers. In the  $\alpha$ -electron manifold, the LUMO contains 33.5% Cu 4s and 38.5% Cu 3d AO contributions. In the  $\beta$ -electron manifold, the LUMO contains 29.4% Cu 4s and 45.1% Cu 3d. Based on this analysis of the frontier molecular orbitals (MOs), excitations from the HSOMOs and HSOMO-1s to the LUMOs will mainly be of  $\mu$ -oxo 2p  $\rightarrow$  Cu 3d/4s charge transfer character.

*5.3.1.4. Methane activation and electronic structure:* After activation of the methane C-H bond, one possible intermediate is strongly-bound methanol is shown in Figure 5.1d. We chose to analyze the electronic structure of this species (**1d**) due to spectroscopic observations of methanol, after contacting methane with activated zeolites. This is even prior to treatment with water. The frontier orbitals for the singlet state this species are shown in Figure 5.3. For this species, the singlet state is 39.8 kcal/mol more stable than the triplet state. Interestingly, there are no frontier orbitals with significant  $\mu$ -oxo 2p AO contributions after methane activation. Indeed between HSOMO and HSOMO-30, a span of about 4.5 eV (36432  $\text{cm}^{-1}$ ), the highest  $\mu$ -oxo 2p contributions

to any MO are less than 3%. Close examination reveals that the  $\mu$ -oxo 2p AOs are significantly stabilized due to hybridization with the methyl C 2p AOs.

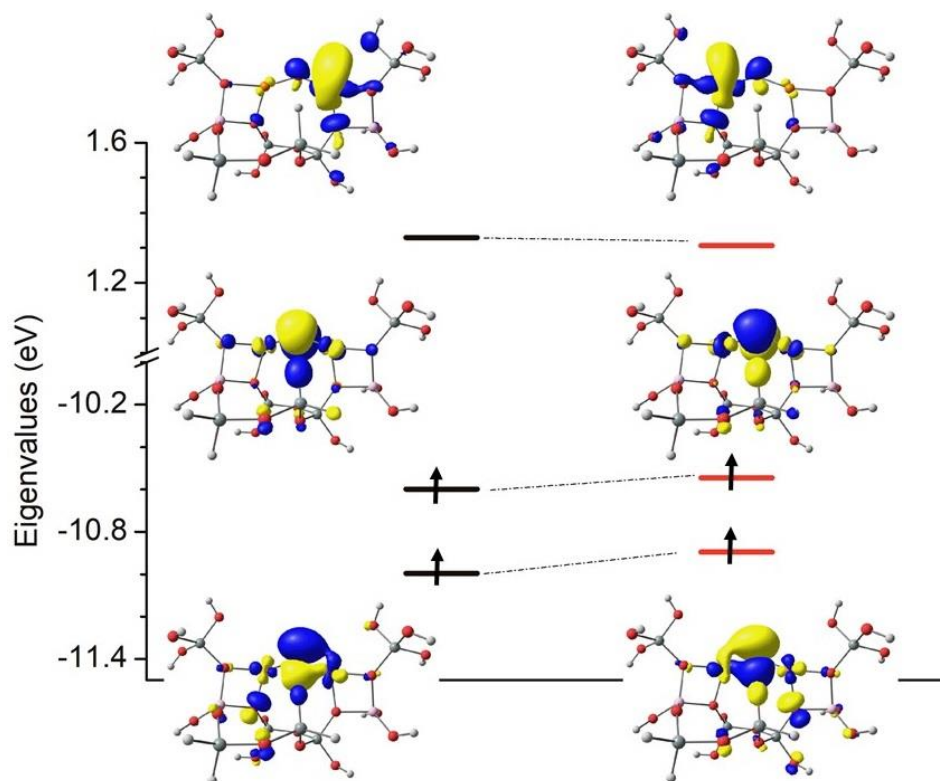


**Figure 5.2: Frontier orbitals of the open-shell singlet ground state of the  $[\text{Cu}_2\text{O}]^{2+}$  cluster model obtained with the  $\omega\text{B2LYP}$  functional and cc-pVDZ basis sets.**

These MOs now have eigenvalues around -16 to -20 eV, Figure 5.2, in contrast to the situation before methane activation, Figure 5.2, where they have eigenvalues of around -11 eV. Thus, the nature of the HSOMO and HSOMO-1 have dramatically changed. After methane activation, these are now predominantly Cu based. As example, HSOMO contains 52.2% contribution from Cu 3d AOs. Interestingly, the LUMOs are now predominantly of Cu 4s and 4p character after methane activation. Indeed, there are very little contributions from Cu 3d AOs to the LUMOs, a stark contrast to the situation before methane activation.

Based on the stabilization of the C 2p and O 2p hybrid orbitals; the 3d character of HSOMO and HSOMO-1; as well as significant 4p character of the LUMOs, Figure 5.3, we conclude that methane activation is accompanied by electron transfer from MOs with significant  $\mu$ -oxo 2p AO character to MOs with significant Cu 3d character. This indicates a 2-electron reduction of both  $\text{Cu}^{2+}$  centers in  $[\text{Cu}_2\text{O}]^{2+}$  [ $2\text{Cu}^{2+} \rightarrow 2\text{Cu}^+$  or  $2\text{Cu}^{2+} \rightarrow \text{Cu} + \text{Cu}^{2+}$ , depending on the exchange-correlation density functional]. Additionally, the significant contribution of 4p AOs to the LUMOs

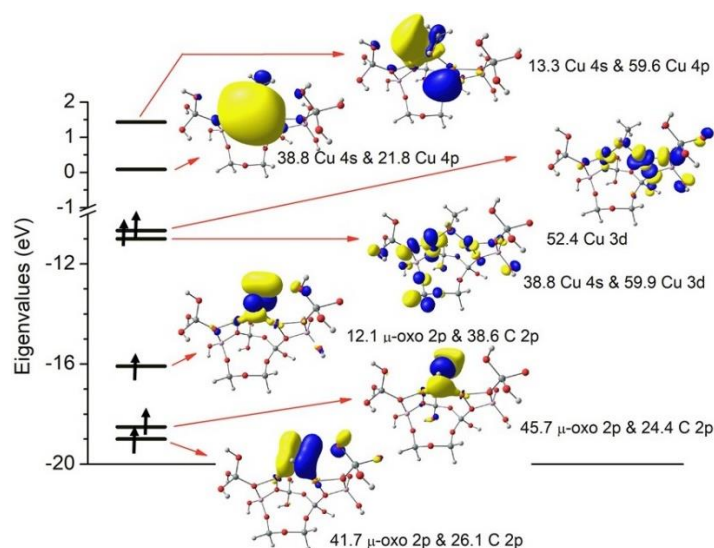


**Figure 5.3: Frontier orbitals of the open-shell singlet ground state of the  $[\text{Cu}_2\text{O}]^{2+}$  active site after methane activation. These were obtained at the  $\omega\text{B2LYP/cc-pVDZ}$  level.**

after methane activation is indicative of a more diffuse and Rydberg-like character, see Figures 5.2 and 5.3. This would suggest poor spatial overlap during electronic transitions involving these orbitals. Thus, it is reasonable to expect that methane activation will lead to significant reduction in the oscillator strengths of transitions to the low-lying Cu 4s and 4p LUMOs.

**5.3.1.5. Methane activation and TDA-DFT spectra:** The spectra obtained at the  $\omega\text{B2PLYP/cc-pVDZ}$  level for the  $[\text{Cu}_2\text{O}]^{2+}$  cluster model before (Figure 5.1a) and after methane activation (Figure 5.1b-d) are shown in Figure 5.4. Before methane activation, there is a prominent feature

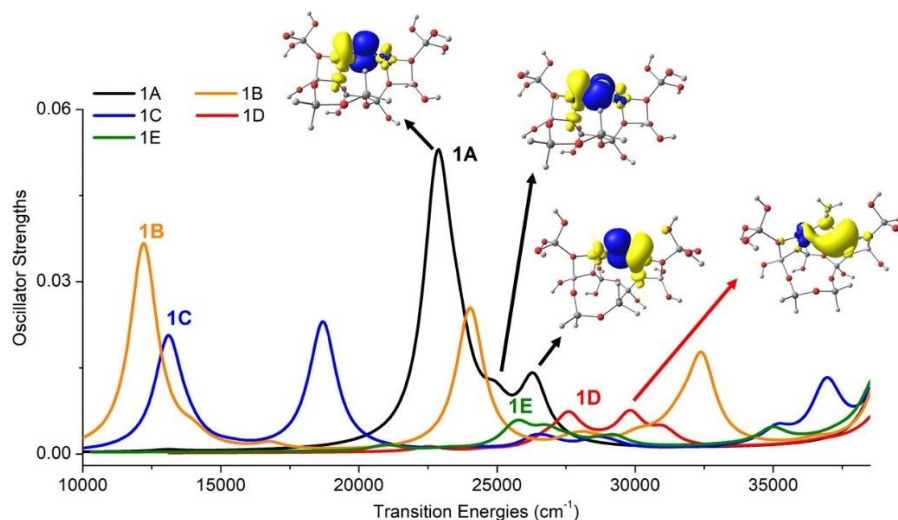


**Figure 5.4: Calculated spectra obtained at the  $\omega\text{B2PLYP/cc-pVDZ}$  level for the  $[\text{Cu}_2\text{O}]^{2+}$  cluster model and possible intermediates after methane activation. The difference densities between the ground and excited states are shown as insets.**

feature at  $22889\text{ cm}^{-1}$ , in great agreement with the experimental band at  $22700\text{ cm}^{-1}$ . We and Woertink et al. have previously described this feature as being due to  $\mu$ -oxo  $2p \rightarrow \text{Cu } 3d/4s$  charge transfer.<sup>30,45</sup> Indeed, it is specifically due to transitions from the  $\mu$ -oxo  $2p$  HSOMO and HSOMO-1 to the Cu  $4s/3d$  LUMO, Figure 5.3. The difference density illustrates clearly the charge-transfer nature of this transition, see inset of Figure 5.4.

Indeed, the difference density reveals depletion of electron density on the  $\mu$ -oxo atom (blue color) and aggregation of electron densities in the excited state on the Cu centers (yellow). In addition to the feature at  $22889\text{ cm}^{-1}$ , TDA-DFT also yields a significantly less intense charge-transfer peak at  $26307\text{ cm}^{-1}$ . Moreover, Groothaert reported a signature  $22700\text{ cm}^{-1}$  peak as well as a relatively weaker band near  $30000\text{ cm}^{-1}$  in their characterization of  $\text{O}_2$ -activated Cu-ZSM-5. Thus, our calculations agree quite well with experimental data.

After methane C-H activation, the features at  $22889$  and  $26307\text{ cm}^{-1}$  have disappeared in the intermediate with strongly bound methanol, **1d**. There are now only minor peaks at  $27566$ ,  $29841$  and  $31063\text{ cm}^{-1}$ , Figure 5.4. As noted earlier, these are weaker as they involve transitions to Cu  $4s/4p$  diffuse Rydberg-type orbitals, Figure 5.3. The energy shift is due to the fact that the nature of the occupied frontier orbitals changed dramatically upon methane activation, Figures 5.3 and 4. Interestingly, the disappearance of the  $22700\text{ cm}^{-1}$  feature from the experimental UV-Vis spectra of  $\text{O}_2$ -activated Cu-ZSM-5 has been used to monitor the kinetics of methane activation.<sup>30</sup> Therefore,  $\omega$ B2PLYP can reproduce these experimental observations as well as furnish a molecular-level understanding of the peak's disappearance.

Interestingly, Figure 5.4 shows that both **1c** also has reduced intensities in the  $20000$ - $35000$  region. However, it now features lower-energy transitions below  $20000\text{ cm}^{-1}$ . This is also the case for **1b**. The new features below  $20000\text{ cm}^{-1}$  and in the case of **1b**, around  $32300\text{ cm}^{-1}$ , have not been reported experimentally. On the other hand, **1e** features reduced intensities near  $20000\text{ cm}^{-1}$  and has no new features, just like **1d**. Examination of the electronic structures of **1e** reveals similar stabilization of the frontier MOs with  $\mu$ -oxo  $2p$  AOs character as well as presence of significant  $4s/4p$  character of the LUMOs, as was seen for **1d**. Similarity between the spectra of **1d**, and **1e** shows a limitation of UV-Vis spectroscopy; experimental observations could be due to multiple intra-zeolite intermediates.

### 5.3.2. Tricopper Trioxo $[\text{Cu}_3\text{O}_3]^{2+}$ System:

5.3.2.1. *Cluster models*: To create a cluster model for  $[\text{Cu}_3\text{O}_3]^{2+}$ , we took the metal oxo core and

added two aluminate tetrahedra to the first coordination sphere of the metals, Figure 5.5. This leads to a cluster model of the 8MR of zeolite mordenite (MOR). This model has been previously used to study methane over-oxidation as well as electronic structure and spectroscopic properties of  $[\text{Cu}_3\text{O}_3]^{2+}$ . Additionally, many claims of unique preparations of the tricopper site have been for copper-exchanged MOR.

For  $[\text{Cu}_3\text{O}_3]^{2+}$ , the exact natures of the intermediates formed after methane activation are unknown. As such, we have considered various arrangements of the methyl and proton around the active site, Figure 5.5b-i. First, we considered situations where the separated proton and methyl groups are sited at different  $\mu$ -oxo atoms (**5.5b**, **5.5c** and **5.5d**). The methyl could also rebound to the reactive  $\mu$ -oxo atom (**5.5e** and **5.5f**). Interestingly, recent experimental and theoretical reports have suggested that the methyl group is actually not stabilized at the active site. Several workers have shown that the methoxy is formed at Brønsted acid sites.<sup>75-77</sup> We have also shown that stabilization of the methyl at the active site is a recipe for over-oxidation.<sup>78,79</sup> Considering these, we optimized the geometries of other possible structures. First, the methyl group could be stabilized away from the active site. This leads to structure **5.5g** in Figure 5.5g. Conversely, the methyl could be stabilized on framework aluminates in exchange for a proton. This proton can be located at a new  $\mu$ -oxo atom (**5.5h**) or at the reactive  $\mu$ -oxo atom (**5.5i**).

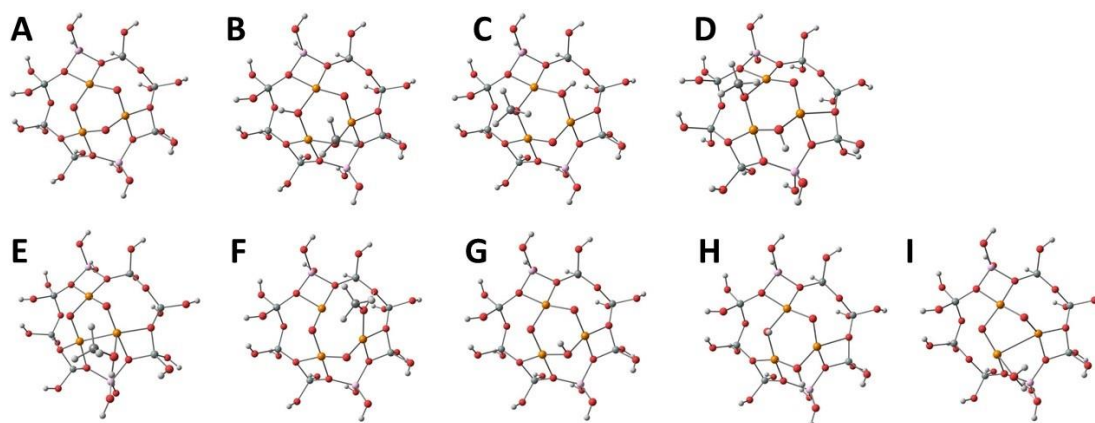


**Figure 5.5: Optimized structures of the cluster models of  $[\text{Cu}_3\text{O}_3]^{2+}$ . A is the cluster model for the active site. B-I are possible intermediates formed after methane C-H activation. The ground spin states of these species are provided.**

*5.3.2.2. Spin state of  $[\text{Cu}_3\text{O}_3]^{2+}$  active site:* We previously discussed that GGA density functionals predict the doublet state of the  $[\text{Cu}_3\text{O}_3]^{2+}$  active site is more stable the high-spin quartet state.<sup>80</sup> Vogiatzis et al. reported that the energy difference between the doublet and quartet states

is consistent between GGA functionals and multireference methods.<sup>81</sup> As such, we shall focus our discussions on the doublet state of our cluster model, Figure 5.5a.

**5.3.2.3. Ground state electronic structure:** The frontier orbitals of the singlet state of the  $[\text{Cu}_3\text{O}_3]^{2+}$  cluster model are shown in Figures 5.6 and 5.7. In the  $\alpha$ -spin manifold, the HSOMO consists largely of 2p AOs from two  $\mu$ -oxo atoms of the  $[\text{Cu}_3\text{O}_3]$  core; 79.4% 2p AOs from both. It also contains 6.4% from Cu 3d AOs, Figure 5.7. A similar situation is seen for HSOMO-1; 71.8%  $\mu$ -oxo and 7.8 % 3d. HSOMO-2 has significant 2p contributions from an aluminate oxo group, Figure 5.6. However, the second largest contribution to this orbital is from  $\mu$ -oxo 2p AOs. The dominance of the  $\mu$ -oxo 2p AOs in the frontier  $\alpha$ -spin orbitals extends to HSOMO-3 and HSOMO-4. HSOMO-4 has 36% contribution from  $\mu$ -oxo 2p AOs as well as 8.9% from Cu 3d AOs from Cu. It also has about 33.6% contribution from an aluminate oxo group. The LUMO has some antibonding character containing also 74.9% 2p AO contributions from two  $\mu$ -oxo atoms. It also contains a minor contribution of 4.0% from Cu 4p orbitals. The LUMO+1 orbital is however dominated by Cu 4s and 4p AOs; 46.2 and 5.6% respectively.

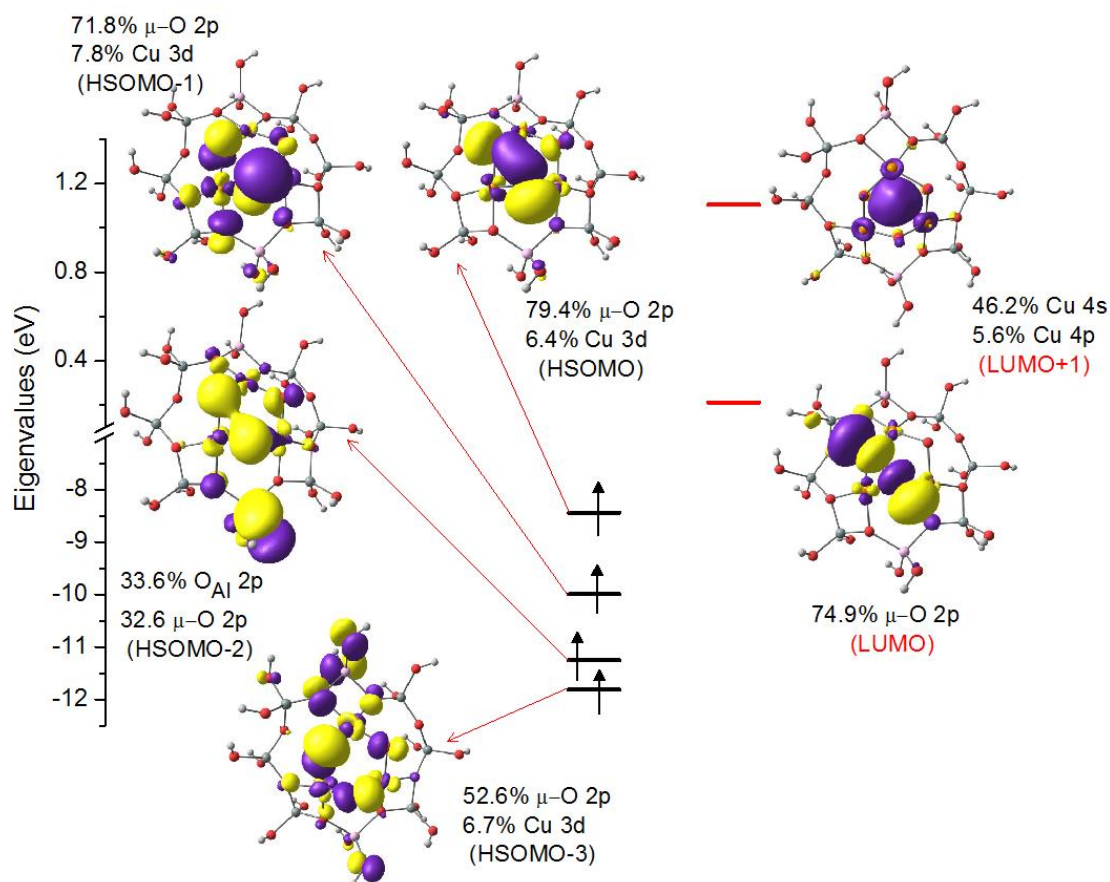


**Figure 5.6: Frontier  $\alpha$ -orbitals of the  $[\text{Cu}_3\text{O}_3]^{2+}$  cluster model at  $\omega\text{B2LYP/cc-pVDZ}$  level.**



Examination of the  $\beta$ -spin orbitals shows that the LUMO+1 is also largely centered on the Cu centers, with 45.7% Cu 4s and 4.2% Cu 3d. The LUMO, HSOMO and HSOMO-1 are however dominated by  $\mu$ -oxo 2p AOs, just like for the  $\alpha$ -spin orbitals. Based on Figures 5.6 and 5.7, we can conclude that excitations into the LUMOs will be of  $\mu$ -oxo 2p  $\rightarrow$  2p character. Excitations into LUMO+1 will have significant ligand-to-metal charge transfer character ( $\mu$ -oxo 2p  $\rightarrow$  Cu 4s).

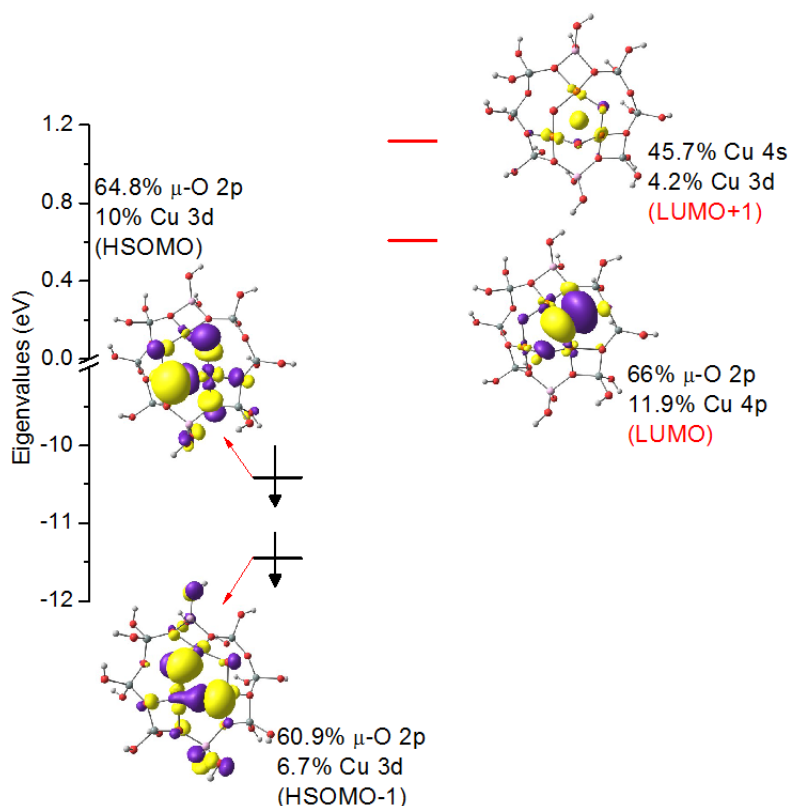


**Figure 5.7: Frontier  $\beta$ -orbitals of the  $[\text{Cu}_3\text{O}_3]^{2+}$  cluster model at  $\omega\text{B2LYP/cc-pVDZ}$  level.**

**5.3.2.3. Methane activation and TDA-DFT spectra:** Several workers have examined methane activation by the  $[\text{Cu}_3\text{O}_3]^{2+}$  active site in the 8MR of MOR. It was reported that the reflectance of the band near  $31000\text{ cm}^{-1}$  decreases after contact with methane.<sup>9,48,82</sup> Indeed, a difference spectrum reported by Ikuno et al. showed reduction for features between  $23000$  and  $38000\text{ cm}^{-1}$ .<sup>82</sup> As stated earlier, the exact natures of the intermediate species formed after methane activation by  $[\text{Cu}_3\text{O}_3]^{2+}$  are somewhat unknown. For this reason, the TDA-DFT spectrum of **5.5a** is compared to spectra for **5.5b-5.5i** in Figures 5.8 and 5.9. Assignment of the spectral features of the  $[\text{Cu}_3\text{O}_3]^{2+}$  active site, **5.5a**, is presented in Table 5.1. We highlight that unlike the features at  $14530$ ,  $25383$  and  $30110\text{ cm}^{-1}$ , the peaks at  $34139$  and  $36563\text{ cm}^{-1}$  have significant contributions from Cu-centered 4s, 4p and 3d AOs in the relevant virtual orbitals.

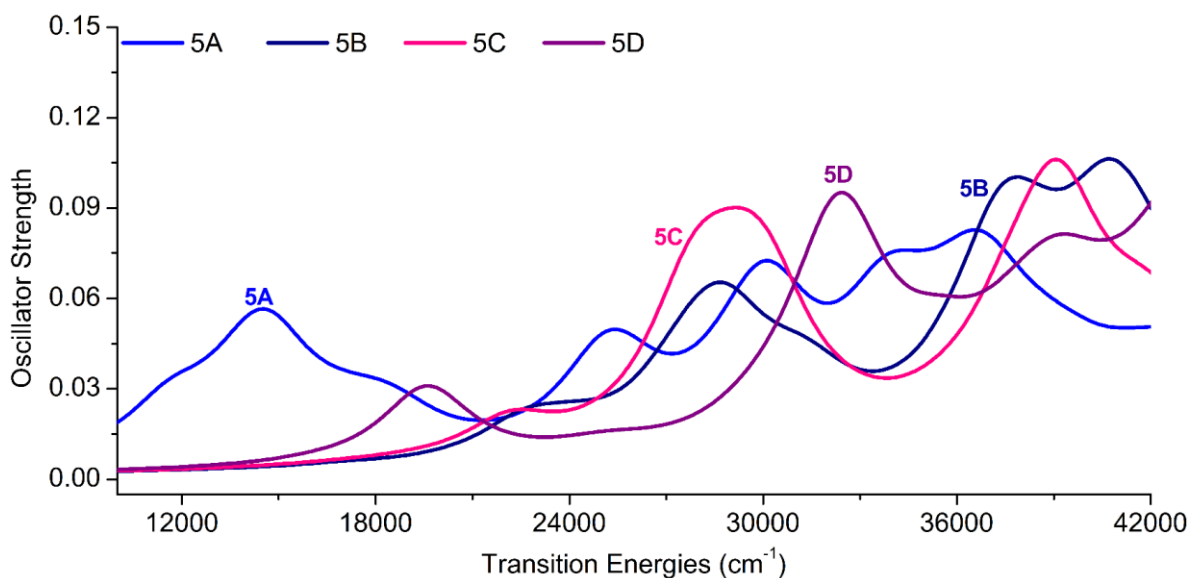


**Figure 5.8: Comparison of calculated spectra of  $[\text{Cu}_3\text{O}_3]^{2+}$  to several possible intermediates for methane activation, 5.5b-5.5d.**

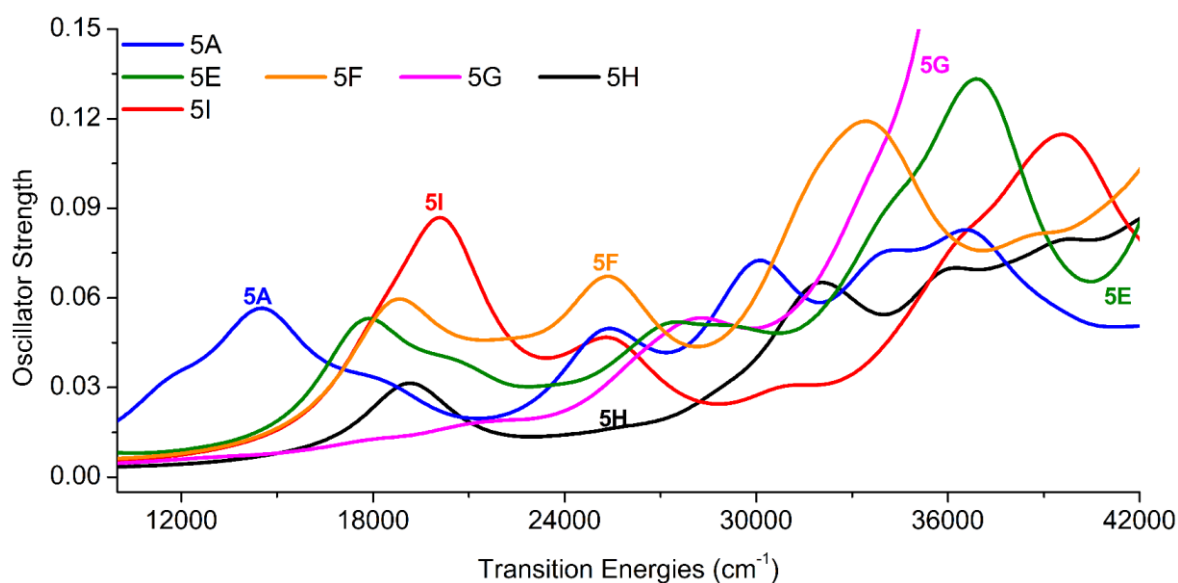


**Figure 5.9: Comparison of calculated spectra of  $[\text{Cu}_3\text{O}_3]^{2+}$  to several possible intermediates for methane activation, 5.5e-5.5i.**

There are a couple of important things to note regarding the spectra shown in Figures 5.8 and 5.9. First, the peak at  $14530\text{ cm}^{-1}$  has disappeared in most of the intermediate species. This suggests that the absorbance of the feature near  $12000\text{ cm}^{-1}$  should decrease after methane activation. However, the behavior of the feature at  $12000\text{ cm}^{-1}$  in the experimental data appears to depend on the set up. Several workers have reported a modest decrease in the reflectance of this region after methane activation.<sup>9,82</sup> Others have reported an increase.<sup>82</sup> All experimental reports are however



consistent regarding decrease in the reflectance of the 23000-38000  $\text{cm}^{-1}$  region. As such, we shall focus our emphasis on this region.

**Table 5.1: Characters of the dominant excitations, in  $\text{cm}^{-1}$ , in the TDA-DFT spectrum of  $[\text{Cu}_3\text{O}_3]^{2+}$ .**

Calculated	Experiment	Character
14530	10000-2000	$\mu\text{-oxo } 2p \rightarrow \mu\text{-oxo } 2p$
25383	$\sim 24000$	framework $\rightarrow$ active-site CT
30110	$\sim 31000$	framework $\rightarrow$ active-site CT
34139	$\sim 34000$	$\mu\text{-oxo } 2p \rightarrow \mu\text{-oxo } 2p$ and $\mu\text{-oxo } 2p \rightarrow \text{Cu } 4s$
36563	$\sim 38500$	$\mu\text{-oxo } 2p \rightarrow \text{Cu } 4s/3d$ $\mu\text{-oxo } 2p \rightarrow \mu\text{-oxo } 2p$ and $\text{Cu } 4p$

Second, of the possible intermediates that we considered, only **5.5b**, **5.5c**, **5.5d** and **5.5h** show lower oscillator strengths in portions of the 23000-38000  $\text{cm}^{-1}$  region, Figures 5.8 and 5.9. We repeat that in **5.5b-d**, the methyl rebounds to the active site whereas in **5.5h**, the separated methyl is exchanged with a Brønsted acid proton, Figure 5.5. These 2 possibilities have emerged as candidates for the stabilized strongly-bound methoxy.<sup>75,76,78,79,83-85</sup> Examination of the calculated spectra shows that **5.5b-c** predict substantial decrease in the intensities at 23000-25000  $\text{cm}^{-1}$  and 30000-36000  $\text{cm}^{-1}$ . They however have higher intensities near 29000  $\text{cm}^{-1}$ . **5.5d** has higher intensities than **5.5a** near 32500  $\text{cm}^{-1}$ , Figure 5.8. **5.5h** has similar intensities as **5.5a** near 32000  $\text{cm}^{-1}$ , Figure 5.9. For **5.5b-d** and **5.5h**, the intensities are also higher in the regions above 39000  $\text{cm}^{-1}$ . Overall, the intensities for **5.5h** are more consistently lower than for **5.5a** across the whole 23000-38000  $\text{cm}^{-1}$  region.

Other possible intermediates have higher intensities in the 23000-38000  $\text{cm}^{-1}$  region. For example, **5.5e** predict significantly higher intensities near 37000  $\text{cm}^{-1}$ . Also **5.5i** predicts a huge jump in intensity near 20000  $\text{cm}^{-1}$ . These do not conform to the experimental findings.<sup>9,48,82</sup> Based on these considerations, we focus subsequent discussions on **5.5h**. We again repeat that recent experimental results have shown that the separated methyl group is stabilized at BASs.<sup>75,76,85</sup> Quantum-mechanical computations have shown that exchange of the acidic proton of a BAS with the methyl is indeed energetically feasible.<sup>79</sup> Stabilization of the acidic proton at the active site  $\mu\text{-oxo}$  atom and the methyl at a basic framework aluminate has been shown to be a crucial mechanism for avoiding over-oxidation.<sup>75,78</sup> All of these point towards **5.5h**.

**5.3.2.4. Impact of structural dynamics:** We performed ab initio molecular dynamics (AIMD) simulations on the periodic structure of **5.5h** at 300 K. After equilibration for 8 ps, we performed 3 simulations of 8 ps length, starting from 3 different structures. From the resulting trajectories, we randomly selected 5 structures of each. These were truncated to the size of the species in Figure 5.5. Dangling oxygen atoms were capped with protons and positions of the protons were optimized. Full details are provided in the Supporting Information. We then computed the UV-Vis spectra at the  $\omega$ B2PLYP/cc-pVDZ level. These are compared with spectra for the optimized structure at 0 K in Figure 5.10 and in the Supporting Information.

Overall, the clusters from AIMD display the same general property as the DFT-optimized structure. They all have lower intensities near the 23000-38000  $\text{cm}^{-1}$  region than **5.5a**. Some of these AIMD clusters also shift the 19000  $\text{cm}^{-1}$  feature of **5.5h** to lower energies; to near 17500  $\text{cm}^{-1}$  in the case of **5.5h-3**, as an example, Figure 5.10. However, like the DFT-optimized structure, all the AIMD species feature higher intensities beyond 38000  $\text{cm}^{-1}$  than **5.5a**.

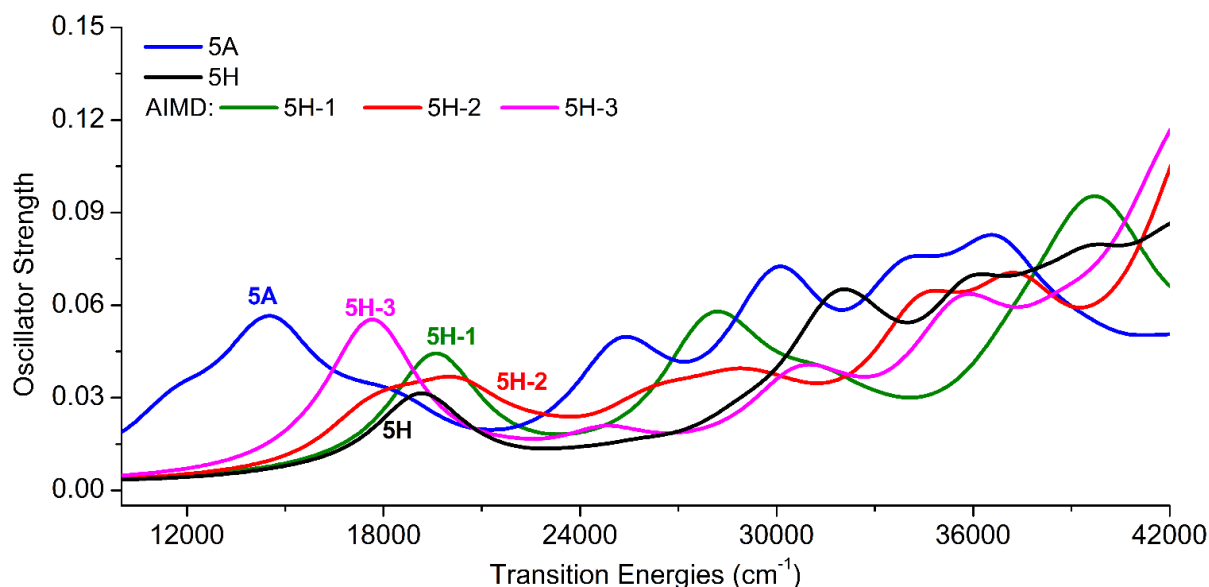


**Figure 5.10:** TDA-DFT spectra of cluster models of **5.5h** obtained from AIMD simulations (1-3) are compared to geometry optimized models for **5.5a** and **5.5h**.

**5.3.2.5. Methane activation and Electronic Structure:** The frontier orbitals of **5h** are presented in Figure 5.11. Before methane activation, there were 6  $\mu$ -oxo 2p-dominated MOs, containing 6 electrons. Two of these had significant  $\sigma$ -type character, with associated unoccupied  $\sigma^*$ -type orbitals, Figures 5.7 and 5.8. As discussed earlier, transitions between these orbitals are responsible for the peak at 14530  $\text{cm}^{-1}$ .

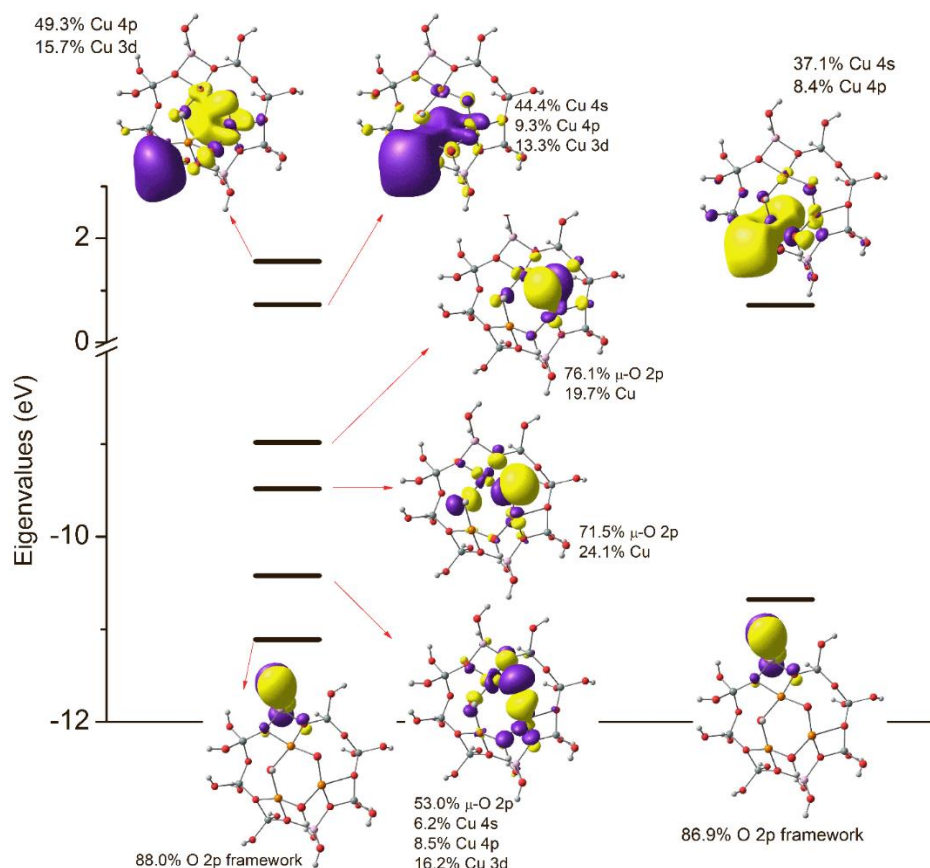


**Figure 5.11: Frontier orbitals of the doublet state of the  $[\text{Cu}_3\text{O}_3]^{2+}$  active site after methane activation to form structure **5.5h**. These were obtained at the  $\omega\text{B2LYP/cc-pVDZ}$  level.**

Crucially, after methane activation, some  $\mu$ -oxo 2p-dominated orbitals still remain in the frontier region, albeit with significantly higher contributions from Cu 3d and Cu 4p orbitals. Specifically, the  $\alpha$ -spin HSOMO, HSOMO-1, HSOMO-2 orbitals of **5.5h** have 19.7%, 24.1% and 30.9% contributions from Cu AOs, respectively, Figure 5.11. Indeed, after formation of **5h**, the  $\sigma^*$ -type  $\mu$ -oxo 2p orbitals are no longer in the frontier region. The frontier region is now thoroughly dominated by orbitals with significant Cu character, rather than  $\mu$ -oxo 2p. In Figure 5.11, we show that the  $\alpha$ -spin LUMO has 67% AOs contribution from Cu while the LUMO+1 has 65%. Similarly, the  $\beta$ -spin LUMO has 66.9% contribution from Cu AOs. We are to compare these with the  $\alpha$ -spin and  $\beta$ -spin LUMOs for **5.5a** which contain 74.9% and 66.0% from **Cu AOs**, respectively. Close examination of Figures 5.6, 5.7 and 5.11 also indicate that the frontier virtual orbitals of **5.5h** are more unstable (more positive eigenvalues) than those of **5.5a**. Also, the frontier occupied orbitals of **5.5h** are more stable (more negative eigenvalues) than those of **5.5a**. These findings are quite similar to those of the  $[\text{Cu}_2\text{O}]^{2+}$  system, see Sections 3.1.4 and 3.1.5. The significant contribution

of Cu AOs to the LUMOs after methane activation (indicative of a more diffuse and Rydberg-like character) and stabilization of frontier  $\mu$ -oxo 2p occupied orbitals suggests poor spatial overlap during transitions between these orbitals. Thus, methane activation leads to significant reduction in the oscillator strengths of transitions to the low-lying Cu-based LUMOs. We also expect a shift to higher transition energies.

Table 5.2 shows the assignment of the calculated spectral features of **5.5h**. A peak at 19128  $\text{cm}^{-1}$  contains excitations from the  $\mu$ -oxo 2p occupied orbitals  $\alpha$ -HSOMO-1 to HSOMO, LUMO and LUMO+1. These final orbitals have significant contributions from Cu AOs. Thus, compared to **5.5a**, this peak is shifted to higher energies and is less intense. The same phenomenon plays out across the 23000-38000  $\text{cm}^{-1}$  region. The intensities for **5.5h** are thus lower than that of **5.5a** across this region. Interestingly, beyond 38000  $\text{cm}^{-1}$  the intensities of **5.5h** are larger than for **5.5a**, Figure 5.9. For **5.5a**, the computed peak at 36563  $\text{cm}^{-1}$  underestimates the experimental feature near 38500-41000  $\text{cm}^{-1}$ . Thus, one would expect that based on Figure 5.11, the absorption intensities of the intra-zeolite intermediates would exceed that of  $[\text{Cu}_3\text{O}_3]^{2+}$  beyond the 38500-41000  $\text{cm}^{-1}$  region.

**Table 5.2: Characters of the dominant excitations, in  $\text{cm}^{-1}$ , in the TDA-DFT spectrum of 5.5h.**

Calculated	Character
19128	$\mu$ -oxo 2p $\rightarrow$ $\mu$ -oxo 2p; Cu 4s, 4p 3d
32090	framework $\rightarrow$ active-site CT
36238	$\mu$ -oxo 2p $\rightarrow$ $\mu$ -oxo 2p
39521	framework $\rightarrow$ $\mu$ -oxo 2p

## 5.4 CONCLUSIONS

The UV-Vis spectra of copper-oxo active sites within copper-exchanged zeolites are analyzed with cluster-model Tamm-Dancoff time-dependent DFT (TDA-DFT) calculations. These systems are of interest due to their ability to activate the methane C-H bond, selectively converting it to methanol. Specifically, TDA-DFT calculations with  $\omega$ B2PLYP were used to probe evolution of electronic structure properties and optical spectra of the  $[\text{Cu}_2\text{O}]^{2+}$  and  $[\text{Cu}_3\text{O}_3]^{2+}$  active sites during methane activation. We provide molecular-level understanding of changes in the UV-Vis spectra of copper-exchanged zeolites after contact with methane.

It is established that prior to methane activation,  $\omega$ B2PLYP provides great agreement with the

experimental optical spectra of  $[\text{Cu}_2\text{O}]^{2+}$  and  $[\text{Cu}_3\text{O}_3]^{2+}$ . Particularly for  $[\text{Cu}_3\text{O}_3]^{2+}$ , it provides bands at 14530, 25383, 30110, 34139 and 36563  $\text{cm}^{-1}$ , in agreement with experimental features near 12000,  $\sim 24000$ , 31000, 34000 and 38500-40000  $\text{cm}^{-1}$ . The signature peak observed for  $[\text{Cu}_2\text{O}]^{2+}$  at 22700  $\text{cm}^{-1}$  is predicted to be at 22889  $\text{cm}^{-1}$  with  $\omega\text{B2PLYP}$ . The less intense feature near 30000  $\text{cm}^{-1}$  in the experimental data is also captured with  $\omega\text{B2PLYP}$ .

After methane activation by  $[\text{Cu}_2\text{O}]^{2+}$ , the calculated optical of  $[\text{Cu-O(H)(H)-Cu}]$  and  $[\text{Cu-O(H)(CH}_3\text{)-Cu}]$  clearly show a disappearance of 22889  $\text{cm}^{-1}$  feature. By contrast, the spectra for  $[\text{Cu-O(H)-Cu}]$  and  $[\text{Cu-O(CH}_3\text{)-Cu}]$  either do not lead to sufficient reduction of the 22889  $\text{cm}^{-1}$  feature or also provide extraneous new features in the 10000-20000  $\text{cm}^{-1}$  region. These new features are in great disaccordance with previously reported experimental data. In  $[\text{Cu-O(H)(H)-Cu}]$  and  $[\text{Cu-O(H)(CH}_3\text{)-Cu}]$ , electrons in the  $\mu$ -oxo 2p-dominated orbitals of  $[\text{Cu}_2\text{O}]^{2+}$  become stabilized and hybridized with C 2p and/or H 1s orbitals from the separated methyl and proton of methane. Electronic structure analysis show a clear transfer of 2 electrons to the copper centers. This dramatically changes the nature of the low-lying unoccupied orbitals. Specifically the  $\mu$ -oxo 2p contributions to low-lying unoccupied orbitals are removed. Additionally, contributions from Cu 4s and 4p atomic orbitals to these orbitals become dramatically higher. The virtual orbitals thus acquire a more diffuse Rydberg-like character, leading to decreased spatial and/or energy overlaps with the occupied valence orbitals. These effects shift the energies and leads to a dramatic decrease in the oscillator strengths of the 22889  $\text{cm}^{-1}$  feature. This concurs with the disappearance of the 22700  $\text{cm}^{-1}$  band after methane activation, as seen in our TDA-DFT spectra and previous experimental data.

For the more complicated  $[\text{Cu}_3\text{O}_3]^{2+}$  system, previous reports stated that methane activation is associated with a decrease in intensity in the 23000-38000  $\text{cm}^{-1}$  region. However, the exact structure of the intermediate species formed after methane activation by  $[\text{Cu}_3\text{O}_3]^{2+}$  is unknown. Using a set of 8 possible structures, we found that several structures exhibited reduced oscillator strengths in parts of the 23000-38000  $\text{cm}^{-1}$  region. Interestingly, these species correspond to rebound of the methyl group to an active site  $\mu$ -oxo atom or remotely in exchange for a Brønsted acid proton. Recent experimental and theoretical studies have described how stabilization of the methyl at Brønsted acid sites is crucial for preventing over-oxidation. Our TDA-DFT results are thus another evidence supporting such assertions. To understand the lower intensities in the 23000-38000  $\text{cm}^{-1}$  region, we discovered that a similar phenomenon as seen in  $[\text{Cu}_2\text{O}]^{2+}$  results in shifting

the spectra to higher energies and lower intensities (predominance of Cu atomic orbital contributions in the low-lying virtual orbitals as well as stabilization of the frontier occupied orbitals due to hybridization with H 1s orbitals).

Thus, we conclude that  $\omega$ B2PLYP is useful for studying the UV-Vis spectra of copper-oxo active site species implicated in methane-to-methanol conversion. It is capable of describing the evolution of these species during the conversion process. Using this approach, we gain a molecular-level understanding into the properties of copper-oxo species implicated in methane-to-methanol conversion.

## REFERENCES

- (1) Dunn, S. Hydrogen futures: toward a sustainable energy system, *Int. J. Hydrogen Energ.* **2002**, 27, 235.
- (2) Muradov, N. Z.; Veziroglu, T. N. From hydrocarbon to hydrogen-carbon to hydrogen economy, *Int. J. Hydrogen Energ.* **2005**, 30, 225.
- (3) Lunsford, J. H. Catalytic conversion of methane to more useful chemicals and fuels: a challenge for the 21st century, *Catal. Today* **2000**, 63, 165.
- (4) Narsimhan, K.; Iyoki, K.; Dinh, K.; Román-Leshkov, Y. Catalytic Oxidation of Methane into Methanol over Copper-Exchanged Zeolites with Oxygen at Low Temperature, *ACS Cent. Sci.* **2016**, 2, 424.
- (5) Alayon, E. M.; Nachtegaal, M.; Ranocchiari, M.; van Bokhoven, J. A. Catalytic conversion of methane to methanol over Cu-mordenite, *Chem. Commun.* **2012**, 48, 404.
- (6) Alayon, E. M. C.; Nachtegaal, M.; Ranocchiari, M.; van Bokhoven, J. A. Catalytic Conversion of Methane to Methanol Using Cu-Zeolites, *Chimia* **2012**, 66, 668.
- (7) Beznis, N. V.; Weckhuysen, B. M.; Bitter, J. H. Cu-ZSM-5 Zeolites for the Formation of Methanol from Methane and Oxygen: Probing the Active Sites and Spectator Species, *Catal. Lett.* **2010**, 138, 14.
- (8) Pappas, D. K.; Martini, A.; Dybala, M.; Kvande, K.; Teketel, S.; Lomachenko, K. A.; Baran, R.; Glatzel, P.; Arstad, B.; Berlier, G.; Lamberti, C.; Bordiga, S.; Olsbye, U.; Svelle, S.; Beato, P.; Borfecchia, E. The Nuclearity of the Active Site for Methane to Methanol Conversion in Cu-Mordenite: A Quantitative Assessment, *J. Am. Chem. Soc.* **2018**, 140, 15270.
- (9) Grundner, S.; Markovits, M. A. C.; Li, G.; Tromp, M.; Pidko, E. A.; Hensen, E. J. M.; Jentys, A.; Sanchez-Sanchez, M.; Lercher, J. A. Single-site trinuclear copper oxygen clusters in mordenite for selective conversion of methane to methanol, *Nat. Commun.* **2015**, 6, 7546.
- (10) Artiglia, L.; Sushkevich, V. L.; Palagin, D.; Knorpp, A. J.; Roy, K.; van Bokhoven, J. A. In Situ X-ray Photoelectron Spectroscopy Detects Multiple Active Sites Involved in the Selective Anaerobic Oxidation of Methane in Copper-Exchanged Zeolites, *ACS Catal.* **2019**, 9, 6728.
- (11) Dinh, K. T.; Sullivan, M. M.; Serna, P.; Meyer, R. J.; Dinca, M.; Roman-Leshkov, Y. Viewpoint on the Partial Oxidation of Methane to Methanol Using Cu- and Fe-Exchanged Zeolites, *ACS Catal.* **2018**, 8, 8306.
- (12) Groothaert, M. H.; Smeets, P. J.; Sels, B. F.; Jacobs, P. A.; Schoonheydt, R. A. Selective Oxidation of Methane by the Bis( $\mu$ -oxo)dicopper Core Stabilized on ZSM-5 and

Mordenite Zeolites, *J. Am. Chem. Soc.* **2005**, *127*, 1394.

(13) Groothaert, M. H.; van Bokhoven, J. A.; Battiston, A. A.; Weckhuysen, B. M.; Schoonheydt, R. A. Bis( $\mu$ -oxo)dicopper in Cu-ZSM-5 and Its Role in the Decomposition of NO: A Combined in Situ XAFS, UV-Vis-Near-IR, and Kinetic Study, *J. Am. Chem. Soc.* **2003**, *125*, 7629.

(14) Kulkarni, A. R.; Zhao, Z. J.; Siahrostami, S.; Norskov, J. K.; Studt, F. Cation-exchanged zeolites for the selective oxidation of methane to methanol, *Catal. Sci. Technol* **2018**, *8*, 114.

(15) Kvande, K.; Pappas, D. K.; Borfecchia, E.; Lomachenko, K. A. Advanced X-ray Absorption Spectroscopy Analysis to Determine Structure-Activity Relationships for Cu-Zeolites in the Direct Conversion of Methane to Methanol, *Chemcatchem* **2020**, *12*, 2385.

(16) Martini, A.; Signorile, M.; Negri, C.; Kvande, K.; Lomachenko, K. A.; Svelle, S.; Beato, P.; Berlier, G.; Borfecchia, E.; Bordiga, S. EXAFS wavelet transform analysis of Cu-MOR zeolites for the direct methane to methanol conversion, *Phys. Chem. Chem. Phys.* **2020**, *22*, 18950.

(17) Newton, M. A.; Knorpp, A. J.; Pinar, A. B.; Sushkevich, V. L.; Palagin, D.; van Bokhoven, J. A. On the Mechanism Underlying the Direct Conversion of Methane to Methanol by Copper Hosted in Zeolites; Braiding Cu K-Edge XANES and Reactivity Studies, *J. Am. Chem. Soc.* **2018**, *140*, 10090.

(18) Newton, M. A.; Knorpp, A. J.; Sushkevich, V. L.; Palagin, D.; van Bokhoven, J. A. Active sites and mechanisms in the direct conversion of methane to methanol using Cu in zeolitic hosts: a critical examination, *Chemical Society Reviews* **2020**, *49*, 1449.

(19) Palomino, G. T.; Bordiga, S.; Zecchina, A.; Marra, G. L.; Lamberti, C. XRD, XAS, and IR Characterization of Copper-Exchanged Y Zeolite, *J. Phys. Chem. B* **2000**, *104*, 8641.

(20) Park, M. B.; Ahn, S. H.; Mansouri, A.; Ranocchiari, M.; van Bokhoven, J. A. Comparative Study of Diverse Copper Zeolites for the Conversion of Methane into Methanol, *Chemcatchem* **2017**, *9*, 3705.

(21) Ravi, M.; Sushkevich, V. L.; Knorpp, A. J.; Newton, M. A.; Palagin, D.; Pinar, A. B.; Ranocchiari, M.; van Bokhoven, J. A. Misconceptions and challenges in methane-to-methanol over transition-metal-exchanged zeolites, *Nat. Catal.* **2019**, *2*, 485.

(22) Snyder, B. E. R.; Bols, M. L.; Schoonheydt, R. A.; Sels, B. F.; Solomon, E. I. Iron and Copper Active Sites in Zeolites and Their Correlation to Metalloenzymes, *Chemical Reviews* **2018**, *118*, 2718.

(23) Snyder, B. E. R.; Vanelderen, P.; Bols, M. L.; Hallaert, S. D.; Bottger, L. H.; Ungur, L.; Pierloot, K.; Schoonheydt, R. A.; Sels, B. F.; Solomon, E. I. The active site of low-temperature methane hydroxylation in iron-containing zeolites, *Nature* **2016**, *536*, 317.

(24) Sushkevich, V. L.; Safonova, O. V.; Palagin, D.; Newton, M. A.; van Bokhoven, J. A. Structure of copper sites in zeolites examined by Fourier and wavelet transform analysis of EXAFS, *Chem. Sci.* **2020**, *11*, 5299.

(25) Tomkins, P.; Ranocchiari, M.; van Bokhoven, J. A. Direct Conversion of Methane to Methanol under Mild Conditions over Cu-Zeolites and beyond, *Accounts Chem. Res.* **2017**, *50*, 418.

(26) Zhao, X. L.; Xu, J.; Deng, F. Solid-state NMR for metal-containing zeolites: From active sites to reaction mechanism, *Front. Chem. Sci. Eng.* **2020**, *14*, 159.

(27) Avila Ferrer, F. J.; Cerezo, J.; Stendardo, E.; Improta, R.; Santoro, F. Insights for an Accurate Comparison of Computational Data to Experimental Absorption and Emission Spectra: Beyond the Vertical Transition Approximation, *J. Chem. Theory Comput.* **2013**, *9*, 2072.

- (28) Casida, M. E. In *Recent Advances in Density Functional Methods*, p 155.
- (29) Rowe, D. J. An interpretation of time-dependent Hartree-Fock theory, *Nucl. Phys.* **1966**, *80*, 209.
- (30) Woertink, J. S.; Smeets, P. J.; Groothaert, M. H.; Vance, M. A.; Sels, B. F.; Schoonheydt, R. A.; Solomon, E. I. A  $[\text{Cu}_2\text{O}]^{2+}$  core in Cu-ZSM-5, the active site in the oxidation of methane to methanol, *P. Natl. Acad. Sci. USA* **2009**, *106*, 18908.
- (31) Li, H.; Paolucci, C.; Khurana, I.; Wilcox, Laura N.; Göttl, F.; Albarracin-Caballero, J. D.; Shih, A. J.; Ribeiro, F. H.; Gounder, R.; Schneider, W. F. Consequences of exchange-site heterogeneity and dynamics on the UV-visible spectrum of Cu-exchanged SSZ-13, *Chem. Sci.* **2019**, *10*, 2373.
- (32) Göttl, F.; Conrad, S.; Wolf, P.; Müller, P.; Love, A. M.; Burt, S. P.; Wheeler, J. N.; Hamers, R. J.; Hummer, K.; Kresse, G.; Mavrikakis, M.; Hermans, I. UV-Vis and Photoluminescence Spectroscopy to Understand the Coordination of Cu Cations in the Zeolite SSZ-13, *Chem. Mater.* **2019**, *31*, 9582.
- (33) Salpeter, E. E.; Bethe, H. A. A Relativistic Equation for Bound-State Problems, *Phys. Rev.* **1951**, *84*, 1232.
- (34) Blase, X.; Duchemin, I.; Jacquemin, D.; Loos, P.-F. The Bethe–Salpeter Equation Formalism: From Physics to Chemistry, *J. Phys. Chem. Lett.* **2020**, *11*, 7371.
- (35) Ipek, B.; Wulfers, M. J.; Kim, H.; Göttl, F.; Hermans, I.; Smith, J. P.; Booksh, K. S.; Brown, C. M.; Lobo, R. F. Formation of  $[\text{Cu}_2\text{O}_2]^{2+}$  and  $[\text{Cu}_2\text{O}]^{2+}$  toward C–H Bond Activation in Cu-SSZ-13 and Cu-SSZ-39, *ACS Catal.* **2017**, *7*, 4291.
- (36) Cramer, C. J.; Truhlar, D. G. Density functional theory for transition metals and transition metal chemistry, *Phys. Chem. Chem. Phys.* **2009**, *11*, 10757.
- (37) Chan, B.; Gill, P. M. W.; Kimura, M. Assessment of DFT Methods for Transition Metals with the TMC151 Compilation of Data Sets and Comparison with Accuracies for Main-Group Chemistry, *J. Chem. Theory Comput.* **2019**, *15*, 3610.
- (38) Harvey, J. N. On the accuracy of density functional theory in transition metal chemistry, *Annu. Rep. Prog. Chem., Sect. C: Phys. Chem* **2006**, *102*, 203.
- (39) Hieringer, W.; Görling, A. Failure of time-dependent density functional methods for excitations in spatially separated systems, *Chem. Phys. Lett.* **2006**, *419*, 557.
- (40) Marques, M. A. L.; Gross, E. K. U. Time-dependent density functional theory, *Annu. Rev. Phys. Chem.* **2004**, *55*, 427.
- (41) Kümmel, S. Charge-Transfer Excitations: A Challenge for Time-Dependent Density Functional Theory That Has Been Met, *Adv. Energy Mater.* **2017**, *7*, 1700440.
- (42) Casanova-Páez, M.; Dardis, M. B.; Goerigk, L.  $\omega$ B2PLYP and  $\omega$ B2GPPLYP: The First Two Double-Hybrid Density Functionals with Long-Range Correction Optimized for Excitation Energies, *J. Chem. Theory Comput.* **2019**, *15*, 4735.
- (43) Casanova-Páez, M.; Goerigk, L. Assessing the Tamm–Dancoff approximation, singlet–singlet, and singlet–triplet excitations with the latest long-range corrected double-hybrid density functionals, *J. Chem. Phys.* **2020**, *153*, 064106.
- (44) Goerigk, L.; Casanova-Paéz, M. The Trip to the Density Functional Theory Zoo Continues: Making a Case for Time-Dependent Double Hybrids for Excited-State Problems, *Aust. J. Chem.* **2020**,
- (45) Curtis, K.; Panthi, D.; Odoh, S. O. A Time-Dependent DFT Study of Copper (II) Oxo Active Sites for Methane-to-Methanol Conversion in Zeolites, *Inorg. Chem.* **2020**, *submitted*,
- (46) Head-Gordon, M.; Rico, R. J.; Oumi, M.; Lee, T. J. A doubles correction to



electronic excited states from configuration interaction in the space of single substitutions, *Chem. Phys. Lett.* **1994**, 219, 21.

(47) Grimme, S.; Neese, F. Double-hybrid density functional theory for excited electronic states of molecules, *J. Chem. Phys.* **2007**, 127, 154116.

(48) Kim, Y.; Kim, T. Y.; Lee, H.; Yi, J. Distinct activation of Cu-MOR for direct oxidation of methane to methanol, *Chem. Commun.* **2017**, 53, 4116.

(49) Becke, A. D. Density-functional thermochemistry. III. The role of exact exchange, *J. Chem. Phys.* **1993**, 98, 5648.

(50) Lee, C.; Yang, W.; Parr, R. G. Development of the Colle-Salvetti correlation-energy formula into a functional of the electron density, *Phys. Rev. B.* **1988**, 37, 785.

(51) Stephens, P. J.; Devlin, F. J.; Chabalowski, C. F.; Frisch, M. J. Ab Initio Calculation of Vibrational Absorption and Circular Dichroism Spectra Using Density Functional Force Fields, *J. Phys. Chem.* **1994**, 98, 11623.

(52) Grimme, S.; Antony, J.; Ehrlich, S.; Krieg, H. A consistent and accurate ab initio parametrization of density functional dispersion correction (DFT-D) for the 94 elements H-Pu, *J. Chem. Phys.* **2010**, 132, 154104.

(53) Grimme, S.; Ehrlich, S.; Goerigk, L. Effect of the damping function in dispersion corrected density functional theory, *J. Comput. Chem.* **2011**, 32, 1456.

(54) Becke, A. D.; Johnson, E. R. A density-functional model of the dispersion interaction, *J. Chem. Phys.* **2005**, 123, 154101.

(55) Becke, A. D.; Johnson, E. R. Exchange-hole dipole moment and the dispersion interaction, *J. Chem. Phys.* **2005**, 122, 154104.

(56) Laun, J.; Vilela Oliveira, D.; Bredow, T. Consistent gaussian basis sets of double- and triple-zeta valence with polarization quality of the fifth period for solid-state calculations, *J. Comput. Chem.* **2018**, 39, 1285.

(57) Neese, F. Software update: the ORCA program system, version 4.0, *WIREs Comput. Mol. Sci.* **2018**, 8, e1327.

(58) Hirata, S.; Head-Gordon, M. Time-dependent density functional theory within the Tamm–Dancoff approximation, *Chem. Phys. Lett.* **1999**, 314, 291.

(59) Jr., T. H. D. Gaussian basis sets for use in correlated molecular calculations. I. The atoms boron through neon and hydrogen, *J. Chem. Phys.* **1989**, 90, 1007.

(60) Kendall, R. A.; Jr., T. H. D.; Harrison, R. J. Electron affinities of the first-row atoms revisited. Systematic basis sets and wave functions, *J. Chem. Phys.* **1992**, 96, 6796.

(61) Woon, D. E.; Jr., T. H. D. Gaussian basis sets for use in correlated molecular calculations. III. The atoms aluminum through argon, *J. Chem. Phys.* **1993**, 98, 1358.

(62) Kossmann, S.; Neese, F. Efficient Structure Optimization with Second-Order Many-Body Perturbation Theory: The RIJCOSX-MP2 Method, *J. Chem. Theory Comput.* **2010**, 6, 2325.

(63) Weigend, F.; Ahlrichs, R. Balanced basis sets of split valence, triple zeta valence and quadruple zeta valence quality for H to Rn: Design and assessment of accuracy, *Phys. Chem. Chem. Phys.* **2005**, 7, 3297.

(64) Petrakis, L. Spectral line shapes: Gaussian and Lorentzian functions in magnetic resonance, *J. Chem. Educ.* **1967**, 44, 432.

(65) Kokotailo, G. T.; Lawton, S. L.; Olson, D. H.; Meier, W. M. Structure of synthetic zeolite ZSM-5, *Nature* **1978**, 272, 437.

(66) Arvidsson, A. A.; Zhdanov, V. P.; Carlsson, P. A.; Gronbeck, H.; Hellman, A. Metal

dimer sites in ZSM-5 zeolite for methane-to-methanol conversion from first-principles kinetic modelling: is the  $[\text{Cu-O-Cu}]^{2+w}$  motif relevant for Ni, Co, Fe, Ag, and Au?, *Catal. Sci. Technol.* **2017**, *7*, 1470.

(67) Tsai, M.-L.; Hadt, R. G.; Vanelderen, P.; Sels, B. F.; Schoonheydt, R. A.; Solomon, E. I.  $[\text{Cu}_2\text{O}]^{2+}$  Active Site Formation in Cu-ZSM-5: Geometric and Electronic Structure Requirements for  $\text{N}_2\text{O}$  Activation, *J. Am. Chem. Soc.* **2014**, *136*, 3522.

(68) Oord, R.; Schmidt, J. E.; Weckhuysen, B. M. Methane-to-methanol conversion over zeolite Cu-SSZ-13, and its comparison with the selective catalytic reduction of  $\text{NO}_x$  with  $\text{NH}_3$ , *Catal. Sci. Technol.* **2018**, *8*, 1028.

(69) Wu, J.-F.; Gao, X.-D.; Wu, L.-M.; Wang, W. D.; Yu, S.-M.; Bai, S. Mechanistic Insights on the Direct Conversion of Methane into Methanol over Cu/Na-ZSM-5 Zeolite: Evidence from EPR and Solid-State NMR, *ACS Catal.* **2019**, *9*, 8677.

(70) Kolganov, A. A.; Gabrienko, A. A.; Yashnik, S. A.; Pidko, E. A.; Stepanov, A. G. Nature of the Surface Intermediates Formed from Methane on Cu-ZSM-5 Zeolite: A Combined Solid-State Nuclear Magnetic Resonance and Density Functional Theory Study, *J. Phys. Chem. C* **2020**, *124*, 6242.

(71) Mahyuddin, M. H.; Tanaka, T.; Shiota, Y.; Staykov, A.; Yoshizawa, K. Methane Partial Oxidation over  $[\text{Cu}_2(\mu\text{-O})]^{2+}$  and  $[\text{Cu}_3(\mu\text{-O})_3]^{2+}$  Active Species in Large-Pore Zeolites, *ACS Catal.* **2018**, *8*, 1500.

(72) Mahyuddin, M. H.; Staykov, A.; Shiota, Y.; Miyanishi, M.; Yoshizawa, K. Roles of Zeolite Confinement and Cu-O-Cu Angle on the Direct Conversion of Methane to Methanol by  $\text{Cu}_2(\mu\text{-O})^{2+}$ -Exchanged AEI, CHA, AFX, and MFI Zeolites, *ACS Catal.* **2017**, *7*, 3741.

(73) Mahyuddin, M. H.; Tanaka, T.; Staykov, A.; Shiota, Y.; Yoshizawa, K. Dioxygen Activation on Cu-MOR Zeolite: Theoretical Insights into the Formation of  $\text{Cu}_2\text{O}$  and  $\text{Cu}_3\text{O}_3$  Active Species, *Inorg. Chem.* **2018**, *57*, 10146.

(74) Yanai, T.; Tew, D. P.; Handy, N. C. A new hybrid exchange–correlation functional using the Coulomb-attenuating method (CAM-B3LYP), *Chem. Phys. Lett.* **2004**, *393*, 51.

(75) Dyballa, M.; Thorshaug, K.; Pappas, D. K.; Borfecchia, E.; Kvande, K.; Bordiga, S.; Berlier, G.; Lazzarini, A.; Olsbye, U.; Beato, P.; Svelle, S.; Arstad, B. Zeolite Surface Methoxy Groups as Key Intermediates in the Stepwise Conversion of Methane to Methanol, *Chemcatchem* **2019**, *11*, 5022.

(76) Sushkevich, V. L.; Verel, R.; van Bokhoven, J. A. Pathways of Methane Transformation over Copper-Exchanged Mordenite as Revealed by In Situ NMR and IR Spectroscopy, *Angewandte Chemie International Edition* **2020**, *59*, 910.

(77) Zheng, J.; Lee, I.; Khramenkova, E.; Wang, M.; Peng, B.; Gutierrez, O. Y.; Fulton, J. L.; Camaioni, D. M.; Khare, R.; Jentys, A.; Haller, G. L.; Pidko, E. A.; Sanchez-Sanchez, M.; Lercher, J. A. Importance of Methane Chemical Potential for Its Conversion to Methanol on Cu-Exchanged Mordenite, *Chem-Eur. J.* **2020**, *26*, 7563.

(78) Odoh, S. O.; Adeyiga, O. Methane Over-Oxidation by Extra-Framework Copper-Oxo Active Sites of Copper-Exchanged Zeolites: Crucial Role of Traps for the Separated Methyl Group, *ChemPhysChem*, *n/a*,

(79) Suleiman, O.; Adeyiga, O.; Panthi, D.; Odoh, S. O. Copper-Oxo Active Sites in the 8MR of Zeolite Mordenite: DFT Investigation of the Impact of Acid Sites on Methanol Yield and Selectivity, *J. Phys. Chem. C* **2021**, *125*,

(80) Dandu, N. K.; Adeyiga, O.; Panthi, D.; Bird, S. A.; Odoh, S. O. Performance of density functional theory for describing hetero-metallic active-site motifs for methane-to-methanol

conversion in metal-exchanged zeolites, *J. Comput. Chem.* **2018**, *39*, 2667.

(81) Vogiatzis, K. D.; Li, G.; Hensen, E. J. M.; Gagliardi, L.; Pidko, E. A. Electronic Structure of the  $[\text{Cu}_3(\mu\text{-O})_3]^{2+}$  Cluster in Mordenite Zeolite and Its Effects on the Methane to Methanol Oxidation, *J. Phys. Chem. C* **2017**, *121*, 22295.

(82) Ikuno, T.; Grundner, S.; Jentys, A.; Li, G.; Pidko, E.; Fulton, J.; Sanchez-Sanchez, M.; Lercher, J. A. Formation of Active Cu-oxo Clusters for Methane Oxidation in Cu-Exchanged Mordenite, *J. Phys. Chem. C* **2019**, *123*, 8759.

(83) Sushkevich, V. L.; van Bokhoven, J. A. Effect of Brønsted acid sites on the direct conversion of methane into methanol over copper-exchanged mordenite, *Catal. Sci. Technol* **2018**, *8*,

(84) Sushkevich, V. L.; van Bokhoven, J. A. Kinetic study and effect of water on methane oxidation to methanol over copper-exchanged mordenite, *Catal. Sci. Technol* **2020**, *10*, 382.

(85) Zheng, J.; Lee, I.; Khramenkova, E.; Wang, M.; Peng, B.; Gutiérrez, O. Y.; Fulton, J. L.; Camaioni, D. M.; Khare, R.; Jentys, A.; Haller, G. L.; Pidko, E. A.; Sanchez-Sanchez, M.; Lercher, J. A. Importance of Methane Chemical Potential for Its Conversion to Methanol on Cu-exchanged Mordenite, *Chem-Eur. J.* **2020**, *26*, 7515.

## CHAPTER 6. HETEROMETALLIC $[\text{Cu-O-M}]^{2+}$ ACTIVE SITES FOR METHANE C-H ACTIVATION IN ZEOLITES: STABILITY, REACTIVITY, FORMATION MECHANISM AND RELATIONSHIP TO OTHER ACTIVE SITES

Olajumoke Adeyiga<sup>#</sup>, Dipak Panthi<sup>#</sup> and Samuel O. Odoh<sup>\*</sup>

Department of Chemistry, University of Nevada Reno, 1664 N. Virginia Street, Reno, NV  
89557-0216

“Reprinted (adapted) with permission from *Catal. Sci. Technol.*, 2021, *11*, 5671-5683.

Copyright (2021) Royal Society of Chemistry”

**ABSTRACT:** The formation and reactivities of  $[\text{Cu-O-M}]^{2+}$  species (M = Ti-Cu, Zr-Mo and Ru-Ag) in metal-exchanged zeolites, as well as stabilities of these species towards autoreduction by  $\text{O}_2$  elimination are investigated with density functional theory. These species were investigated in zeolite mordenite in search of insights into active site formation mechanisms, relationship between stability and reactivity as well as discovery of heterometallic species useful for isothermal methane-to-methanol conversion (MMC). Several  $[\text{Cu-O-M}]^{2+}$  species (M = Ti-Cr and Zr-Mo) are substantially more stable than  $[\text{Cu}_2\text{O}]^{2+}$ . Other  $[\text{Cu-O-M}]^{2+}$  species, (M = Mn-Ni and Ru-Ag) have similar formation energies as  $[\text{Cu}_2\text{O}]^{2+}$ , to within  $\pm 10$

kcal/mol. Interestingly, only  $[\text{Cu-O-Ag}]^{2+}$  is more active for methane activation than  $[\text{Cu}_2\text{O}]^{2+}$ .  $[\text{Cu-O-Ag}]^{2+}$  is however more susceptible to  $\text{O}_2$  elimination. By considering the formation energies, autoreduction, cost and activity towards the methane C-H bond, we can only conclude that  $[\text{Cu}_2\text{O}]^{2+}$  is best suited for MMC. Formation of  $[\text{Cu}_2\text{O}]^{2+}$  is initiated by proton transfer from aquo ligands to the framework and proceeds mostly via dehydration steps. Its  $\mu$ -oxo bridge is formed via water-assisted condensation of two hydroxo groups. To evaluate the relationship between  $[\text{Cu}_2\text{O}]^{2+}$  and other active sites, we also examined the formation energies of other species. The formation energies follow the trend: isolated  $[\text{Cu-OH}]^+ < \text{paired } [\text{Cu-OH}]^+ < [\text{Cu}_2\text{O}]^{2+} < [\text{Cu}_3\text{O}_3]^{2+}$ . Inclusion of Gibbs free-energy corrections indicate activation temperatures of 257, 307 and 327 and 331 °C for isolated  $[\text{Cu-OH}]^+$ , paired  $[\text{Cu-OH}]^+$ ,  $[\text{Cu}_2\text{O}]^{2+}$  and  $[\text{Cu}_3\text{O}_3]^{2+}$ , respectively. The provocative nature of the lower-than-expected activation temperature for isolated  $[\text{Cu-OH}]^+$  species is discussed.

## 6.1 INTRODUCTION

Methane is the major component of natural gas and activation of methane to produce commodity chemicals has generated significant interest. This is due to the desire to exploit natural gas reserves and address environmental concerns from widespread flaring of natural gas.<sup>1-3</sup> Currently, methane utilization involves energy-intensive pathways via generation of syngas.<sup>4-6</sup> These routes are used on a large scale but are not economically feasible for small-scale facilities, such as at remote gas fields. Hence, new approaches for methane conversion are of interest. Foremost amongst these is the direct selective oxidation of methane to methanol.<sup>7-</sup>

<sup>11</sup> Direct oxidation of methane to methanol occurs naturally in microorganisms, catalyzed by methane monooxygenase (MMO) enzymes. These contain di-iron and di-copper active centers.<sup>12-14</sup> As such, development of artificial catalysts for methane activation has focused on mimicking the structures of these active sites.<sup>15</sup> Zeolites have been considered as good candidates for hosting metallic centers that are reminiscent of those in MMO enzymes.<sup>16-18</sup> Many zeolites have been studied for this purpose. However, copper-exchanged mordenite (Cu-MOR) zeolites are some of the most interesting ones. Their large pores facilitate desorption of reaction products from copper active sites.<sup>7, 19-21</sup> Methane to methanol conversion, MMC, in zeolites like Cu-MOR is often carried out in a stepwise fashion. The process begins with

generation of copper active sites under oxidizing conditions. This is followed by contact with methane, leading to formation of intra-zeolite methoxy intermediates. Recent work has revealed that the methoxy intermediates are stabilized at Brønsted acid sites.<sup>22-25</sup> These methoxy groups are extracted as methanol in a third step, with water. At the end of each loop, the active sites are regenerated via thermal treatment with oxidants like O<sub>2</sub>, H<sub>2</sub>O and H<sub>2</sub>O<sub>2</sub>.<sup>26-28</sup> The activation and regeneration steps occur at 350-550 °C, while methane activation is carried out near 200 °C.

Active site species responsible for MMC in copper-exchanged zeolites have been extensively studied. Some of the proposed active sites are [Cu-OH]<sup>+</sup>, [Cu<sub>2</sub>O]<sup>+</sup> and [Cu<sub>3</sub>O<sub>3</sub>]<sup>2+</sup>. Many studies have focused on the relationships between these active sites, their speciation in various zeolites and under various synthesis conditions, their spectroscopic properties and their reactivities with methane.<sup>29-33</sup> Crucially, there is renewed interest in the capabilities of spectroscopic techniques for investigating the nuclearity of copper-oxo active sites.<sup>26, 29-32, 34, 35</sup> Additionally, there is an ongoing debate regarding preparation of zeolites with unique [Cu<sub>3</sub>O<sub>3</sub>]<sup>2+</sup> sites.<sup>13, 26, 33, 36</sup> In many cases, experimental investigations of copper-exchanged zeolites have been complemented with quantum-mechanical computations. However, the literature contains very little theoretical investigations of the pathway for forming the copper active sites during the activation step.<sup>19, 37</sup> In this work, we investigate the formation pathway for mono-(μ-oxo) dicopper [Cu<sub>2</sub>O]<sup>2+</sup> active sites. We also investigate the extent to which the thermodynamics for forming [Cu<sub>2</sub>O]<sup>2+</sup> species provide insights into activation temperatures. We focus on [Cu<sub>2</sub>O]<sup>2+</sup> as it is the only spectroscopically verified and the most ubiquitous active site motif under typical activation conditions.<sup>38</sup>

Several workers have used density functional theory (DFT)<sup>39, 40</sup> calculations to examine the stabilities and reactivities of heterobimetallic [Cu-O-M]<sup>2+</sup> active sites in various zeolites. These sites are analogous to [Cu<sub>2</sub>O]<sup>2+</sup> but with one copper center replaced with another metal. Zheng et al. examined how methane C-H activation barriers of [Cu-O-M]<sup>2+</sup> species are affected by the electronic structure properties of the μ-oxo site as well as the Cu-O-M bond angle in ZSM-5. They considered cases where M is Ag, Au, Cu or Zn.<sup>41</sup> Wang et al. performed a similar analysis for the MAZ zeolite using [Cu-O-M]<sup>2+</sup> species where M = Pd, Pt, Fe, Co, Ni, Au and Ag.<sup>42</sup> Kulkarni et al. also examined methane C-H reactivities of [Cu-O-Co]<sup>2+</sup>, [Cu<sub>2</sub>O]<sup>2+</sup>, [Cu-O-Fe]<sup>2+</sup> and [Cu-O-Ni]<sup>2+</sup>.<sup>43</sup> The stabilities of these [Cu-O-M]<sup>2+</sup> active sites are generally referenced against an oxidant (for example O<sub>2</sub> or N<sub>2</sub>O) and mono-cations bound to the zeolite, Cu<sup>+</sup> and M<sup>+</sup>.

Thus, the formation energies of  $[\text{Cu-O-M}]^{2+}$  sites were nearly always negative, exothermic. However, typical experimental setups involve calcining at high temperatures, sometimes initially in helium gas followed by exposure to oxidants. As such, modeling the relative stabilities of  $[\text{Cu}_2\text{O}]^{2+}$  and  $[\text{Cu-O-M}]^{2+}$  species must capture the endothermicity of the combined dehydration and oxidation steps. It is for this reason that we previously referenced the formation of various active sites against  $[\text{Cu}(\text{H}_2\text{O})_6]^{2+}$ .<sup>24</sup> This approach ensures that formation of the metal-oxo active sites is an endothermic process, thus allowing estimations of activation temperatures. It also aids quantitative descriptions of contributions from the dehydration and oxidation steps.

Lastly, van Bokhoven et al. have reported successful MMC under isothermal conditions near 200 °C.<sup>44</sup> In these experiments, the copper-exchanged zeolite is activated at the same temperature for reaction with methane. This is a path for removing thermal and temporal gradients between the activation and methane loading steps. However at 200 °C, it is generally thought that dehydrated  $[\text{Cu-OH}]^+$ ,  $[\text{Cu}_2\text{O}]^+$  and  $[\text{Cu}_3\text{O}_3]^{2+}$  active sites cannot exist. For this reason, there is significant interest in determining the natures of the copper species that engender MMC under isothermal conditions. In this work, we take a somewhat different approach. We consider whether tuning the heterometallic nature of the  $[\text{Cu-O-M}]^{2+}$  sites could lead to species that are sufficiently stable as to be activated near 200 °C. We do this by considering M as 3d (Ti-Ni) or 4d (Zr-Mo and Ru-Ag) transition metals. Additionally, heterometallic active sites like the  $[\text{Cu-O-M}]^{2+}$  species are considered interesting for chemical catalysis, especially in the spirit of mimicking heterobimetallic cores found in some metalloenzymes.<sup>45-50</sup> Here, we assess the usefulness of the  $[\text{Cu-O-M}]^{2+}$  species with DFT calculations of their formation, auto-reduction as well as their reactivities with methane. These computations will save great time in experimental investigations.

## 6.2 COMPUTATIONAL DETAILS

**6.2.1 Periodic DFT Calculations:** Periodic calculations were carried out with the Quantum Espresso software suite, version 6.4.1.<sup>51, 52</sup> We used periodic cells of the proton-form of zeolite mordenite,  $\text{H}_4\text{MOR}$ . In this system, there are four aluminate tetrahedra, with their charges balanced by four protons, Figure 6.1. The Si/Al ratio in  $\text{H}_4\text{MOR}$  is 11/1, matching well with previously studied experimental systems.<sup>36</sup> There are two aluminate tetrahedra at the mouth of the eight-membered ring, 8MR.

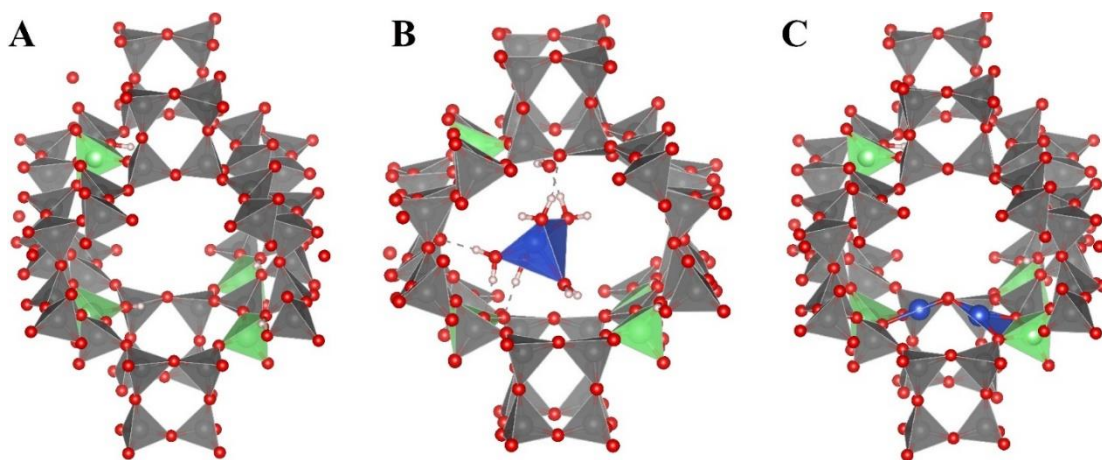
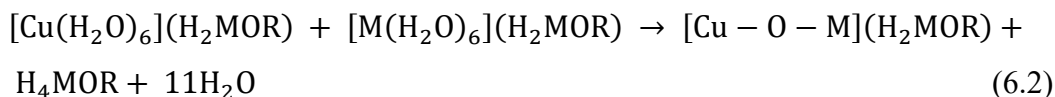


**Figure 6.1: Structures of (A) H<sub>4</sub>MOR, (B) [Cu(H<sub>2</sub>O)<sub>6</sub>](H<sub>2</sub>MOR) and (C) [Cu<sub>2</sub>O](H<sub>2</sub>MOR). O, Si, Al and Cu atoms are represented with red, grey, green and blue polyhedra, respectively. Locations of the charge-balancing protons are visible and the aluminates conform to Lowenstein's rule.**

These are used as the sites for the copper-oxo active sites, in agreement with previous reports.<sup>24, 25, 34, 36, 53</sup> The optimized structure of H<sub>4</sub>MOR was used to construct [Cu(H<sub>2</sub>O)<sub>6</sub>](H<sub>2</sub>MOR) and [Cu<sub>2</sub>O](H<sub>2</sub>MOR) species, Figure 6.1. In these, 2 protons are replaced by [Cu(H<sub>2</sub>O)<sub>6</sub>]<sup>2+</sup> and [Cu<sub>2</sub>O]<sup>2+</sup>, respectively. All other intermediate structures were also created from H<sub>4</sub>MOR. Additionally, for the species shown in Figure 6.1, the two aluminates in the bottom 8MR are separated by 3 silicates. Projected augmented wave pseudopotentials were used with charge density and wavefunction cut-offs set to 350.0 Ry and 50.0 Ry respectively.<sup>54, 55</sup> The PBE density functional<sup>56</sup> was employed with dispersion corrections included using the D3 scheme<sup>57, 58</sup> (PBE-D3). Sampling of the Brillouin zone was set to the  $\Gamma$  point. For transition state searches, the nudge elastic band (NEB) approach was used.<sup>59</sup> There are 6-8 images between each set of reactant and intermediate/product endpoints.

**6.2.2 Formation Reaction:** Formation energy of [Cu<sub>2</sub>O]<sup>2+</sup> sites can be obtained by considering 6.1. In this reaction, the copper-oxo site is formed via dehydration and oxidation of [Cu(H<sub>2</sub>O)<sub>6</sub>](H<sub>2</sub>MOR). [Cu(H<sub>2</sub>O)<sub>6</sub>](H<sub>2</sub>MOR) is a good the starting point for activation of copper-zeolites under near-neutral pH conditions.<sup>24</sup> With 6.1 we are referencing the stability of [Cu<sub>2</sub>O]<sup>2+</sup> active sites against [Cu(H<sub>2</sub>O)<sub>6</sub>]<sup>2+</sup>. There is a universal consensus that Cu assumes a hexaquo octahedral coordination after ion-exchange with zeolites in acidic pH conditions.<sup>36, 60-62</sup> Thus, it is eminently reasonable to reference the stabilities of the copper active sites against the hexaquo complex. Previous workers have considered the stabilities of copper-oxo species relative to bulk copper oxides, Cu<sup>+</sup> or [Cu-OH]<sup>+</sup>. For the heterometallic analogues of the

$[\text{Cu}_2\text{O}]^{2+}$  site, we use reaction 6.2. As stated earlier, M includes all  $3d$  transition metals (Ti-Ni) as well as all  $4d$  transition metals (Zr-Ag), except for Tc. We note that Lamberti et al. have previously reported that thermal activation of copper species in MOR causes desorption of water molecules.<sup>63</sup> Dehydration is accompanied by aggregation into  $[\text{Cu}_2\text{O}]^{2+}$  moieties. 6.1 and 6.2 conform to these experimental observations.



Interestingly, the aquo ligands in  $[\text{Cu}(\text{H}_2\text{O})_6](\text{H}_2\text{MOR})$  and  $[\text{M}(\text{H}_2\text{O})_6](\text{H}_2\text{MOR})$  can be arranged in various ways. Indeed, an octahedral structure as shown in Figure 6.1 is not necessarily the lowest energy geometry. As such, we initially performed an initial ab initio molecular dynamics, AIMD, simulation on these structures. Details of the AIMD protocol have been previously provided.<sup>34</sup> After a 20 ps equilibration step, we randomly extracted 20 structures over 40 ps simulation time. These were re-optimized Quantum Espresso. The most stable structures for  $[\text{Cu}(\text{H}_2\text{O})_6](\text{H}_2\text{MOR})$  and  $[\text{M}(\text{H}_2\text{O})_6](\text{H}_2\text{MOR})$  were used to compute reaction energies of 6.1 and 6.2. The considered spin states as well as relative spin state energies of all species involved in 6.1 and 6.2 are provided in the supporting information. The ground spin multiplicities of the  $[\text{Cu}-\text{O}-\text{M}](\text{H}_2\text{MOR})$  species are also provided in Table 6.1.

**Table 6.1: Ground state multiplicities (2S+1) of the  $[\text{Cu}-\text{O}-\text{M}]^{2+}$  active sites in the MOR zeolite.**

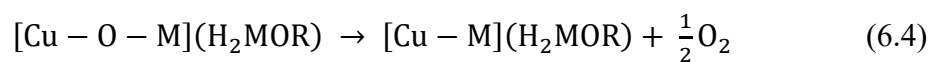
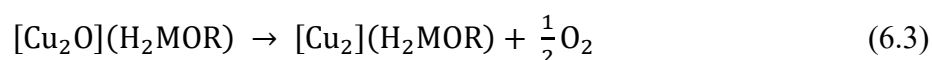
$3d$	Ti	V	Cr	Mn
	2	3	4	5
$4d$	Zr	Nb	Mo	
	2	3	4	
$3d$	Fe	Co	Ni	Cu
	4	5	4	0
$4d$	Ru	Rh	Pd	Ag
	2	1	2	3

To determine the impact of the exchange-correlation functional on the calculated reaction energies, we used the formation of  $[\text{Cu}_2\text{O}](\text{H}_2\text{MOR})$  as a testbed. Single-point calculations on



the PBE-D3-optimized structures were performed with rVV10<sup>64, 65</sup> and rev-vdW-DF2.<sup>66</sup> We also re-optimized the geometries with rVV10 for detailed comparison.

**6.2.3 Decomposition with Oxygen Elimination:** It has been reported that thermal treatment of zeolites containing  $[\text{Cu}_2\text{O}]^{2+}$  sites leads to elimination of molecular oxygen,  $\text{O}_2$ .<sup>61, 63</sup> Indeed, autoreduction of  $\text{Cu}^{2+}$  to  $\text{Cu}^+$  has been hypothesized to be due to emission of  $\text{O}_2$  from  $\mu$ -oxo bridges of  $[\text{Cu}_2\text{O}]^{2+}$  active sites.<sup>63</sup> This process is described in reaction 6.3. The thermodynamics of 6.3 has been used to previously gauge the stability of  $[\text{Cu}_2\text{O}]^{2+}$  active sites. Here, we extend this to heterometallic species containing all 3d and 4d transition metals, except Tc. Decomposition of the heterometallic species under anaerobic conditions is described by 6.4.



To summarize, these active sites are formed by dehydration and oxidation of aquo  $\text{Cu}^{2+}$  species, via thermal treatment. These steps are contained in reactions 6.1-6.2 and thus formation energies are appropriately referenced against aquo complexes. However, further thermal treatment of the active sites leads to autoreduction, as seen in 6.3-6.4. As such, we do not use 6.3 or 6.4 to describe the formation of the active sites, but rather to describe their stability towards  $\text{O}_2$  elimination. The spin states and relative spin state energies of species involved in 6.3 and 6.4 are also provided in the supporting information.

**6.2.4 Cluster-model Calculations:** Periodic DFT calculations provide accurate reaction energies for 6.1-6.4. However, obtaining Gibbs free-energy corrections with periodic DFT is very expensive. As such, we turn to representative cluster models for obtaining these corrections. Geometry optimizations and vibrational frequency analyses were carried out with cluster models for the isolated  $[\text{Cu}-\text{OH}]^+$ , paired  $[\text{Cu}-\text{OH}]^+$ ,  $[\text{Cu}_2\text{O}]^{2+}$  and  $[\text{Cu}_3\text{O}_3]^{2+}$  active sites in the 8MR of MOR, Figure 6.2. The terminating oxo sites of the cluster models were capped with protons. The positions of these protons were first optimized and then fixed in all other calculations. These cluster-model calculations were performed at the scalar relativistic level with the Priroda code<sup>67, 68</sup> while using the PBE functional and double- $\zeta$ -polarized quality basis sets for the large component and appropriate kinetically balanced basis sets for the small components.<sup>69, 70</sup> Vibrational frequency analyses were carried out with the harmonic approximation. This allows us to obtain Gibbs free-energy corrections at various temperatures (25 - 750 °C).

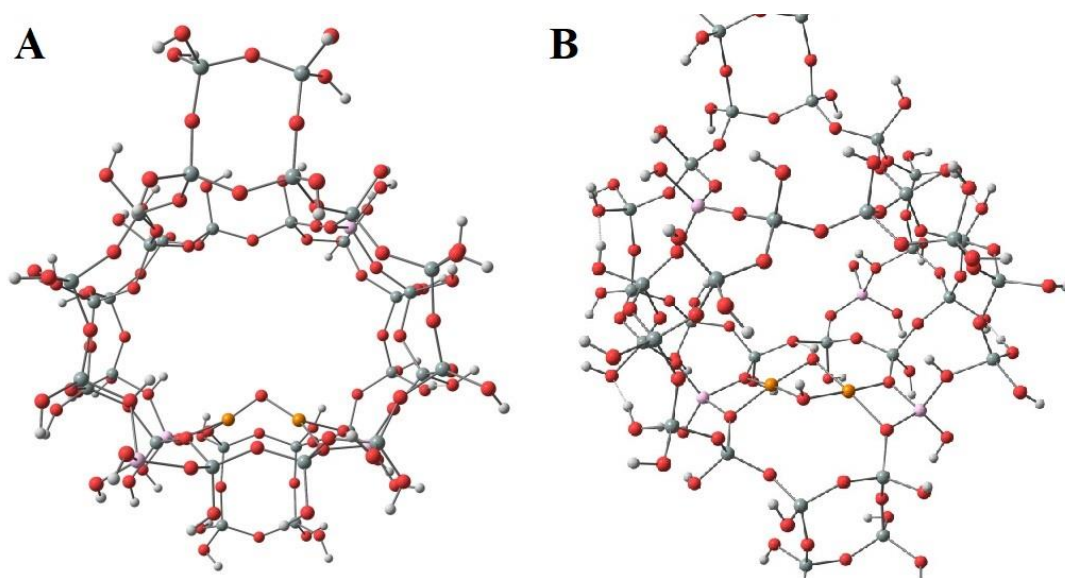


**Figure 6.2:** Cluster-model structures of (A)  $[\text{Cu}_2\text{O}]^{2+}$  and (B) paired  $[\text{Cu-OH}]^+$  in MOR. The latter is slightly rotated to allow easy visualization of the copper site. H, O, Si, Al and Cu atoms are represented with white, red, grey, pink and orange spheres, respectively.

## 6.3 RESULTS & DISCUSSION

We first present the lowest energy structures of the species involved in 6.1-6.2. We then discuss formation energies for  $[\text{Cu}_2\text{O}]^{2+}$  and  $[\text{Cu-O-M}]^{2+}$  active sites. The density functional dependence of the calculated formation energies are also discussed. The stabilities of the  $[\text{Cu}_2\text{O}]^{2+}$  and  $[\text{Cu-O-M}]^{2+}$  sites towards  $\text{O}_2$  elimination during thermal treatment are then described. This leads us to a description of the detailed mechanism for forming  $[\text{Cu}_2\text{O}]^{2+}$  sites. Lastly, the Gibbs free-energy corrections to the formation energy of  $[\text{Cu}_2\text{O}]^{2+}$  allows us to compare it to other copper active sites.

**6.3.1 Optimized Structures:** For  $[\text{Cu}(\text{H}_2\text{O})_6](\text{H}_2\text{MOR})$  and  $[\text{Cu}_2\text{O}](\text{H}_2\text{MOR})$ , we considered how the total energy is influenced by the sitings of the aluminate tetrahedra. In the latter, aluminates in the bottom 8MR bind directly to  $[\text{Cu}_2\text{O}]^{2+}$ . The aluminates can be separated by 2 or 3 silicates, leading to Al-Si-Si-Si-Al, Figure 6.1, or Al-Si-Si-Al arrangements, Figure 6.3. In  $[\text{Cu}_2\text{O}](\text{H}_2\text{MOR})$ , the total energies are largely indifferent to Al-Si-Si-Al or Al-Si-Si-Si-Al arrangements of the aluminates to which  $[\text{Cu}_2\text{O}]^{2+}$  is coordinated.<sup>71</sup> Indeed, species with Al-Si-Si-Al or Al-Si-Si-Si-Al differ only by 0.1-0.9 kcal/mol. For  $[\text{Cu}(\text{H}_2\text{O})_6](\text{H}_2\text{MOR})$ , structures in which the aluminates of the bottom 8MR possess the Al-Si-Si-Si-Al arrangement are more stable than those with Al-Si-Si-Al arrangement by 3.5-9.5 kcal/mol. Thus, we consider only species with the Al-Si-Si-Si-Al arrangement in all our subsequent discussions.

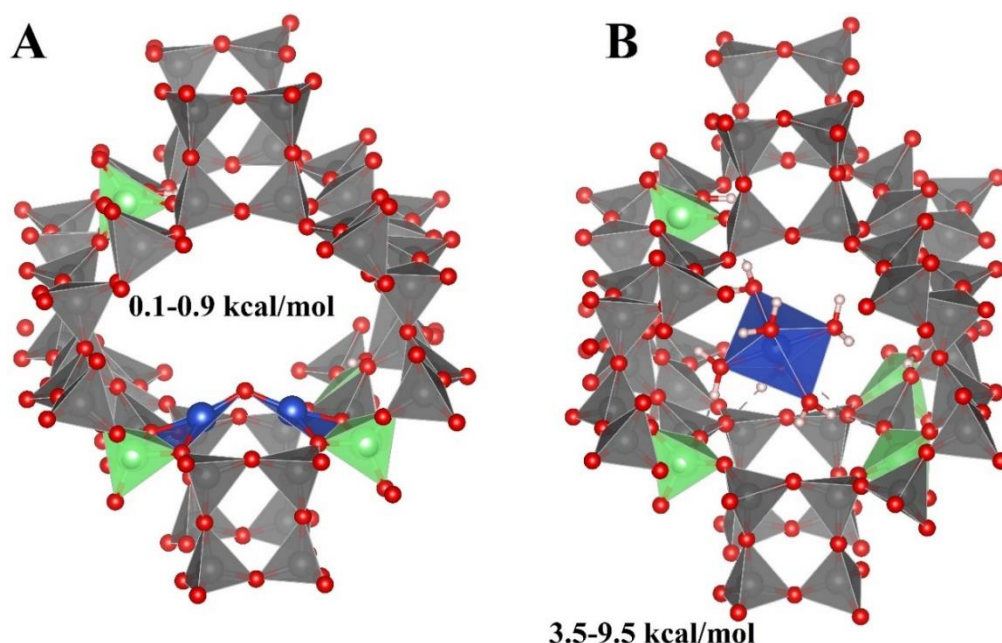


**Figure 6.3:** Periodic structures of (A)  $[\text{Cu}_2\text{O}](\text{H}_2\text{MOR})$  and (B)  $[\text{Cu}(\text{H}_2\text{O})_6](\text{H}_2\text{MOR})$  with Al-Si-Si-Al arrangements of the aluminates in the lower 8MR channel.

**6.3.2 Formation Energies:** Reaction energies for formation of  $[\text{Cu}_2\text{O}](\text{H}_2\text{MOR})$  via 6.1 are presented in Table 6.2. Results for rev-vdW-DF2 and rVV10 were obtained with PBE atomic pseudopotentials. The formation energy for  $[\text{Cu}_2\text{O}]^{2+}$  is 222.5 kcal/mol with PBE-D3. With rev-vdW-DF2, the formation energy is 214.8 kcal/mol. This is within 7.7 kcal/mol of PBE-D3. However, with rVV10, we obtain 233.3 kcal/mol, 10.7 kcal/mol higher than for PBE-D3. After re-optimizing the relevant geometries with rVV10, we obtained a reaction energy of 233.2 kcal/mol, Table 6.2. Overall, deviations due to the choice of exchange-correlation density functional as well as the structural dynamics of the  $[\text{Cu}(\text{H}_2\text{O})_6](\text{H}_2\text{MOR})$  reactants, Figure 6.3, allow us to estimate that there is likely an error bar of  $\pm 15$  kcal/mol associated with the calculated formation energies. Importantly, the formation energy for  $[\text{Cu}_2\text{O}]^{2+}$  is always positive, endothermic. Therefore, the temperature must be raised to dehydrate and oxidize  $[\text{Cu}(\text{H}_2\text{O})_6](\text{H}_2\text{MOR})$  reactants of reaction 6.1. This conforms to experimental protocols. As noted earlier, previous evaluations of the stabilities of copper-oxo active sites have used bulk copper oxides,  $[\text{Cu}-\text{OH}]^{+72}$  or  $\text{Cu}^+$  as references. In such cases, the formation reactions were exothermic. These are clearly in disaccordance with experimental practice of activating zeolites by raising the temperature.

**Table 6.2:** Calculated formation energies for the  $[\text{Cu}_2\text{O}]^{2+}$  active site.

Structure optimization	Single-point calculation	Reaction energy (kcal/mol)
------------------------	--------------------------	----------------------------

PBE-D3	PBE-D3	222.5
	rev-vdW-DF2	214.8
	rVV10	233.3
rVV10	rVV10	233.2

The formation energies for heterometallic  $[\text{Cu} - \text{O} - \text{M}](\text{H}_2\text{MOR})$  species display some trends, Figure 6.4. 3d elements in groups 7-10, Mn-Ni, give formation energies of  $[\text{Cu-O-M}]^{2+}$  similar to that of  $[\text{Cu}_2\text{O}]^{2+}$ . The formation energy of  $[\text{Cu-O-Ni}]^{2+}$  is 8.1 kcal/mol higher than for  $[\text{Cu}_2\text{O}]^{2+}$ . However, the formation energies of  $[\text{Cu-O-Mn}]^{2+}$ ,  $[\text{Cu-O-Fe}]^{2+}$  and  $[\text{Cu-O-Co}]^{2+}$  are all within 3 kcal/mol of  $[\text{Cu}_2\text{O}]^{2+}$ . By contrast, 3d elements in groups 4-6, Ti-Cr, yield formation energies below that of  $[\text{Cu}_2\text{O}]^{2+}$ . Formation energies of  $[\text{Cu-O-Ti}]^{2+}$ ,  $[\text{Cu-O-V}]^{2+}$  and  $[\text{Cu-O-Cr}]^{2+}$  are 27.3, 12.5 and 10.0 kcal/mol respectively lower than for  $[\text{Cu}_2\text{O}]^{2+}$ .

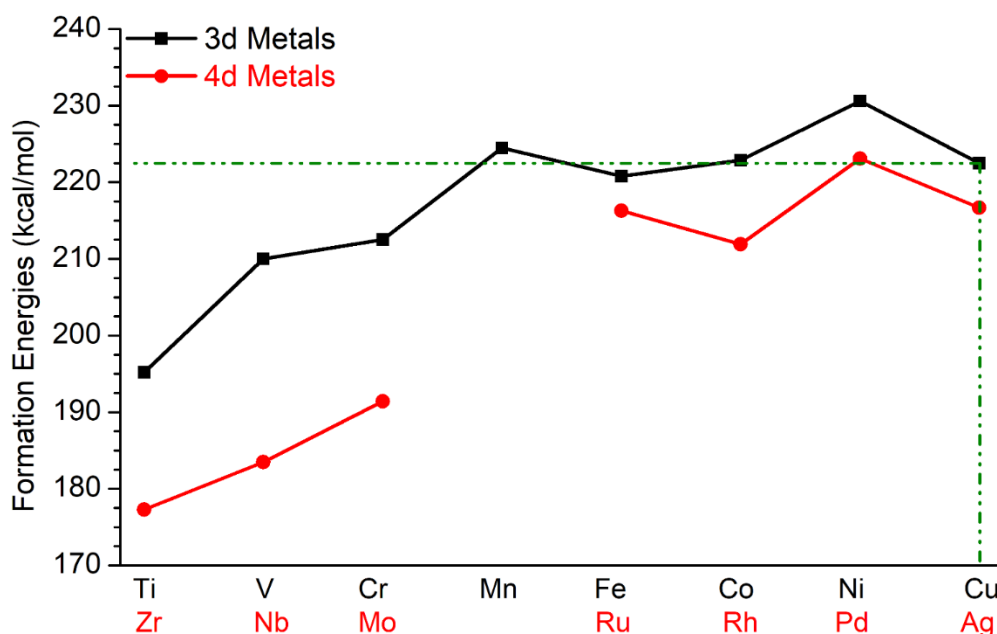


**Figure 6.4:** Formation energies of  $[\text{Cu-O-M}](\text{H}_2\text{MOR})$  species from  $[\text{Cu}(\text{H}_2\text{O})_6][\text{H}_2\text{MOR}]$  and  $[\text{M}(\text{H}_2\text{O})_6][\text{H}_2\text{MOR}]$  species.

The formation energies for all 4d-metal-containing  $[\text{Cu-O-M}]^{2+}$  species are lower than those of  $[\text{Cu}_2\text{O}]^{2+}$ , with Mo, Nb and Zr being the lowest, Figure 6.4. Indeed, the formation energies of  $[\text{Cu-O-Zr}]^{2+}$ ,  $[\text{Cu-O-Nb}]^{2+}$  and  $[\text{Cu-O-Mo}]^{2+}$  are 45.2, 39.0 and 31.1 kcal/mol lower than for  $[\text{Cu}_2\text{O}]^{2+}$ , respectively. The lower formation energies of these species suggest that they could be candidates for utilization under isothermal conditions. Also, the formation energies of  $[\text{Cu-O-Ru}]^{2+}$  and  $[\text{Cu-O-Rh}]^{2+}$  are 6.2 and 10.6 kcal/mol lower than for  $[\text{Cu}_2\text{O}]^{2+}$ , respectively. However, heterometallic Ru and Rh sites are not as stable as the Mo, Nb and Zr species.

Kulkarni et al. have previously described an inverse correlation between the formation energy of the active site motif and its reactivity towards methane.<sup>19, 43</sup>  $[\text{Cu-O-Ru}]^{2+}$  and  $[\text{Cu-O-Rh}]^{2+}$  could thus be the optimal trade-off between stability and reactivity. For this reason, we shall carefully consider  $[\text{Cu-O-Cr}]^{2+}$ ,  $[\text{Cu-O-V}]^{2+}$ ,  $[\text{Cu-O-Ti}]^{2+}$ ,  $[\text{Cu-O-Mo}]^{2+}$ ,  $[\text{Cu-O-Nb}]^{2+}$ ,  $[\text{Cu-O-Zr}]^{2+}$ ,  $[\text{Cu-O-Ru}]^{2+}$  and  $[\text{Cu-O-Rh}]^{2+}$  in subsequent discussions.

**6.3.3 Decomposition via Oxygen Elimination:** Reactions 6.3 and 6.4 involve elimination of  $\text{O}_2$  as well as reduction of  $\text{Cu}^{2+}$  to  $\text{Cu}^+$  and  $\text{M}^{2+}$  to  $\text{M}^+$ . These reduction processes would be favored under anaerobic conditions. In addition to the report of Lamberti et al., this autoreduction process has been widely reported, even in the presence of  $\text{O}_2$ .<sup>61</sup> The reaction energies for 6.3 and 6.4 are presented in Table 3. The calculated  $\text{O}_2$  elimination energy for  $[\text{Cu}_2\text{O}]^{2+}$  is 53.9 kcal/mol. This indicates that  $[\text{Cu}_2\text{O}]^{2+}$  is stable against  $\text{O}_2$  elimination. To achieve autoreduction of the  $\text{Cu}^{2+}$  sites of  $[\text{Cu}_2\text{O}]^{2+}$  to  $\text{Cu}^+$ , the temperature must be raised. This agrees with experimental observations of  $[\text{Cu}_2\text{O}]^{2+}$  aggregates prior to signatures for autoreduction, as the temperature is raised.<sup>61, 63, 73</sup> Compared to other  $3d$   $[\text{Cu-O-M}]^{2+}$  species, the  $\text{O}_2$  elimination energy of  $[\text{Cu}_2\text{O}]^{2+}$  is the smallest while the one for  $[\text{Cu-O-Ti}]^{2+}$  is the highest. We therefore see that the active sites are less stable against auto-reduction as one moves down the period. A similar trend occurs for  $4d$   $[\text{Cu-O-M}]^{2+}$  species, with  $[\text{Cu-O-Zr}]^{2+}$  being most stable and  $[\text{Cu-O-Ag}]^{2+}$  being least stable. Additionally, for elements in groups 4-8, the  $4d$  species are more stable than the  $3d$  species towards  $\text{O}_2$  elimination by 2.8-12.5 kcal/mol. By contrast, for elements in groups 9-11, the  $3d$  species are more resistant towards  $\text{O}_2$  elimination. Importantly, our 8 species of interest,  $[\text{Cu-O-Cr}]^{2+}$ ,  $[\text{Cu-O-V}]^{2+}$ ,  $[\text{Cu-O-Ti}]^{2+}$ ,  $[\text{Cu-O-Mo}]^{2+}$ ,  $[\text{Cu-O-Nb}]^{2+}$ ,  $[\text{Cu-O-Zr}]^{2+}$ ,  $[\text{Cu-O-Ru}]^{2+}$  and  $[\text{Cu-O-Rh}]^{2+}$ , provide  $\text{O}_2$  elimination energies that are higher than for  $[\text{Cu}_2\text{O}]^{2+}$ .

**Table 6.3: Energies, kcal/mol, for O<sub>2</sub> elimination from [Cu<sub>2</sub>O]<sup>2+</sup> and [Cu-O-M]<sup>2+</sup> active sites.**

3d	Ti	V	Cr	Mn
	114.9	105.7	88.6	73.1
4d	Zr	Nb	Mo	
	117.7	118.2	101.1	
3d	Fe	Co	Ni	Cu
	72.7	71.7	63.7	53.9
4d	Ru	Rh	Pd	Ag
	79.5	65.6	45.8	26.1

**6.3.4 Reactivity with Methane:** The activation barrier for the methane C-H bond is often used to evaluate the reactivities of copper-oxo active site. This makes sense in light of our recent report where we found that between methane and formates, the transition state for the first hydrogen atom abstraction step has the highest energy.<sup>25</sup> Thus, the methane C-H activation step is the rate-determining step. We therefore use the barriers associated with this step to evaluate the reactivities of the [Cu-O-M]<sup>2+</sup> species. We considered two possible routes for methane C-H dissociation. The first involves a radical-like transition state. This has been previously described.<sup>18, 76</sup> The second possibility is a surface-stabilized transition state in which the separated methyl group becomes bound to one of the metal centers.<sup>41, 77, 78</sup> However, prior to discussing the calculated barriers associated with the radical-like and surface-stabilized mechanisms, we first consider the energies of the species formed after methane C-H activation. In Table 6.4, the energies of the separated- (radical-like pathway) and surface-stabilized- (surface-stabilized pathway) -methyl intermediates are given relative to the adduct complex of methane and the active site. The separated-methyl intermediate is always less stable than the starting adduct complex. This conforms with the finding of Latimer et al.<sup>79</sup> for [Cu<sub>2</sub>O]<sup>2+</sup>. It gradually becomes less stable as we proceed from Cu (endothermic by +13.6 kcal/mol) to Ti (endothermic by +65.9 kcal/mol). The separated-methyl intermediates of [Cu-O-Cr]<sup>2+</sup>, [Cu-O-V]<sup>2+</sup> and [Cu-O-Ti]<sup>2+</sup> are so unstable that there is really no point considering the associated transition states. Indeed, for these species, we were not able to obtain the transition states for the surface-stabilized and separated-methyl mechanisms. The resulting barriers are sure to be high enough to prohibit methane activation at 200 °C. This is the case regardless of which spin state we considered. For these species, the barriers preclude methane activation at 200 °C.

Thus, while  $[\text{Cu-O-Cr}]^{2+}$ ,  $[\text{Cu-O-V}]^{2+}$  and  $[\text{Cu-O-Ti}]^{2+}$  are interesting from a stability perspective (activation temperatures), they are nonetheless not useful as they are unreactive at the moderate temperatures that favor methanol selectivity.

**Table 6.4: Relative energies (kcal/mol) of the intermediates formed after methane C-H activation by various  $[\text{Cu-O-M}]^{2+}$  active sites. The associated transition state barriers are given in parenthesis.**

	Separated $\text{CH}_3$	Surface-stabilized $\text{CH}_3$
Cu	+13.6 (19.9)	-10.4 (15.6)
Ni	+21.6 (23.5)	-13.4 (24.0)
Co	+24.2 (25.5)	-9.7 (28.1)
Fe	+28.3 (28.7)	-2.7 (30.3)
Mn	+29.1 (29.9)	-4.8 (30.9)
Cr	+43.4	+1.5 (42.7)
V	+53.0	+4.0
Ti	+65.9	+7.9
	Separated $\text{CH}_3$	Surface-stabilized $\text{CH}_3$
Ag	+4.5 (5.0)	-15.1 (5.1)
Pd	+19.2 (20.0)	-24.6 (20.1)
Rh		-12.5 (9.1)
Ru		-5.1 (24.7)
Mo		+7.9
Nb		+13.8
Zr		+7.6

For  $[\text{Cu}_2\text{O}]^{2+}$ , the barriers for the radical-like and surface-stabilized mechanisms are 19.9 and 15.6 kcal/mol, respectively, Table 6.4. These barriers indicate that  $[\text{Cu}_2\text{O}]^{2+}$  can activate methane at 200 °C. For the heterometallic Ni, Co, Fe and Mn species, the magnitudes of the barriers for both mechanisms also indicate the ability to activate methane at 200 °C. The barriers follow the trend  $\text{Cu} < \text{Ni} < \text{Co} < \text{Fe} \sim \text{Mn}$ , Table 6.4.

For 4d transition metals, the energies of the surface-stabilized intermediates for  $[\text{Cu-O-Mo}]^{2+}$ ,  $[\text{Cu-O-Nb}]^{2+}$  and  $[\text{Cu-O-Zr}]^{2+}$  are either similar or more positive than those of their 3d analogues. Thus, these species are also likely unreactive. For these species, we were not able to obtain the separated-methyl intermediates as well as the transition states involved in the surface-stabilized mechanism. Overall, the calculated barriers indicate that only  $[\text{Cu}_2\text{O}]^{2+}$ ,  $[\text{Cu-O-Ni}]^{2+}$ ,  $[\text{Cu-O-Co}]^{2+}$ ,  $[\text{Cu-O-Fe}]^{2+}$ ,  $[\text{Cu-O-Mn}]^{2+}$ ,  $[\text{Cu-O-Ag}]^{2+}$ ,  $[\text{Cu-O-Pd}]^{2+}$ ,  $[\text{Cu-O-Rh}]^{2+}$  and  $[\text{Cu-O-Ru}]^{2+}$  can activate methane at 200 °C. Of these, only  $[\text{Cu-O-Rh}]^{2+}$  and  $[\text{Cu-O-Ru}]^{2+}$  have

formation energies that are lower than for  $[\text{Cu}_2\text{O}]^{2+}$ , respectively 10.6 and 6.2 kcal/mol in Figure 6.4. With a likely error bar of  $\pm 15$  kcal/mol in the formation energies, it is unlikely that  $[\text{Cu-O-Rh}]^{2+}$  and  $[\text{Cu-O-Ru}]^{2+}$  can be formed at substantially lower temperatures than  $[\text{Cu}_2\text{O}]^{2+}$ . Their methane C-H activation barriers are also somewhat higher than that of  $[\text{Cu}_2\text{O}]^{2+}$ , suggesting lower methane conversions at 200 °C, Table 6.4. The only great advantage that  $[\text{Cu-O-Rh}]^{2+}$  and  $[\text{Cu-O-Ru}]^{2+}$  have over  $[\text{Cu}_2\text{O}]^{2+}$  lies in their greater resistance to autoreduction via  $\text{O}_2$  elimination, Table 6.3. On the other hand,  $[\text{Cu-O-Ag}]^{2+}$  provides significantly lower C-H activation barriers than  $[\text{Cu}_2\text{O}]^{2+}$ . However, it will be formed at nearly the same temperature as  $[\text{Cu}_2\text{O}]^{2+}$ , due to similar formation energies, Figure 6.4. It would also be more susceptible to autoreduction via  $\text{O}_2$  elimination, Table 6.3. Lastly, considering the difficulties associated with potential synthesis routes for  $[\text{Cu-O-Rh}]^{2+}$ ,  $[\text{Cu-O-Ru}]^{2+}$  and  $[\text{Cu-O-Ru}]^{2+}$  as well as the costs of Rh, Ru and Ag, one can only conclude that  $[\text{Cu}_2\text{O}]^{2+}$  is the best suited bis( $\mu$ -oxo) dinuclear active site for methane activation under moderate reaction conditions.

**6.3.5 Formation Mechanism of  $[\text{Cu}_2\text{O}]^{2+}$  Sites:** Having shown that  $[\text{Cu}_2\text{O}]^{2+}$  is the optimal balance between formation energies, methane C-H reactivity, autoreduction and cost, we now turn to the mechanism by which this species is formed from hexaaquo  $\text{Cu}^{2+}$  species. Interestingly, the mechanism for formation of copper active sites has been experimentally investigated.<sup>36, 60, 61, 63, 72, 80-83</sup> It is understood that dissociation of water molecules transforms the  $[\text{Cu}(\text{H}_2\text{O})_6]^{2+}$  complex to hydroxylated  $[\text{Cu}(\text{H}_2\text{O})_x(\text{OH})]^{+}$  species. These findings will guide our description of a plausible mechanism for forming the  $[\text{Cu}_2\text{O}]^{2+}$  active site, in the absence of  $\text{O}_2$  or other oxidants. As written in 6.1, the  $\text{Cu}^{2+}$  sites of two  $[\text{Cu}(\text{H}_2\text{O})_6](\text{H}_2\text{MOR})$  unit cells need to be dehydrated prior to formation of  $[\text{Cu}_2\text{O}]^{2+}$ . We repeat again that 6.1 is the overall formation reaction. Additionally, we will carry out dissociation of water in one unit cell while the other cell remains unchanged. The hydroxylated Cu species from water dissociation then migrates to condensate with the unchanged Cu center. By doing this, we are implying that migration of Cu ions within the zeolitic framework is crucial to formation of the active sites. We are also implying that reduction of some of the Cu centers (via water dissociation and formation of hydroxyl ligands) is essential for migration. These resonate *clearly* with previous experimental reports.<sup>62</sup>

For  $[\text{Cu}(\text{H}_2\text{O})_6](\text{H}_2\text{MOR})$ , initial loss of two aquo ligands leads to  $[\text{Cu}(\text{H}_2\text{O})_4](\text{H}_2\text{MOR})$ , 6.5. This is an endothermic process, 46.4 kcal/mol. Subsequently, transfer of a proton from an aquo



ligand to a framework aluminate leads to formation of  $[\text{Cu}(\text{H}_2\text{O})_3(\text{OH})](\text{H}_3\text{MOR})$ , 6.6. This step is also endothermic, by 16.0 kcal/mol and has a reaction barrier of 16.9 kcal/mol. The low reaction barrier is due to a network-like stabilization of the aquo protons, Figure 6.5. The central copper complex of  $[\text{Cu}(\text{H}_2\text{O})_3(\text{OH})](\text{H}_3\text{MOR})$  then rearranges to form a species reminiscent of  $[\text{Cu}(\text{H}_2\text{O})_2(\text{OH})_2]$ , 6.7. This step costs only 0.6 kcal/mol. In  $[\text{Cu}(\text{H}_2\text{O})_2(\text{OH})_2](\text{H}_4\text{MOR})$ , both water molecules stabilize the two protons transferred to the framework, Figure 6.5. By transferring both protons, the framework is converted from  $\text{H}_2\text{MOR}$  to  $\text{H}_4\text{MOR}$ . In other words, the charges of all four aluminates in the unit cell are now balanced with protons, Figure 6.5.  $\text{H}_4\text{MOR}$  is one of the final products of reaction 6.1.

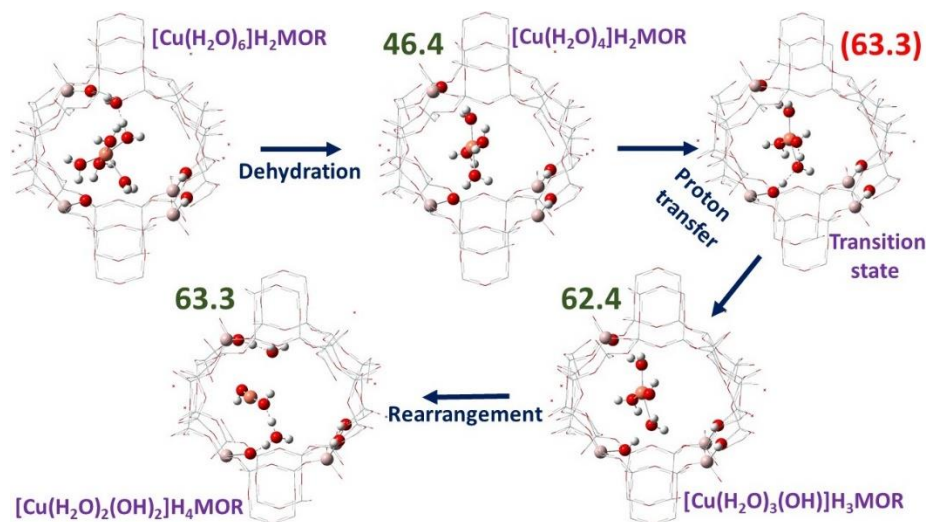
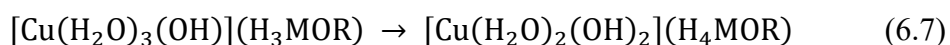
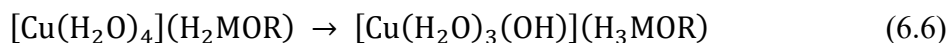
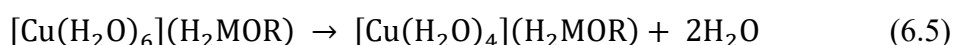
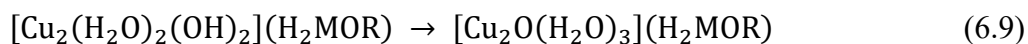
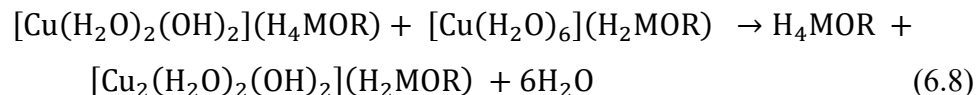


**Figure 6.5: Pathway for hexaaquo core of  $[\text{Cu}(\text{H}_2\text{O})_6](\text{H}_2\text{MOR})$  during formation of  $[\text{Cu}_2\text{O}]^{2+}$  sites. Reaction energies are given in green and kcal/mol. Barriers are given in red and parenthesis. These are all relative to  $[\text{Cu}(\text{H}_2\text{O})_6](\text{H}_2\text{MOR})$ . The four aluminates of the unit cell are also shown.**

Examination of the  $[\text{Cu}(\text{H}_2\text{O})_2(\text{OH})_2]$  group in  $[\text{Cu}(\text{H}_2\text{O})_2(\text{OH})_2](\text{H}_4\text{MOR})$  shows that it can diffuse along the main channel to adjacent 8MRs. As the  $[\text{Cu}(\text{H}_2\text{O})_2(\text{OH})_2]$  group migrates from its cell, it leaves behind  $\text{H}_4\text{MOR}$ . The migrating moiety can coalesce with the  $[\text{Cu}(\text{H}_2\text{O})_6]^{2+}$  core of a  $[\text{Cu}(\text{H}_2\text{O})_6](\text{H}_2\text{MOR})$  unit cell. In this process, the six aquo ligands of the  $[\text{Cu}(\text{H}_2\text{O})_6]^{2+}$  core are eliminated, 6.8. This combined aggregation and dehydration step brings the overall reaction energy to 158.7 kcal/mol and leads to  $[\text{Cu}_2(\text{H}_2\text{O})_2(\text{OH})_2](\text{H}_2\text{MOR})$ ,

which possesses a dinuclear core with two  $\mu$ -hydroxo groups, Figure 6.6. In summary, reactions 6.5-6.8 are a series of water-dissociation steps to form Cu-hydroxyl species, migration of these Cu-hydroxyl centers and finally condensation of the Cu-hydroxyl species to framework aluminate tetrahedra.<sup>62</sup>



Condensation of the two hydroxo groups leads to a mono-( $\mu$ -oxo) bridge between the copper centers and an aquo group, 6.9. This condensation costs 7.5 kcal/mol and brings the total reaction energy to 166.4 kcal/mol. However, the condensation proceeds in two steps, first breaking of a  $\mu(\text{OH})$ -Cu bond to create a dangling hydroxo group and second, a proton transfer from the  $\mu$ -hydroxo to the dangling hydroxo. The OH-Cu scission step costs 6.2 kcal/mol while the proton transfer step costs 1.3 kcal/mol. These OH-Cu scission and proton transfer steps have transition state barriers of 11.2 and 12.9 kcal/mol. Loss of 3 water ligands from  $[\text{Cu}_2\text{O}(\text{H}_2\text{O})_3](\text{H}_2\text{MOR})$

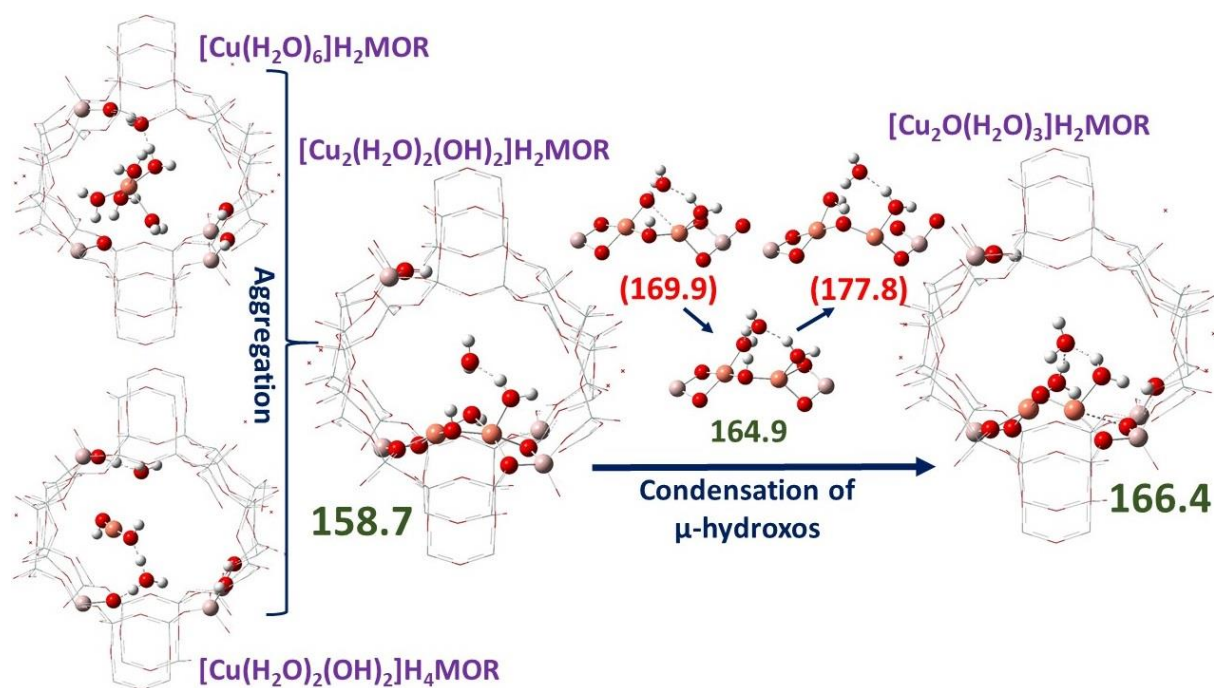


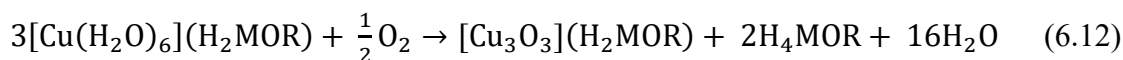
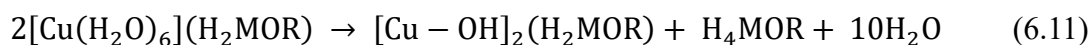
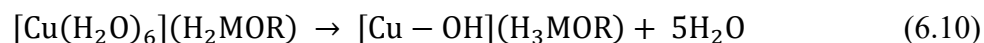
**Figure 6.6: Aggregation and dehydration steps during formation of  $[\text{Cu}_2\text{O}]^{2+}$ . Reaction energies are given in green and kcal/mol. Barriers are given in red and parenthesis. These are all relative to two  $[\text{Cu}(\text{H}_2\text{O})_6](\text{H}_2\text{MOR})$  reactants. Details of the condensation of  $\mu$ -hydroxo groups are shown.**

leads to  $[\text{Cu}_2\text{O}](\text{H}_2\text{MOR})$ , in which the charges of two aluminate groups are balanced by the  $[\text{Cu}_2\text{O}]^{2+}$  site. This dehydration step brings the overall reaction energy to 222.5 kcal/mol, Table 6.2.

Our results, Figures 6.4 and 6.5, reveal that dehydration steps are the most energy-consuming portions of the formation pathway for  $[\text{Cu}_2\text{O}]^{2+}$ . Additionally,  $[\text{Cu}_2\text{O}]^{2+}$  is formed via condensation of two hydroxo groups formed by proton transfer to framework aluminates. Thus, the  $\mu$ -oxo atom of  $[\text{Cu}_2\text{O}]^{2+}$  originates from water, rather than oxidants like  $\text{O}_2$  or  $\text{N}_2\text{O}$ .<sup>63, 72</sup> Lastly, transition states for the proton transfer and hydroxo condensation steps are stabilized greatly by hydrogen interactions with nearby water molecules. This further supports the crucial role of water during formation of the copper-oxo site. Overall, the calculated mechanism conforms to the experimental observations of Lamberti et al.<sup>63</sup>

**6.3.5 Free Energy Corrections and Comparison to other copper-oxo Sites:** The calculated electronic formation energy for  $[\text{Cu}_2\text{O}]^{2+}$  via 6.1 is 222.5 kcal/mol at the periodic PBE-D3 level, Table 6.2. Also, although all transition states are only 11.3-16.9 kcal/mol above their intermediates, it is crucial to note that the highest-energy transition state in the mechanism for  $[\text{Cu}_2\text{O}]^{2+}$  formation is 177.8 kcal/mol above the initial  $[\text{Cu}(\text{H}_2\text{O})_6](\text{H}_2\text{MOR})$  reactants, Figures 6.4 and 6.5. It becomes important that we consider Gibbs free-energy corrections, at least to the overall reaction energies. Additionally, comparing the formation free-energy of  $[\text{Cu}_2\text{O}]^{2+}$  to those of  $[\text{Cu}_3\text{O}_3]^{2+}$ , isolated  $[\text{Cu}-\text{OH}]^+$  and paired or dinuclear  $[\text{Cu}-\text{OH}]^+$  will provide insights into its relationships with other highly active copper-oxo species.

In our previous work, we showed that we could obtain reasonable estimates of the reaction free-energies.<sup>24</sup> We did this by considering only free-energy corrections for the central  $[\text{Cu}(\text{H}_2\text{O})_6]^{2+}$  core of  $[\text{Cu}(\text{H}_2\text{O})_6](\text{H}_2\text{MOR})$  and the eliminated water molecules. To further refine our approach, we here obtain the free-energy corrections using cluster-models that are representative of the MOR unit cell, see Supporting Information. The formation energies of, isolated  $[\text{Cu}-\text{OH}]^+$ , paired  $[\text{Cu}-\text{OH}]^+$  and  $[\text{Cu}_3\text{O}_3]^{2+}$  are calculated according to 6.10-6.12.



In Table 6.5, we present the formation energies of  $[\text{Cu}_2\text{O}]^{2+}$ ,  $[\text{Cu}_3\text{O}_3]^{2+}$ , isolated  $[\text{Cu}-\text{OH}]^+$  and paired  $[\text{Cu}-\text{OH}]^+$  obtained with periodic DFT and cluster-model calculations. The formation

energies follow the trend: isolated  $[\text{Cu-OH}]^+ < \text{paired } [\text{Cu-OH}]^+ < [\text{Cu}_2\text{O}]^{2+} < [\text{Cu}_3\text{O}_3]^{2+}$ . This matches well with the fact that 5, 10, 11 and 16 water molecules are released during the formation of isolated  $[\text{Cu-OH}]^+$ , paired  $[\text{Cu-OH}]^+$ ,  $[\text{Cu}_2\text{O}]^{2+}$  and  $[\text{Cu}_3\text{O}_3]^{2+}$  respectively. Also, the formation energies obtained from the cluster models are higher than those from periodic DFT, Table 6.5. This is likely because the cluster models are not able to capture long-range relaxation effects that occur in the crystal lattice after introduction of the copper active sites. However, the terminating protons of all model species in 6.1 and 6.10-6.12 are fixed at exactly the same positions. As such, we expect the Gibbs free-energy corrections for these reactions to be quite useful, Figure 6.7. There are several important things to note regarding results in Table 6.5 and Figure 6.7. First, paired  $[\text{Cu-OH}]^+$ ,  $[\text{Cu}_2\text{O}]^{2+}$  and  $[\text{Cu}_3\text{O}_3]^{2+}$  have formation energies of 232.2, 264.1 and 361.0 kcal/mol, respectively, from cluster-model DFT. By considering the free-energy corrections, these species are expected to be formed at 297, 327 and 331 °C, respectively. However, there is likely an error bar of  $\pm 15$  kcal/mol in the calculated formation energies, as discussed earlier.

**Table 6.5: Energies, kcal/mol, for formation of  $[\text{Cu}_2\text{O}]^{2+}$ ,  $[\text{Cu}_3\text{O}_3]^{2+}$ , isolated  $[\text{Cu-OH}]^+$  and paired  $[\text{Cu-OH}]^+$  active sites. Temperatures at which  $\Delta G$  becomes 0.0 kcal/mol are in °C.**

		$[\text{Cu}_2\text{O}]^{2+}$	$[\text{Cu}_3\text{O}_3]^{2+}$
Periodic structure:	$\Delta E$	222.5	348.1
PBE-D3			
Cluster-model: PBE	$\Delta E$	264.1	361.0
	$\Delta G$ at 25 °C	123.1	170.0
	Temp. for $\Delta G=0$	327	331
		$[\text{Cu-OH}]^+$	
		Isolated	Dinuclear/paired
Periodic structure:	$\Delta E$	106.7	190.2
PBE-D3			
Cluster-model: PBE	$\Delta E$	110.2	232.2
	$\Delta G$ at 25 °C	43.9	103.5
	Temp. for $\Delta G=0$	257	297

Thus, paired  $[\text{Cu-OH}]^+$ ,  $[\text{Cu}_2\text{O}]^{2+}$  and  $[\text{Cu}_3\text{O}_3]^{2+}$  can be formed at 267-347, 285-357 and 300-354 °C, respectively, Figure 6.7. These ranges are compatible with typical experimental protocols. Additionally, these temperature ranges suggest that paired  $[\text{Cu-OH}]^+$ ,  $[\text{Cu}_2\text{O}]^{2+}$  and  $[\text{Cu}_3\text{O}_3]^{2+}$  can co-exist or compete under certain conditions. We note that a recent report by Knorpp et al. identified paired  $[\text{Cu-OH}]^+$  as the active site species in zeolite omega.<sup>84</sup>

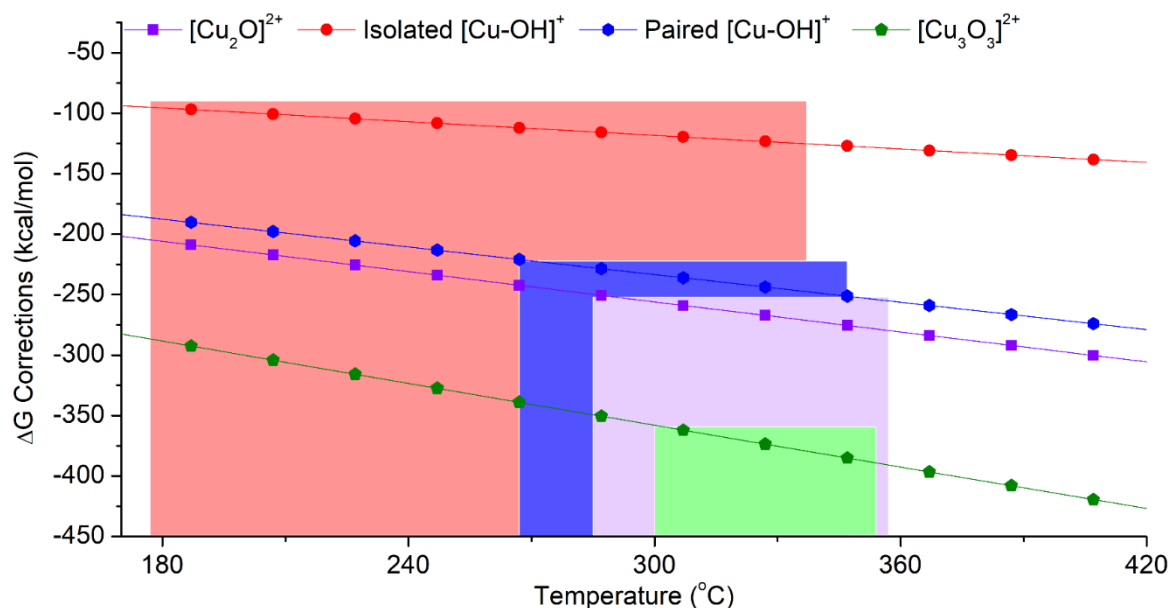


**Figure 6.7: Temperature-dependent free-energy corrections for formation of copper active sites in zeolite MOR. The shaded regions represent  $\pm 15$  kcal/mol around the electronic formation energies.**

Second, for isolated  $[\text{Cu-OH}]^+$  species, the formation energy is 110.2 kcal/mol from the cluster-model calculations. Free-energy corrections indicate that this species will be formed at 257 °C. This is quite low. Such a low activation temperature implicates isolated  $[\text{Cu-OH}]^+$  as a precursor for other copper active sites. This is consistent with the mechanism presented in Figure 6.6, where  $[\text{Cu}_2\text{O}]^{2+}$  is formed from ion pairs of  $[\text{Cu-OH}]^+$  as  $[\text{Cu}_2(\text{H}_2\text{O})_2(\text{OH})_2](\text{H}_2\text{MOR})$  species. The low activation temperature also implicate  $[\text{Cu-OH}]^+$  in previous isothermal MMC experiments near 200 °C.<sup>85-87</sup> This is particularly interesting given Kulkarni et al.'s report that  $[\text{Cu-OH}]^+$  activates the methane C-H bond with a barrier of 26.3 kcal/mol.<sup>88</sup> However, we emphasize that our calculations are relatively simple models of rather complex zeolite synthesis systems. We are also using the reaction thermodynamics to obtain insights into the activation temperatures. An error bar of  $\pm 15$  kcal/mol in the formation energies implies that isolated  $[\text{Cu-OH}]^+$  species will definitely be formed between 177 and 337 °C, Figure 6.7. It is thus quite likely that the active sites responsible for MMC in the isothermal MMC experiments are hydrated  $[\text{Cu-OH}]^+$  species.

## 6.4 CONCLUSIONS

Using scalar-relativistic periodic DFT, nudged elastic band and representative cluster-model calculations, we have investigated the formation energies of  $[\text{Cu}_2\text{O}]^{2+}$  and its heterometallic  $[\text{Cu-O-M}]^{2+}$  analogues (where  $\text{M} = \text{Ti-Cu}, \text{Zr-Mo}$  and  $\text{Ru-Ag}$ ) in the eight-membered ring of

zeolite mordenite, MOR. The heterometallic active site motifs are interesting from the perspective of mimicking the multi-metal centers of some metalloenzymes. We here use DFT calculations to examine their properties, prior to future experimental preparations and characterizations which might prove tedious and expensive. Particularly, the susceptibilities of these active site motifs to autoreduction by  $O_2$  elimination as well as their reactivities with the methane C-H bond were also investigated. A mechanism for the formation of  $[Cu_2O]^{2+}$  from copper-aquo species was provided. Lastly, to refine the absolute electronic energies obtained in this work, we calculated temperature-dependent Gibbs free-energy corrections. These are useful for estimating the activation temperatures of copper active sites and provide us a framework for comparing  $[Cu_2O]^{2+}$  to isolated  $[Cu-OH]^+$ , paired  $[Cu-OH]^+$  and  $[Cu_3O_3]^{2+}$ .

Our findings can be summarized thus:

- 4) The calculated formation energies divide the dinuclear active sites into two classes. On the one hand are  $[Cu-O-Cr]^{2+}$ ,  $[Cu-O-V]^{2+}$ ,  $[Cu-O-Ti]^{2+}$ ,  $[Cu-O-Mo]^{2+}$ ,  $[Cu-O-Nb]^{2+}$ ,  $[Cu-O-Zr]^{2+}$ , which are substantially more stable than  $[Cu_2O]^{2+}$ . These species will be expected to form at much lower temperatures than  $[Cu_2O]^{2+}$ . On the other hand are  $[Cu-O-Mn]^{2+}$ ,  $[Cu-O-Fe]^{2+}$ ,  $[Cu-O-Co]^{2+}$ ,  $[Cu-O-Ni]^{2+}$ ,  $[Cu-O-Ru]^{2+}$ ,  $[Cu-O-Rh]^{2+}$ ,  $[Cu-O-Pd]^{2+}$  and  $[Cu-O-Ag]^{2+}$  which have similar formation energies as  $[Cu_2O]^{2+}$ , to within 10 kcal/mol.
- 5) The autoreduction energies via  $O_2$  elimination indicate that only  $[Cu-O-Pd]^{2+}$  and  $[Cu-O-Ag]^{2+}$  are more susceptible towards autoreduction than  $[Cu_2O]^{2+}$ .
- 6) The C-H activation barrier was used to characterize the reactivities of the dinuclear active sites towards methane. Based on the calculated barriers, only  $[Cu_2O]^{2+}$ ,  $[Cu-O-Mn]^{2+}$ ,  $[Cu-O-Fe]^{2+}$ ,  $[Cu-O-Co]^{2+}$ ,  $[Cu-O-Ni]^{2+}$ ,  $[Cu-O-Ru]^{2+}$ ,  $[Cu-O-Rh]^{2+}$ ,  $[Cu-O-Pd]^{2+}$  and  $[Cu-O-Ag]^{2+}$  are useful for methane C-H activation at 200 °C. Only  $[Cu-O-Ag]^{2+}$  provides barriers lower than that of  $[Cu_2O]^{2+}$ . All other species (Ti-Cr and Zr-Mo) provide prohibitively high reaction barriers for methane activation at this temperature.
- 7) Based on the formation energies, autoreduction energies, cost and methane C-H bond reactivities, we can only conclude that  $[Cu_2O]^{2+}$  is best suited for methane-to-methanol conversion (MMC).
- 8) The mechanism for forming  $[Cu_2O]^{2+}$  from copper hexaaquo species was described. The reaction proceeds via proton transfer from the aquo ligands to aluminates. This is followed by migration of a  $Cu(OH)_2$ -type moiety to another unit cell where it aggregates

with  $\text{Cu}^{2+}$  to form a dinuclear bis( $\mu$ -hydroxo) species. Condensation of the hydroxo linkers is assisted by the proton-network of neighboring water molecules.

- 9) Gibbs free-energy corrections to the calculated formation energies of isolated  $[\text{Cu-OH}]^+$ , paired  $[\text{Cu-OH}]^{2+}$ ,  $[\text{Cu}_2\text{O}]^{2+}$  and  $[\text{Cu}_3\text{O}_3]^{2+}$  reveal that these species will be formed around 257, 297, 327 and 331 °C, respectively. Thus, these dicopper and tricopper species can co-exist and compete under certain conditions. The estimated activation temperature for isolated  $[\text{Cu-OH}]^+$  is very low. This indicates that  $[\text{Cu-OH}]^+$  is a precursor for other copper active sites. The low activation temperature also suggests that  $[\text{Cu-OH}]^+$  is likely involved in isothermal MMC experiments. By examining the limitations of our calculations, we conclude that isolated  $[\text{Cu-OH}]^+$  sites would definitely be formed between 170 and 340 °C and that the species involved in isothermal MMC experiments are most likely hydrated forms of isolated or paired  $[\text{Cu-OH}]^+$ .

## REFERENCES

1. G. A. Olah, *Angewandte Chemie International Edition*, 2005, **44**, 2636-2639.
2. J. H. Lunsford, *Catalysis Today*, 2000, **63**, 165-174.
3. J. Rostrup-Nielsen, France, 2004.
4. A. Holmen, *Catalysis Today*, 2009, **142**, 2-8.
5. P. Tang, Q. Zhu, Z. Wu and D. Ma, *Energy & Environmental Science*, 2014, **7**, 2580-2591.
6. K. Li, H. Wang and Y. Wei, *Journal of Chemistry*, 2013, **2013**, 294817.
7. M. Álvarez, P. Marín and S. Ordóñez, *Molecular Catalysis*, 2020, **487**, 110886.
8. N. V. Beznis, B. M. Weckhuysen and J. H. Bitter, *Catalysis Letters*, 2010, **138**, 14-22.
9. S. E. Bozbag, P. Sot, M. Nachtegaal, M. Ranocchiari, J. A. van Bokhoven and C. Mesters, *ACS Catalysis*, 2018, **8**, 5721-5731.
10. C. Hammond, M. M. Forde, M. H. Ab Rahim, A. Thetford, Q. He, R. L. Jenkins, N. Dimitratos, J. A. Lopez-Sanchez, N. F. Dummer, D. M. Murphy, A. F. Carley, S. H. Taylor, D. J. Willock, E. E. Stangland, J. Kang, H. Hagen, C. J. Kiely and G. J. Hutchings, *Angewandte Chemie-International Edition*, 2012, **51**, 5129-5133.
11. C. Hammond, R. L. Jenkins, N. Dimitratos, J. A. Lopez-Sanchez, M. H. ab Rahim, M. M. Forde, A. Thetford, D. M. Murphy, H. Hagen, E. E. Stangland, J. M. Moulijn, S. H. Taylor, D. J. Willock and G. J. Hutchings, *Chemistry-a European Journal*, 2012, **18**, 15735-15745.
12. M. O. Ross, F. MacMillan, J. Wang, A. Nisthal, T. J. Lawton, B. D. Olafson, S. L. Mayo, A. C. Rosenzweig and B. M. Hoffman, *Science*, 2019, **364**, 566.
13. B. E. R. Snyder, M. L. Bols, R. A. Schoonheydt, B. F. Sels and E. I. Solomon, *Chemical Reviews*, 2018, **118**, 2718-2768.
14. R. Balasubramanian, S. M. Smith, S. Rawat, L. A. Yatsunyk, T. L. Stemmler and A. C. Rosenzweig, *Nature*, 2010, **465**, 115-119.
15. L. Frunz, R. Prins and G. D. Pirngruber, *Chemistry of Materials*, 2007, **19**, 4357-4366.

16. A. W. Petrov, D. Ferri, O. Krocher and J. A. van Bokhoven, *Acs Catalysis*, 2019, **9**, 2303-2312.
17. M. B. Park, S. H. Ahn, A. Mansouri, M. Ranocchiari and J. A. van Bokhoven, *ChemCatChem*, 2017, **9**, 3705-3713.
18. M. H. Mahyuddin, Y. Shiota and K. Yoshizawa, *Catalysis Science & Technology*, 2019, **9**, 1744-1768.
19. Z.-J. Zhao, A. Kulkarni, L. Vilella, J. K. Nørskov and F. Studt, *ACS Catalysis*, 2016, **6**, 3760-3766.
20. E. M. Alayon, M. Nachtegaal, M. Ranocchiari and J. A. van Bokhoven, *Chemical Communications*, 2012, **48**, 404-406.
21. J. Zheng, I. Lee, E. Khramenkova, M. Wang, B. Peng, O. Y. Gutiérrez, J. L. Fulton, D. M. Camaioni, R. Khare, A. Jentys, G. L. Haller, E. A. Pidko, M. Sanchez-Sanchez and J. A. Lercher, *Chemistry – A European Journal*, 2020, **26**, 7563-7567.
22. M. Dyballa, K. Thorshaug, D. K. Pappas, E. Borfecchia, K. Kvande, S. Bordiga, G. Berlier, A. Lazzarini, U. Olsbye, P. Beato, S. Svelle and B. Arstad, *ChemCatChem*, 2019, **11**, 5022-5026.
23. V. L. Sushkevich and J. A. van Bokhoven, *Catalysis Science & Technology*, 2018, **8**, 4141-4150.
24. O. Suleiman, O. Adeyiga, D. Panthi and S. O. Odoh, *The Journal of Physical Chemistry C*, 2021, **125**, 6684-6693.
25. O. Adeyiga and S. O. Odoh, *Chemphyschem*, 2021, **22**, 1101-1109.
26. M. A. Newton, A. J. Knorpp, V. L. Sushkevich, D. Palagin and J. A. van Bokhoven, *Chemical Society Reviews*, 2020, **49**, 1449-1486.
27. M. H. Groothaert, P. J. Smeets, B. F. Sels, P. A. Jacobs and R. A. Schoonheydt, *Journal of the American Chemical Society*, 2005, **127**, 1394-1395.
28. Z. Liu, E. Huang, I. Orozco, W. Liao, R. M. Palomino, N. Rui, T. Duchoň, S. Nemšák, D. C. Grinter, M. Mahapatra, P. Liu, J. A. Rodriguez and S. D. Senanayake, *Science*, 2020, **368**, 513.
29. K. Curtis, D. Panthi and S. O. Odoh, *Inorganic Chemistry*, 2021, **60**, 1149-1159.
30. A. Martini, M. Signorile, C. Negri, K. Kvande, K. A. Lomachenko, S. Svelle, P. Beato, G. Berlier, E. Borfecchia and S. Bordiga, *Physical Chemistry Chemical Physics*, 2020, **22**, 18950-18963.
31. E. Borfecchia, D. K. Pappas, M. Dyballa, K. A. Lomachenko, C. Negri, M. Signorile and G. Berlier, *Catalysis Today*, 2019, **333**, 17-27.
32. E. Borfecchia, P. Beato, S. Svelle, U. Olsbye, C. Lamberti and S. Bordiga, *Chemical Society Reviews*, 2018, **47**, 8097-8133.
33. M. A. Newton, A. J. Knorpp, A. B. Pinar, V. L. Sushkevich, D. Palagin and J. A. van Bokhoven, *Journal of the American Chemical Society*, 2018, **140**, 10090-10093.
34. O. Suleiman, D. Panthi, O. Adeyiga and S. O. Odoh, *Inorganic Chemistry*, 2021, DOI: 10.1021/acs.inorgchem.0c03279, accepted.
35. A. A. Kolganov, A. A. Gabrienko, S. A. Yashnik, E. A. Pidko and A. G. Stepanov, *The Journal of Physical Chemistry C*, 2020, **124**, 6242-6252.
36. S. Grundner, M. A. C. Markovits, G. Li, M. Tromp, E. A. Pidko, E. J. M. Hensen, A. Jentys, M. Sanchez-Sanchez and J. A. Lercher, *Nature Communications*, 2015, **6**, 7546.
37. M. H. Mahyuddin, T. Tanaka, A. Staykov, Y. Shiota and K. Yoshizawa, *Inorganic Chemistry*, 2018, **57**, 10146-10152.
38. B. E. R. Snyder, M. L. Bols, R. A. Schoonheydt, B. F. Sels and E. I. Solomon, *Chem*



- Rev*, 2018, **118**, 2718-2768.
39. P. Hohenberg and W. Kohn, *Physical Review*, 1964, **136**, B864-B871.
  40. W. Kohn and L. J. Sham, *Phys. Rev.*, 1965, **140**, A1133-A1138.
  41. G. Wang, L. Huang, W. Chen, J. Zhou and A. Zheng, *Physical Chemistry Chemical Physics*, 2018, **20**, 26522-26531.
  42. L. Wang, Z. Li, Z. Wang, X. Chen, W. Song, Z. Zhao, Y. Wei and X. Zhang, *Industrial & Engineering Chemistry Research*, 2021, **60**, 2400-2409.
  43. A. R. Kulkarni, Z.-J. Zhao, S. Siahrostami, J. K. Nørskov and F. Studt, *Catalysis Science & Technology*, 2018, **8**, 114-123.
  44. P. Tomkins, A. Mansouri, S. E. Bozbag, F. Krumeich, M. B. Park, E. M. C. Alayon, M. Ranocchiari and J. A. van Bokhoven, *Angewandte Chemie International Edition*, 2016, **55**, 5467-5471.
  45. P. Buchwalter, J. Rose and P. Braunstein, *Chemical Reviews*, 2015, **115**, 28-126.
  46. M. Can, F. A. Armstrong and S. W. Ragsdale, *Chemical Reviews*, 2014, **114**, 4149-4174.
  47. S. A. Cook, E. A. Hill and A. S. Borovik, *Biochemistry*, 2015, **54**, 4167-4180.
  48. I. Garcia-Bosch, X. Ribas and M. Costas, *European Journal of Inorganic Chemistry*, 2012, DOI: 10.1002/ejic.201100957, 179-187.
  49. Y. Lyu, J. N. Jocz, R. Xu, O. C. Williams and C. Sievers, *Chemcatchem*, DOI: 10.1002/cctc.202100268.
  50. S. Van de Vyver and Y. Roman-Leshkov, *Angewandte Chemie-International Edition*, 2015, **54**, 12554-12561.
  51. P. Giannozzi, S. Baroni, N. Bonini, M. Calandra, R. Car, C. Cavazzoni, D. Ceresoli, G. L. Chiarotti, M. Cococcioni, I. Dabo, A. Dal Corso, S. de Gironcoli, S. Fabris, G. Fratesi, R. Gebauer, U. Gerstmann, C. Gougoussis, A. Kokalj, M. Lazzeri, L. Martin-Samos, N. Marzari, F. Mauri, R. Mazzarello, S. Paolini, A. Pasquarello, L. Paulatto, C. Sbraccia, S. Scandolo, G. Sclauzero, A. P. Seitsonen, A. Smogunov, P. Umari and R. M. Wentzcovitch, *Journal of Physics: Condensed Matter*, 2009, **21**, 395502.
  52. P. Giannozzi, O. Andreussi, T. Brumme, O. Bunau, M. Buongiorno Nardelli, M. Calandra, R. Car, C. Cavazzoni, D. Ceresoli, M. Cococcioni, N. Colonna, I. Carnimeo, A. Dal Corso, S. de Gironcoli, P. Delugas, R. A. DiStasio, A. Ferretti, A. Floris, G. Fratesi, G. Fugallo, R. Gebauer, U. Gerstmann, F. Giustino, T. Gorni, J. Jia, M. Kawamura, H. Y. Ko, A. Kokalj, E. Küçükbenli, M. Lazzeri, M. Marsili, N. Marzari, F. Mauri, N. L. Nguyen, H. V. Nguyen, A. Otero-de-la-Roza, L. Paulatto, S. Poncé, D. Rocca, R. Sabatini, B. Santra, M. Schlipf, A. P. Seitsonen, A. Smogunov, I. Timrov, T. Thonhauser, P. Umari, N. Vast, X. Wu and S. Baroni, *Journal of Physics: Condensed Matter*, 2017, **29**, 465901.
  53. K. D. Vogiatzis, G. Li, E. J. M. Hensen, L. Gagliardi and E. A. Pidko, *The Journal of Physical Chemistry C*, 2017, **121**, 22295-22302.
  54. P. E. Blöchl, *Physical Review B*, 1994, **50**, 17953-17979.
  55. G. Kresse and D. Joubert, *Physical Review B*, 1999, **59**, 1758-1775.
  56. J. P. Perdew, K. Burke and M. Ernzerhof, *Phys. Rev. Lett.*, 1996, **77**, 3865-3868.
  57. S. Grimme, J. Antony, S. Ehrlich and H. Krieg, *The Journal of Chemical Physics*, 2010, **132**, 154104.
  58. S. Grimme, S. Ehrlich and L. Goerigk, *Journal of Computational Chemistry*, 2011, **32**, 1456-1465.
  59. G. Henkelman, B. P. Uberuaga and H. Jónsson, *The Journal of Chemical Physics*, 2000, **113**, 9901-9904.

60. E. M. C. Alayon, M. Nachtegaal, M. Ranocchiari and J. A. van Bokhoven, *Chimia*, 2012, **66**, 668-674.
61. T. Ikuno, S. Grundner, A. Jentys, G. Li, E. Pidko, J. Fulton, M. Sanchez-Sanchez and J. A. Lercher, *The Journal of Physical Chemistry C*, 2019, **123**, 8759-8769.
62. L. Tao, I. Lee and M. Sanchez-Sanchez, *Catalysis Science & Technology*, 2020, **10**, 7124-7141.
63. F. X. Llabrés i Xamena, P. Fisicaro, G. Berlier, A. Zecchina, G. T. Palomino, C. Prestipino, S. Bordiga, E. Giamello and C. Lamberti, *The Journal of Physical Chemistry B*, 2003, **107**, 7036-7044.
64. R. Sabatini, T. Gorni and S. de Gironcoli, *Physical Review B*, 2013, **87**, 041108.
65. O. A. Vydrov and T. V. Voorhis, *The Journal of Chemical Physics*, 2010, **133**, 244103.
66. I. Hamada, *Physical Review B*, 2014, **89**, 121103.
67. D. N. Laikov, *Chemical Physics Letters*, 2005, **416**, 116-120.
68. D. N. Laikov and Y. A. Ustynyuk, *Russian Chemical Bulletin*, 2005, **54**, 820-826.
69. D. N. Laikov, *Theoretical Chemistry Accounts*, 2019, **138**, 40.
70. D. N. Laikov, *The Journal of Chemical Physics*, 2020, **153**, 114121.
71. P. Vanelderen, B. E. R. Snyder, M.-L. Tsai, R. G. Hadt, J. Vancauwenbergh, O. Coussens, R. A. Schoonheydt, B. F. Sels and E. I. Solomon, *J. Am. Chem. Soc.*, 2015, **137**, 6383-6392.
72. B. Ipek, M. J. Wulfers, H. Kim, F. Göttl, I. Hermans, J. P. Smith, K. S. Booksh, C. M. Brown and R. F. Lobo, *ACS Catalysis*, 2017, **7**, 4291-4303.
73. G. Turnes Palomino, P. Fisicaro, S. Bordiga, A. Zecchina, E. Giamello and C. Lamberti, *The Journal of Physical Chemistry B*, 2000, **104**, 4064-4073.
74. O. Adeyiga, O. Suleiman and S. O. Odoh, *Inorganic Chemistry*, 2021, **60**, 8489-8499.
75. O. Suleiman, D. Panthi, O. Adeyiga and S. O. Odoh, *Inorganic Chemistry*, 2021, **60**, 6218-6227.
76. M. H. Mahyuddin, A. Staykov, Y. Shiota, M. Miyanishi and K. Yoshizawa, *ACS Catalysis*, 2017, **7**, 3741-3751.
77. A. A. Arvidsson, V. P. Zhdanov, P.-A. Carlsson, H. Grönbeck and A. Hellman, *Catalysis Science & Technology*, 2017, **7**, 1470-1477.
78. M. H. Mahyuddin, T. Tanaka, Y. Shiota, A. Staykov and K. Yoshizawa, *ACS Catalysis*, 2018, **8**, 1500-1509.
79. A. A. Latimer, A. R. Kulkarni, H. Aljama, J. H. Montoya, J. S. Yoo, C. Tsai, F. Abild-Pedersen, F. Studt and J. K. Nørskov, *Nature Materials*, 2017, **16**, 225-229.
80. C. W. Andersen, E. Borfecchia, M. Bremholm, M. R. V. Jørgensen, P. N. R. Vennestrøm, C. Lamberti, L. F. Lundegaard and B. B. Iversen, *Angewandte Chemie International Edition*, 2017, **56**, 10367-10372.
81. K. T. Dinh, M. M. Sullivan, K. Narsimhan, P. Serna, R. J. Meyer, M. Dincă and Y. Román-Leshkov, *Journal of the American Chemical Society*, 2019, **141**, 11641-11650.
82. S. Grundner, W. Luo, M. Sanchez-Sanchez and J. A. Lercher, *Chemical Communications*, 2016, **52**, 2553-2556.
83. Y. Kim, T. Y. Kim, H. Lee and J. Yi, *Chemical Communications*, 2017, **53**, 4116-4119.
84. A. J. Knorpp, A. B. Pinar, C. Baerlocher, L. B. McCusker, N. Casati, M. A. Newton, S. Checchia, J. Meyet, D. Palagin and J. A. van Bokhoven, *Angewandte Chemie International Edition*, 2021, **60**, 5854-5858.
85. J.-P. Lange, V. L. Sushkevich, A. J. Knorpp and J. A. van Bokhoven, *Industrial & Engineering Chemistry Research*, 2019, **58**, 8674-8680.

86. D. Palagin, V. L. Sushkevich and J. A. van Bokhoven, *ACS Catalysis*, 2019, **9**, 10365-10374.
87. V. L. Sushkevich, D. Palagin, M. Ranocchiari and J. A. van Bokhoven, *Science*, 2017, **356**, 523-527.
88. A. R. Kulkarni, Z.-J. Zhao, S. Siahrostami, J. K. Nørskov and F. Studt, *ACS Catalysis*, 2016, **6**, 6531-6536.

## CHAPTER 7. SUMMARY AND CONCLUSIONS

The studies in this thesis provide insights into the reactivity of actinide species and copper-oxo active site motifs towards transformation of small molecules like H<sub>2</sub>O and CH<sub>4</sub>. Chapter 2 and 3 focused on actinide complexes, while Chapters 4 to 6 focused on works involving copper-exchanged zeolite.

In Chapter 2, we explored the possibility of applying multiconfigurational pair density functional theory (MC-PDFT) for structural, electronic and redox properties of actinyl species, specifically uranium, neptunium and plutonium. Comparing our results to experimental data when available, it was observed the ft-PBE, a fully translated MC-PDFFT functional had the best performance. The ft-PBE results were similar to those obtained using KS-DFT, thereby justifying the extensive use of standard KS-DFT functionals in actinide chemistry. Our results indicate that ft-PBE can be particularly useful for systems with greater static electron correlation effect, systems for which standard KS-DFT functionals might perform rather poorly.

In the following chapter, using scalar-relativistic and spin-orbit coupling DFT calculations, we examined the impact of ligand modulation on hydrogen evolution reaction (HER). In some cases, ligand substitution provided improved reactivities. We observed that ligand substitutions and environment (steric effects) can impact reactivity. In general, provided the ligand framework is favorable, An-O  $\rightarrow$  An-N ligand substitution makes the actinide complexes more reactive towards H<sub>2</sub> for hydride capture. Similarly for the electrocatalytic reduction of water, HER, we observed lower barriers by about 4 kcal/mol upon Np-O  $\rightarrow$  Np-NH substitution.

Moving on from actinide chemistry, in Chapter 4, we described mechanistic pathways for methane over-oxidation by copper-oxo active site motifs in mordenite zeolite. Using [Cu<sub>3</sub>O<sub>3</sub>]<sup>2+</sup> active site motif, we show that in the absence of oxygen, extra-framework [Cu<sub>3</sub>O<sub>3</sub>]<sup>2+</sup> can undergo four successive hydrogen atom abstraction (HAA) to form gaseous CO, an undesired over-oxidation product. Understanding the mechanism of over-oxidation is important, because this knowledge can be used guide reactions towards high methanol selectivities. We found that after the first HAA, the methyl group must be stabilized far away from the active site and trapped at an unreactive site to avoid further abstraction and ensure high methanol selectivity.

In Chapter 5, using Tamm-Dancoff time-dependent density functional theory (TDA-DFT) with  $\omega$ B2PLYP as our functional of choice, we analyzed changes in the optical spectra of activated

Cu-exchanged zeolites. In  $[\text{Cu}_2\text{O}]^+$ , our computed spectra produced a peak around  $22700\text{ cm}^{-1}$  matching the experimentally observed peak peculiar to this active site motif. Since, our computational protocol is capable of capturing important spectra changes, we were able to extend it to  $[\text{Cu}_3\text{O}_3]^{2+}$  active site, proposing possible species implicated in the methane-to-methanol activation process.

In conclusion, Chapter 6 highlights our effort towards the discovery of heterometallic species capable of methane to methanol conversion in an isothermal fashion with the overall aim of making the process economically viable. Substituting on of the Cu atoms in  $[\text{Cu}_2\text{O}]^{2+}$ , we studied several  $[\text{Cu-O-M}]^{2+}$  ( $M=3d$  and  $4d$  transition metals) and we found that several species are more stable than  $[\text{Cu}_2\text{O}]^{2+}$ . However, upon further examination of formation energies, autoreduction energies and C-H activation barriers, only  $[\text{Cu-O-Pd}]$  and  $[\text{Cu-O-Ag}]$  provide significant improvement compared to  $[\text{Cu}_2\text{O}]^{2+}$ . Unfortunately, the cost implication for these systems will impact industrial application.

## LIST OF PUBLICATIONS

1. N. K. Dandu, **O. Adeyiga**, D. Panthi, S.A. Bird, and S. O. Odoh. Performance of density functional theory for describing hetero-metallic active-site motifs for methane-to-methanol conversion in metal-exchanged zeolites. *Journal of Computational Chemistry*, **2018**, 39, 2667.
2. D. Panthi, **O. Adeyiga**, N.K. Dandu, and S. O. Odoh. Nitrogen reduction by multimetallic trans-uranium actinide Complexes: A theoretical comparison of Np and Pu to U. *Inorganic Chemistry*, **2019**, 58, 6731.
3. **O. Adeyiga**, O. Suleiman, N.K. Dandu, and S. O. Odoh. Ground-state actinide with scalar-relativistic Multiconfiguration pair-density functional theory. *The Journal of Chemical Physics*, **2019**, 151,134102.
4. **O. Adeyiga**<sup>#</sup>, D. Panthi<sup>#</sup>, O. Suleiman<sup>#</sup>, D. Stetler, R.W. Long, and S. O. Odoh. Activating water and hydrogen by ligand-modified uranium and neptunium complexes: A density functional theory study. *Inorganic Chemistry*, **2020**, 59, 3102. (*equally contributed first author*)
5. F. Chalyavi, **O. Adeyiga**, J.M. Weiner, J.N. Monzy, A.J. Schmitz, J.K. Nguyen, E.E. Fenlon, S.H. Brewer, S.O. Odoh, M.J. Tucker. 2D-1R studies of cyanamides (NCN) as spectroscopic reporters of dynamics in biomolecules: Uncovering the origin of mysterious peaks. *The Journal of Chemical Physics*, **2020**, 152, 074201.
6. D. Panthi, **O. Adeyiga**, and S.O. Odoh. DFT Analysis of methane C-H activation and over-oxidation by [Cu<sub>2</sub>O<sub>2</sub>]<sup>2+</sup> Sites in zeolite mordenite: Intra- versus inter-site over-oxidation. *ChemPhysChem*, **2021**, 22, 2517.
7. **O. Adeyiga** and S.O. Odoh. Methane over-oxidation by extra-framework copper-oxo active sites of copper-exchanged zeolites: Crucial role of traps for the separated methyl group. *ChemPhysChem*, **2021**, 22, 1101.
8. **O. Adeyiga**<sup>#</sup>, D. Panthi<sup>#</sup>, and S.O. Odoh. Heterometallic [Cu-O-M]<sup>2+</sup> active sites for methane C-H activation in zeolites: stability, reactivity, formation mechanism, and relationship to other active sites. *Catalysis Science & Technology*, **2021**, 11, 5671. (*equally contributed first author*)

9. O. Suleiman<sup>#</sup>, D. Panthi<sup>#</sup>, **O. Adeyiga<sup>#</sup>**, and S.O. Odoh. Methane C–H Activation by  $[\text{Cu}_2\text{O}]^{2+}$  and  $[\text{Cu}_3\text{O}_3]^{2+}$  in copper-exchanged zeolites: Computational analysis of redox chemistry and X-ray absorption spectroscopy. *Inorganic Chemistry*, **2021**, 60, 6218. (*equally contributed first author*)
10. O. Suleiman, **O. Adeyiga**, D. Panthi, and S.O. Odoh. Copper-oxo active sites in the 8MR of zeolite mordenite: DFT investigation of the impact of acid sites on methanol yield and selectivity. *Journal of Physical Chemistry C*, **2021** 125, 6684.
11. **O. Adeyiga**, O. Suleiman and S.O. Odoh. Copper-oxo active sites for methane C-H activation in zeolites: molecular understanding of impact of methane hydroxylation on UV-Vis spectra. *Inorganic Chemistry*, **2021**, 60, 8489.
12. B. Walls, O. Suleiman, C. Arambula, A. Hall, **O. Adeyiga**, F. Boumelhem, J. Koh, S.O. Odoh, Z.R. Woydziak. Improving the brightness of pyronin fluorophore systems through quantum-mechanical predictions. *The Journal of Chemical Physics Letters*, **2022**, 13, 8312.

#### **Submitted Manuscripts**

13. D. Panthi, **O. Adeyiga**, K. Curtis, O. Suleiman, and S.O. Odoh. Electronic structure and reactivity of the  $[\text{Cu}_2\text{AlO}_3]^{2+}$  cluster in the mordenite zeolite: Higher intrinsic  $\text{Cu}^{3+}$  and  $\text{O}^{2-}$  characters than  $[\text{Cu}_3\text{O}_3]^{2+}$ . *Submitted 2022*.
14. K. Curtis, **O. Adeyiga**, O. Suleiman and S.O. Odoh. Building on the strength of a double-hybrid density functional for excitation energies and inverted singlet-triplet gaps. *Submitted 2022*.